Earthquake Nucleation and Rupture at a Range of Scales: Laboratories, Gold Mines, and Subduction Zones

by

Eliza Bonham Richardson

A.B., Princeton University (1996)

Submitted to the Department of Earth, Atmospheric, & Planetary Sciences
in partial fulfillment of the requirements for the degree of

Doctor of Philosophy

at the

MASSACHUSETTS INSTITUTE OF TECHNOLOGY

June 2002

© Massachusetts Institute of Technology 2002. All rights reserved.

Author .....
Department of Earth, Atmospheric, & Planetary Sciences
March 5, 2002

Certified by .....
Thomas H. Jordan
Professor
Thesis Supervisor

Accepted by .....
Ronald G. Prinn
Department Head

WITHDRAWN
MASSACHUSETTS INSTITUTE OF TECHNOLOGY
FROM
JUL 19 2002
MIT LIBRARIES
LIBRARIES

Earthquake Nucleation and Rupture at a Range of Scales: Laboratories, Gold Mines, and Subduction Zones

by

Eliza Bonham Richardson

Submitted to the Department of Earth, Atmospheric, & Planetary Sciences
on March 5, 2002, in partial fulfillment of the
requirements for the degree of
Doctor of Philosophy

Abstract

We measured spectral and time-domain properties of seismic events over a size range that spans magnitudes $M \approx -2$ to 8 in order to study earthquake source processes. In addition, we conducted laboratory experiments to study interseismic behaviors that can influence earthquake nucleation and we developed a model of eathquake rupture to explain the scaling behaviors we observe. To bridge the scale gap between laboratory data and global seismic observations, we studied data from five deep gold mines in the Far West Rand region of South Africa. These mines are seismically active due to daily underground blasting and record ≈ 1000 events per day from $-2 \leq M \leq 3+$ close to their sources. Frequency-magnitude relations, spatio-temporal clustering relations and observations of seismic spectra provide evidence that there are two types of events that occur in these mines, which we designate as Type A and Type B.

Type-A events are fracture-dominated ruptures of previously intact rock and show an upper magnitude cutoff at $M \approx 0.5$. They are tightly clustered in space and time and occur close to active stope faces. They have scaling properties that agree with other studies of fresh-fracturing seismicity in that apparent stress decreases with magnitude and stress drop increases with magnitude. In contrast, Type-B events are temporally and spatially distributed throughout the active mining region. They have a lower magnitude cutoff at $M \approx 0$. From frictional scaling laws and observations of source spectra, we deduce that that this lower magnitude cutoff represents the critical patch size for earthquake nucleation in this mining environment. We find that the critical patch size is on the order of 10 m with a critical slip distance on the order of 10^{-4} m. Type-B events have scaling properties that match extrapolations from tectonic earthquakes. For example, apparent stress and particle velocity increase with magnitude. We develop a kinematic model of increasing rupture velocity with increasing source size to account for the observed scaling of frictional shear events.

Thesis Supervisor: Thomas H. Jordan
Title: Professor

Acknowledgments

I owe a great deal of thanks to the many individuals without whose support, advice, assistance, discussions, love, and good humor I would not have been able to complete my graduate studies nearly as effectively or happily. First and foremost I must thank the members of my family. I look forward to every day spent now and in the future growing together with Chris, Vicki, and Dan Marone. My parents Bon and Linda Richardson continue to support my endeavors in all fields. My sister Lucy Richardson will always be an inspiration to me because she downplays her many talents and is the fun engaging person the rest of us have to try so hard to be. I would not have looked forward to my visits to USC for the end game of papers and this thesis nearly so much without the hospitality of my aunt and uncle Barb and Joe Davis.

I probably learned more science from being in the company of my fellow grad students and Jordan group members than from any other source. In particular, thanks to Jeff McGuire, Frederik Simons, Margaret Boettcher, Keli Kárason, Clint Conrad, Jim Gaherty, Rafi Katzmann, Jun Korenaga, Kevin Frye, Steve Karner, Karen Mair, Hugh Cox, Oded Aharonson, Maureen Long, Li Zhao, and Liangjun Chen. In addition, Mark Behn and Noah Snyder contributed to my New England education by sharing with me the ins and outs of the special and depressing world of Red Sox nation.

I made several trips to South Africa during the course of my research and I am grateful to many people there for their assistance. I (probably literally) wouldn't have survived without Sue Webb. She, Lew Ashwal, and Mike Knoper gave me a fun place to stay on weekends, good scientific advice, all the 100's and 1000's bars I could eat, and listened to my conspiracy theories involving espionage at Wits University. I thank the miners and seismologists at Western Deep Levels for taking me on the many underground visits, copying data for me and providing me with all the background details necessary to understand the workings of the gold mines. I am especially

indebted to Dragan Amidzic, Vlok Visser, Lindsay Andersen, Friedemann Essrich, Gerard Finnie, and Alan Naismith. I learned quite a bit about the field of mining seismology from those at ISSI, including Alex Mendecki, Gerrie Van Aswegen, and Willem DeBeer. I had useful discussions with Steve Spottiswoode and Ewan Sellers at Miningtek and with Dave Ortlepp.

Thanks to Tom Jordan whose creative vision in seismology fueled our work together. Tom's time is always at a premium and I was fortunate that he spent so much of it with me at MIT, in the field, at meetings, and at USC. Thanks to my committee: Maria Zuber, Greg Hirth, Rob van der Hilst, and Wiki Royden.

I continue to profit from discussions with all the other scientists I have met during my time at MIT, including Chris, of course, Jim Rice, Renata Dmowska, Norm Sleep, Rachel Abercrombie, Bill Ellsworth, Demian Saffer, Nick Beeler, Mike Blanpied, Terry Tullis, Joan Gomberg, and John Vidale. I am looking forward to the road ahead at Penn State and I've already had the pleasure of interacting with the grad students and faculty there. They have made the transition easy and fun.

It was no doubt difficult for the EAPS administrative staff to deal with an absentee student and advisor in these last semesters, but they did an admirable job of everything from faxing the necessary paperwork to registering me for classes to keeping me informed about the status of elevator #3.

Thanks again to you all.

Contents

Chapter 1

Introduction

The initiation and propagation of material flaws is a phenomenon that occurs at a wide continuum of scale lengths: from lattice dislocations at the atomic level to the great earthquakes that rift the crust. The physics of earthquake processes is most often studied at two endmember size ranges – at large (kilometer) scales through direct seismic observations or at small (micron) scales in experimental laboratory work on fault frictional properties. Seismic waves are usually recorded on regional seismometer networks located kilometers or more from the earthquake hypocenters, limiting the resolution of these data to scales of faulting that are typically greater than 100 m, corresponding to events with $M > 2$, in which M is moment magnitude as defined by *Hanks and Kanamori* [1979]. As an example of seismology at large scales, Chapter 6 of this thesis details the source mechanisms of over 100 intermediate-focus (50-300 km depth) large ($M > 6$) earthquakes recorded by global networks. Experiments under controlled laboratory conditions are feasible only on synthetic faults with dimensions less than about 1 m ($M < -2$). These experiments are nonetheless crucial for understanding basic fault properties and the mechanics of brittle failure that occur during earthquakes. Chapter 2 describes a set of such laboratory experiments carried out in order to study the effect of transient stresses on faults during the earthquake cycle.

Studying large tectonic events and laboratory fault zones alone results in an observational gap in the sampling of seismic processes that spans about four orders of

magnitude in event size. Considerable progress has been made to shrink this gap using local arrays, e.g. *Rubin et al.* [1999] and instrumented boreholes, e.g. *Abercrombie* [1995]; *Nadeau and Johnson* [1998]; *Nadeau and McEvilly* [1999]; *Prejean and Ellsworth* [2001]. These studies recorded seismicity down to $M \approx -1$ and have produced important results in extending and improving our knowledge of source scaling and fault behavior.

Such small-magnitude events are also of interest in the study of earthquake nucleation and the related phenomena of slip and stress heterogeneity on faults. The initiation of rapidly propagating shear ruptures on weak faults is thought to be governed by a critical slip distance D_c over which fault friction drops from a static to a dynamic value [*Ida*, 1972; *Andrews*, 1976a; *Dieterich*, 1986; *Scholz*, 1988]. Constitutive rate- and state-dependent friction laws have been used to model laboratory data [*Dieterich*, 1979; *Ruina*, 1983]; they yield estimates of D_c for bare surfaces on the order of 10^{-5} m [*Marone and Kilgore*, 1993; *Marone*, 1998a]. According to slip-weakening models, nucleation proceeds quasi-statically at an overstressed point on a fault until the slipping patch reaches a critical radius r_c, when dynamic rupture will begin [*Ida*, 1973; *Palmer and Rice*, 1973; *Andrews*, 1976a; *Dieterich*, 1979]. These models treat D_c as the nucleation distance over which slip is incurred on a finite process zone ahead of a propagating crack tip, which for friction-dominated ruptures scales with the critical nucleation patch size. This inner dynamical scale specifies a minimum earthquake magnitude $M_{\min}$. For example, a stress drop $\Delta\sigma = 0.3$ MPa, a shear modulus $G = 30$ GPa and a $D_c = 10^{-5}$ m, yields $r_c \approx (G/\Delta\sigma)D_c \approx 1$ m, corresponding to $M_{\min} \approx -2.2$. Events of this magnitude are far below the detection thresholds of most surface seismometer and strainmeter networks.

It is not clear how best to extrapolate laboratory results to the scales of crustal faults. Large values of D_c (> 10 cm) have been inferred from the high-frequency spectral cutoffs and barrier strengths observed for tectonic earthquakes [*Ida*, 1973; *Aki*, 1979; *Papageorgiou and Aki*, 1983a], which imply much higher minimum magnitudes: $M_{\min} > 2.5$ for stress drops less than 30 MPa. A possible explanation is that the effective critical slip distance increases with fault-zone width W according to a

strain-weakening model of the form $D_c = \gamma_c W$ [*Andrews*, 1976a; *Aki*, 1979]. Laboratory data are consistent with a critical strain of $\gamma_c = 10^{-2}$, provided W is interpreted as the width of the fault zone actually participating in the slip–i.e., the integrated shear-band thickness [*Marone and Kilgore*, 1993; *Sammis and Steacy*, 1994; *Marone*, 1998a]. The seismically-derived values of D_c thus require wide (on the order of 1m) shear-band thicknesses or additional mechanisms, such as near-fault damage, for energy dissipation at the rupture front. In the former case, the effects of the inner dynamical scale, including the lower magnitude cutoff, should be observable in the seismographic data. *Aki* [1987] presented evidence for a falloff in seismicity below $M \approx 3$ from borehole-seismometer records in southern California, which he interpreted as support for a strain-weakening model with a large W. Studies of events in the Hokkaido corner and intermediate-focus earthquakes in Romania have shown similar seismicity falloffs at $M < 3$ [*Rydelek and Sacks*, 1989; *Taylor et al.*, 1990; *Trifu and Radulian*, 1991]. On the other hand, *Abercrombie* [1995] analyzed data from the deeper and more sensitive Cajon Pass borehole seismometers and detected no significant deviations from the Gutenberg-Richter frequency-magnitude relationship down to about $M = 1$ for southern California. Further studies of small earthquakes are necessary to understand the relationship between laboratory, local, regional, and global observations.

Mining-induced seismicity not only occurs at scales between those in the laboratory and those on tectonic faults, but can be recorded at the depth of seismic nucleation using in-mine seismometers, thus creating an excellent "natural laboratory" in which to study the physics of earthquake rupture. Mine seismicity has been the subject of extensive investigation for nearly forty years [*Cook*, 1963; *Spottiswoode and McGarr*, 1975; *McGarr*, 1984a; *Gibowicz and Kijko*, 1994]. The goals of minimg seismology have generally been twofold. The first is assessment of hazardous areas in a mine in which "rockbursts" (damaging seismic events) or "falls of ground" (caused by shaking during an event) are most likely to result in costly damage and delays to the ore extraction process. The second goal is fast and accurate location and magnitude determination of events so that the affected area can be stabilized or rescue

teams can be sent to free trapped miners. This is why the seismology unit at most South African mines is usually housed in the mine safety department rather than with other geophysically-oriented units such as surveying and exploration. There has been a good deal of scientific study of rockbursts, well-summarized in *Gibowicz and Kijko* [1994], yet limited attention is given to this field in the United States, compared to seismological studies of large earthquakes. Since the performance and sensitivity of the seismic networks has been greatly improved during the last five years by the installation of on-reef, three-component geophones, digital recording systems, and improved software for data processing [*Mendecki*, 1997], we have the ability to use mining-induced seismicity extensively to bridge the scale gap between laboratory data and tectonic events.

Chapters 3 and 4 describe in detail the mine environment, provide an analysis of the kinds of events that occur in mines and discuss first-order observations of their source properties, such as their frequency-magnitude statistics and their spatio-temporal relationships. In addition, evidence supporting the hypothesis of the existence of a minimum "critical" event size in this environment is put forth. Chapter 5 presents source scaling relations relating energy, stress drop, apparent stress and near-source ground velocity derived from combining this mining-induced seismicity dataset with both laboratory and tectonic datasets of previous workers.

Chapter 2

Effects of Normal Stress Vibrations on Frictional Healing

Published in *Journal of Geophysical Research* by E. Richardson and C. Marone, **104**, 28,859-28,878, 1999. Copyright by the American Geophysical Union.

Abstract. We conducted laboratory experiments to study frictional healing and the effects of normal stress vibrations on healing. The experiments were carried out using a servo-controlled double-direct shear apparatus on 10 cm x 10 cm blocks separated by a 3 mm-thick gouge layer of fine-grained (grain size of 75-212 μm) quartz powder. We performed slide-hold-slide tests in which sliding surfaces were driven at a constant velocity, halted for a given interval, then restarted at the prior driving velocity. Healing varied systematically with cumulative displacement, and by conducting several sets of identical slide-hold-slides we calibrated and removed these effects. Forward modeling of the healing and relaxation curves using the rate- and state-dependent friction laws shows that a displacement-dependent increase in the parameter b can account for our observations. To study the effects of vibration, we varied the mean normal stress of 25 MPa during holds by double amplitudes ranging from 1 to 13 MPa at a frequency of 1 Hz. Vibrations increased rates and magnitudes of frictional relaxation and healing, most likely due to increased gouge compaction. These effects increased with increasing amplitude of vibration. We performed normal

stress step tests and used the results to model the vibrational slide-hold-slide tests. Rate- and state-dependent constitutive laws cannot adequately describe the behavior we observed experimentally because they neglect gouge compaction. Mechanisms such as normal force oscillations may explain faster fault healing rates than would be predicted by standard laboratory measurements at constant stress.

2.1 Introduction

Time-dependent frictional healing between slip events is a crucial part of the seismic cycle and is observable in both laboratory experiments [*Dieterich*, 1972, 1979; *Johnson*, 1981] and natural faults [*Vidale et al.*, 1994; *Marone et al.*, 1995]. Static and dynamic stress changes due to nearby earthquakes have been observed to affect fault healing and stability [*Mavko et al.*, 1985; *Spudich et al.*, 1995; *Wang and Cai*, 1997] or to trigger other earthquakes [*Hill et al.*, 1993; *Gomberg et al.*, 1997]. These effects have largely been interpreted and modeled only in the case of changes in shear stress resolved on to the fault [*Rice and Gu*, 1983; *Dieterich*, 1988], although often the accompanying change in normal stress is significant as well [*Mavko et al.*, 1985; *Linker and Dieterich*, 1992]. In addition, most laboratory rock friction experiments are conducted at constant normal stresses, thus preventing direct comparison of laboratory data with models and observations of the effect of stress changes during frictional healing.

Previous laboratory studies in rock friction have characterized the effects of changes in normal stress on steady state friction [*Linker and Dieterich*, 1992; *Dieterich and Linker*, 1992; *Wang and Scholz*, 1994]. These experiments have determined that a sudden change in normal stress produces a direct response in the direction of the normal stress change followed by a relaxation and subsequent evolution to a new steady state in friction. This process is analogous to the effect on friction of a sudden change in load point velocity. *Linker and Dieterich* [1992] have interpreted these results in the framework of the rate- and state-variable friction laws, while *Wang and Scholz*

[1994] explained them in terms of a micromechanical contact model.

Studies of vibrated granular material [*Kudrolli et al.*, 1997; *Delour et al.*, 1999] have focused on establishing the fundamental behavior of particles subjected to vibrations. This includes particle velocities, trajectories, and collision energies. These experiments have typically been conducted at low normal stresses (< 1 MPa), at high velocities (10^0-10^3 mm/s), and with very high frequency stress oscillations (10^2-10^4 Hz). Nevertheless, their results are interesting in a geophysical context because understanding the dynamic properties of vibrated granular materials can lead to a better understanding of how stress variations such as vibrations lead to changes in frictional parameters.

Effects of stress oscillations during steady sliding have been studied experimentally for metallic friction (e.g. *Broniec and Lenkiewicz* [1982]; *Skåre and Ståhl* [1992] and *Polycarpou and Soom* [1995a, b]). Since these investigators have been concerned primarily with the mechanical stability and wear experienced by moving machine parts, their experiments have also been conducted at low normal stresses, high velocities, and high frequencies compared to values that we expect to be relevant in tectonic environments. The experimental results have been somewhat inconsistent. All found that friction decreases in response to any vibrations in the direction of shearing. However, normal force vibrations are observed to cause either increases or decreases in friction. The former has been explained as contact welding or hardening between the metallic surfaces [*Broniec and Lenkiewicz*, 1982; *Skåre and Ståhl*, 1992], and the latter likely occurs when the amplitude of external vibrations is large enough to cause loss of contact between the surfaces or when their frequency is close to the resonant frequency of one of the contacting materials [*Broniec and Lenkiewicz*, 1982; *Hess and Soom*, 1991; *Tworzydlo and Becker*, 1991]. Additional observations from these experiments include the reduction of stick-slip behavior during vibration and the decrease in friction with increasing frequency of vibration [*Skåre and Ståhl*, 1992].

In this paper we report the impact of dynamic stressing on the rate and degree of frictional healing in laboratory friction experiments. We found that normal stress oscillations during quasi-stationary contact enhanced both frictional healing and re-

laxation and that this effect increased with increasing amplitude of oscillation.

2.2 Experimental Procedure

The experiments we describe were performed in a biaxial loading apparatus at room temperature, pressure, and humidity in the double-direct shear geometry (Figure 2-1 inset). The vertical ram driving the central block was controlled in displacement feedback, and the horizontal ram used to maintain normal stress was controlled in load feedback. The position and force of each ram are measured by displacement transducers (DCDTs) and load cells mounted on the rams. The shear load point position is measured at the end of the vertical ram where load is measured. The machine stiffness for the vertical load frame, which applies shear, is 5 MN/cm (250 MPa/cm for a 10 cm $\times$ 10 cm sample). Slip on the frictional surfaces and changes in gouge layer thickness were calculated using the calibrated apparatus stiffness from the load point and horizontal ram displacement, respectively. However, during dynamic variation in normal stress, we made direct measurements of gouge layer compaction using DCDTs mounted on the sample. Additional details of the experimental apparatus are given by *Karner and Marone* [2001].

Two 3-mm layers of fine-grained (91% of grains between 75 and 212 μm) silica powder (U.S. Silica F-110, 99.8% $Si0_2$) were sheared between either steel or Westerly granite samples. For the steel samples the side blocks measured 10 $\times$ 10 $\times$ 4 cm and the central block measured 10 $\times$ 15 $\times$ 4 cm. For the Westerly samples the side blocks measured 10 $\times$ 10 $\times$ 4 cm and the central block measured 10 $\times$ 15 $\times$ 8 cm. In this configuration the nominal area of frictional contact remains constant (10 cm $\times$ 10 cm) during sliding. The surfaces of the steel blocks contain horizontal grooves so that shear was forced to occur within the gouge layer. The surfaces of Westerly granite were surface ground flat to $\pm$0.001 inch over their extent and then sand-blasted to increase roughness and inhibit boundary shear.

The normal force steps and vibrations were achieved by adding an external signal

Table 2.1: Experimental Data. Amplitudes are double amplitudes for vibration experiments and single amplitudes for the step experiments

Exp.	Type	Amplitude (MPa)
m081	displacement	0
m083	displacement	0
m085	displacement	0
m089	σ_n vibration	5.5
m092	σ_n vibration	1.0
m093	σ_n vibration	3.8
m095	σ_n vibration	3.7
m107	displacement	0
m113	σ_n vibration	5.6
m114	σ_n vibration	11.5
m117	σ_n vibration	5.6
m134	σ_n vibration	12.5
m223	σ_n vibration	3.7, 5.6
m224	σ_n vibration	4.7, 2.8
m225	σ_n vibration	10.4, 5.2
m226	σ_n vibration	9.1, 8.0
m237	σ_n step	0.2, 1.0
m238	σ_n step	0.4, 1.2, 1.6, 2.2
m272	σ_n step	1.2, 2.0, 2.5, 4.5
m272	σ_n vibration	1.3, 1.9, 2.8, 3.8

to the constant horizontal force maintained by servo-control (250 kN for all these experiments). A square wave with zero minimum or a trapezoidal wave with an instant increase but a ramp decrease was used for the normal stress steps. For the oscillations the added signal was a 1-Hz harmonic oscillation with zero mean. The amplitude of the steps and oscillations was controlled by adjusting the magnitude of the external signal and was set to zero during the parts of the experiments that were performed at constant normal stress (Table 2.1).

2.3 Data and Observations

We performed slide-hold-slide tests to measure frictional healing using the same

method as outlined by *Dieterich* [1972] and *Beeler et al.* [1994]. In typical slide-hold-slide tests the load point is driven at a constant velocity, halted for a given length of time, then restarted at the previous driving velocity. During the interval in which the load point is stationary, frictional strength relaxes as the shearing surfaces continue to creep. Upon reloading, the shearing surfaces restrengthen to some peak value of static friction, then evolve over some characteristic displacement, eventually returning to the same steady state value of sliding friction prior to the hold. We next present observations of frictional relaxation and healing that were used to characterize the effects of total displacement and variable normal stress on frictional restrengthening during quasi-stationary contact.

2.3.1 Effects of Displacement

In order to compare data from slide-hold-slide tests that included normal force vibrations to data from tests at constant stress, we first sought to eliminate other second-order effects that would also contribute to the rate and degree of frictional healing. Therefore we used a constant load point velocity, gouge layer thickness, and mean normal stress among all experiments. Within individual experiments, absolute displacement of the sliding surfaces also has an effect on frictional healing. To calibrate this effect, we performed several identical sets of slide-hold-slide tests over a range of absolute displacements (Figure 2-1).

This experiment was performed at a constant normal stress of 25 MPa. Before any shear load was placed on the sample, the normal load was set at 25 MPa, as with all the experiments. Then the vertical ram was started at a driving velocity of 10 μm/s. Next, a "load cycle" was performed in which the vertical ram was retracted at 10 μm/s until the shear load was removed completely, after which the ram was driven forward again, forming the hysteresis loop shown in Figure 2-1. Next, we executed a series of velocity step tests. During these tests, the load point velocity was rapidly increased from 10 to 20 μm/s. After a new steady state value of sliding friction was reached, the load point velocity was returned to 10 μm/s. This cycle was repeated

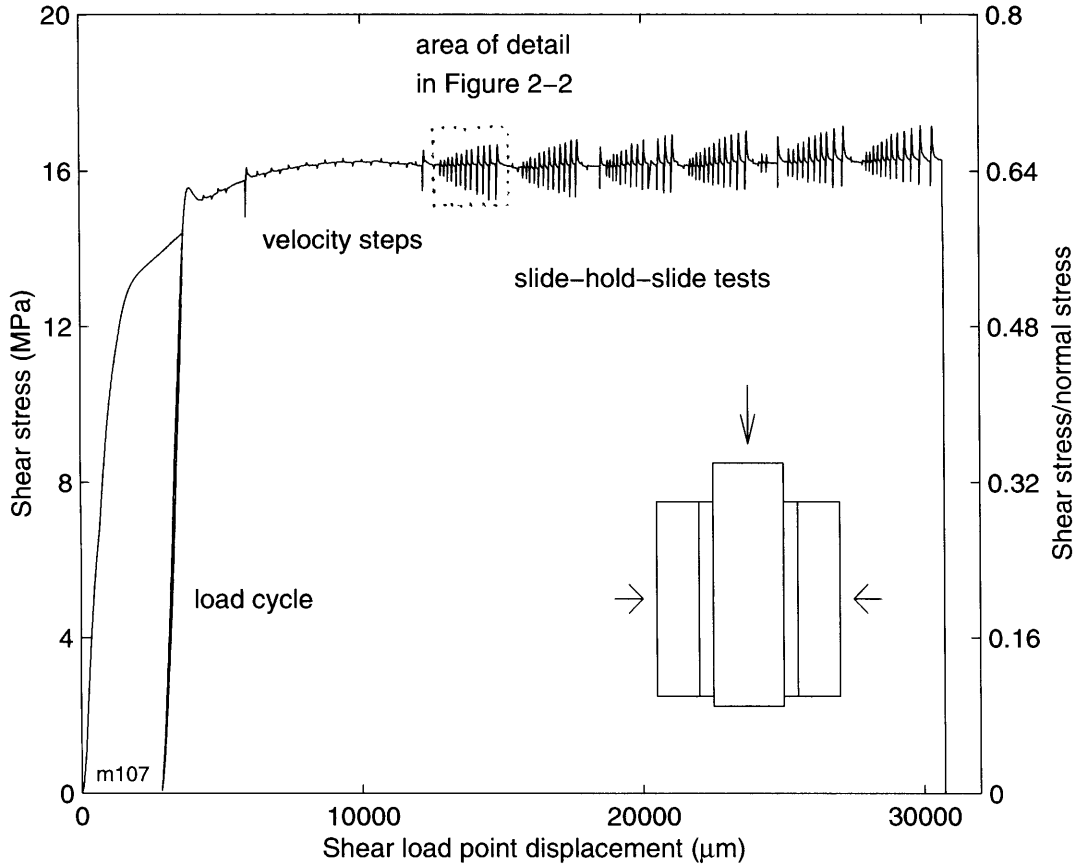

Figure 2-1: Shear stress versus shear displacement for a 3-mm gouge layer sheared at 10 μm/s between rough steel surfaces at 25 MPa normal stress. Shown are the initial loading, a load cycle, velocity steps, and six sets of slide-hold-slide tests. Detail of the first set of these is shown in Figure 2-2. Inset shows the double-direct shear configuration. The number in the bottom left corner refers to the experiment number in Table 2.1.

continuously over the first 12 mm of displacement.

After $\sim$ 9 mm of shear displacement the system evolved from a strain-hardening regime to a velocity-weakening regime in which frictional resistance decreased with increasing slip speed. This transition has been noted by previous investigators and is thought to occur in response to the development of localized shear bands within the gouge layer [*Dieterich*, 1979; *Tullis and Weeks*, 1986; *Marone et al.*, 1990]. We waited until velocity weakening was reached before performing the slide-hold-slide tests.

The experiment shown in Figure 2-1 included six identical sets of slide-hold-slide tests. Each set was accomplished at a load point velocity of 10 μm/s and included two holds each for 3, 10, 30, 100, 300, and 1000 s (Figure 2-2). For each hold in each set we measured frictional healing ($\Delta\tau$) as the difference between steady state sliding shear stress just prior to stopping the load point and the peak value of shear stress reached upon reload. We measured frictional relaxation ($\Delta\tau_{\mathrm{min}}$) as the difference between steady state sliding shear stress and the minimum value of shear stress reached just before the load point was restarted. We also measured fault gouge compaction as the decrease in gouge layer thickness during the quasi-stationary hold (Figure 2-2b). We report values for healing and relaxation in terms of shear stress rather than friction to avoid confusion when we describe later experiments in which the normal stress was varied.

The magnitude of frictional healing, relaxation, and gouge compaction increases linearly with the logarithm of hold time (Figures 2-3a, 2-3b, and 2-3c). This result is in agreement with observations from previous studies that have measured frictional healing [*Dieterich*, 1972; *Johnson*, 1981; *Beeler et al.*, 1994] as well as relaxation and gouge compaction [*Marone*, 1998b; *Karner and Marone*, 1998]. In an individual experiment the magnitude of healing for equal hold times increases with displacement. In addition, the dependence of healing on log hold time increases with displacement. The dependence of the relaxation and compaction on displacement (Figures 2-3b and 2-3c) show just the opposite trend.

The 1000-s holds in each of the six sets of tests (Figures 2-3d, 2-3e, and 2-3f) show that healing, relaxation, and gouge compaction vary approximately logarithmically

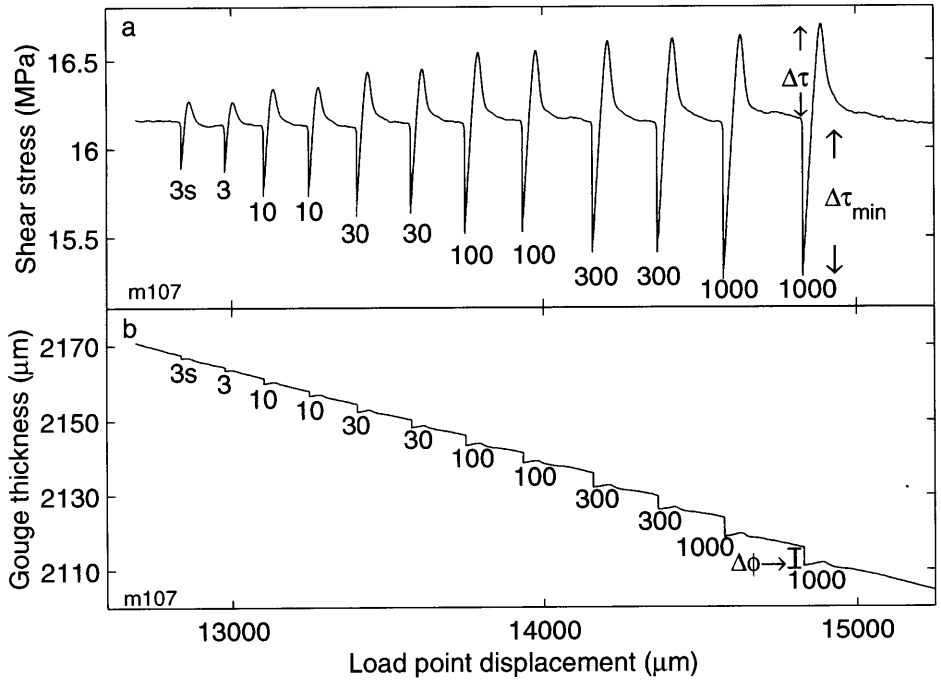

Figure 2-2: (a) Shear stress and (b) gouge layer thickness versus shear displacement for the first set of slide-hold-slide tests from Figure 2-1. Hold time in seconds is labeled beneath each hold. The measured quantities healing ($\Delta\tau$), relaxation ($\Delta\tau_{\min}$), and gouge compaction ($\Delta\phi$) are labeled on the last 1000-s hold. The continuous geometrical thinning of the gouge layer is inherent in the double-direct shear geometry [*Scott et al.*, 1994].

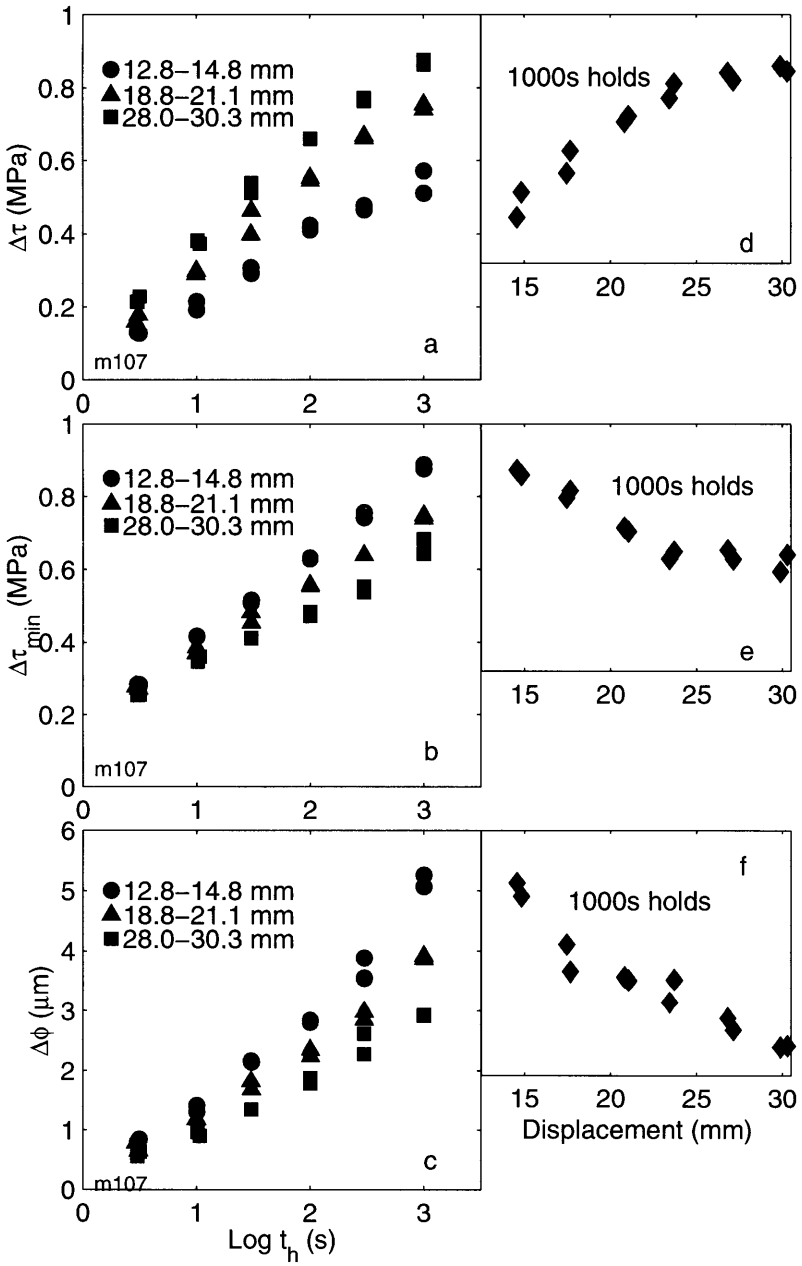

Figure 2-3: Time dependence of healing, relaxation, and compaction. For the first, third, and sixth sets of slide-hold-slide tests shown in Figure 2-1, (a) $\Delta\tau$, (b) $\Delta\tau_{min}$, and (c) $\Delta\phi$ are plotted versus $\log_{10}$ of hold time. Absolute shear displacement for each set is shown in the upper left. (d,e,f) Healing, relaxation, and compaction for each of the 1000-s holds in all six sets of slide-hold-slide tests as a function of absolute displacement.

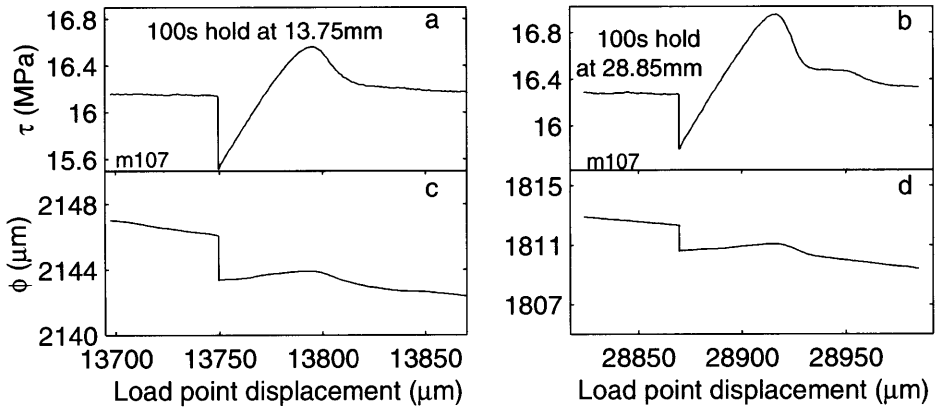

Figure 2-4: (a,b) Shear stress and (c,d) gouge layer thickness versus shear load point displacement for two 100-s slide-hold-slides at different displacements shown at the same scale. The slide-hold-slide on the left (Figures 4a and 4c) underwent greater relaxation and gouge compaction but less healing than the test at larger displacement (Figures 4b and 4d).

with increasing shear displacement. This effect of absolute displacement is also evident in the actual time series data (Figure 2-4) in which we compare two 100-s holds from the first and sixth tests at exactly the same scale.

We characterized the effects of displacement on the evolution of shear friction in order to eliminate them from our data. Once these effects were removed, we could determine the effects of other second-order variations, such as changes in normal stress.

2.3.2 Normal Stress Steps

We performed experiments similar to those described by *Linker and Dieterich* [1992] in which we rapidly stepped the normal force during steady sliding in order to observe the evolution of friction (Figure 2-5). For these experiments, sliding surfaces were driven at a constant speed of 10 μm/s, and the initial normal stress was 25 MPa. The magnitude of our normal stress steps ranged from 0.2 to 2.5 MPa, or 1-10% of the initial normal stress.

Like *Linker and Dieterich* [1992], we observed that shear stress increased instantly

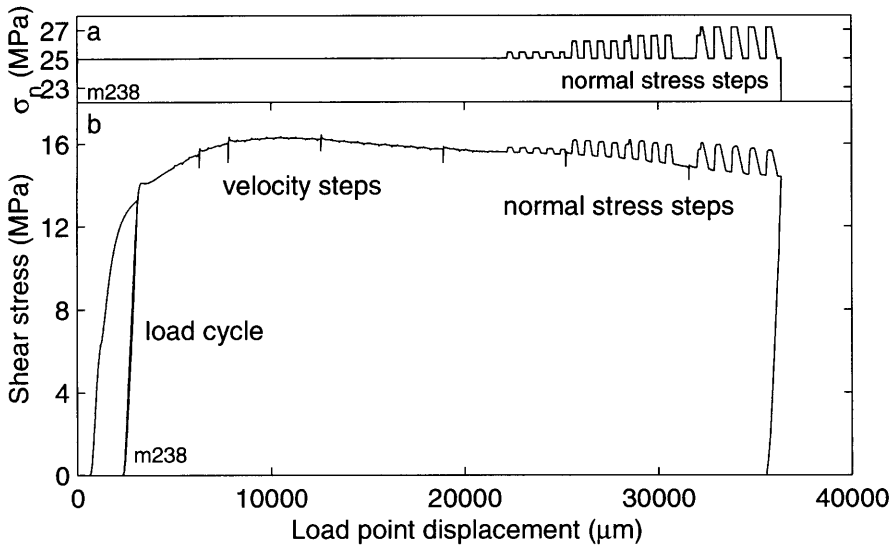

Figure 2-5: (a) Normal stress and (b) shear stress versus shear load point displacement for an experiment including four sets of normal stress steps (0.42, 1.20, 1.61, and 2.20 MPa). Normal stress was increased as rapidly as possible under servo control (each step occurred <0.2 s), but was ramped down to its initial value to prevent unstable sliding.

when the normal stress was stepped due to the Poisson effect. However, we found that the ratio of shear stress change to normal stress change was ~ 0.01 for Westerly granite testing blocks and 0.02 for steel blocks. This is smaller by an order of magnitude than the ratio observed by *Linker and Dieterich* [1992]. This discrepancy is most likely due to the fact that they mounted their DCDTs directly on their sample blocks, and thus their effective stiffness was larger, and because their apparatus may have been slightly misaligned [*Linker and Dieterich*, 1992].

Following the Poisson effect, we observed elastic shear loading and subsequent evolution to steady state sliding at constant stresses. We measured the difference in shear stress between its value at the end of the elastic loading period and its subsequent steady state value in order to determine the quantity that *Linker and Dieterich* [1992] term "α," in which

$$\alpha = \frac{\Delta\tau_{\text{step}}/\sigma_{\text{final}}}{\ln(\sigma_{\text{final}}/\sigma_{\text{initial}})}. \tag{2.1}$$

Figure 2-6 shows one normal stress step. The point at which shear loading deviates

from a linear elastic loading curve (τ_{elastic}) is marked with a circle. Note that the Poisson effect (marked with a diamond) is barely observable (Figure 2-6). It is clearly visible in the vibration tests with larger normal stress variations shown in later figures. The quantity $\Delta\tau_{\text{step}}$ is the difference between the steady state shear stress following the normal stress step and τ_{elastic} and is of interest because it is the evolution in shear stress that occurs with slip after the normal stress change. In order to determine the value of τ_{elastic} we incrementally fit a line to the shear loading curve, beginning with the data point corresponding to the beginning of the normal stress step. Each successive fit included one additional data point. We defined τ_{elastic} to be the data point corresponding to the last local minimum in the error of fit, thus the final data point that belonged to the best fit line in a least squares sense.

Observations of the evolution of the gouge layer are as important as observations of shear stress in determining the effect of sudden normal stress steps on the frictional state of the system. We measured the changes in gouge layer thickness with two linear voltage differential transducers (LVDTs) mounted directly on the front face of the sample. The data we show (Figure 2-6c) are an average of the signal from these two sample-mounted LVDTs. As soon as the 2.5-MPa normal stress step was executed, the gouge layer compacted by about 5 μm. The gouge layer continued to compact rapidly during elastic loading. The point in displacement that marked the end of the elastic shear loading is marked on the gouge layer record with a circle (Figure 2-6c). The gouge layer continued to compact faster than at steady state over the same interval in displacement that corresponds to $\Delta\tau_{\text{step}}$, after which a new steady state was reached.

The slope (α) of the least-squares best fit line to measurements of $\Delta\tau_{\text{elastic}}/\sigma_{\text{final}}$ constrained to pass through the origin is 0.30 (Figure 2-7). *Linker and Dieterich* [1992] used an approximately similar method to determine τ_{elastic} and to find α; they obtained $\alpha = 0.2$. However, they also argue that α may be as large as 0.5; therefore our value seems reasonable. In sections 4.2-4.3, we use α to model data for normal stress steps and vibrational slide-hold-slide tests.

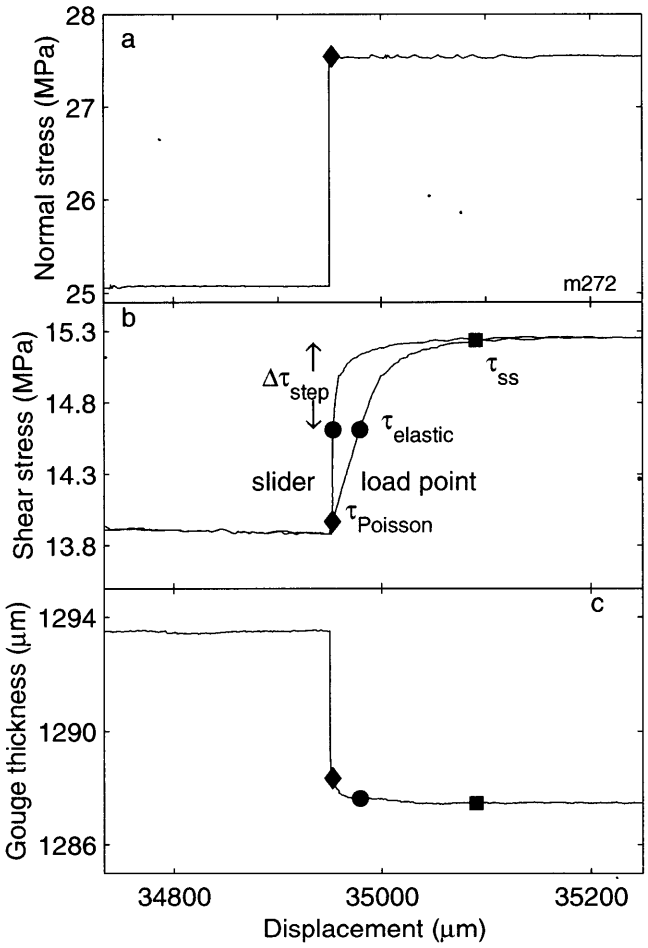

Figure 2-6: (a) Normal stress, (b) shear stress, and (c) gouge layer thickness as a function of shear displacement for one normal stress step. Normal stress and layer thickness are shown versus the load point displacement; shear stress is shown versus both load point displacement and slip measured directly across the sliding surfaces. The 2.5-MPa step in normal stress was accomplished in (<0.2 s). The shear stress increased instantaneously by 0.05 MPa due to Poisson expansion of the central forcing block (marked with a diamond). The shear stress followed an elastic loading curve until τ_{elastic} (marked with a circle), then evolved to a new steady state (marked with a square); the difference between the new steady state and τ_{elastic} is $\Delta\tau_{\text{step}}$. The displacements at which τ_{Poisson}, τ_{elastic}, and τ_{ss} occur are also marked on the layer thickness curve. The effects of continual geometric layer thinning have been removed.

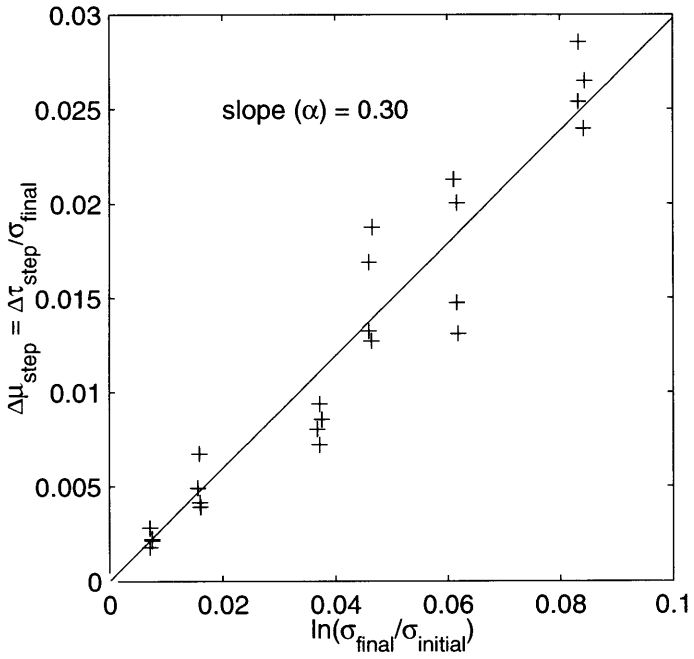

Figure 2-7: Nonelastic change in shear strength ($\Delta\tau_{\text{step}}$) upon a step change in normal stress (see Figure 2-6b). $\Delta\tau_{\text{step}}$ is normalized by final normal stress and plotted versus the natural logarithm of the ratio of the final to the initial normal stress for 24 normal stress step tests. The line is the least squares best fit line to the data constrained to pass through the origin. Its slope, 0.30, equals α [*Linker and Dieterich*, 1992].

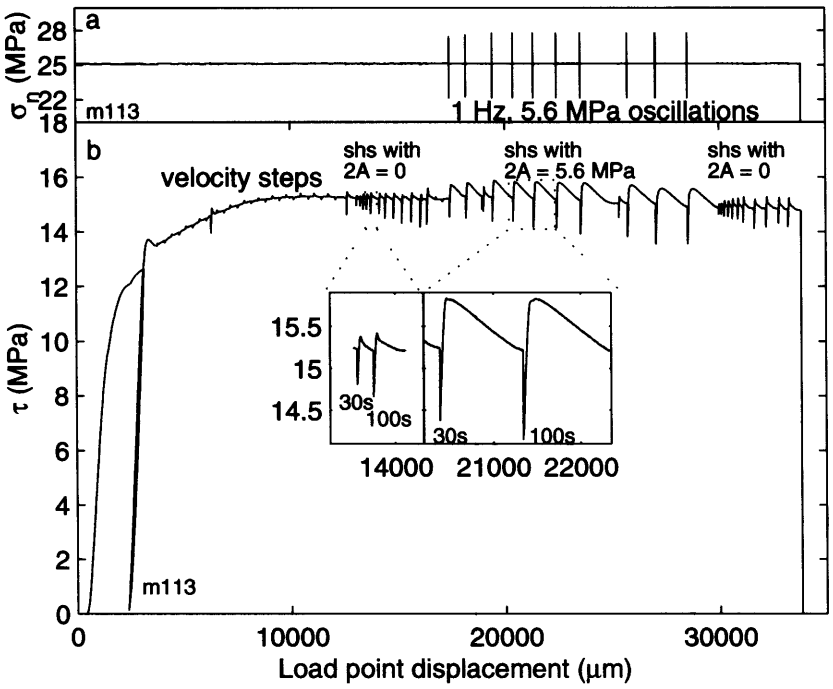

Figure 2-8: (a) Normal stress and (b) shear stress versus shear displacement for a 3-mm gouge layer sheared at 10 μm/s between sand-blasted Westerly granite surfaces. The first and third sets of slide-hold-slide tests were performed at constant normal stress (25 MPa). During the second set of slide-hold-slide tests, normal stress was oscillated at 1 Hz and a $2A = 5.6$ MPa for the duration of the hold, then returned to 25 MPa at the end of the hold. The Figure 2-8b inset figure shows four slide-hold-slides (right) with and (left) without vibrations.

2.3.3 Normal Stress Vibrations

We tested the effects of normal stress oscillations on frictional healing by vibrating at a constant amplitude and frequency during the quasi-stationary intervals of the slide-hold-slide tests. All of the experiments with normal stress oscillations were started exactly the same way as the experiment in Figure 2-1. Following the standard loadup and initial shearing procedure, slide-hold-slide tests with normal force oscillations were performed. These were usually followed by another set at constant stress or by another set of slide-hold-slides with oscillations (Figure 2-8).

Normal stress vibrations were accomplished by first stopping the vertical ram as in a standard slide-hold-slide, then ramping up the amplitude of the normal force

oscillations to some constant amplitude ($2A = 5.6$ MPa for the experiment in Figure 2-8). These oscillations were maintained for a given time interval, then reduced to zero amplitude again before the vertical ram was restarted. Figure 2-9 shows this procedure in detail for one 30-s slide-hold-slide test with normal force oscillations of 4.7-MPa double amplitude.

There was a lag of a few seconds at the beginning (t_1 - t_2 in Figure 2-9) and end (t_5 - t_6) of every vibrational hold since the vibration amplitude was adjusted by hand. Similarly, there was a finite time over which the normal force oscillations were increased to the chosen amplitude (t_2 - t_3) and decreased back to zero (t_4 - t_5). We chose to increase/decrease the amplitude of the oscillations gradually in order to maintain constant frequency and so that the total signal to the servo-control varied smoothly at the onset and end of the vibrations. This prevented unstable sliding at the beginning of holds associated with large-amplitude reductions in normal stress. These short time lags were approximately constant for all holds because they only depended on the reflexes of the operator. The vibrational hold time was generally 5-7 s less than the total "hold time"; however, we always report the total hold time. This discrepancy necessarily affects short holds more than long ones, but we assume the effect is negligible and do not correct for it in any way.

Frictional Healing. The most significant effect of vibration during holds was the overall degree of frictional relaxation and subsequent restrengthening. The inset detail in Figure 2-8 compares two nonvibrational holds with two vibrational holds of equal times. These two pairs are shown at the same scale. Clearly, relaxation and especially healing, which more than doubled in comparison to the holds at constant stress, increased greatly during vibration. Notice that the peak level of friction upon reloading is not as clearly defined in the vibrational holds as in the constant stress holds. This rounded shape at peak friction was characteristic of vibrational holds. For the purpose of measuring frictional healing, we defined the peak friction as the greatest value attained after the hold, even if this value occurs at some displacement after an apparent local maximum in friction (e.g., the 100-s hold shown in Figure 2-8 inset).

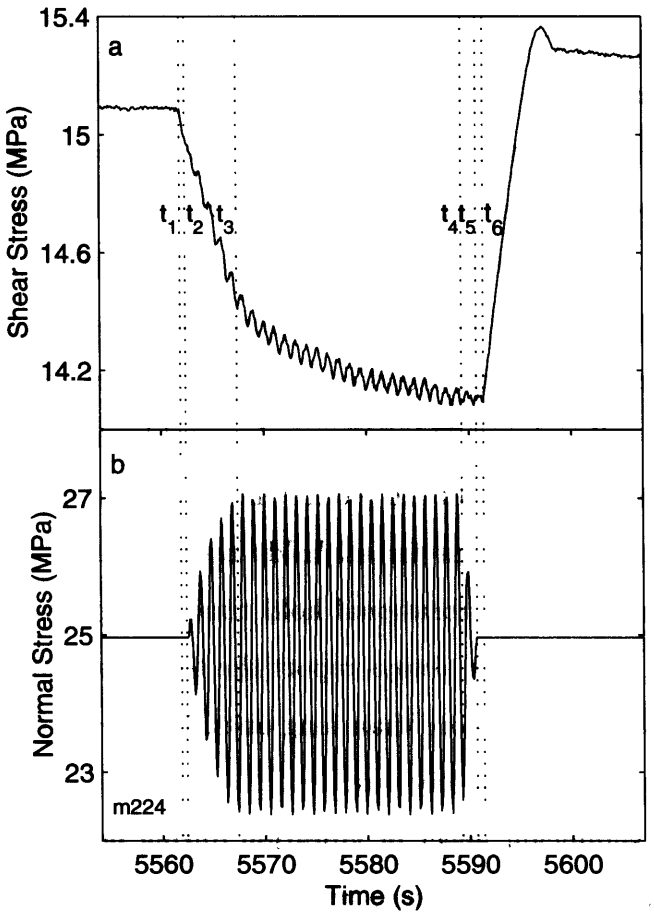

Figure 2-9: (a) Shear stress and (b) normal stress versus time for one 30-s hold with 4.7-MPa normal stress oscillations. The vertical ram was stopped at t_1. At t_2, the sinusoidal normal stress oscillations were started, reaching 5.6-MPa double amplitude at t_3. At t_4 the amplitude of the oscillations was decreased gradually, becoming zero at t_5. The vertical ram was restarted at t_6, ending the hold. The apparent 10-s modulation in amplitude of the normal stress during oscillations was due to a data-sampling rate of 10 Hz slightly out of phase with the 1-Hz oscillations. The oscillations in shear stress are due to direct elastic coupling (Poisson effect) between the normal and shear stress resolved on the central forcing block.

Another typically observed consequence of normal force vibrations was the unusually large displacement over which sliding friction returned to its previous steady state value (Figure 2-8). This displacement is greater than that for longer constant normal stress holds that reached equivalent values of healing and peak friction. In addition, it is clear that frictional healing depends less strongly on hold time for vibrational holds than for holds at constant stress (compare slopes of the open and solid symbols in Figure 2-10b). This feature is common for vibrational holds and seems to be related to the amplitude of vibration. Specifically, increasing vibration amplitude decreases the healing rate, β, defined here as $\beta = \Delta\tau/\Delta \log t_h$ in which t_h is the hold time [*Marone*, 1998b]. In fact, for very large amplitude vibrations ($2A \approx$ 10-13 MPa), $\beta \approx 0$ for the range of hold times in these experiments; however, unstable sliding marked by sudden shear stress drops tended to occur during holds with large-amplitude vibrations, making these data and the related relaxation data somewhat difficult to interpret. In contrast to frictional healing and relaxation, gouge layer compaction consistently increased with hold time to a greater degree during vibrational holds than during constant stress holds (Figure 2-10).

Figure 2-10 compares healing ($\Delta\tau$), relaxation ($\Delta\tau_{\min}$), and gouge layer compaction ($\Delta\phi$) for holds with and without normal stress oscillations for the three sets of slide-hold-slide tests displayed in Figure 2-8. Figures 2-10a, 2-10b, and 2-10c show measurements made on raw data, and Figures 2-10d, 2-10e, and 2-10f show measurements that have been corrected for the effects of absolute displacement. The displacement correction was determined by fitting a logarithmic curve to data of healing (or relaxation or gouge compaction) as a function of displacement (Figure 2-3) taken from the displacement calibration experiments such as the one shown in Figure 2-1 and others (see Table 2.1). The difference in healing on the calibration curve between the actual displacement and some reference displacement was the value of the correction added to the data and was applied identically to all the vibration experiments detailed here. We assumed that since the initial shear loadup was the same in each experiment, the effects of displacement were nearly identical for all of our experiments for the ranges of displacements ($\approx$ 10-35 mm) at which we conducted

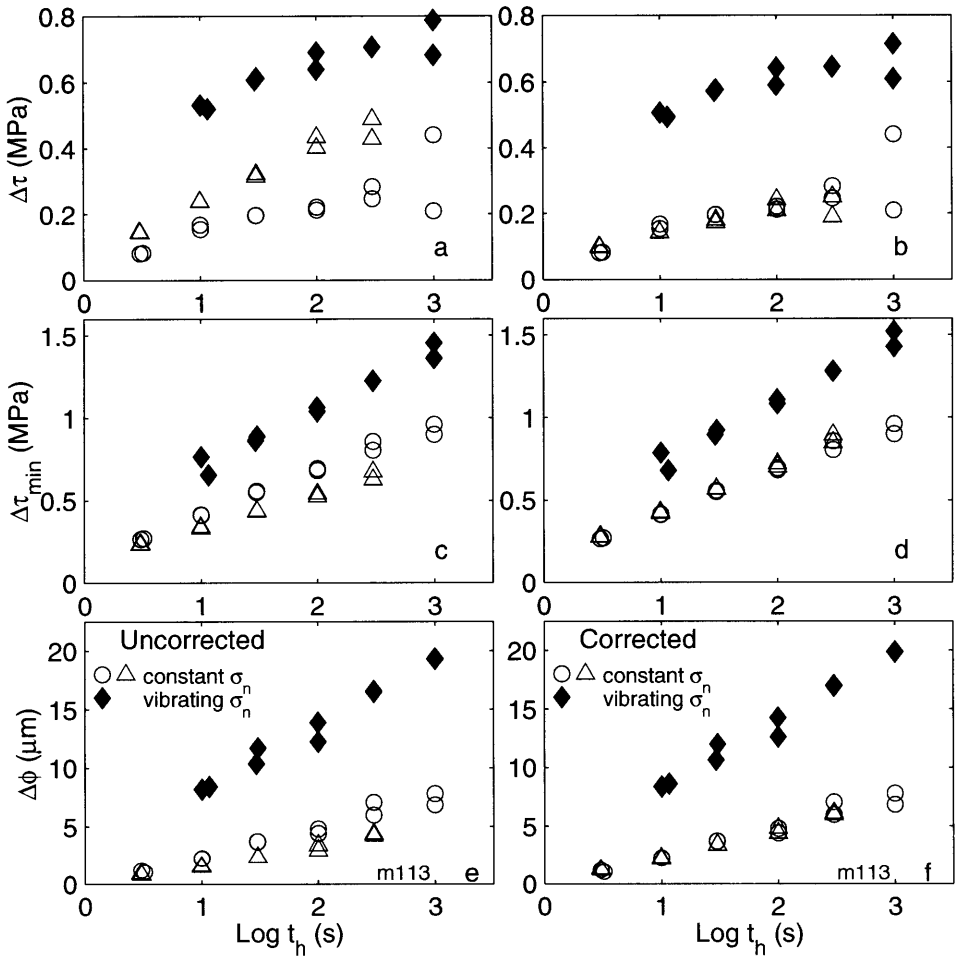

Figure 2-10: (a,b) Measurements of $\Delta\tau$, (c,d) $\Delta\tau_{\min}$, and (e,f) $\Delta\phi$ plotted versus $\log_{10}$ of hold time for the three sets of slide-hold-slide tests in Figure 2-8. Effects of absolute displacement have been accounted for in the data on the right (Figures 10b, 10d, and 10f). Open circles and triangles represent the data from the first and third sets of slide-hold-slide tests, respectively, that were performed at constant normal stress. Solid diamonds represent the data from the second set with oscillating normal stress ($2A = 5.6$ MPa).

the slide-hold-slide tests. In the plots on the right of Figure 2-10, all the data are shown at a reference displacement of 15 mm. We did not observe any permanent effects of vibration, as is evident from the good agreement between the data from first and third slide-hold-slide tests.

Frictional healing increases with the log of hold time for both constant stress and vibrational holds (Figures 2-10a and 2-10b). The absolute level of healing is much larger for vibrational holds. An extrapolation of a least squares best fit line to these data implies that a hold of $\sim 3 \times 10^5$s at constant normal stress will result in the same level of frictional healing as a 10 s hold with 5.6-MPa vibrations (Figure 2-10).

Frictional relaxation also increases with the logarithm of hold time for both types of holds (Figures 2-10c and 2-10d). Relaxation depends more strongly on hold time for vibrational holds (i.e., the slope of the best fit line is slightly steeper for the vibrational set), and the absolute level of relaxation is greater by approximately the same amount as that for healing (note the factor of 2 change in vertical scale between the healing and relaxation panels of Figure 2-10). This was observed consistently in all experiments. Gouge compaction greatly increased during normal force oscillations and also depends more strongly on hold time than it does under a constant normal load (Figures 2-10e and 2-10f). Inspection of the gouge layer after an experiment with large-amplitude vibrations revealed that the gouge had consolidated to form weakly cohesive plates of the order of centimeters in area and fractions of a millimeter in width due to the great compaction induced by the vibrations. Gouge layer effects are probably the most important for characterizing the effects of vibration as will be discussed.

Effects of Vibration Amplitude. We conducted several slide-hold-slide tests using different vibration amplitudes (Figure 2-11). For equal hold times the total change in shear stress during the hold and reload, $\Delta\tau + \Delta\tau_{\min}$, (Figure 2-11d), and the gouge compaction during the hold (Figure 2-11e) both increase approximately linearly with vibration amplitude. The delayed return to steady state friction and the rounded peak in friction following a hold are also enhanced with increasing amplitude (Figures 2-11a, 2-11b, and 2-11c). We measure total change in shear stress

($\Delta\tau + \Delta\tau_{min}$) in Figure 2-11d because 75% of holds with double amplitudes of 6 MPa and greater experienced unstable sliding at the onset of vibrations, creating a small but unrecoverable shear stress drop (e.g., Figure 2-12). These stress drops could sometimes be eliminated by a longer ramp in vibration amplitude or a longer lag at the beginning of the hold before starting the vibrations.

Gouge Layer Effects. We measured the degree of gouge layer compaction as the change in layer thickness during the hold (Figures 2-2b and 2-13a) and dilatation as the change in gouge layer thickness between the end of the hold and the new steady state reached after the end of the hold (Figure 2-13a). We have already noted that healing, relaxation, and compaction vary linearly with the logarithm of hold time (Figures 2-3 and 2-10) and that gouge compaction and the total change in shear stress both vary approximately linearly with the amplitude of vibration for a given hold time (Figure 2-11). Thus the relationship between changes in shear stress and changes in the gouge layer during slide-hold-slide tests may be important in characterizing the effects of vibration.

In fact, we found that total change in shear stress varies linearly with both compaction and dilatation (Figures 2-13b and 2-13c) over a range of vibration amplitudes. In the experiment shown in Figures 2-13b and 2-13c, hold times ranged from 3 to 1000 s. As hold time increases, compaction and total change in shear stress increase, so even though time is not explicitly plotted, the hold time increases from left to right within each of the three data sets. Note that a 1000-s hold with no vibrations underwent approximately the same amount of compaction as a 12-s hold with 8.0-MPa vibrations. Likewise, shorter hold times with 9.1-MPa vibrations achieved greater compaction and thus greater healing and relaxation than longer hold times with 8.0-MPa vibrations. This suggests that the effect of vibrations during a hold is essentially to trade time for compaction. Most dilatation measurements approached the minimum resolution of our LVDTs, so there is more scatter in this data set. However, it is still evident that there is a similar trade-off between time and dilatation when the gouge layer undergoes vibration. We will later discuss how the changing state of the gouge layer can be important in modeling the effects of normal force vibrations

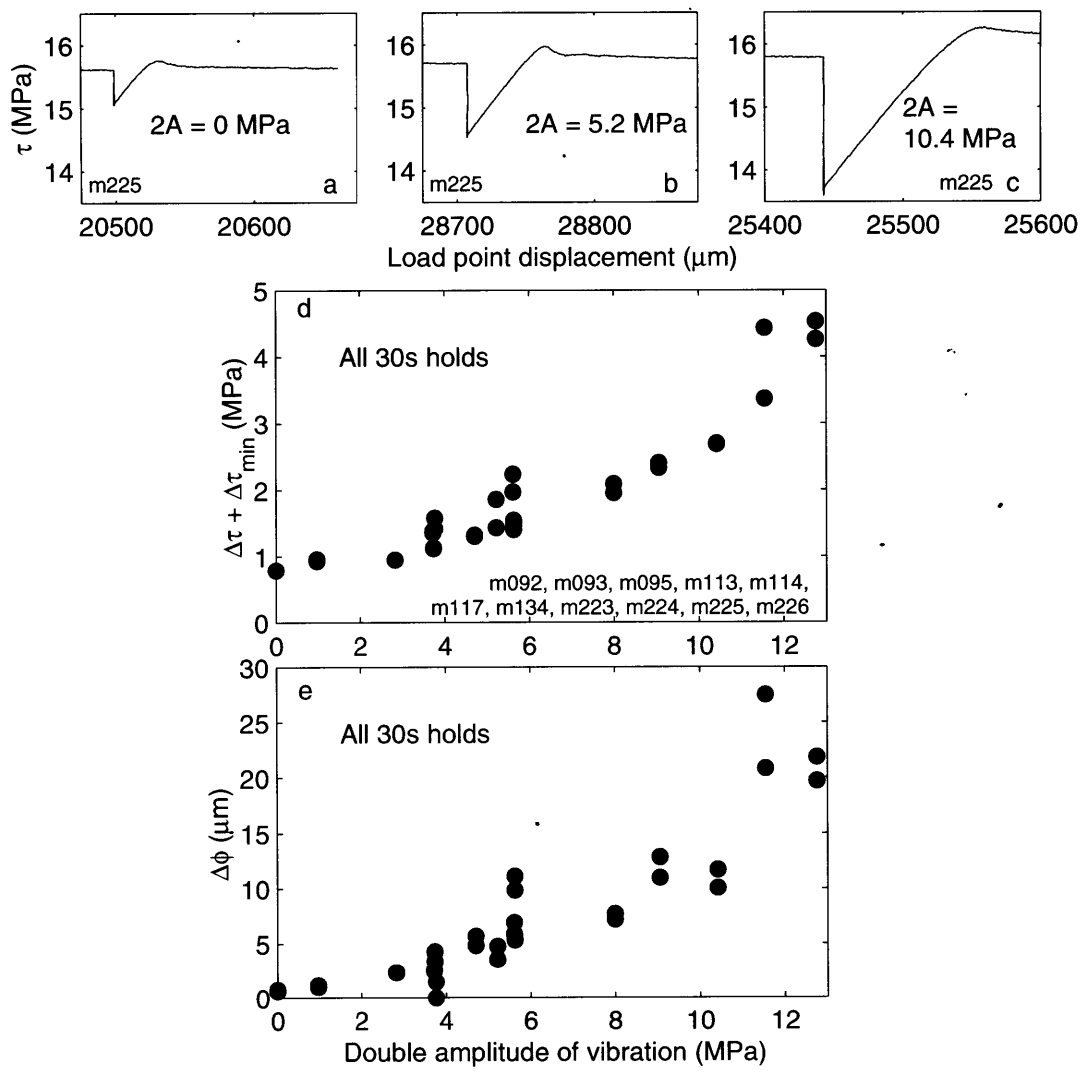

Figure 2-11: Shear stress versus shear load point displacement for 30-s holds from one experiment at (a) constant normal stress, (b) $2A = 5.2$ MPa, and (c) $2A = 10.4$ MPa. Total shear stress change ($\Delta\tau + \Delta\tau_{min}$) versus (d) $2A$ and (e) $\Delta\phi$ are presented at a reference displacement of 30 mm.

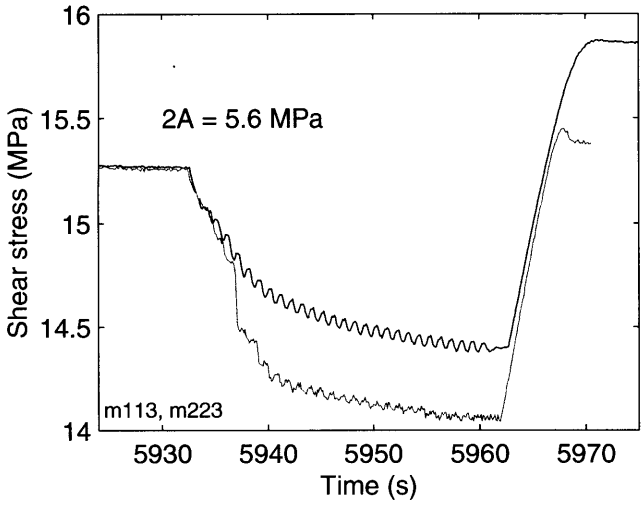

Figure 2-12: Shear stress versus time for two 30-s hold times with the same double amplitude of σ_n vibrations from different experiments. One has a small stress drop (shaded), and the other does not (solid). At the end of the hold, relaxation and healing differ between the two by an amount approximately equal to that of the stress drop.

during slide-hold-slide tests.

2.4 Discussion

We have modeled the experiments to determine if the dependence of frictional healing on second-order effects such as cumulative slip and variable normal stress are consistent with the existing framework of the rate and state friction laws. Although other theoretical interpretations are possible and plausible, we are only considering the empirical rate- and state-dependent friction laws here.

In the case of the constant stress holds, we adopted the standard law

$$\mu = \mu_0 + a \ln \left(\frac{V}{V_0} \right) + b \ln \left(\frac{V_0 \theta}{D_c} \right) \tag{2.2}$$

in which μ_0 is the coefficient of friction at the steady state sliding velocity V_0, V is the slip rate, θ is the state variable that can represent average contact lifetime, D_c is the characteristic slip distance over which friction evolves to a new steady state

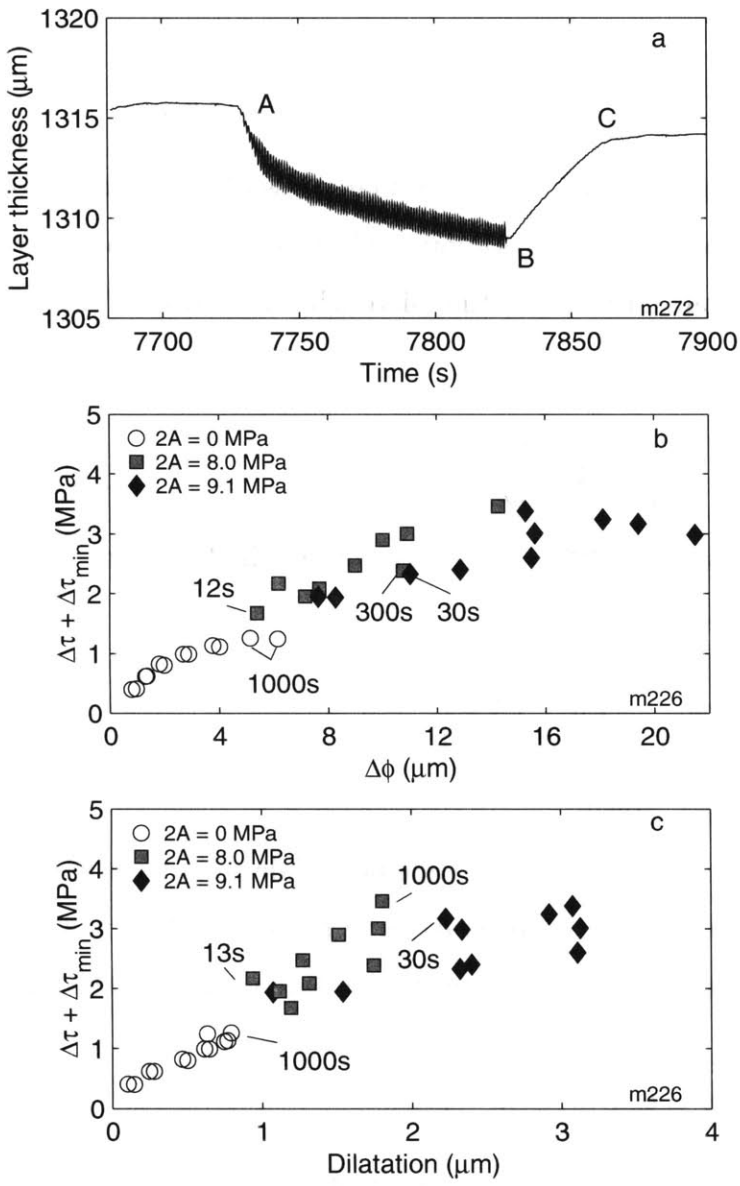

Figure 2-13: Layer thickness (a) versus time for one slide-hold-slide test and measurements of $\Delta\tau + \Delta\tau_{min}$ as a function of (b) compaction and (c) dilatation (c) for several hold times. The data shown in Figure 2-13a are from an LVDT mounted directly on the sample, and geometric thinning has been removed. Compaction is the difference between A and B and dilatation is the difference between C and B. Open circles show slide-hold-slide tests without vibrations ($3 \leq t_h \leq 1000$ s), shaded squares show tests with $2A = 8$ MPa ($12 \leq t_h \leq 1000$ s), and solid diamonds show slide-hold-slide tests with $2A = 9.1$ MPa ($11 \leq t_h \leq 1000$ s).

following a change in velocity, and a and b are empirical constants. Equation (2.2) was coupled to a single-degree-of-freedom elastic relationship,

$$\frac{d\mu}{dt} = k(V_{lp} - V) \tag{2.3}$$

in which k is the apparatus stiffness divided by the normal stress ($1 \times 10^{-3}\mu\text{m}^{-1}$ for our apparatus) and V_{lp} is the slip rate of the load point, which is set equal to V_0. We tested two evolution laws with our data. One, the Dieterich, or "slowness" law, is given by

$$\frac{d\theta}{dt} = 1 - \frac{V\theta}{D_c} \tag{2.4}$$

in which θ evolves with time [*Dieterich*, 1978, 1979]. The other, the Ruina, or "slip" law, is given by

$$\frac{d\theta}{dt} = \frac{-V\theta}{D_c} \ln\left(\frac{V\theta}{D_c}\right) \tag{2.5}$$

in which θ evolves with slip [*Ruina*, 1983].

In the case of the normal stress steps and the slide-hold-slide tests with normal stress oscillations, we followed the formulation of *Linker and Dieterich* [1992] in which a change in normal stress causes an immediate change in the state variable of the form

$$\theta = \theta_0 \left(\frac{\sigma_{\text{initial}}}{\sigma_{\text{final}}}\right)^{\alpha/b}, \tag{2.6}$$

where α is defined in (2.1). After this sudden decrease in state, θ evolves according to either (2.4) or (2.5) [*Linker and Dieterich*, 1992].

2.4.1 Displacement

In the case of total displacement, other workers have noticed changes in friction parameters with increased accumulated slip [*Dieterich*, 1981; *Lockner et al.*, 1986; *Beeler et al.*, 1996]. Such effects are generally considered to be a transient phase that

occurs at low total displacements after which friction parameters become independent of accumulated slip if the wear rate is low and gouge particle size distribution does not continue to evolve. Previous work in characterizing the effect of displacement on frictional behavior has generally concentrated on slip stability, the friction rate parameter, and gouge layer thickness and roughness [*Marone*, 1998a]. For example, it has been established that thick gouge layers tend to stabilize slip at small displacements [*Marone et al.*, 1990]. As displacement accumulates, the friction rate parameter decreases for gouge layers and becomes velocity weakening [*Dieterich*, 1981; *Beeler et al.*, 1996]. We also observe this transition at $\sim$ 7-10 mm of total displacement. Further detailed discussion of displacement effects has been given by *Marone* [1998a] and is not repeated here.

Our observations suggest that for thick gouge layers, shear localization evolves further over the course of an experiment, as discussed by *Marone and Kilgore* [1993], an important consideration when comparing data from different parts of an experiment. The conclusion that gouge evolution continues after the transition to velocity weakening is also supported by the results of *Beeler et al.* [1996], who found that gouge returns to a velocity-strengthening regime in their rotary shear experiments after very large displacements (>100 mm).

We simulated the healing and relaxation data by solving (2.2) and (2.3) numerically with either the Dieterich or Ruina evolution law. We used values of a, b, and D_c taken from inversions of velocity steps from the same experiments. The Dieterich law fits both the healing and relaxation data sets from the first set of tests in the experiment shown in Figure 2-1 (solid circles in Figures 2-14a and 2-14c) acceptably with $a = 0.008$, $b = 0.005$, and $D_c = 15\mu$m (solid lines in Figures 2-14a and 2-14c). The Ruina law fit to the same data had $a = 0.008$, $b = 0.007$, and $D_c = 15\mu$m (solid lines in Figure 2-14b and 2-14d). In order to fit the healing and relaxation measurements from the sixth set of slide hold slide tests in the same experiment (Figure 2-14, shaded squares), we increased b to 0.007 in the Dieterich law and to 0.015 in the Ruina law but kept other parameters the same. The increase in b simultaneously reproduced the increased rate of frictional healing and the reduced degree of frictional relaxation

(Figure 2-14, shaded lines). In general, we were able to simulate the slip dependence of frictional healing entirely with an increase in b.

We also compared the forward model to the time series data (Figure 2-15). The forward model used the same values of a, b, and D_c as the fit to healing data (Figure 2-14); thus there are no free parameters in the comparison of Figure 2-15. These fits are reasonable and show that the change in frictional healing and relaxation that we observe as a function of cumulative slip can be accounted for entirely by an increase in b. An increase in the parameter b was found to occur along with a decrease in gouge layer thickness in the triaxial experiments of *Marone et al.* [1990]. This may be relevant to what we observe. Probably, the gradual compaction of the gouge layer and localization of shear bands is the cause of the change in healing and relaxation that we observe with displacement.

This displacement effect is significant well after the transition to velocity weakening or steady state sliding friction, both of which usually occurred in our experiments between 7 and 10 mm of total slip. It is important to take this effect into account, especially when comparing data from the same experiment in which the effects of other second-order effects are being tested, such as variable normal stress or driving velocity.

2.4.2 Normal Stress Steps

The key difference in describing the evolution of the state variable after a change in normal stress as opposed to a change in driving velocity is that upon stepping the normal stress, state immediately decreases, as described by (2.6). Micromechanically, this situation can be thought of as a decrease in the average lifetime of contacts in the system, since new ones have been created by the sudden compaction of the granular layer induced by the increase in normal stress. In addition, if the instantaneous growth of preexisting contacts is considered not as an increase in the lifetime of the old contacts but, rather, as new contacts immediately adjacent to old ones, then the net effect is to decrease the average age of contacts overall. As shearing continues, the

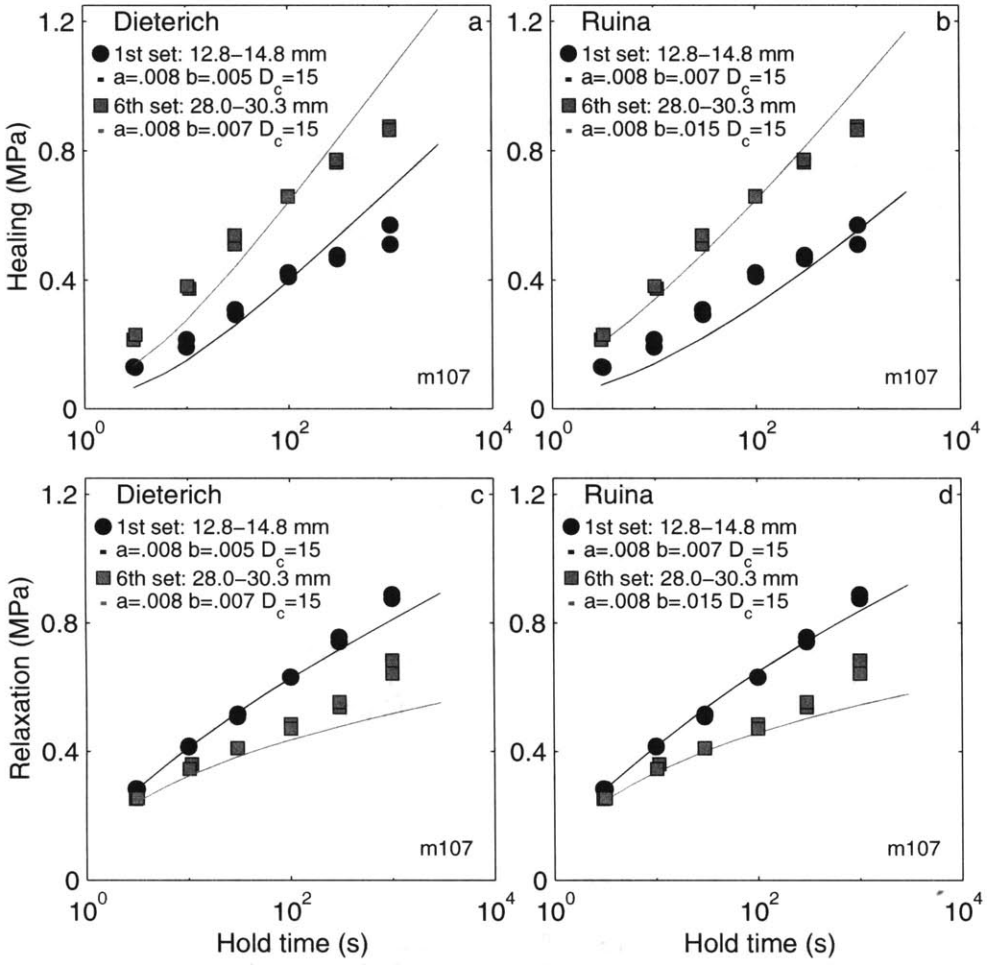

Figure 2-14: Data (symbols) and simulations (lines) obtained from forward modeling the first and sixth set of (a,b) healing and (c,d) relaxation measurements from the experiment in Figure 2-1. Circles and solid lines represent data and simulations from the first set, squares and shaded lines represent data and simulations from the sixth set of slide-hold-slide tests. The left and right sets of plots show the same data, but the models on the left (Figures 14a and 14c) use the Dieterich evolution law while the models on the right (Figures 14b and 14d) use the Ruina law. These plots show results of four, not eight, simulations: one each for each data set using each law. For instance, the healing and relaxation data for the first set of slide-hold-slide tests in Figures 14a and 14c are both fit simultaneously by the same Dieterich model.

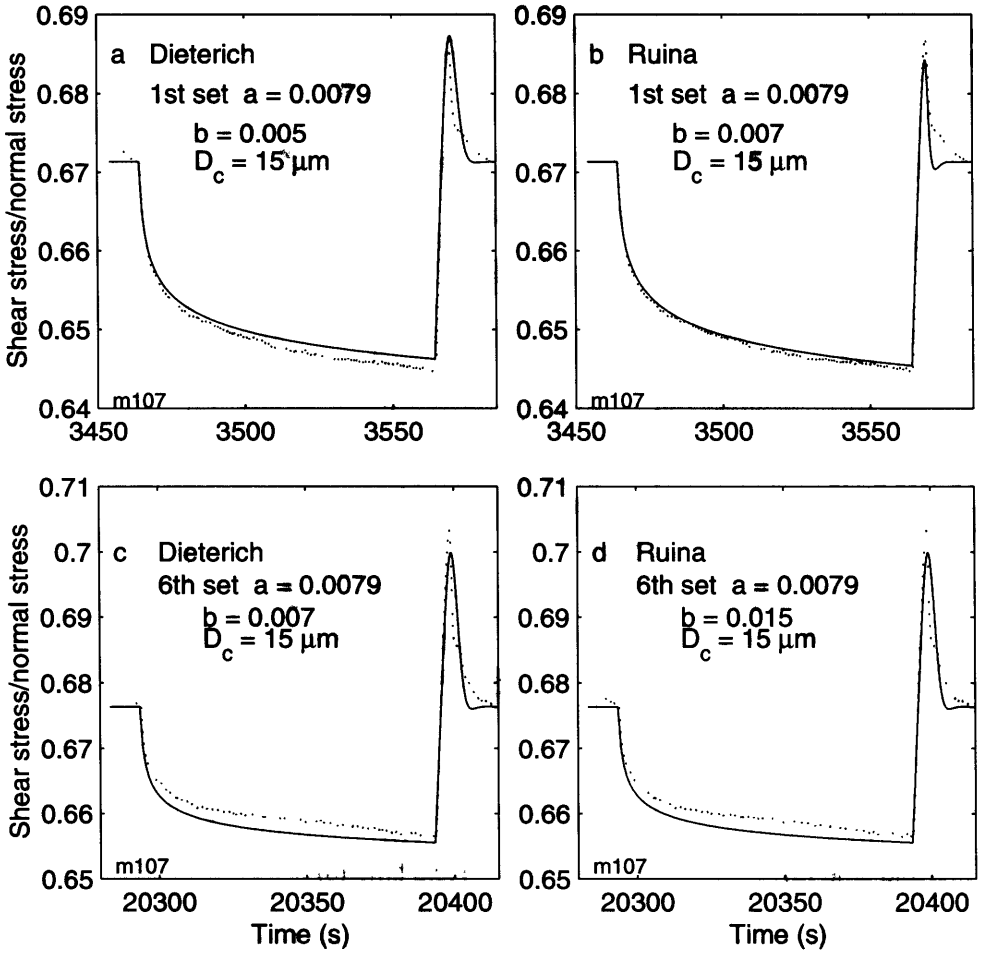

Figure 2-15: Fit to two 100-s slide-hold-slide tests from the (a,b) first and (c,d) sixth sets of holds in the experiment from Figure 2-1. Both sets of plots show the same data (dotted lines), but the plots on the left (Figures 15a and 15c) show models using the Dieterich law and the plots on the right (Figures 15b and 15d) show models using the Ruina law (solid lines). We used the same parameters in these forward models as in Figure 2-14. These fits are good considering that there were no free parameters.

subsequent evolution of state and friction may be described by either the Dieterich or Ruina evolution laws.

We fit both the Dieterich and Ruina laws to the normal stress step simulations through forward modeling by solving (2.2), (2.3), and (2.6) using either (2.4) or (2.5) as the evolution law. A fifth-order Runga-Kutta method was used and our modeling included the measured effects of Poisson expansion for our apparatus ($\Delta\tau/\Delta\sigma_n$), determined to be 0.01 for the Westerly testing blocks and 0.02 for steel testing blocks. We found appropriate parameters for a, b, and D_c from a least squares iterative inversion of velocity steps performed during the same experiment as the normal stress steps. We found that in general, $\alpha = 0.3$ (Figure 2-7) did not fit the data well, as the Dieterich model overshoots the the final steady state sliding stress and the Ruina model does not match the slope of the data during elastic shear loading (Figure 2-16a). Using $\alpha = 0.2$ provided a better fit (Figure 2-16b). The Ruina model matches the data quite well, especially on the initial shear loading, but the Dieterich model still overshoots the final steady state shear stress. None of our data show such overshoots. For the range of friction parameters that we considered "reasonable" based on fits to velocity steps in the same experiments (e.g., velocity weakening), we found that the Dieterich model consistently overshot the final steady state shear stress. Even though the Dieterich model does not fit the data well in general, since the Ruina law does a good job when $\alpha = 0.2$, this is the value of α we used in the simulations of vibrational slide-hold-slide tests discussed next.

2.4.3 Normal Stress Oscillations

Harmonic oscillations of the normal stress during quasi-stationary contact increases the absolute level of frictional healing by an amount that is roughly proportional to the amplitude of oscillations. This result can be approximately compared to the results of the normal stress "pulse tests" of *Linker and Dieterich* [1992], who found that a sudden very short (0.2-s) increase in normal stress during a 1-s hold was followed by a peak in friction that was larger than peak friction for holds of similar

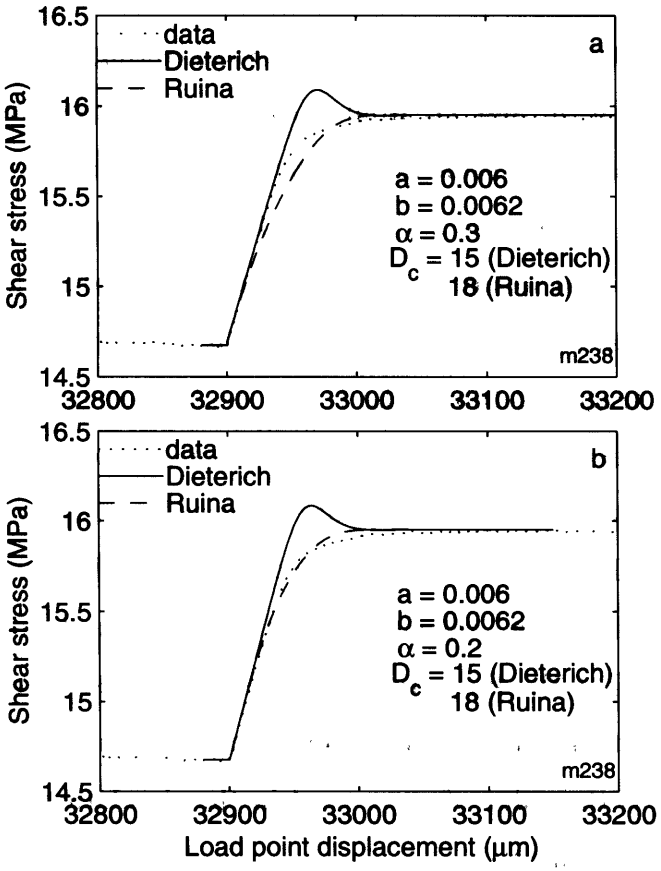

Figure 2-16: Shear stress (MPa) versus shear load point displacement (μm) for one normal stress step of 8.8% of the initial normal stress. The frictional parameters used here were $a = 0.006, b = 0.0062, D_c = 18$ μm (Ruina), $D_c = 15$ μm (Dieterich), (a) $\alpha = 0.3$ and (b) $\alpha = 0.2$. The parameters a, b, and D_c were obtained from modeling a velocity step from this same experiment.

duration without a normal stress pulse. Likewise, they found that the absolute level of peak friction increased as the magnitude of the stress pulses increased. Their experiments were carried out in double-direct shear as well, but with sample sizes of 5×5 cm and a mean normal stress of only 5 MPa. The similarity between our results and theirs suggests that our results are valid for at least this range of laboratory scales.

We modeled vibrational slide-hold-slide data with two goals in mind. We tried to fit data from single holds with forward models using parameters derived from modeling velocity steps, and we also tried to use similar parameters to model the frictional healing trends. We added normal stress vibrations to the simulations by specifying a 1-Hz sine wave as the normal stress during the hold. In order to match the experimental time series of a given slide-hold-slide test, we lagged the start of the normal stress vibrations in relation to the beginning of the hold. This lag corresponded to t_1-t_2 in Figure 2-9, for example. We also ramped the normal stress sine wave amplitude in the simulation up to the final vibrational amplitude linearly over the same ramp time as was done manually during the experiments (t_2-t_3 in Figure 2-9). In experiments we ramped down normal stress at the end of the hold in order to maintain constant vibration frequency and to avoid sudden, uncontrolled changes in normal stress associated with jumping back to our nominal normal stress. In the simulations we ended the hold at a zero crossing of the sine wave.

Figure 2-17 shows data and models for one hold from the experiment in Figure 2-8. In this example, initial lag time was 1 s, and the initial ramp was 5 s long. The simulated normal stress matches the experimental values well, except for a slight DC level offset resulting from the added experimental signal not being perfectly symmetric around the mean normal stress (Figure 2-17b). The simulations of shear stress during and after a hold with vibrations shown in Figure 2-17a are examples of typical results of forward models that used friction parameters derived from modeling earlier velocity steps and constant stress slide-hold-slide tests. The Dieterich evolution law (shaded line) fits the data well during the hold but gives a peak shear stress that is too large and a subsequent return to steady state that is too fast. We could not simultaneously

fit relaxation during the hold and peak stress after the hold for any reasonable range of parameters ($0.006 \leq a \leq 0.015, -0.002 \leq (a-b) \leq 0.002$, 5 μm $\leq D_c \leq$ 30 μm). In all cases the Dieterich law gave a sharp peak friction, which we did not observe in the data.

The Ruina law (dotted line) does not fit the relaxation time series data very well because of an early stress drop. We often observed similar stress drops in the experiments for large-amplitude holds (Figure 2-12), but models using the Ruina law and reasonable friction parameters consistently resulted in stress drops that were larger than observed. To suppress these large stress drops, D_c had to be $\sim$ 200 μm, over an order of magnitude larger than we expected based on models of velocity steps or slide-hold-slide tests at constant stress. At the end of the hold the Ruina model has a more rounded peak in friction, which is encouragingly similar to experimental observations but, like the Dieterich model, returns to steady state friction faster than observed in the data. When velocity strengthening conditions were specified ($a - b > 0$), the Ruina model exhibited a value and shape of peak friction that was similar to what we found experimentally, but we could never reproduce the delayed return to steady state. The slow return to steady state observed experimentally and large effective D_c are probably due to gouge layer effects such as reformation of vibrationally disrupted shear bands, which cannot be accommodated by the present constitutive laws *Sleep et al.* [2000].

Though the rate- and state-variable formulation that we use does not reproduce time series data of individual holds well (Figure 2-17), it is still important to test whether macroscopic behaviors of the system, such as healing and relaxation rates, are described well. If so, we can conclude that this formulation approaches the correct solution. Therefore we used forward models of both evolution laws and the same friction parameters used in Figure 2-17 to fit healing curves from an experiment with 11.5-MPa vibrations (Figure 2-18). We used a single set of friction parameters for each law and modeled sets of slide-hold-slide tests both at constant stress and with 11.5-MPa double amplitude over the range in hold times of 3-1000 s. The simulation that used the Ruina law does a good job of fitting both the absolute level of total

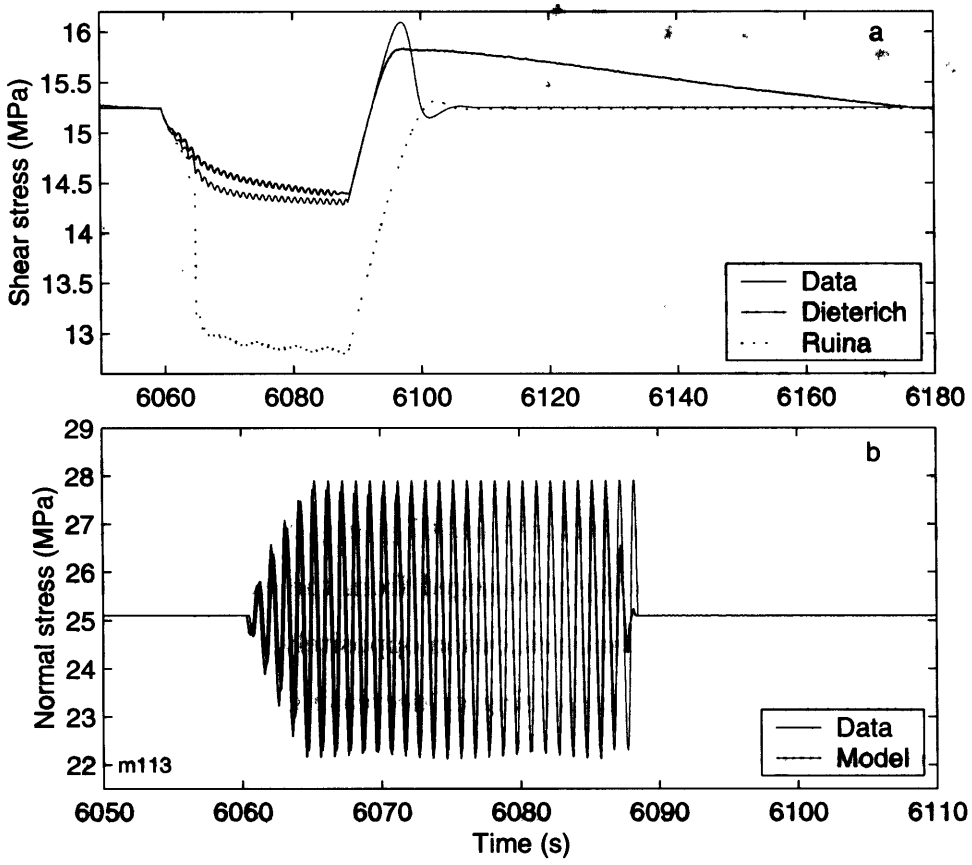

Figure 2-17: (a) Shear stress and (b) normal stress as a function of time for one 30-s hold from the experiment shown in Figure 2-8. The solid line shows data, the shaded line shows the model using the Dieterich evolution law ($a = 0.011$, $b = 0.013$, $\alpha = 0.2$, $D_c = 15$ μm), and the dotted line shows the model using the Ruina evolution law ($a = 0.012$, $b = 0.0135$, $\alpha = 0.2$, $D_c = 15$ μm). Figure 2-17b shows only one model line since we used the same normal stress time series for both simulations. Note the different time axis scales in (a) and (b).

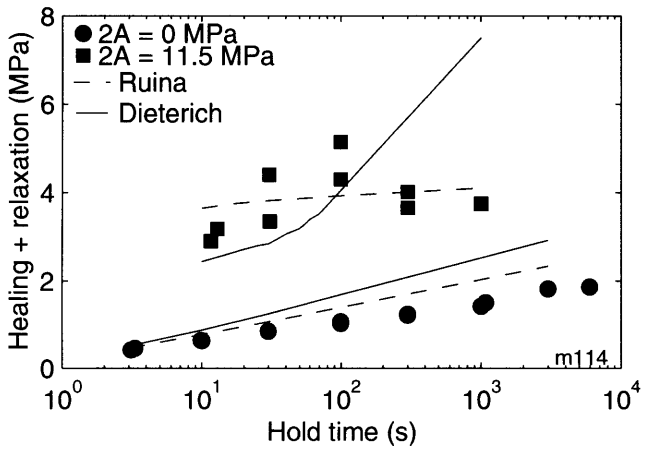

Figure 2-18: Data (solid symbols) and models using the Dieterich (solid line) and Ruina (dashed line) laws of healing plus relaxation as a function of hold time for two sets of slide-hold-slide tests from one experiment. Circles show data without vibrations and squares show data with 11.5-MPa vibrations during the holds. Parameters are the same as in Figure 2-17.

shear stress change as well as the small rate of change with hold time. For the range of reasonable values of a and b that we explored ($0.007 \leq a \leq 0.00135, a - b < 0$), the results of the Ruina model were basically unchanged from the example shown here. Most changes in a and b affect healing and relaxation oppositely; thus adding the two measurements negates these changes. Increasing or decreasing D_c lowered or raised the DC level of the healing curve, respectively. Thus the parameters that we chose based on typical fits to other friction data also give the best global fit to healing data when the Ruina evolution model is used (Figure 2-18).

In contrast, the Dieterich simulation grows too large too fast so that it does not describe the overall behavior of the system well for hold times > 100 s. Exploration of parameter space led to similar results as with the Ruina law in that changes in a and b were negligible and changes in D_c changed the absolute values of the curve but not its slope. Our data consistently showed a nearly flat healing curve as predicted by the Ruina law.

In addition, we fit the data in Figure 2-11d with both laws and the same parameter values as in Figure 2-17 (Figure 2-19). Both laws are able to reproduce the trend of increasing total frictional strength with increasing amplitude of vibration. Therefore

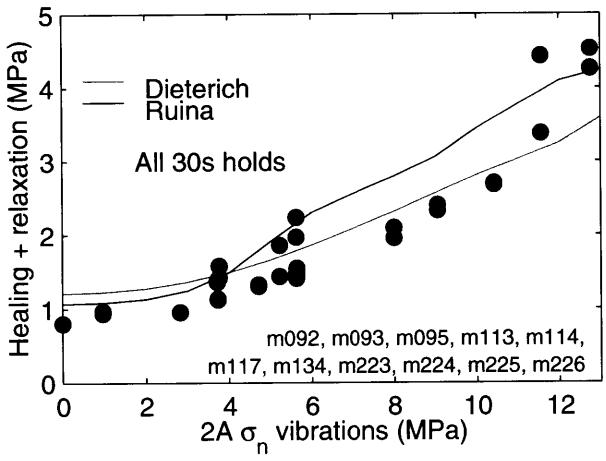

Figure 2-19: Data (solid symbols) and models (lines) of healing plus relaxation as a function of $2A$ for 30-s hold times. Parameters are the same as in Figure 17.

both evolution laws can recover the DC level change in frictional strength that occurs when vibration amplitude is increased for $t_h \leq 100$ s. The Dieterich law does not fit observations at $t_h > 100$ s.

2.4.4 Micromechanical Interpretation

A major shortcoming in the present formulations of the friction constitutive laws is that they do not account for the gouge layer effects which are likely to be extremely important in characterizing the behavior of the system. Mechanical consolidation of gouge has been shown to play a role in the frictional strengthening process [*Nakatani*, 1998]. It is clear from our data of both normal stress steps (Figure 2-6) and holds with vibrations (Figures 2-10 and 2-13) that porosity decreases dramatically in response to an applied external normal stress. In the case of the normal stress steps it is somewhat straightforward to consider that a sudden increase in normal stress compresses the granular material elastically, then shearing continues to compact the grains faster since the pressure is now greater (Figure 2-20). After further shearing, the porosity of the granular assemblage reaches a new steady state that is lower than the previous porosity. Grain contacts become more numerous and larger than at the previous lower normal stress (Figure 2-20).

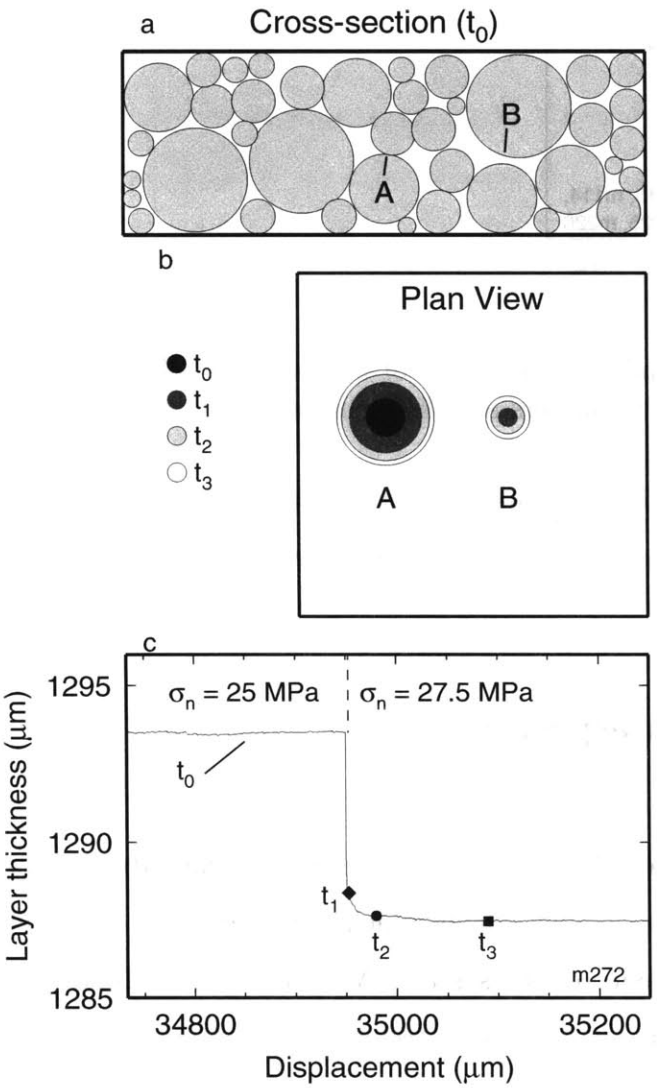

Figure 2-20: Contact junction evolution in a granular medium in response to a sudden increase in normal stress. (a,b) Sketches of the granular assemblage in cross section and of hypothetical contact junctions in plan view. (c) Figure 2-6c is shown for reference. Initially, the system is shearing in steady state with some assemblage of grain sizes and junctions (Figure 20a and section marked t_0 in Figure 20c). Contact A exists, but B does not yet. The normal stress step compacts the layer causing growth of A and producing contact B (t_1). The elastic shear load up (t_2) and evolution to a new steady state (t_3) cause growth of the two contacts.

The behavior of granular layers under normal stress vibrations is probably more complicated. For the displacements of our slide-hold-slide tests (≈10-35 mm), we had reached a steady value of sliding friction and were in the regime characterized by localized shear along Riedel, B, and Y shear bands [*Mair and Marone*, 1999]. In a slide-hold-slide test at constant normal stress we envisage that frictional strengthening occurs throughout the layer as contacts grow and strengthen, then are disturbed as slip is reinitiated, causing the observed peak in friction after the hold. In order to account for the greater degree of both relaxation and compaction that we have observed for vibrational slide-hold-slide tests the external oscillations must physically promote the strengthening of shear bands and regions external to shear bands [*Sleep et al.*, 2000]. If the normal stress were simply increased in a one-sided step during holds, then the shear band restrengthening would be faster solely as a result of the greater pressure. Instead, when normal stress is vibrated, gouge particles become compacted into a lower energy configuration. Our interpretation is that this disrupts the shear band's porosity, width, and boundary configuration. Effectively, we expect that vibrations widen the zone of gouge particles involved in active shearing, thus increasing the barrier to sliding to a greater degree than by mere contact junction growth. This mechanism may also explain the rounded peaks in friction observed on the reload (Figure 2-8). If the shear bands have been disrupted enough, overcoming frictional resistance may occur at slightly different times along parts of the shear band as it reforms, making the overall peak not as clearly evident and increasing the time or displacement to return to steady state.

Without microstructural observations of gouge layers to confirm our hypotheses, it is difficult to conclude exactly what mechanism is responsible for the increased frictional strengthening during vibrational holds. Nevertheless, monitoring changes in porosity of the gouge layer under external stressing is important for determining how to add these effects to the present frictional constitutive laws.

2.4.5 Relevance to Tectonic Faults

The observation that the return to steady state friction was delayed after attaining a peak value of friction following a vibrational hold (Figure 2-8) is consistent with an increase during vibration of the critical slip distance (D_c), which is the characteristic distance over which dynamic rupture is initiated on a fault [*Marone and Kilgore*, 1993]. Furthermore, observations of repeating earthquakes on faults suggest that earthquake stress drops increase with increasing recurrence interval between earthquakes by a factor that is larger than the value obtained from direct extrapolation from laboratory measurements of frictional healing [*Vidale et al.*, 1994; *Marone et al.*, 1995; *Marone*, 1998a]. Our results imply that typical laboratory frictional healing experiments at room conditions are measuring a minimum value of restrengthening since they assume that all applied tectonic loads are constant during quiescent intervals; these results are consistent with work on the effect of shear load on healing [*Karner and Marone*, 1998]. However, our results do not provide information for other conditions, such as low humidity (e.g., ?]).

Nearby faults are likely to interact with one another, as coseismic changes in creep velocities on parts of the San Andreas fault due to nearby moderate earthquakes have shown [*King et al.*, 1977; *Mavko*, 1982]. Our results predict that a transient dynamic normal load during creep can strengthen a fault, a result also predicted from a numerical analysis by *Mavko* [1982] in which a series of earthquakes on the Busch fault in southern California caused decreased slip rates and possibly locking on the adjacent Calaveras fault. Since the Busch fault is nearly perpendicular to the Calaveras fault, most of the stress from the Busch earthquakes would have been resolved onto the Calaveras fault in the normal direction, similar to our laboratory experiment.

We did not attempt to scale the amplitudes and frequencies of normal force variations in our experiments to any particular tectonic system. We also did not test the effects of a range of frequencies or changes in frequency, nor did we test the effects of transient shear stresses [e.g., *Gomberg et al.*, 1998] on frictional healing. Nevertheless, our results can be interpreted in light of such processes as the rate and degree of fault restrengthening and nucleation patch size growth during repeating earthquake cycles.

Experiments such as those we have conducted can be valuable for characterizing the effect of transient stresses on creeping faults.

2.5 Conclusions

We have observed and compared frictional healing and relaxation for slide-hold-slide tests at constant stress for ranges of displacements and found that an increase in the parameter b in the rate and state friction laws adequately accounts for the increase in healing and simultaneous decrease in relaxation that we observe with displacement. We examined the effects of external stressing on fault friction by conducting both normal stress step tests at constant velocity and normal stress vibration tests during quasistationary contact. Our observations of normal stress steps show that following a step change in normal stress, shear stress increases elastically, then evolves to a new steady state, confirming the results of *Linker and Dieterich* [1992]. We also observed an elastic decrease in the porosity of the gouge layer followed by further evolution in the same direction until a new steady state compaction rate was reached. The Ruina law, in general, provided a better fit to the normal stress step data than the Dieterich law. Our observations of normal stress vibrations during slide-hold-slide tests show that frictional relaxation and subsequent healing are both greatly enhanced by vibrations; this enhancement is greater for larger-amplitude vibrations. Modeling the global characteristics of frictional healing as a function of hold time and vibration amplitude were successful at small hold times for the Dieterich law and, in general, for all the ranges of hold times and amplitudes that we tested experimentally for the Ruina law. However, we were unable to reproduce adequately the observed time series data of any given hold with vibrations using either law. We believe that the discrepancies between the observed behavior and that predicted by the present formulation of the friction constitutive laws are due to neglecting the important effects of changing gouge layer porosity and alteration of the shear bands during external normal stressing. Future work will need to focus on this aspect of understanding the

effects of applied stresses if we hope to relate experimental data and simulations to tectonic situations.

Acknowledgments. The authors thank reviewers Terry Tullis, Frederick Chester, and the Associate Editor for suggestions that helped to clarify the presentation. Discussions with Norm Sleep refined our interpretations of the data. We also thank Steve Karner, Karen Mair, and Kevin Frye for lending us their considerable experimental expertise.

Chapter 3

Two Types of Mining-Induced Seismicity

Portions of this chapter are based on "Seismicity in Deep Gold Mines of South Africa: Implications for Tectonic Earthquakes" by E. Richardson and T.H. Jordan, *Bulletin of the Seismological Society of America,* in press, 2002. Copyright by the Seismological Society of America.

3.1 Introduction

In 1939, the first mechanical recorders were placed at the surface of South African gold mines in order to record and locate underground events associated with mining [*Green*, 1990]. Nearly 50 years later, the primary objectives of seismic monitoring in these mines remained locating the events quickly and determining their magnitudes [*Eccles and Ryder*, 1984]. Largely, this was done to assess possible damage to working mine faces and to provide information to rescue teams sent underground to recover trapped or injured miners [*Spottiswoode*, 1984]. At present most gold mines in South Africa use sophisticated underground arrays of geophones and accelerometers to record over 1,000 events per day. Processors at the surface pick P-waves and S-waves and run algorithms to calculate location, seismic moment, magnitude, corner

frequency, and other source parameters that are derived from these measurements such as energy, source radius, stress drop, and apparent stress [*Mendecki et al.*, 1990]. The goal of today's mine seismologists is hazard mitigation through prediction of underground conditions based on information about the seismic sources. Therefore, speed and efficiency of source parameter determination is of paramount importance given the large volume of events that must be processed daily.

Much of the past research involving mining-induced seismicity has involved classification of these sources, and it is now widely accepted that there are two categories of seismic events: "those directly connected with mining operations . . . and those associated with movement on major geologic discontinuities" [*Gibowicz and Kijko*, 1994]. While there has been much qualitative discussion about these two classes of events, relatively little quantitative investigation has been conducted to distinguish differences in their source properties. Some studies in Polish and Canadian mines have recognized that a break in the scaling relationship between number of events and energy occurs near $M = 3$ [*Kijko et al.*, 1987; *Prugger and Gendzwill*, 1990; *Gibowicz and Kijko*, 1994], but these studies were limited to seismicity of $M > 0$.

3.2 Mine Attributes

The data in this study are recorded by on-reef networks of three-component digital geophones operated by AngloGold, Ltd. and Integrated Seismic Systems, International, at five mines in the Far West Rand mining district, South Africa, approximately 80 km southwest of Johannesburg (Figure 3-1).

The five mines Elandsrand, Deelkraal, Mponeng, Savuka, and TauTona are the deepest in the world and extract ore from two gold-bearing quartzite reefs, the Ventersdorp Contact Reef and the deeper Carbon Leader Reef. These two units are separated by 900 m vertically, extend 2-4 km below surface in this region, and dip to the south at about 21° (Figure 3-2). The Far West Rand is in the Kaapvaal cratonic province, a region that is not very tectonically active. These gold mines contain old dykes and faults with two major trends: N 5° E and N 95° E. Many of these fea-

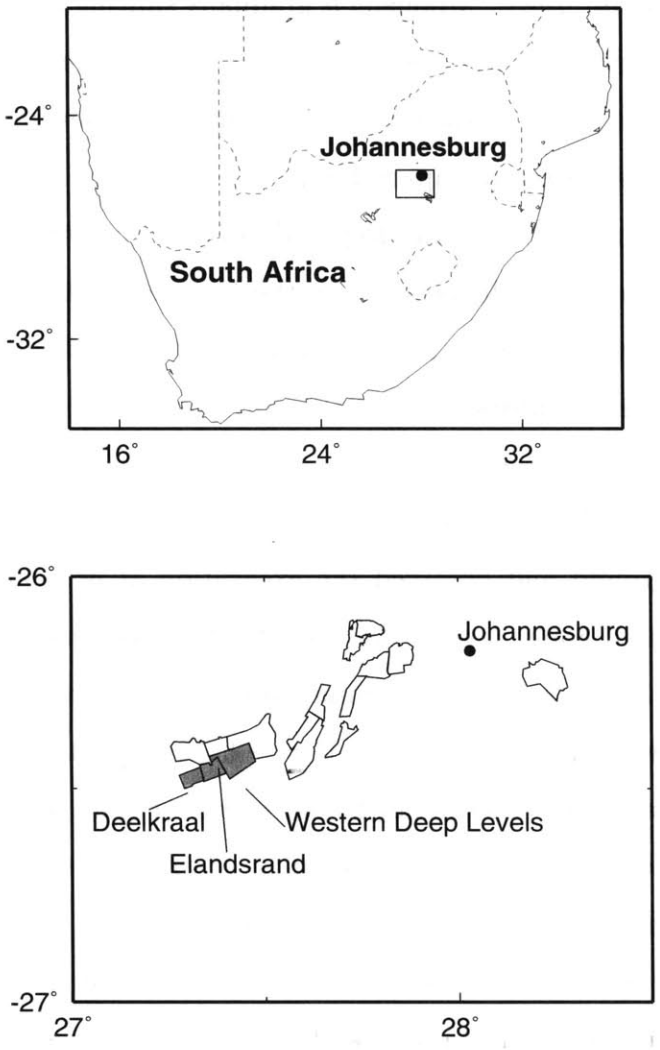

Figure 3-1: Southern Africa (top) and Far West Rand mining district, Republic of South Africa (bottom). The data in this study are from Deelkraal, Elandsrand, and the three Western Deep Levels mines (Mponeng, TauTona, and Savuka). Open outlines are lease areas of other mines in the region.

tures have been reactivated by the mining activity and are the source region of large mining-induced events.

Deelkraal, Savuka, and TauTona use modified longwall system of mining developed in the early 1980s in which pillars of about 20 x 120 m in stope area are permanently left unmined in the ore body [*Tanton et al.*, 1984]. Mponeng is gradually shifting from this system to the system used by Elandsrand called "sequential grid" in which many parallel mining faces are mined simultaneously. These two systems produce somewhat different patterns of seismic activity over time (compare Figure 3-6 to Figure 3-5). Blast charges are set in drill holes that are on order 1m deep and 1m apart on strike. A slow-burning cotton fuse is lit at the charge highest up on the longwall to begin the blasting process. The charges are wired together so that each blast down a single longwall panel of about 40 m occurs within milliseconds of the previous blast.

During the course of this study we made approximately 25 visits underground during working shifts, and at least one visit at each of the five mines. We assisted in mapping geologic features underground and observed the excavation at or near typical active faults and their associated gouge layers. We also observed the seismic array setup and data-processing routines in use. The mines are very seismically active; the networks record $\approx$ 1500 events per day down to $M = -2$. Five months of seismicity recorded by the Mponeng array includes about 80,000 events (Figure 3-3). The data in this study was located, cataloged and processed by mine seismologists (see Table 3.1). Mine locations are given in local coordinates determined at each mine (see Appendix A for explanation of these coordinate systems.) We excluded from our dataset events recorded at fewer than four stations and events that appeared to be blasts that consisted of several small-amplitude high-frequency arrivals spaced milliseconds apart. We included the hundreds of events triggered within seconds of daily blasting. Locations and magnitudes are well-determined in the catalog, therefore we have an extensive dataset for the analysis of frequency-magnitude statistics and spatio-temporal relationships of the seismicity.

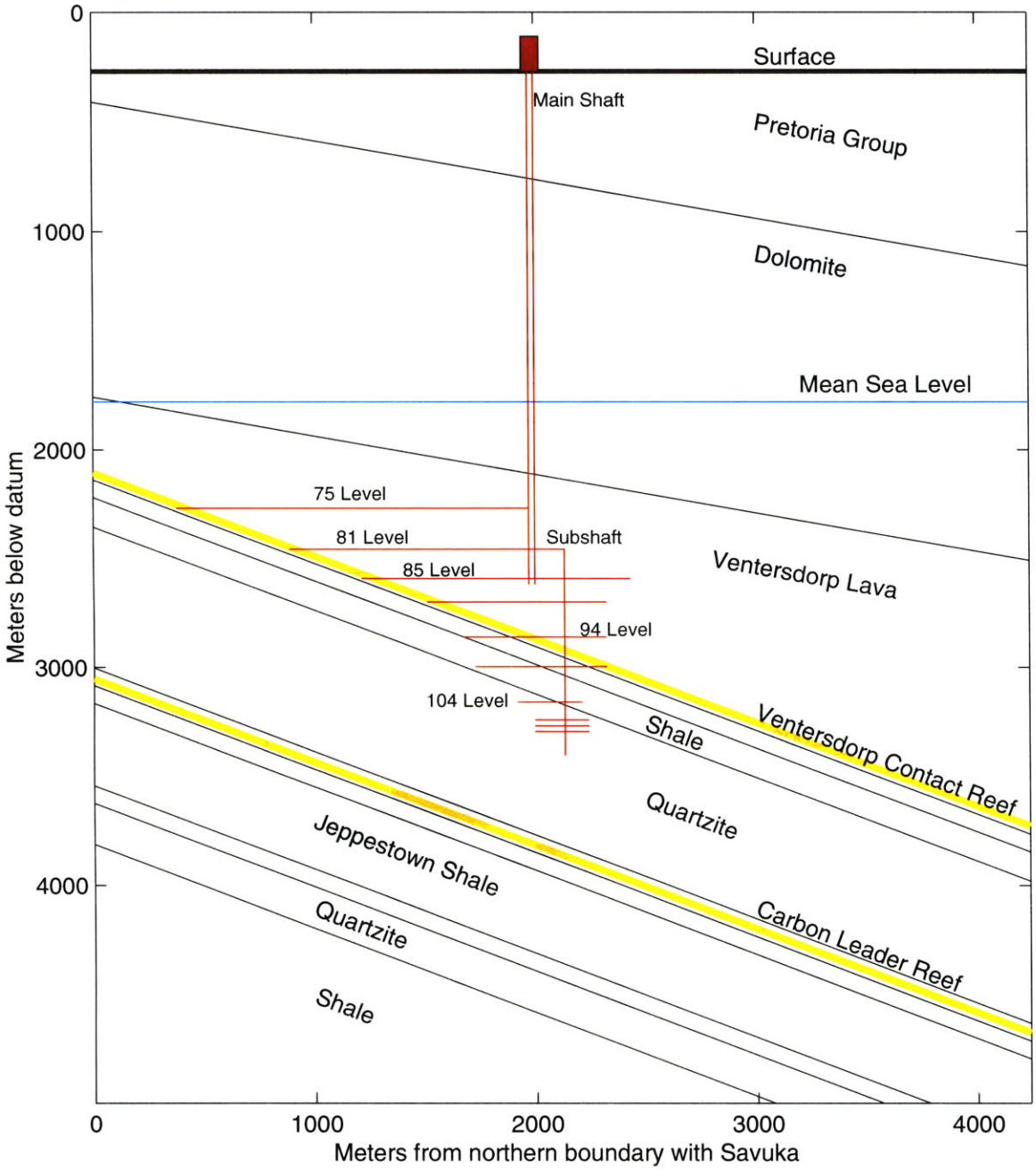

Figure 3-2: Section through the main shaft of Mponeng looking east. The "datum" from which depth is measured is an elevation marker in Johannesburg. At present, Mponeng is extending another subshaft to reach the Carbon Leader Reef.

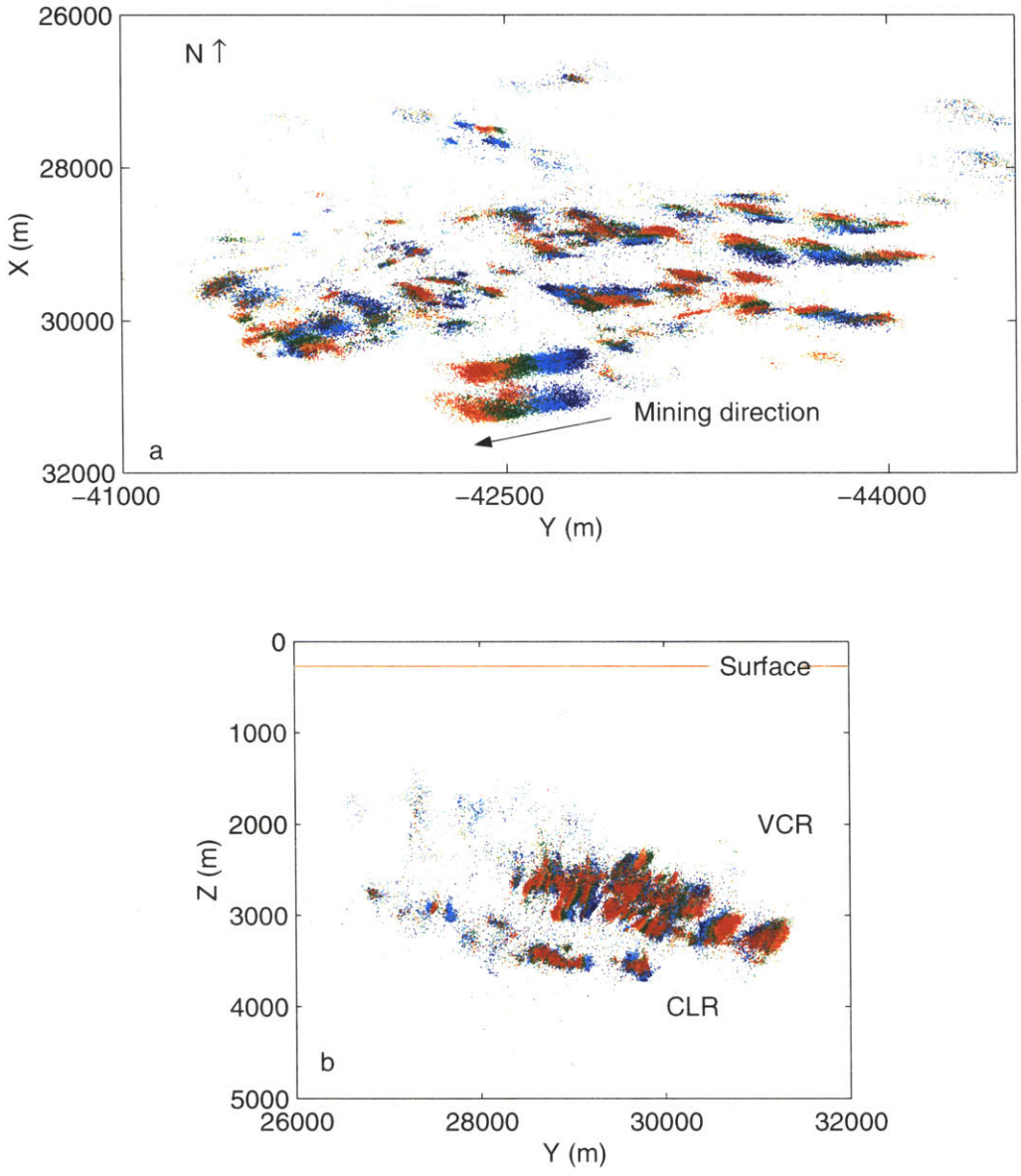

Figure 3-3: Map section in mine coordinates for five months of seismicity (October and November, 1998, January - March, 1999) recorded by the Mponeng array (a), and a cross-section looking east of the same data (b). Colors grade from cool to warm as the events become more recent. Seismicity tracks the progression of mining operations through time as shown by the arrow in (a). In (b), each reef's activity is apparent. Mponeng does not mine the CLR, but its geophones record events on the CLR where Savuka and TauTona operate directly beneath Mponeng.

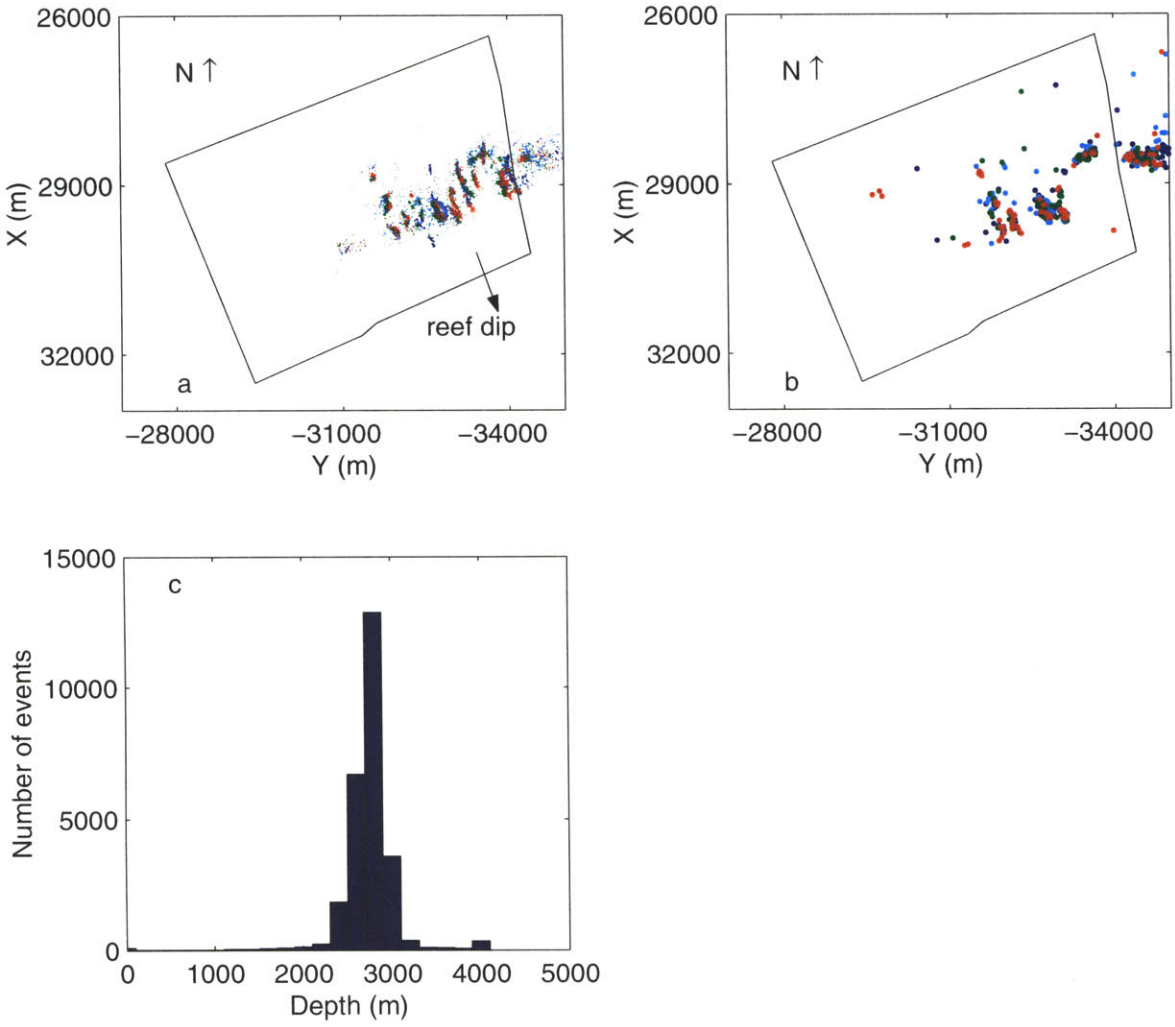

Figure 3-4: Map section in mine coordinates for four months of seismicity (January, April, July, October 1999) at Deelkraal (a), and of $M > 1$ for the same catalog (b). Colors grade from cool to warm as the events become more recent. The small events that dominate (a) track the progression of mining operations. The northwest-southeast trending lineations show seismic activity in the longwalls where the gold-bearing reef is being excavated. The large events in (b) are concentrated on weak geological features. In (a) and (b), the black outline is the lease area of Deelkraal. The Deelkraal network also records some seismicity in Elandsrand, the mine directly adjacent to the east (see Figure 3-5). Histogram of event depths for 1999 at Deelkraal (c).

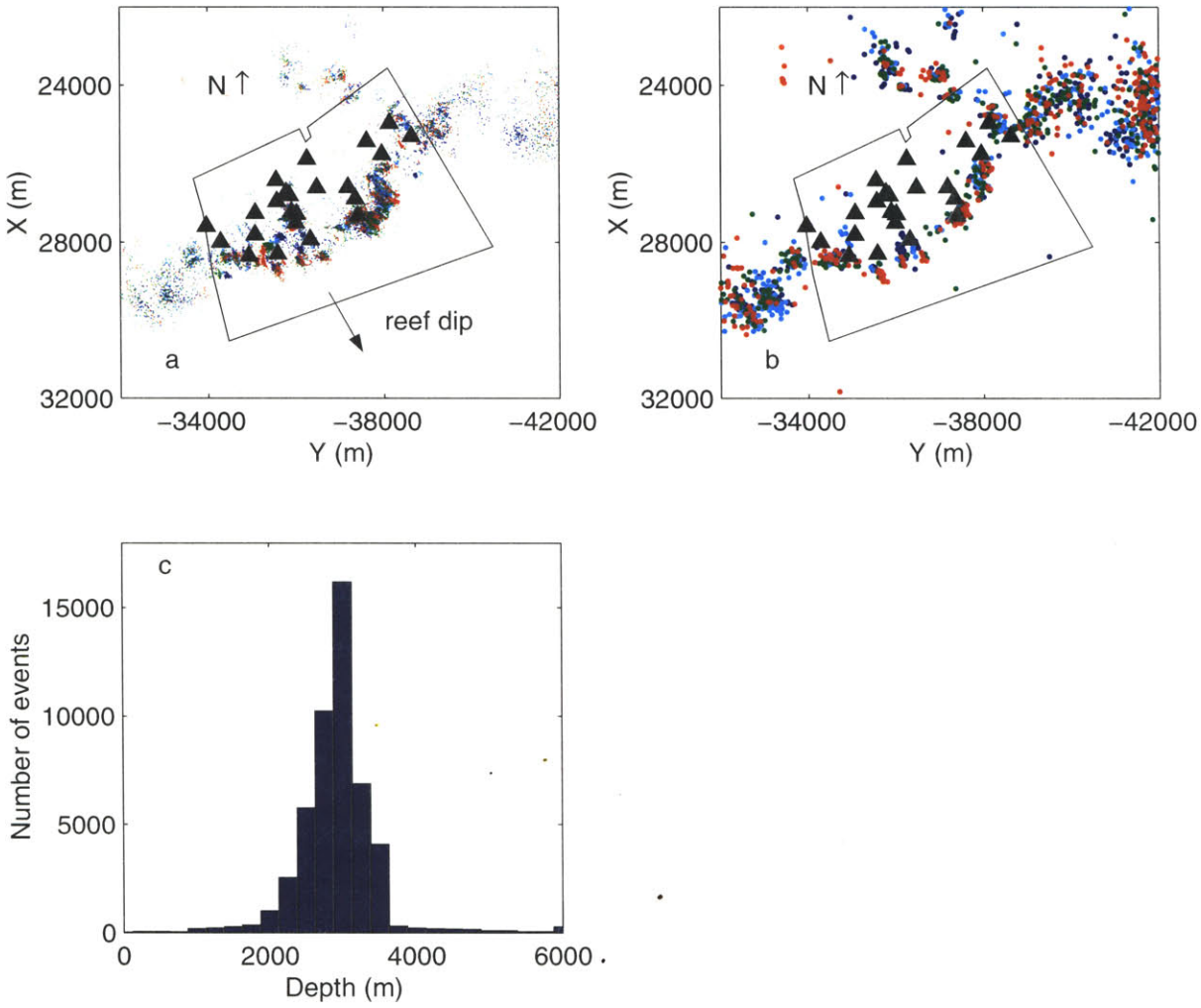

Figure 3-5: Map section in mine coordinates for four months of seismicity (January, April, July, October 1999) at Elandsrand (a), and of $M > 1$ for the same catalog (b). Colors are as in Figure 3-4, and triangles are geophone stations. Elandsrand uses the sequential grid method of mining, so the space-time progression of seismicity is less visible. The black outline shows the lease area of Elandsrand. Events outside the lease area are recorded by the Elandsrand network but occurred in Deelkraal (adjacent to the west) and Savuka (adjacent to the northeast). Histogram of event depths for Elandsrand during 1999 (c).

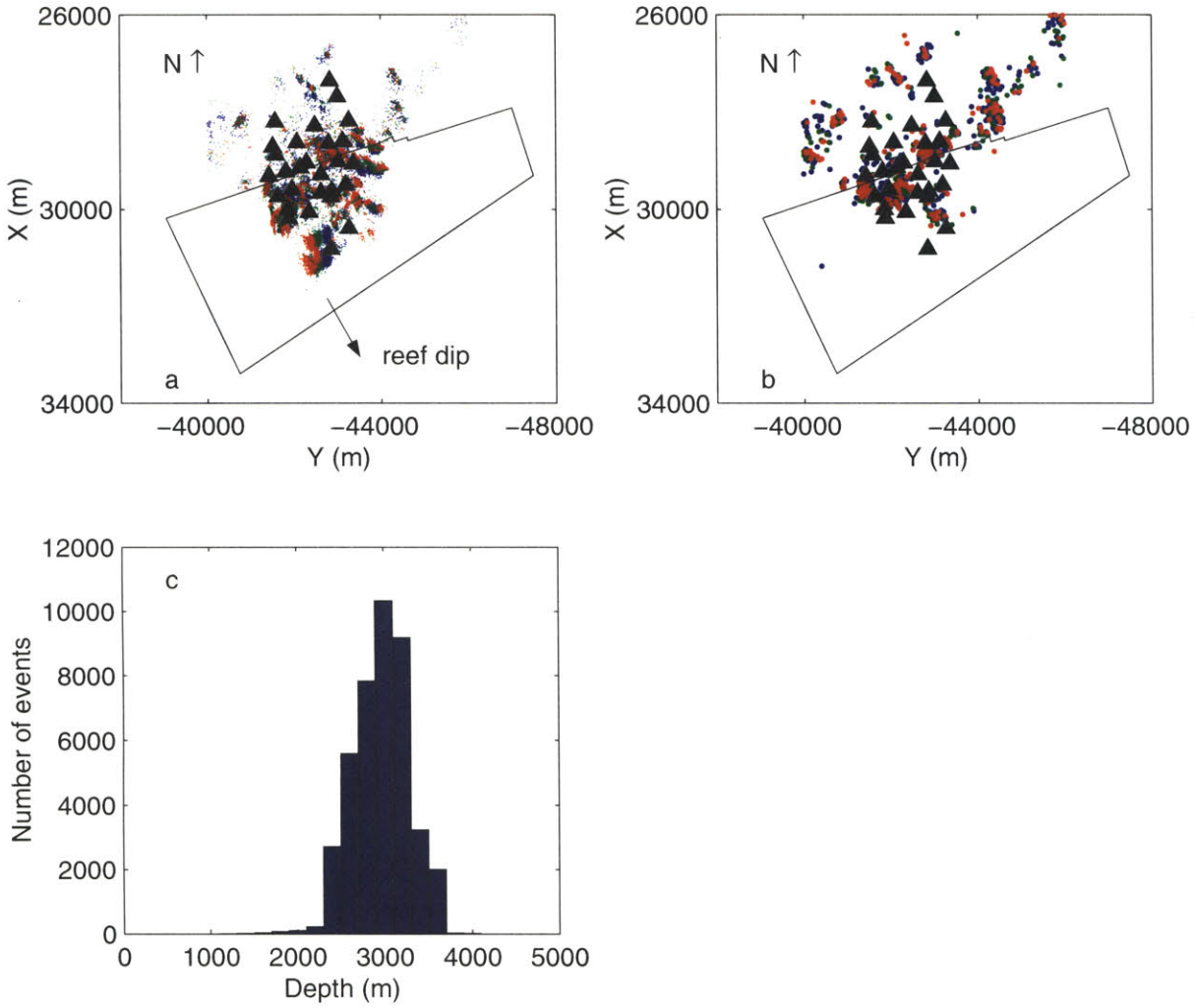

Figure 3-6: Map section in mine coordinates for three months (October 1998, January and March 1999) of seismicity at Mponeng (a), and of $M > 1$ for the same catalog (b). All symbols are as in Figure 3-5. The black outline is the surface lease area. About half of the events and stations locate north of this area because Mponeng overlaps with Savuka and TauTona laterally. Mponeng mines the VCR while the other two mines extract ore from the CLR directly beneath Mponeng. The southern portion of the VCR mined at Mponeng is at approximately the same depth as the CLR under Savuka and TauTona. Histogram of event depths for the same time span at Mponeng (c).

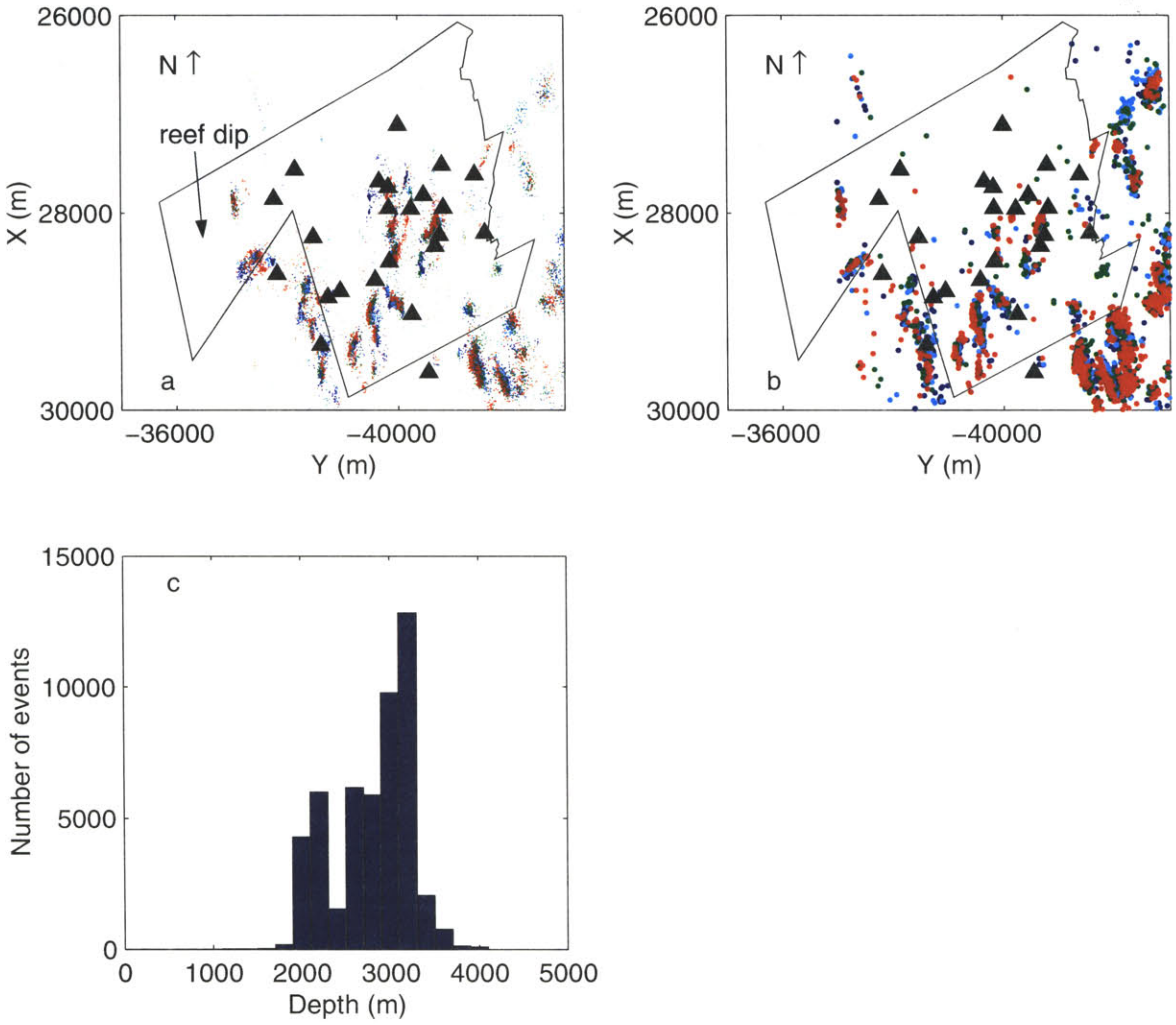

Figure 3-7: Map section in mine coordinates for four months of seismicity (January, April, July, October 1998) at Savuka (a), and of $M > 1$ for the same catalog (b). Symbols are as in Figure 3-5. Stations and seismicity that appear outside the lease area of Savuka are events in the CLR mined by Savuka that lie underneath the mining activities of Elandsrand (to the southwest) and Mponeng (to the southeast) where the VCR is being mined. Histogram of event depths for Savuka for all of 1998 (c). Savuka mines a limited portion of the VCR, accounting for the peak in shallow seismicity around 2000 m, but most of the seismicity occurs on the deeper CLR.

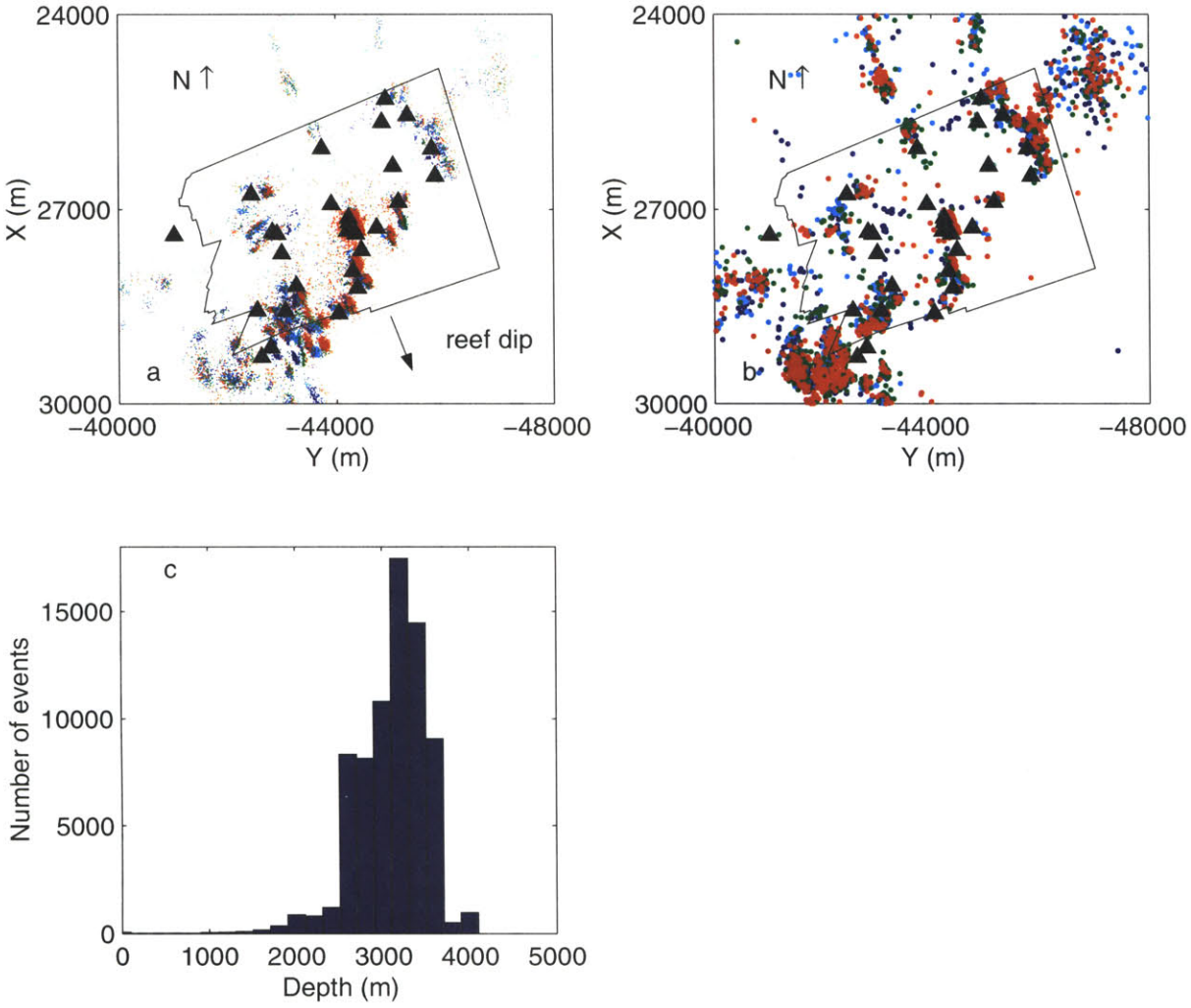

Figure 3-8: Map section in mine coordinates for four months of seismicity (January, April, July, October 1998) at TauTona (a), and of $M > 1$ for the same catalog (b). Symbols are as in Figure 3-5. Stations and seismicity that appear outside the lease area of TauTona are events in the CLR mined at TauTona that lie underneath the mining activity of Mponeng (to the southwest) where the VCR is being mined. Histogram of event depths for TauTona for all of 1998 (c).

Table 3.1: Mine Statistics

Mine	Catalog span	Events	Stations	Reef
Mponeng	Oct-Nov 1998, Jan-Mar 1999	58,068	28	VCR
Savuka	Jan 1998 - Mar 1999	54,125	23	VCR, CLR
Elandsrand	Jan 1994 - Oct 1999	307,038	25	VCR
Deelkraal	Jan 1997 - Oct 1999	70,240	13	VCR
TauTona	Jan 1998 - Dec 1998	57,916	20	VCR, CLR

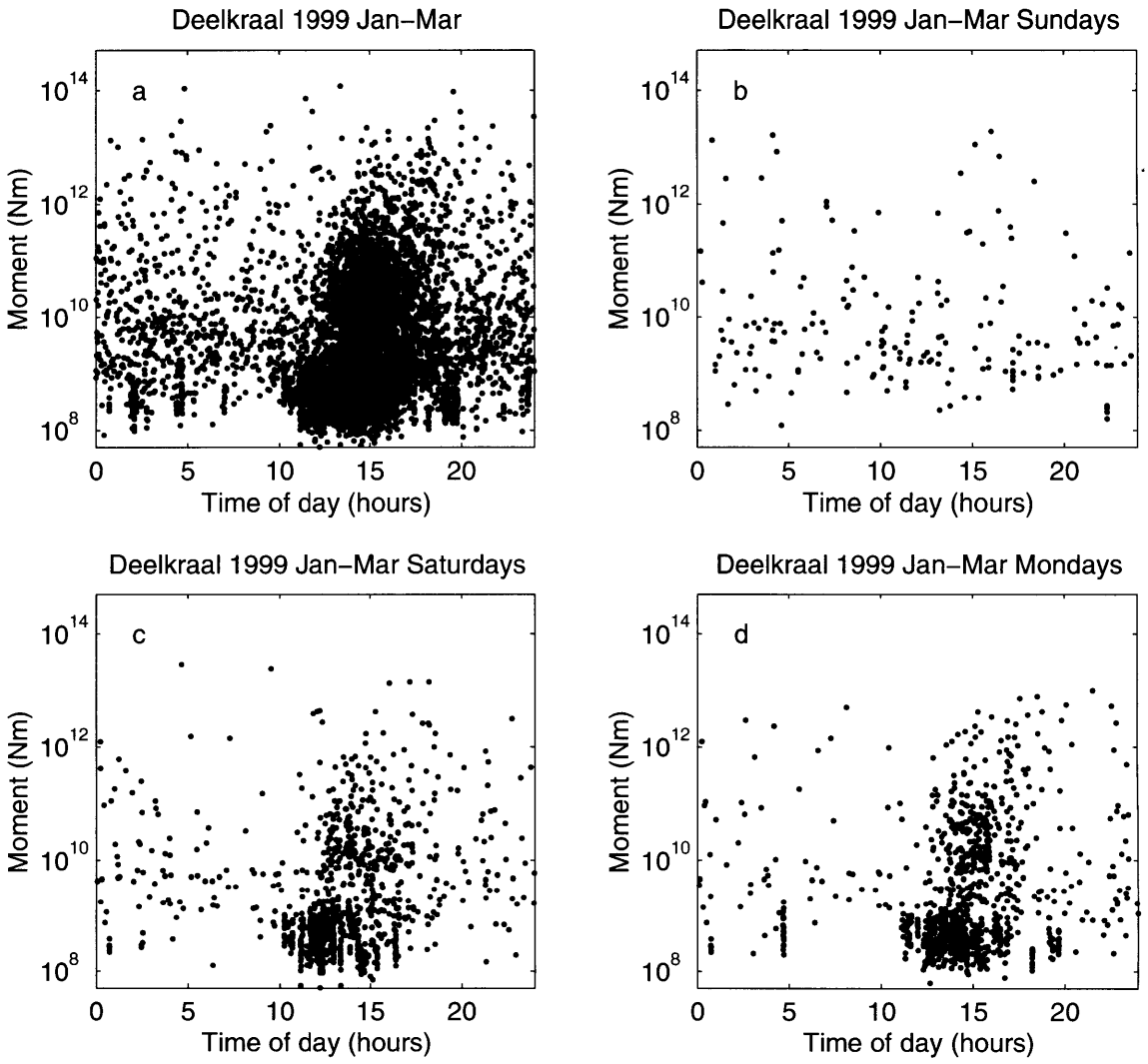

Figure 3-9: Time of day vs. seismic moment at Deelkraal for January, February, and March 1999 (a), seismicity on Sundays only for the same time period (b), Saturdays only (c) and Mondays only (d). The entire three-month period has 7013 events. There were 185 events on Sundays, 1072 events on Saturdays, and 1011 events on Mondays. Deelkraal normally blasts around noon; this is visible as the peak in seismicity there on Monday and Saturday. Generally, no blasting is done on Sundays.

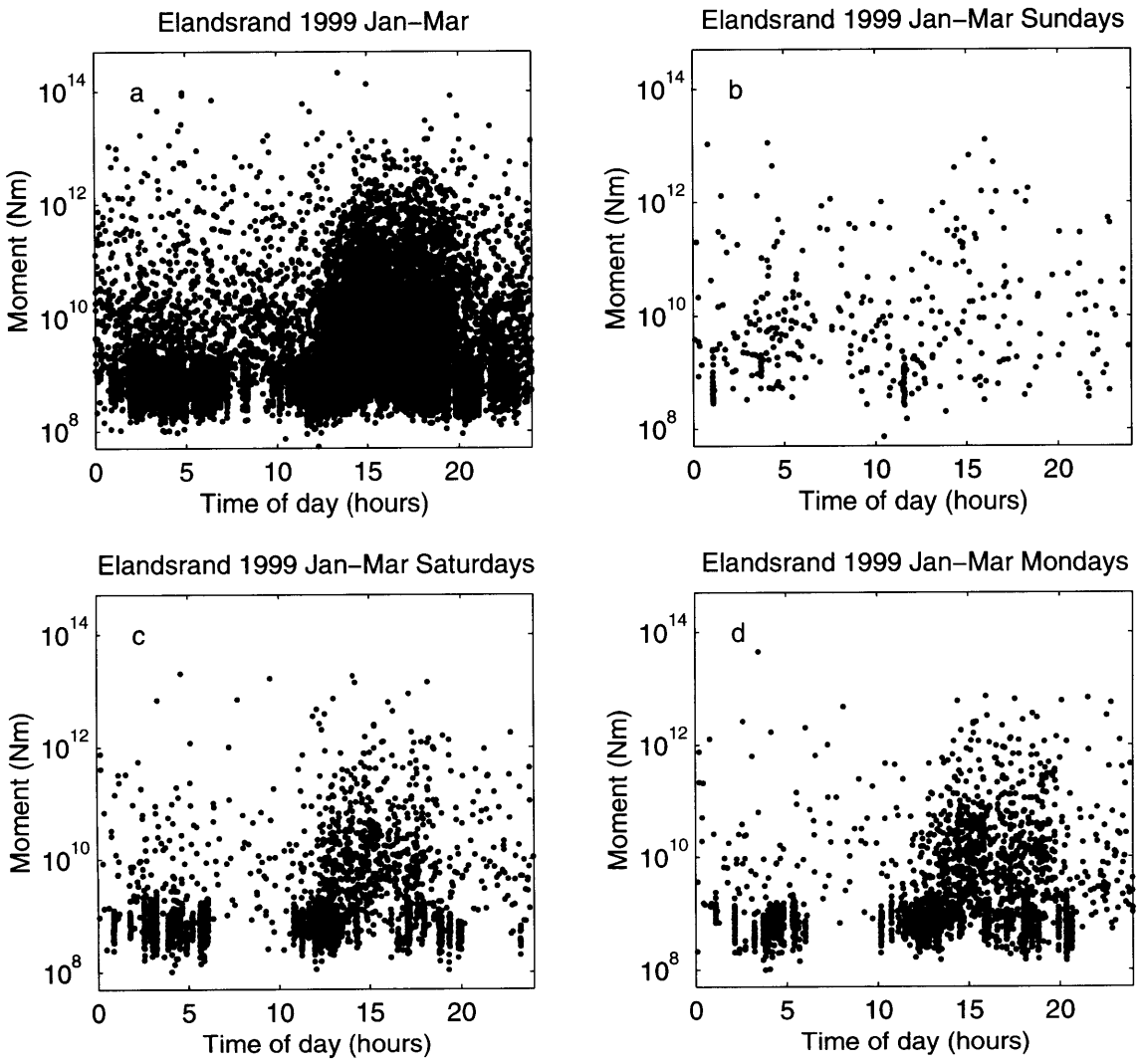

Figure 3-10: Time of day vs. seismic moment at Elandsrand for January, February, and March 1999 (a), seismicity on Sundays only for the same time period (b), Saturdays only (c) and Mondays only (d). The entire three-month period has 18800 events. There were 374 events on Sundays, 2641 events on Saturdays, and 2579 events on Mondays. Elandsrand does development blasting between 12 and 5 am and stope face blasting between 12 and 5 pm. Stope faces are normally only blasted every other Saturday, but there are more events on Saturdays than on Mondays which is a regular blasting day. Generally, no blasting is done on Sundays.

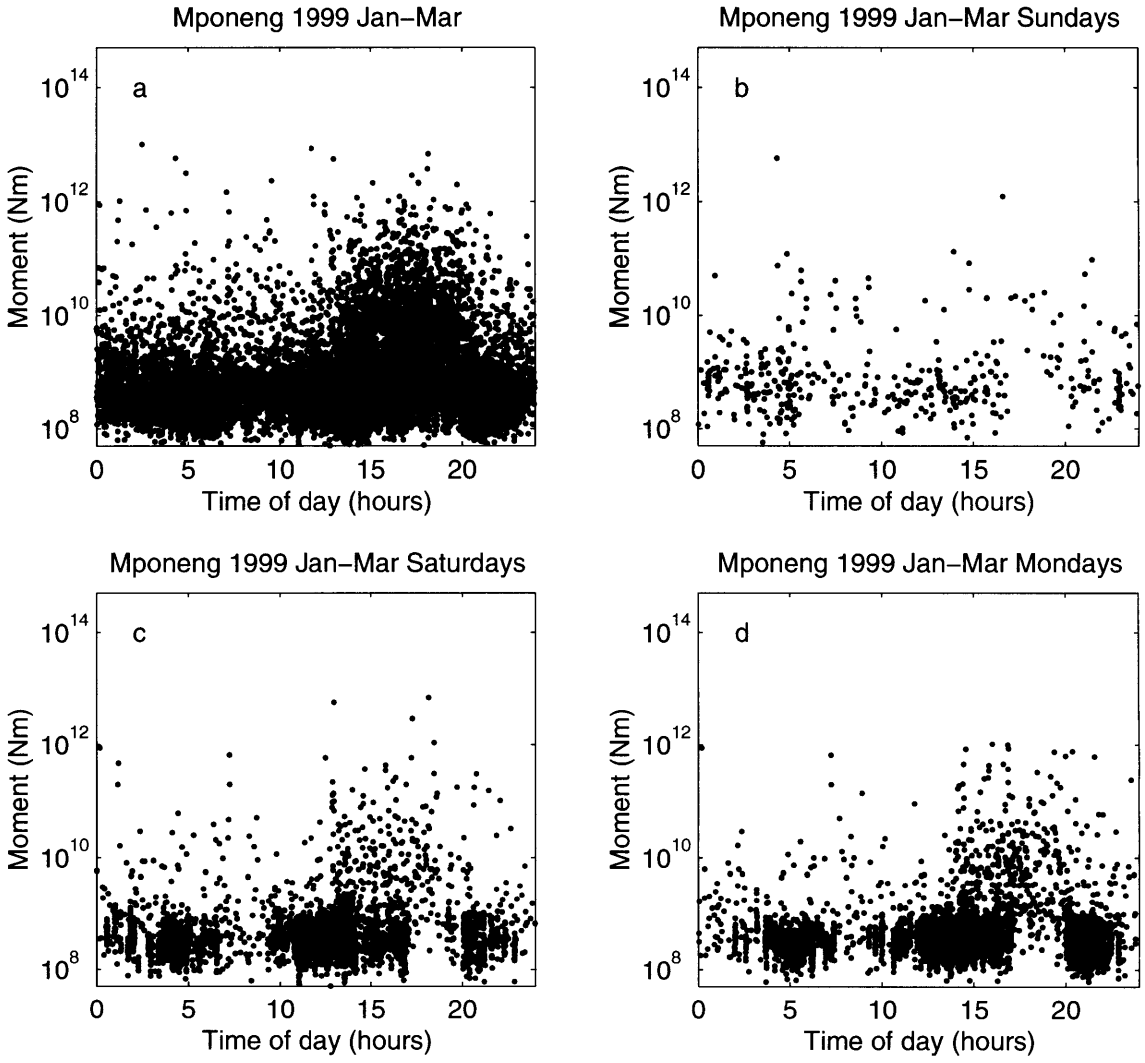

Figure 3-11: Time of day vs. seismic moment at Mponeng for January, February, and March 1999 (a), seismicity on Sundays only for the same time period (b), Saturdays only (c), and Mondays only (d). The entire three-month period has 28837 events. There were 425 events on Sundays, 3959 events on Saturdays, and 4810 events on Mondays. Mponeng normally blasts around 5 pm, though some stope faces are blasted three times per day. Generally, no blasting is done on Sundays.

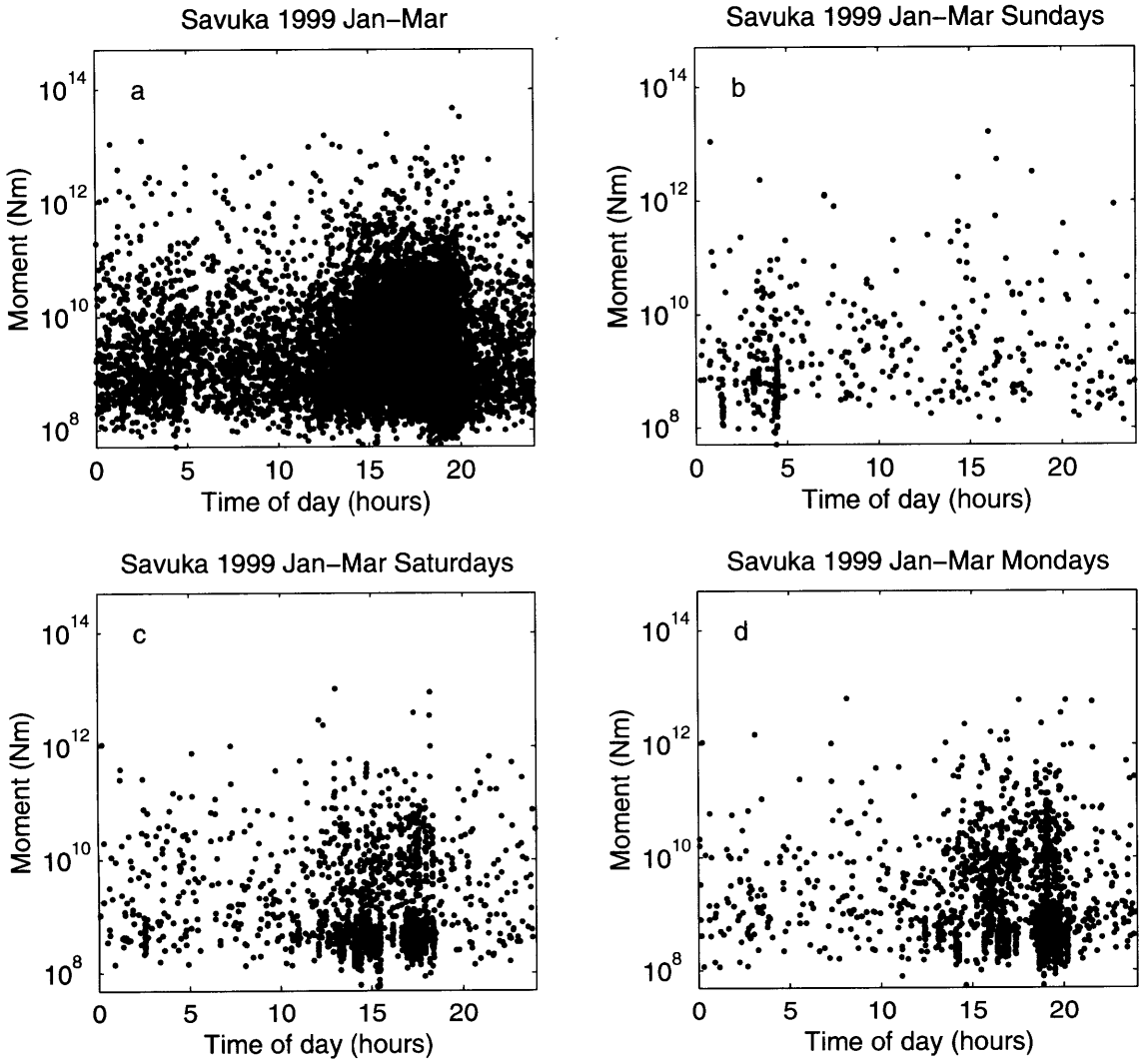

Figure 3-12: Time of day vs. seismic moment at Savuka for January, February, and March 1999 (a), seismicity on Sundays only for the same time period (b), Saturdays only (c), and Mondays only (d). The entire three-month period has 11435 events. There were 448 events on Sundays, 1659 events on Saturdays, and 1792 events on Mondays. Savuka normally blasts in the evening. Generally, no blasting is done on Sundays.

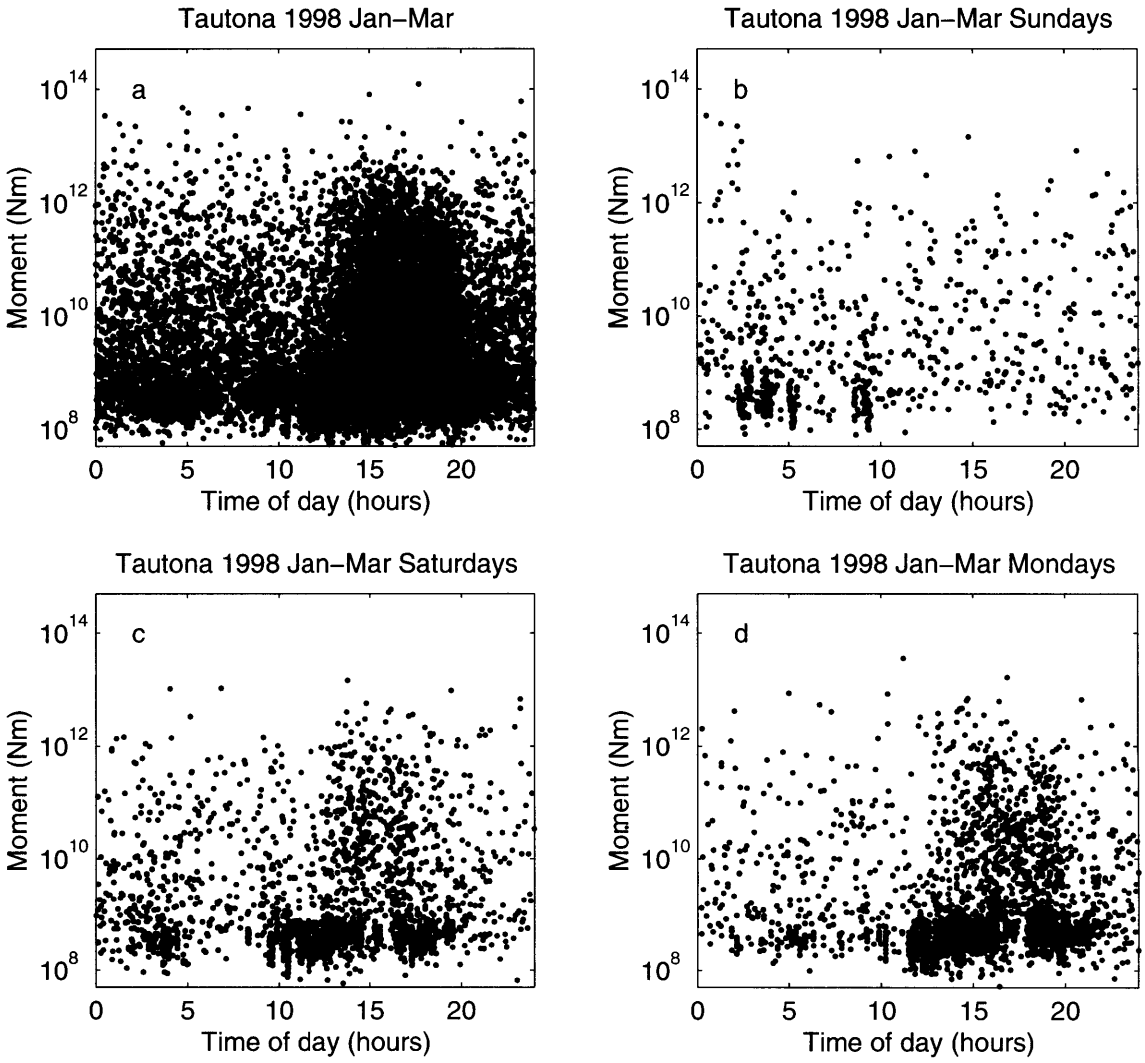

Figure 3-13: Time of day vs. seismic moment at TauTona for January, February, and March 1998 (a), seismicity on Sundays only for the same time period (b), Saturdays only (c), and Mondays only (d). The entire three-month period has 18736 events. There were 777 events on Sundays, 2154 events on Saturdays, and 2863 events on Mondays. TauTona normally blasts stope faces in the evening and some development ends in the morning. Generally, no blasting is done on Sundays.

3.3 Frequency-Magnitude Statistics

The catalogs examined in this study comprise over half a million events (Table 3.1). For each of the five mines, we created frequency-magnitude distributions by binning the data in 0.1-moment magnitude units and normalizing them to 30-day intervals to account for different catalog lengths (Figure 3-14). The detection thresholds of the in-mine networks, as defined by the peaks of the discrete distributions, are all $M = -0.4$, except for Elandsrand, where it is $M = -0.2$. The seismicity rates fall off rapidly below these thresholds, except at TauTona, where the recent installation of a tightly-spaced accelerometer array has increased network sensitivity in a small area (Section 336 of TauTona). This is responsible for the higher cataloged rates observed for TauTona at $M < -1$ (Figure 3-14a).

Above the detection threshold, the frequency-magnitude distributions share several characteristics that distinguish them from the Gutenberg-Richter (power-law) relationships often found for tectonic earthquakes. All show an initially rapid, though variable, roll-off just above the detection threshold, a sharp inflection to a much lower slope at about $M = 0$, a relatively narrow range of roughly self-similar behavior (b-value near unity), then a concave-downward curvature up to a maximum magnitude of about $M = 3$. This shape appears to be caused by the superposition of two populations of events, which we label as Type A and Type B.

The largest event in this dataset has a moment magnitude of 3.3, but this upper cutoff is artificially limited by the catalog timespans. For example, events with $M > 3.5$ occur on an annual basis at Western Deep Levels, and mining-induced earthquakes have been recorded with moment magnitudes as high as 4 in the Far West Rand region. This upper-magnitude limit corresponds to a fault radius on the order of 1 km, which is intermediate to the lengths of the "long walls" commonly used in stoping ($\approx$ 200 m) and the lateral span of a whole mine ($\approx$ 3 km). Therefore, it likely reflects the regional extent of the stress perturbations associated with mining [*McGarr*, 1984b].

The Type-A events form the maxima in the discrete distributions, accounting for

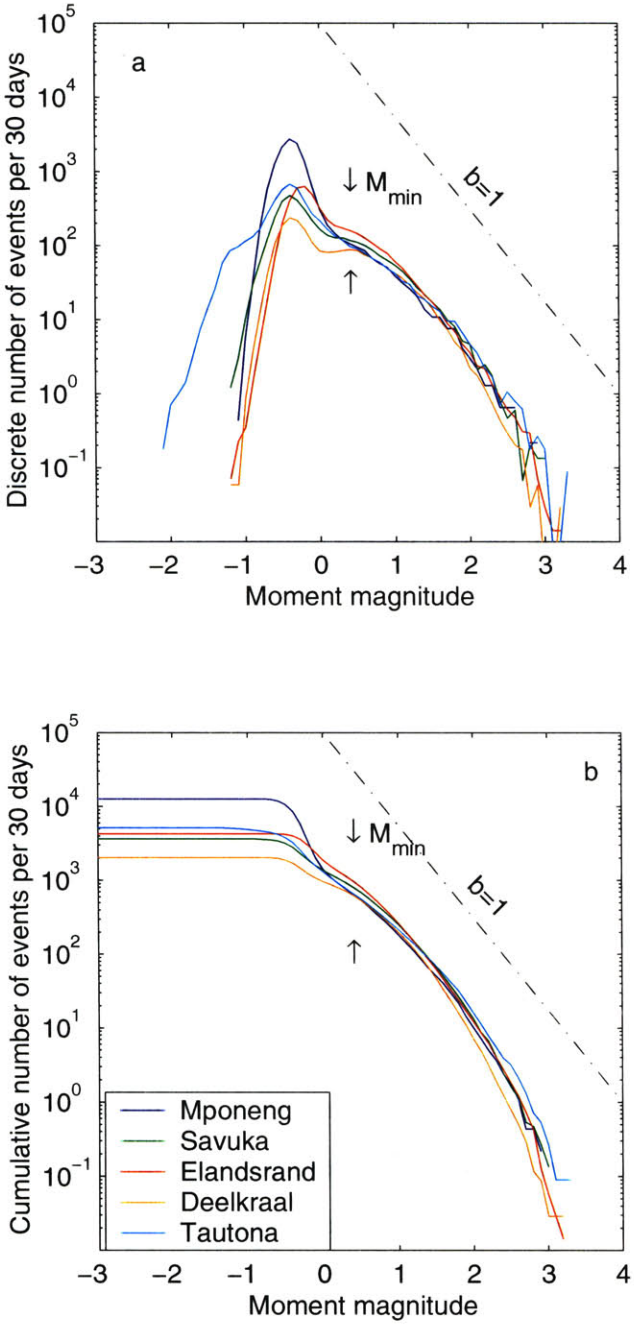

Figure 3-14: Discrete (a) and cumulative (b) Gutenberg-Richter distributions of seismicity per 30-day period in 0.1-magnitude unit bins for Mponeng (blue), Savuka (green), Elandsrand (red), Deelkraal (orange), and TauTona (light blue). All mines have a bimodal frequency-magnitude distribution and are approximately alike above $M \approx 0.3$.

the majority of the cataloged mine seismicity. The rapid rolloff from these peaks toward larger magnitudes indicates that the Type-A events have an upper magnitude cutoff near $M = 0$. The rolloff at low magnitudes reflects the detection threshold of the in-mine arrays, so that the scaling relationship for Type-A seismicity cannot be inferred from the whole-mine catalogs used here. We note that previous work on very small events in situ, such as the study by *Trifu et al.* [1993] from Strathcona Mine, Ontario, Canada, found frequency-magnitude relations suggesting a departure from self-similar scaling due enhanced seismicity in the range of $-0.5 < M < 0$ and their catalogs were complete to $M = -1.5$.

Differences in mining practices probably explain the differences in the distribution of events of $M < 0$ among the five mines. Most of these Type-A events occur shortly after blasting and their rates are therefore causally related to the amount of blasting, which varies from mine to mine. A detailed analysis of this relationship requires the consideration of two different types of blasting: on the stope faces (for mining gold ore) and at the development ends (for extending tunnels, haulages, and spaces for other mine infrastructure). Such an analysis is not attempted here, although we note that the largest peak in the discrete frequency-magnitude distribution is observed for Mponeng, where the development rates are very high and some stope faces are blasted three times per day. Once per day is the norm for the other mines. Deelkraal has the smallest seismicity peak because the excavation rates are the lowest.

Despite the differences in mining practice and rates, the frequency-magnitude distributions for the events with $M > 1$ are similar among all five mines. The spatial and temporal distributions of $M > 1$ earthquakes are not directly correlated with day-to-day mining operations (compare Figures 3-4a and 3-4b or the similar maps from any of the other mines, for example). From several lines of evidence discussed in the next section, we infer that this Type-B seismicity is due to shear failures on zones of weakness and is therefore analogous to tectonic seismicity.

We performed a number of tests to determine whether the "bimodality" of the frequency-magnitude distributions is an intrinsic property of the seismicity, or whether it is an artifact of spatial sampling or another form of network bias that preferentially

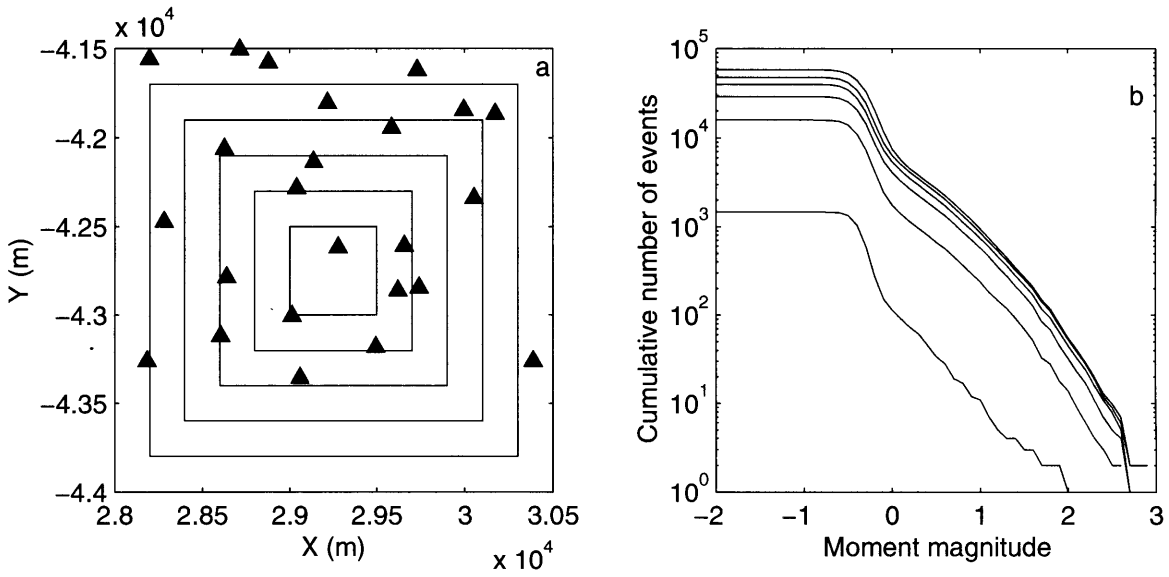

Figure 3-15: Plan view of Mponeng (a). Triangles are stations. Successively smaller boxes show the areas over which cumulative frequency magnitude statistics in 0.1-M bins are calculated in (b). Largest box is 2.5 km on a side; box dimensions decrease by 200 m to inner box, which is 500 m on a side. In (b), the similarity in the cumulative distributions, which all show an inflection near $M = 0$, indicates that the shape is not biased by network sampling. We interpret the inflection to be the transition from Type-A to Type-B events.

samples small events. For example, we compared the distribution in space of events in bins of 0.1 moment-magnitude units between $M = 0$ and $M = 1$ at Mponeng. No anomalous clustering of events was observed, and events of different magnitudes were found to be distributed equally throughout the coverage area of the seismic network. Even the smallest events are recorded across a distance covered by at least half of the array. Furthermore, when all events within 200 m of a station were eliminated from the dataset, the bimodal character of the distribution remained intact. The shape of the distribution also remained intact when the spatial extent of the dataset was successively reduced (Figure 3-15). The top curve in Figure 3-15 is for a box 2.5 km on a side comprising almost 70,000 events from Mponeng, whereas the bottom curve includes only about 1500 events from a 500-m box. The bimodality is preserved at all levels. This series of tests was repeated for the other four mines with the same results.

These tests indicate that the unusual shape of the frequency-magnitude curves in

the vicinity of $M = 0$ is not caused by network bias. In particular, the curvature observed for the Type-B seismicity in the magnitude range $0 < M < 1$ appears to be a genuine feature of the distributions. Deelkraal shows a local maximum at $M = 0.4$, and the discrete distributions for the other mines are consistent with a Type-B maximum at about this value, which we interpret as a lower magnitude cutoff, $M_{\min}$, for Type-B events.

Comparison of frequency-magnitude distributions from time periods during which no blasting was conducted with distributions from time periods with regular blasting schedules confirms this interpretation (Figure 3-16). The frequency-magnitude curve corresponding to the Christmas holiday when there was no blasting (black line) does not show the Type A peak that is apparent during normal mining operations (grey line).

The bimodal morphology apparent in Figure 3-14 has also been observed by *Finnie* [1999b, a]. The existence of different classes of mining-induced seismicity has been noted previously by several workers [*Kijko et al.*, 1987; *Johnston*, 1988; *Johnston and Einstein*, 1990; *Gibowicz*, 1990; *Prugger and Gendzwill*, 1990; *Gibowicz and Kijko*, 1994; *Finnie*, 1999b, a], but only *Finnie* [1999a] successfully separates two types spatially (he calls them "genuine" and "spurious" events) and recombines them to produce a bimodal frequency-magnitude curve. The event populations that we define as Type-A and Type-B are likely similar to these two classes of events.

3.4 A physical model for bimodal seismicity

The attributes of Type-A and Type-B events suggest that they result from two fundamentally different processes of rock failure. Type-A events are hypothesized to be "fracture-dominated" ruptures in a low normal-stress environment involving the failure of intact rock that responds at short time scales (seconds to minutes) to externally-imposed stress changes such as blasting. Type-A events may occur at scales as small as grain microcracks at the acoustic emission level up to scales limited

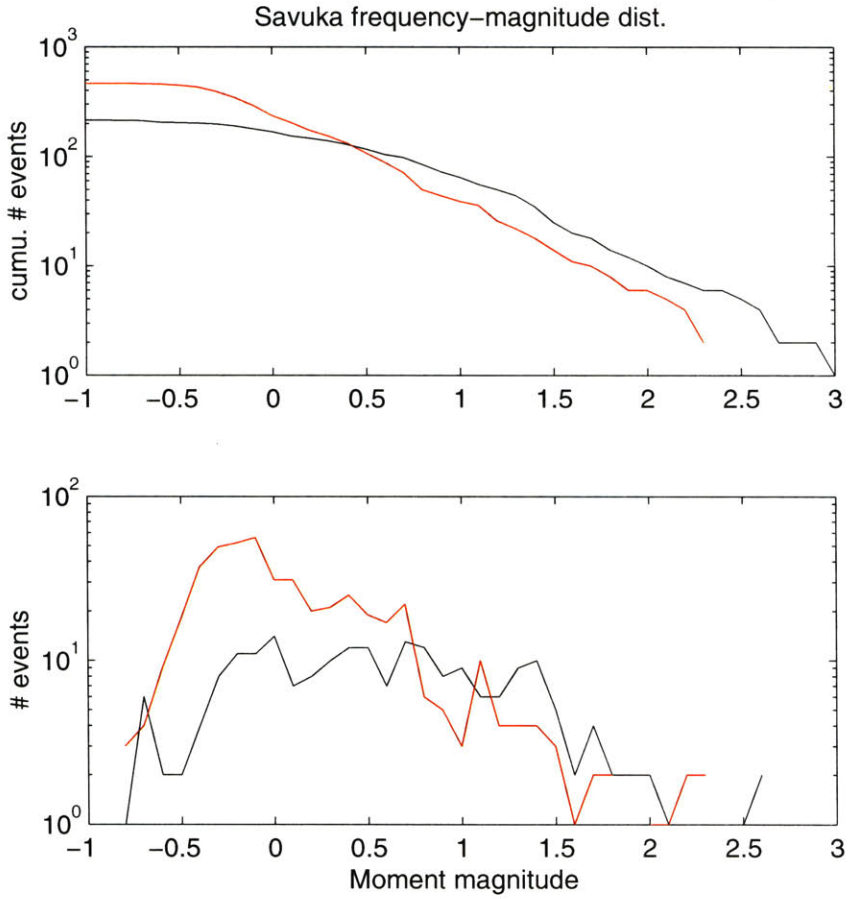

Figure 3-16: Discrete (a) and cumulative (b) frequency-magnitude distributions for Savuka for two 11-day periods. The grey line shows a regular blasting period and the black line shows activity during the Christmas holiday when no blasting was conducted.

by the stress-perturbation aureoles surrounding excavations. Because Type-A events likely involve fresh cracking of rock that may result in little slip accumulation, their process zones are hypothesized to be smaller than the nucleation patch size expected for a slip-weakening model of shear strain [*Barenblatt*, 1959; *Ida*, 1972; *Andrews*, 1976a]. The radiated energy is high compared to that of Type-B events that involve more slip.

Type-B events are hypothesized to be "friction-dominated" ruptures that are also induced by mining but are the result of the removal of ore for a long period of time rather than due to the most recent blasting activity. They entail slip on pre-existing planar zones of weakness, such as bedding planes, dykes, and reactivated faults. These weak zones do not necessarily have to be large well-mapped features; they may be any surface upon which shear strain can easily be accommodated [*Ortlepp*, 1997], including old Type-A fractures. We propose that the process zone of a Type-B event is friction-controlled with a spatial size on the order of the critical patch size r_c, and is larger than that for a Type-A event. Type-B events may run away into the surrounding intact rock as they propagate, so that later excavation of their ruptures shows evidence of fresh fracturing, but their *initiation* is hypothesized to be controlled by the frictional properties of the process zone in which they nucleate. Owing to the similarity of their frequency-magnitude distributions among all five mines, we hypothesize that Type-B seismicity is not affected significantly by different mining practices or rates.

3.4.1 Spatio-temporal Relationships

Type-A events occur as series of distinctive swarms in space and time immediately following blasting and close to blasting sites. In this sense, they may be thought of as "aftershocks" of blasts. (Our knowledge of the response time of the Type-A events relative to blasting is based on personal communication with the mine workers since in general blast times are not accurately recorded or documented.) In contrast, Type-B events occur singly or occasionally as part of a foreshock-mainshock-

aftershock sequence [*Gibowicz*, 1997]. They are distributed on structures throughout the entire mine, instead of occuring only near active mining areas and can happen at any time of day. At Mponeng on 02 Feb 1999 between 1300h-1400h, a Type-B sequence occurred in the same time frame as several Type-A clusters in different localities around the mine (Figure 3-17). Shaded symbols show the Type-B events. They comprise a $M = 3.0$ event, one foreshock, several aftershocks, and three events not related to that sequence. Mine workers have associated the sequence with a previously-known mapped fault whose approximate location is shown by a dashed line (Figure 3-17a). The sequence is linear in space and its events do not cluster tightly in time, distinguishing them from Type-A events. Black symbols show Type-A clusters that are all associated with mine development (Figure 3-17a). The same Type-A events that make up each cluster in space are also clustered tightly in time (Figure 3-17b). All of the Type-A events are smaller than $M_0 \approx 2 \times 10^9$ Nm (Figure 3-17b). We observe that Type-A events of the same cluster have virtually identical waveforms, thus they may represent successive failure of the same overstressed asperity or of the same propagating crack (Figure 3-18).

The fact that Type-A seismicity occurs in tight swarms in space and time allows us to separate the two types of events based on their clustering characteristics. We use an algorithm in which all events within a distance of 100 m and 30 s of another event are classified as Type A except for large ($M > 1$) events and their aftershocks. This separation technique excludes some Type A's that are missed by the chosen box size or time window but it is merely designed to be a simple and quick way to define a large subset of events as clearly either A or B so that the other differences in their properties can be studied. We tested the effectiveness of this algorithm with the 107 events in Figure 3-17. Initally, 37 events were classified as Type B and 70 as Type A. Based on waveform similarity, 4 events were reclassified as Type A. Of these, one had been missed because it fell outside the 30-s time window, and the other three were slightly more than 100 m away from their nearest neighbors in the already-defined Type-A cluster to which they were reassigned. Results of this algorithm used to separate the Deelkraal catalog for 1999 (26743 events) are shown in Figure 3-19.

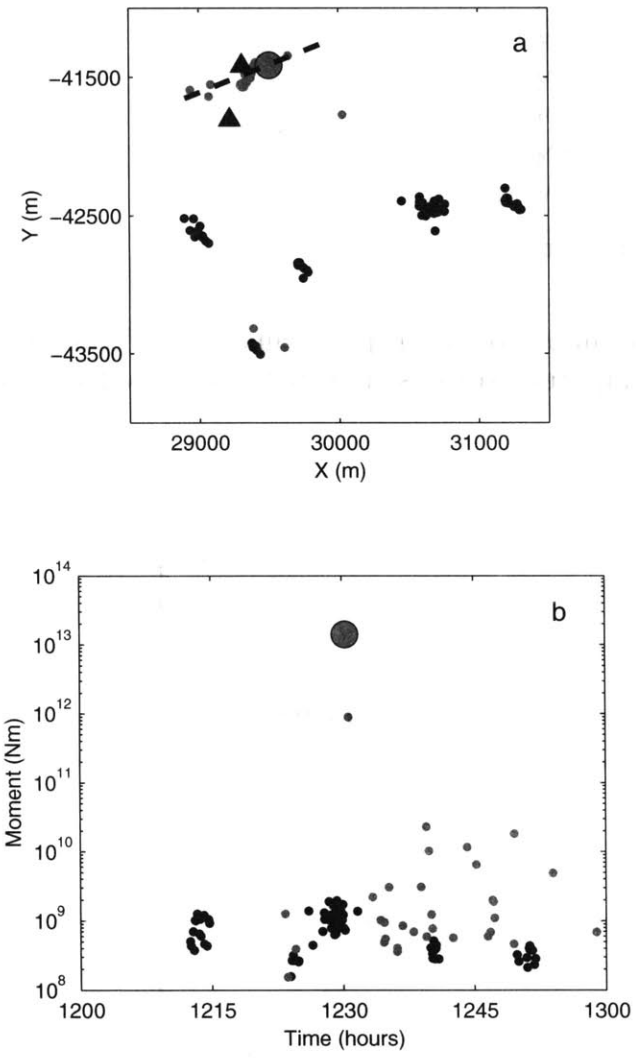

Figure 3-17: Map view of seismicity occurring between 1200h-1300h in Mponeng, 02 Feb 1999 (a) and M_0 vs. time for the same events (b). Type-A events are solid and Type-B events are shaded. In (a), triangles show two seismic stations, and the dashed line shows the approximate location of the normal fault thought to be associated with the Type-B seismicity. The large shaded circle is a $M = 3.0$ event.

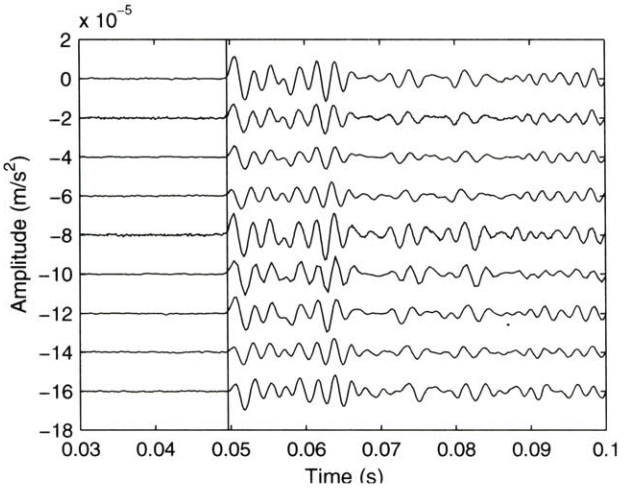

Figure 3-18: Waveforms of nine events in one of the Type A clusters in Figure 3-17 recorded at the same station. The amplitude scale is true, but each waveform has been offset from the others.

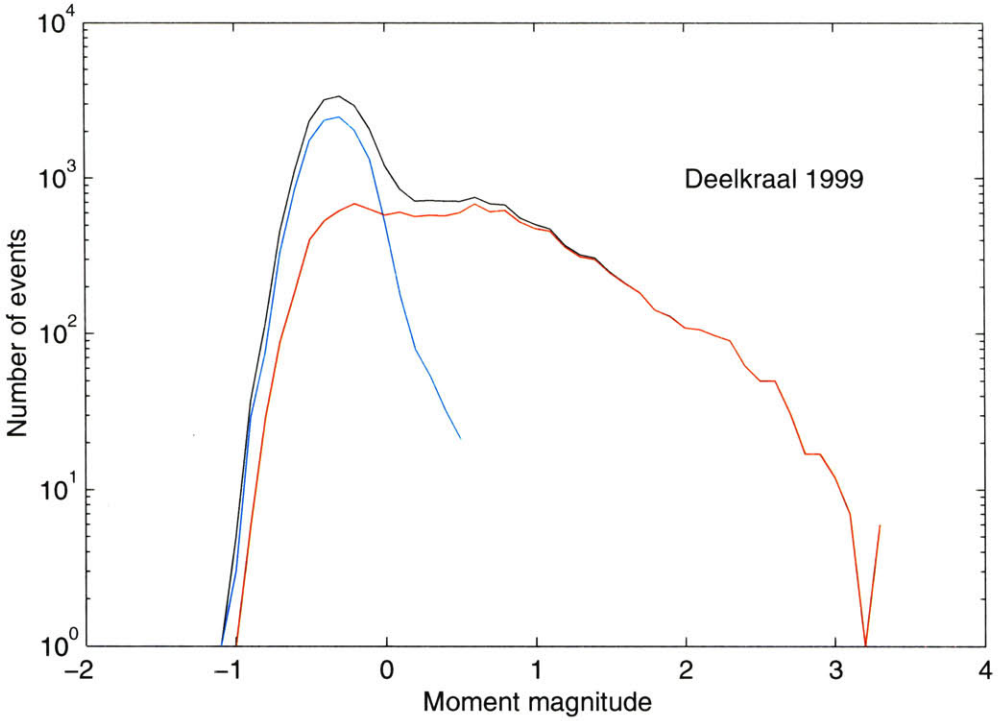

Figure 3-19: Discrete frequency-magnitude curve for the 1999 Deelkraal catalog. The black line shows the whole catalog. The blue line represents the Type A events and the red line is the Type B events. These two populations were separated via the space-time clustering algorithm described in the text.

3.4.2 Mechanisms

The two types of events can be differentiated based on visual inspection of their waveforms and spectra as well (Figure 3-20). Type-A events usually have lower S/P ratios than Type-B events (Figure 3-20a,c) and have higher frequency content (Figure 3-20b,d).

Much of the past study of event mechanisms in the mining environment has been limited by the quality of the available seismic data; therefore, many interpretations among previous workers have been inconsistent. Studies that analyzed P- and S-wave first motions interpreted fractures around stope faces as having isotropic components consistent with implosional mechanisms. These fractures were assumed to be related to closure of excavations and crushing of rock ahead of the stope face [*Joughin*, 1966; *Joughin and Jager*, 1983; *McGarr*, 1992]. First-motion studies have also concluded that explosional isotropic events occur occasionally. However, all these results have been debated because the coverage of the focal sphere often proved inadequate to reject a pure double-couple solution [*Wong and McGarr*, 1990]. In addition, other first-motion studies and waveform analyses found predominantly double-couple sources [*McGarr*, 1971; *Spottiswoode and McGarr*, 1975].

Recent developments using moment tensor inversions to study focal mechanisms corroborate evidence that both pure double-couples and mechanisms with significant isotropic explosional components exist [*Talebi and Young*, 1990; *Feignier and Young*, 1992; *McGarr*, 1992; *Baker and Young*, 1997; *Gibowicz*, 1997; *Andersen*, 1999]. In addition, studies of S/P amplitude ratios conclude that many of the $M < 0$ events have a significant tensile component [*Cichowicz et al.*, 1990; *Gibowicz et al.*, 1991]. Our observations agree with these findings: Type-A events have small S/P amplitude ratios compared to Type-B events of approximately the same size (Figure 3-20). This leads us to hypothesize that Type-A events often have isotropic components, but Type-B events are double-couple shear sources, consistent with our model of Type-A events occurring in a low normal stress environment that could induce Mode I

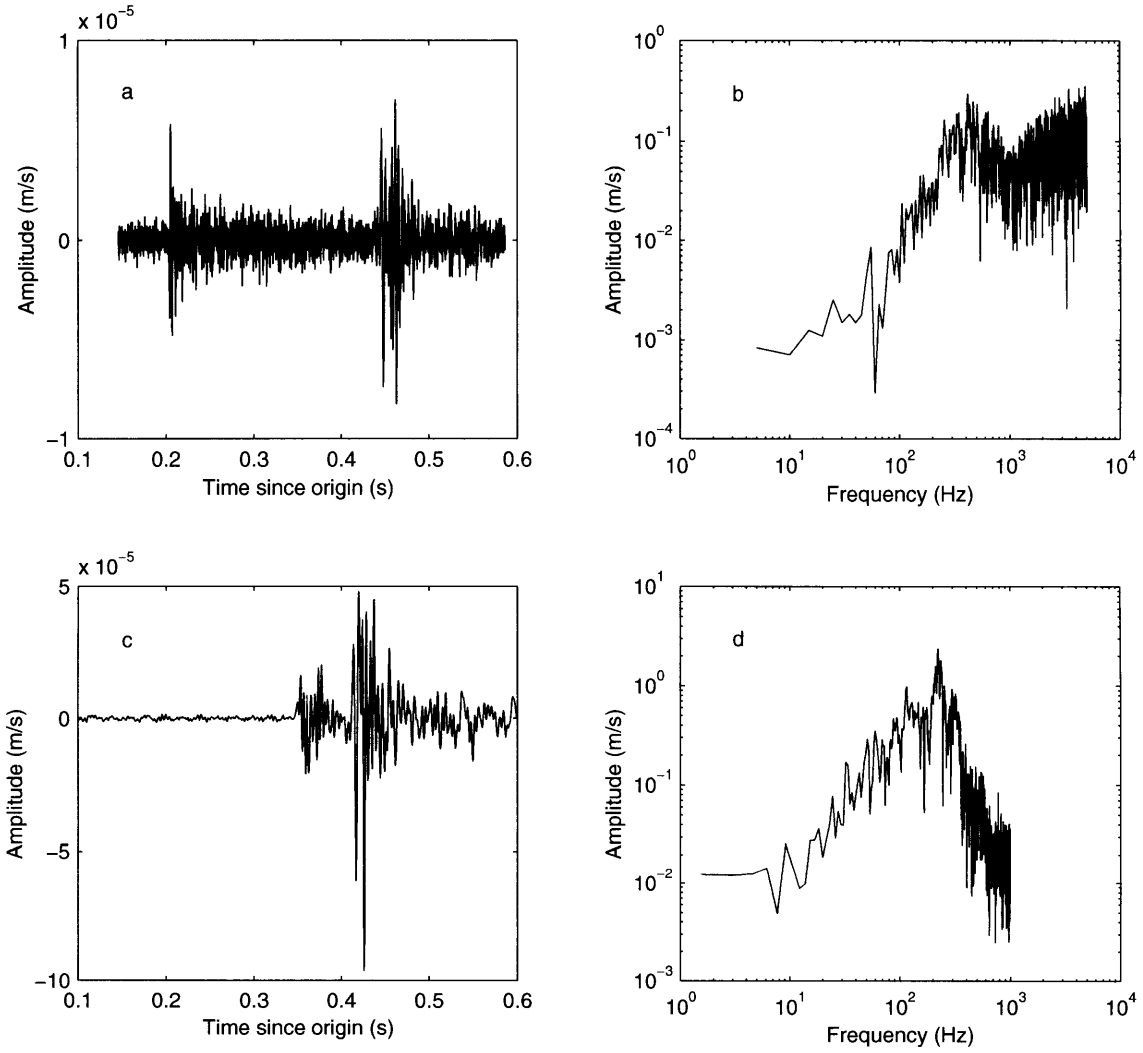

Figure 3-20: Vertical-component velocity seismograms for a Type-A event (a) and a Type-B event (c), recorded at Mponeng on 02 Feb 1999. Each event's acceleration amplitude spectrum is shown to the right of the waveforms in (b) and (d). The Type A event is distinguished from the Type B event by its higher frequency content and its lower S/P amplitude ratio.

fractures while Type-B events occur in friction-dominated environments that induce planar shear ruptures.

3.5 Conclusions

We have used deep South African gold mines as natural laboratories to observe fundamental aspects of rock failure, and we have quantified two distinct types of seismic events that occur in these mines. Previous workers in the field of mining-induced seismicity have discussed the idea of different classes of events (e.g. Gibowicz and Kijko, 1994), and more recently two populations have been separated spatially (Finnie, 1999b). Based on the properties of the seismicity we observe, we put forth a physical model for these two kinds of events. The Type-A population is composed of small events, often related to blasts, whose nucleation occurs under low normal stress in competent rock and propagates as fractures with small process zones at the crack tip. Type-B events nucleate in a friction-controlled environment on pre-existing shear slip planes.

Observations of frequency-magnitude statistics of mine seismicity are a key part of this study. Frequency-magnitude distributions in which $b = 1$ are consistent with the theory of earthquake self-similarity [*Kanamori and Anderson*, 1975; *Rundle*, 1989] in which stress drop is constant and the distribution of earthquake size follows a power law. We hypothesize that the decrease in frequency of the Type-B events relative to a Gutenberg-Richter relationship below $M = 1$ is a departure from self-similarity indicative of a minimum event size for seismic rupture [*Ida*, 1973; *Aki*, 1987]. The bandwidth of our dataset and the existence of the Type-A events strengthens our conclusion that the cutoff in magnitude observable for Type-B events is genuine. The critical minimum event is the subject of the following chapter.

Chapter 4

The Critical Earthquake

Portions of this chapter are based on "Seismicity in Deep Gold Mines of South Africa: Implications for Tectonic Earthquakes" by E. Richardson and T.H. Jordan, *Bulletin of the Seismological Society of America,* in press, 2002. Copyright by the Seismological Society of America.

4.1 Introduction

Type-B events appear to be analogous to tectonic earthquakes based on evidence from their mechanism characteristics and frequency-magnitude statistics. For instance, specific mining practices do no affect the self-similar scaling behavior observed between $0.5 < M < 3$. If the rolloff in rate of seismicity below $M < 1$ is real, then this indicates that there is a minimum event size. We show that with reasonable assumptions about source scaling relationships, we can use information from the inner scale of Type-B seismicity to infer the critical patch size and slip distance for the minimum earthquake nucleating in this tectonic environment.

4.2 Estimate of the Critical Slip Distance

Following *Ida* [1973], *Dieterich* [1979], and *Aki* [1987], we interpret the observed lower magnitude cutoff for a Type-B event in terms of a slip-weakening model that requires a minimum patch size with a critical slip distance for the nucleation of shear failure (see also *Palmer and Rice* [1973], *Andrews* [1976a, b], and *Dieterich* [1986]). Type-B frequency-magnitude distributions are alike among all the mines and have consistent $M_{\min} \approx 0.4$ (Figure 3-14). We take $M_{\min}$ as the local maximum in the discrete distributions, which is visible at Deelkraal and inferred for the other four mines by removing the Type-A peak as in Figure 3-19. We can then calculate the critical patch size R_c and the critical slip distance D_c for seismic nucleation by solving

$$R_c = \left(\frac{7 M_0^{\min}}{16 \Delta\sigma} \right)^{1/3} \tag{4.1}$$

and

$$D_c = \frac{16 \Delta\sigma R_c}{7 \pi G} \tag{4.2}$$

in which $M_0^{\min} = 4.7 \times 10^9$ Nm, the seismic moment corresponding to $M_{\min} \approx 0.4$, the static stress drop $\Delta\sigma = 3$ MPa, a good estimate of the stress drop for the smallest Type-B events in our dataset (see Figure 5-5), and $G = 36$ GPa. We obtain $R_c = 19.0$ m and $D_c = 1.2 \times 10^{-4}$ m. This D_c is equivalent to the critical slip distance derived from standard rate- and state-dependent friction laws [*Dieterich*, 1978, 1979] assuming that $\Delta\sigma = \sigma_n(b - a)$ in which σ_n is normal stress and a and b are empirically-determined constants from the constitutive rate- and state-dependent friction laws (see Chapter 2). Our calculation of D_c using these average values for the mining environment lies between representative results from laboratory data and tectonic earthquakes (Figure 4-1). Uncertainties in D_c, shown by the size of the box in Figure 4-1, arise from several sources. Based on the range of values measured empirically for shear wave speed and rock density, we expect the shear modulus G to have 5% uncertainty. The uncertainty in the average stress drop is about 50%, and the range of $M_{\min}$ has an uncertainty of about 25%. Thus, we expect an error of 20% in our estimation of R_c and 25% in D_c.

The D_c calculated here is considerably smaller than that determined by modeling

large earthquakes [*Scholz*, 1988] but about an order of magnitude larger than values determined in laboratory experiments for bare surfaces or for thin gouge layers [*Dieterich*, 1979; *Biegel et al.*, 1989; *Marone*, 1998a]. If nucleation length scales by the strain across the active shear zone as in *Marone and Kilgore* [1993], mature faults with wide gouge zones require a larger effective D_c to nucleate seismic rupture than do bare surfaces. Shear zones in the mines are observed to have gouge zones that are on the order of millimeters to centimeters in width, in between that of mature faults and laboratory experiments [*Ortlepp*, 1997]. Therefore, our estimate of D_c is consistent with this scaling. In fact, recent friction experiments using a 3-mm thick gouge layer at shear speeds of up to 10 mm/s report values of D_c of up to 1.8×10^{-4} m, agreeing well with our calculations [*Mair and Marone*, 1999].

4.3 Upper Frequency Cutoff

The existence of a critical slip distance for nucleation of rupture makes a prediction about the corner frequency of the minimum earthquake. Average empirically-determined values of P-wave speeds are 6100±60 m/s. We can solve $f_0 = 2.01 v_P / 2\pi R_c$, [*Madariaga*, 1976] to determine the corner frequency of the minimum event. For $M_{\min} = 0.4$ we obtain $\approx$ 100 Hz, but this is uncertain by 30%.

The reason for using estimates of source parameters to predict a corner frequency is that f_0 is an observable quantity in the seismic spectra; therefore, we have another means of testing our calculations of critical dimensions. In fact, the average P-wave corner frequency among all five mines for a $M = 0$ event is $\approx$ 200 Hz, so these scaling relations are consistent with observations. Slip-weakening models predict that "$f_{\max}$", the highest frequency recorded in the seismogram, is equal to the corner frequency of the minimum event because this is the patch size over which radiated energy is smeared out.

We calculated spectra of the events that we reprocessed to test the model of $f_{\max}$ as a source property. As an example, we show the time series accelerogram and

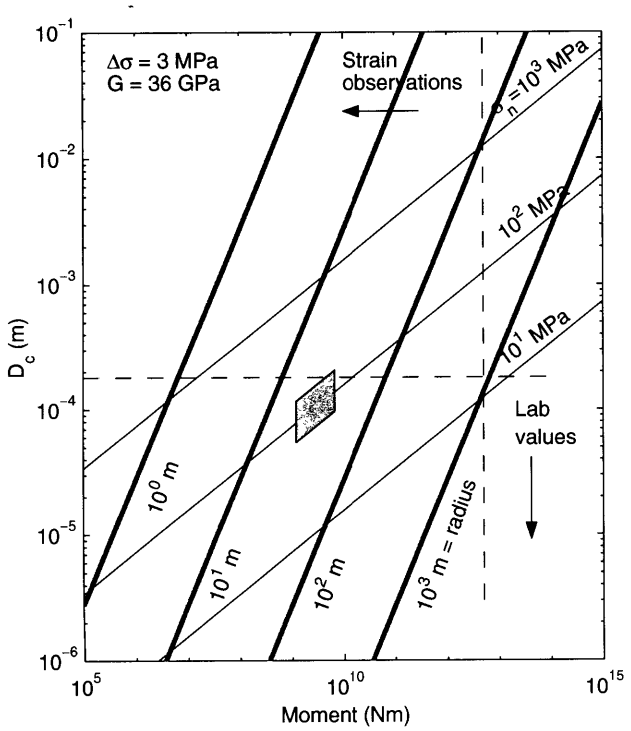

Figure 4-1: D_c vs. M_0 assuming $\Delta\sigma = 3$ MPa and $G = 36$ GPa, respectively. Black lines are lines of constant normal stress from 10-1000 MPa. Grey lines are lines of constant source radius from 1-1000 m. The shaded parallelogram denotes the range of M of approximately 0-0.3 and a range of lithostatic normal stresses of 70-110 MPa, corresponding to the conditions for the critical patch size in the Far West Rand region. The critical patch size is on the order of 10 m and the critical slip distance is on the order of 10^{-4} m.

spectrum recorded 487 m from a $M = 3.0$ event at Mponeng. We determined its corner frequency $f_0 = 13.6$ Hz by a method outlined in Chapter 5, and estimate $f_{\max} \approx 100$ Hz (Figure 4-2). If $f_{\max}$ is a source property, it should be approximately equal for all events controlled by this source mechanism. We stacked several records each of stations approximately 400 m distant from three events each to produce representative acceleration spectra for a large Type-B events ($M = 2$), a small Type-B event ($M = 0$) and a Type-A event ($M = -0.4$). As the magnitude of Type-B events decreases, $f_0 \rightarrow f_{\max} \approx 200$ Hz (Figure 4-3). $f_{\max}$ is the vertical dashed line. The most important aspect of Figure 4-3 is that $f_{\max}$ appears to be constant at 150-200 Hz for Type-B events, but we do not observe any $f_{\max}$ for the Type-A events. This corroborates our hypothesis of the existence of a minimum earthquake at $M \approx 0$, where $f_0 \approx f_{\max}$, for Type-B events.

Hanks [1982] observed a consistent high-frequency cutoff at 13 Hz in strong motion recordings in southern California that he termed "$f_{\max}$". *Aki* [1979, 1984, 1987] and *Papageorgiou* [1988] associated this with a source property and proposed $M_{\min} \approx 3$ for this region; however, studies by *Hanks* [1982, 1984] interpreted this $f_{\max}$ as the result of local site conditions instead. In this case the alluvium or other non-hard rock environment in which the sensor is placed causes rapid decay of spectral amplitudes at $f > f_{\max}$. In tectonic environments in which seismograms are recorded at fairly great hypocentral distances, $f_{\max}$ is influenced by attenuation along the ray path as well [*Anderson and Hough*, 1984; *Anderson*, 1986; *Boore*, 1986]. These sources of misinterpretation of $f_{\max}$ are not as problematic for this study because recordings only a few source radii away are not controlled by attenuation. For example, anelastic attenuation of the form $e^{-\pi f R/Qv_S}$ results in a distance-dependent $f_{\max} \approx Qv_S/\pi R$. For $Q = 300$, $f_{\max} \approx 200$ Hz at 2 km from the source. At 400 m from the source, the approximate distance of the records whose spectra are shown in Figure 4-3, the distance-dependent $f_{\max} \approx 900$ Hz. Therefore, barring unusually small values of Q which are unlikely in this hard-rock environment, $f_{\max}$ is probably not caused by attenuation along the raypath here. Also, the on-reef geophones are placed at depth in hard rock, so the site effects are expected to be small. Furthermore, we observe an

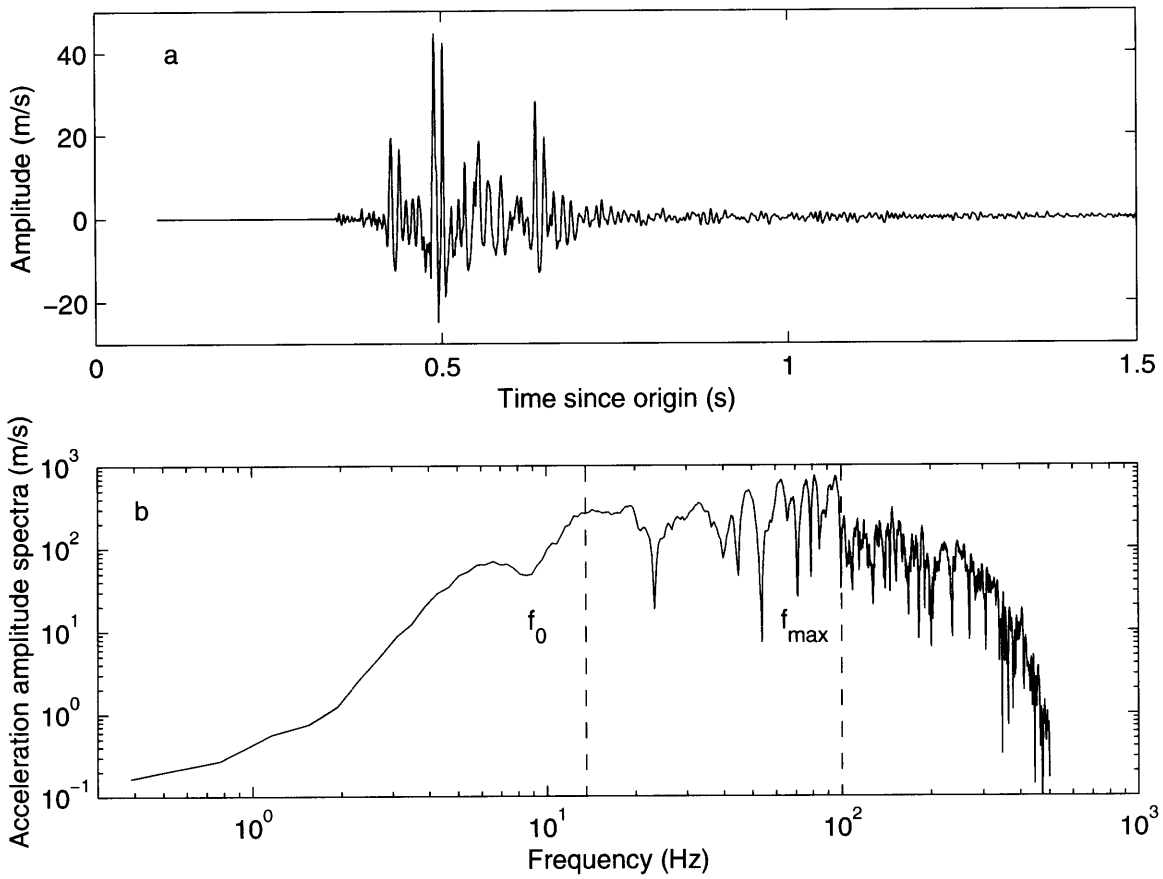

Figure 4-2: Vertical component accelerogram (a) and acceleration amplitude spectrum (b) for a $M = 3.0$ event in Mponeng on 02 February 2000 at 12:30:21 recorded 487 m from the source. In (a) the initial gap is the time diference between the origin of the event and the beginning of the triggered record. We calculated $f_0 = 13.6$ Hz for this event and estimate f_{max} at 100 Hz.

f_{max} for Type-B events, but not for Type-A events, which are recorded by the same instruments at the same sites.

4.4 Discussion

The important outcome of this work is that this is the first time that actual numbers pertaining to the critical patch size for earthquake nucleation from assumptions about scaling relations match both observations of frequency-magnitude scaling and also observations from seismic spectra. The idea of the critical minimum earthquake

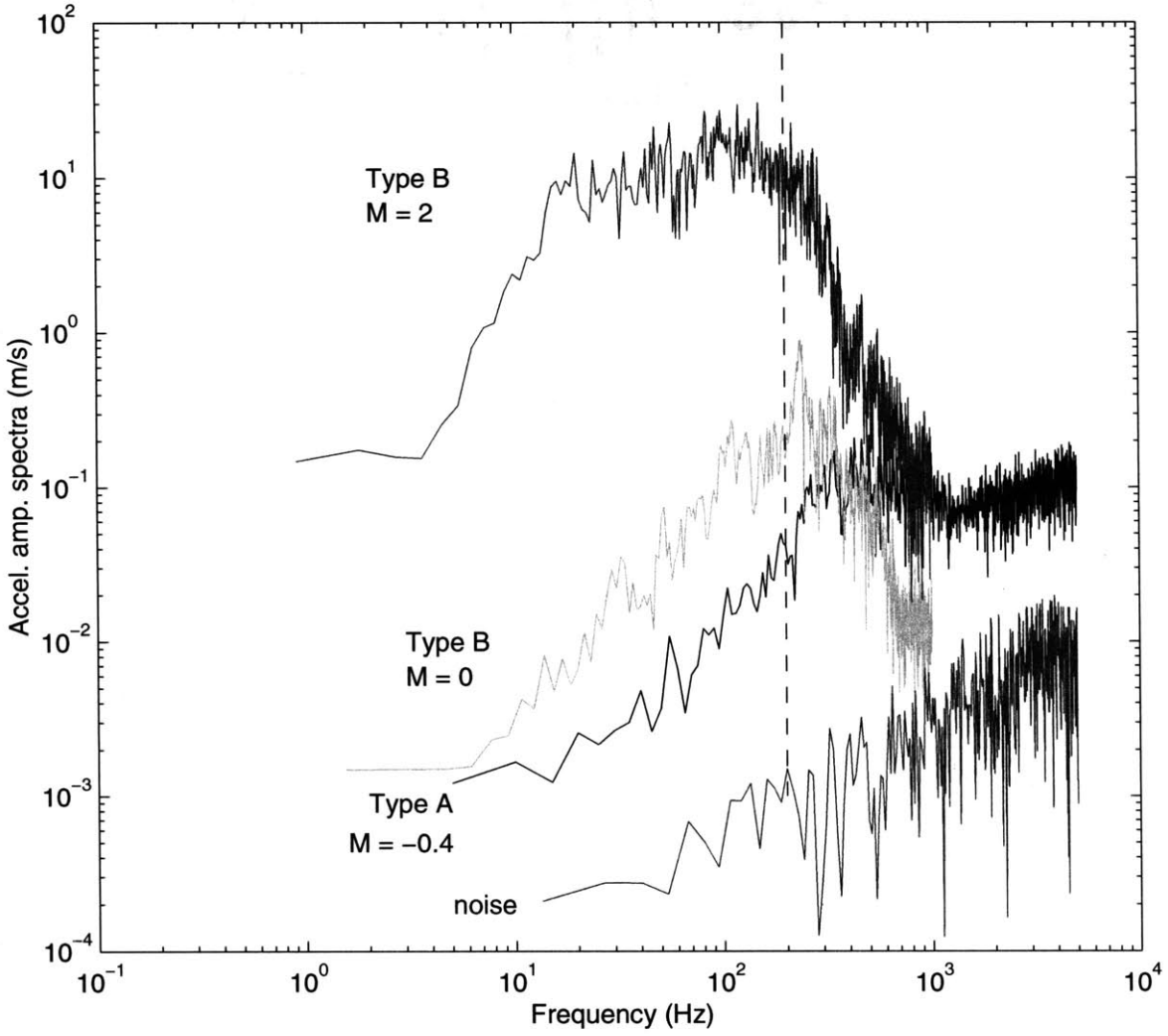

Figure 4-3: Stacked acceleration spectra from three events each of $M \approx$ 2,0,and -0.4 along with a spectrum of noise. $f_{\max}$ is estimated at 150-200 Hz for the Type-B stacks (vertical dashed line), but is not evident for the Type-A stack. The noise spectrum was made by stacking the section of records between the trigger time and the P arrival. The source-receiver distance is approximately 400m for all records.

for a given tectonic environment is not new, in fact it is a requirement of even the simplest slip-weakening law. However, strong corroborative evidence from multiple seismic observations is new.

We interpret our observation of an $f_{\max}$ in the acceleration spectra as further evidence of a minimum earthquake for Type-B events. In so doing, we follow the model proposed by *Papageorgiou and Aki* [1983a, b] in which the maximum frequency recorded in the acceleration power spectra of the largest earthquakes in a region should be approximately equal to the corner frequency of the smallest earthquake in the region. Previous workers have observed an $f_{\max}$ in mining-induced seismicity data. *Cichowicz et al.* [1990] proposed that for very small events ahead of a stope face, $f_{\max} \approx 5$ kHz and *Young et al.* [1989] observed $f_{\max} \approx 3$ kHz. These values are an order of magnitude higher than our observations for Type-B events, so it is likely that the events in these two previous studies were Type-A events. Though we do not observe an $f_{\max}$ for Type-A events, we also do not have the bandwidth in this study to make a reasonable comparison with the studies of *Cichowicz et al.* [1990] and *Young et al.* [1989]. We do note that high $f_{\max}$ (or none) for very small events is consistent with our physical model of Type-A events as having a process zone at the grain-scale level.

Our assumption that Type-B events are analogous to tectonic earthquakes implies that the calculations of the critical dimensions of rupture nucleation for mining seismicity extends to that for tectonic events. An interesting result of these calculations from the point of view of earthquake physics is that observing the nucleation of an event with radius on the order of 10 m with a critical slip distance on the order of 10^{-4} m will be extremely difficult with present surface-based seismographic networks. In fact, this size is approximately the smallest well-recorded source dimension at the Parkfield network [*Nadeau and Johnson*, 1998].

Although there is uncertainty in our estimates of how earthquake sources scale at small magnitudes, fundamental processes such as end-zone size, critical patch size and displacement needed to nucleate seismic slip have not been observed at this level before. Approaching the study of these processes simultaneously from the fields of

earthquake seismology, laboratory friction experiments and mining seismology will aid in bridging the scale gap between observations and theory.

Chapter 5

Scaling Properties of Mining-Induced Seismicity

5.1 Introduction

We compare the results obtained from typical processing done at the mines with an independent but similar method that we developed based on the method of *Andrews* [1986] in order to calibrate the mine catalogs. We then compare the source scaling properties of the mining-induced seismicity in our study to other datasets of seismic events covering a range of source sizes from $10^4 - 10^{20}$ Nm. We observe that apparent stress, stress drop, and particle velocity all scale with seismic moment. To explain these observations, we develop a kinematic model of earthquake rupture based on fracture dynamics in which rupture velocity increases with rupture dimension.

5.2 Catalog Methodology

Source properties of mining-induced seismic events are routinely determined at the Far West Rand gold mines via an automated spectral technique as outlined in *Mendecki* [1997]. Distance-corrected P- and S-wave displacement spectra are stacked

and fit by the spectral shape [*Aki*, 1967; *Brune*, 1970]

$$\Omega(f) = \frac{\Omega_0}{1 + (f/f_0)^2} \tag{5.1}$$

in which Ω_0 is the long-period amplitude and f_0 is the corner frequency. These are the two independent parameters from which seismic moment M_0 and radiated energy E are determined as follows [*Mendecki*, 1997]:

$$M_0 = 4\pi\rho v^3 \Omega_0 \Re^{-1} \tag{5.2}$$

$$E = 8\pi^4 \rho \Omega_0^2 v f_0^3. \tag{5.3}$$

In these, ρ is rock density, v is the P- or S-wave speed, and $\Re$ is the root-mean-square radiation pattern, which is $\sqrt{4/15}$ for P-waves and $\sqrt{2/5}$ for S-waves. Source radius R, apparent stress σ_a and static stress drop $\Delta\sigma$ are also determined using $R = Cv/2\pi f_0$, $\sigma_a = GE/M_0$ and $\Delta\sigma = 7M_0/16r^3$ in which $G = \rho v_S^2$ is the shear modulus and C is a constant, chosen as 2.01 for P-waves and 1.32 for S-waves, following *Madariaga* [1976]. Average values appropriate for the mining environment of the Far West Rand are $\rho = 2700$ kg/m^3, $v_P = 6100$ m/s, and $v_S = 3650$ m/s. For a Brune spectrum, as in (5.1), σ_a and $\Delta\sigma$ are not independent [*Andrews*, 1986]; therefore, using this technique to determine source parameters limits the investigation of source scaling properties.

In addition, the processing routine used at the mines fixes the upper limit of f_0 at 300 Hz. This upper limit does not reflect bandwidth or sampling rate limitations of the instruments; it is merely an artificial ceiling imposed on the way a Brune spectrum is fit to the spectral data (see Figure 5-1). A small event with a corner frequency greater than 300 Hz has a displacement spectrum that looks flat at frequencies less than 300 Hz. This event will then be assigned a corner frequency at or below 300 Hz by default because that is the best that the fitting algorithm can do. In the example event shown in Figure 5-1, the displacement spectrum was calculated from a median stack of five stations (dotted line in Figure 5-1). The part of the spectrum less than

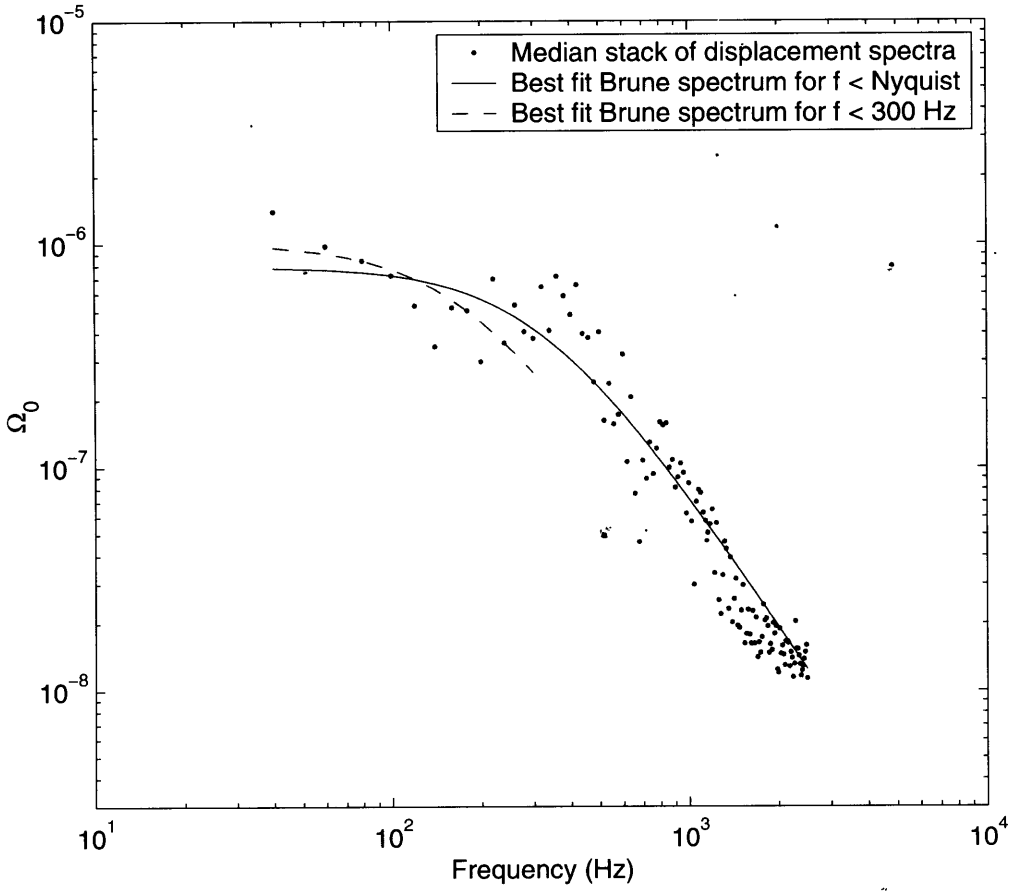

Figure 5-1: Median stack of displacement spectra for an event in Mponeng on 02 February 1999 together with two best fit Brune spectral curves. The solid line is the fit out to the Nyquist frequency (2500 Hz) and has a corner frequency of 315. The dashed line shows the fit out to 300 Hz and has a corner frequency of 178 Hz.

300 Hz contains noise, and the best fit to this part of the spectrum (dashed line) greatly underestimates the corner frequency because it is fitting the noise. The fit to the whole spectrum (solid line in Figure 5-1) results in a corner frequency of 315 Hz. Such underestimation of the corner frequency necessarily affects other source parameters, which, in the mine catalogs, depend on corner frequency. Specifically, this error causes underestimation of E, σ_a, and $\Delta\sigma$ and overestimation of R.

5.3 Catalog Verification

We reprocessed 228 events from Mponeng, Elandsrand, and TauTona in order to confirm the cataloged source parameters using an independent method. In doing so, we followed *Andrews* [1986] and calculated displacement, velocity, and acceleration power spectra for every record of each event. We did not divide the velocity power spectra by 4 as in *Andrews* [1986] because this is a free-surface correction and the stations in this study are at depth embedded in the host rock. We median-stacked each event's spectra and integrated the results up to the Nyquist frequency to determine S_{D^2}, the integral of the displacement power spectra (see Equation 6 of *Andrews* [1986]), S_{V^2}, the integral of the velocity power spectra (see Equation 7 of *Andrews* [1986]), and $\langle A^2 \rangle$, the acceleration power spectral level (see Equation 19 of *Andrews* [1986]). These are used to determine the source parameters radiated energy, seismic moment, and nominal stress drop:

$$E_R = 4\pi\rho v S_{V^2} \tag{5.4}$$

$$M_0 = \frac{8\pi\rho v^3 S_{D^2}^{(3/4)}}{\Re S_{V^2}^{(1/4)}} \tag{5.5}$$

$$\widetilde{\Delta\sigma} = \frac{2\pi f_0 \rho \langle A^2 \rangle}{C\Re}. \tag{5.6}$$

In (5.6), the corner frequency is found by $f_0 = (\sqrt{S_{V^2}/S_{D^2}})/2\pi$. An advantage of this method is that the exponent of the spectral rolloff is not a fixed parameter as in the case of fitting spectra with a Brune-type curve. Values of R and σ_a are calculated from E_R, M_0, and f_0 as in the previous section. An additional benefit of this method is that $\widetilde{\Delta\sigma}$ and σ_a are mathematically independent because the acceleration power spectral level is used to find $\widetilde{\Delta\sigma}$; therefore creating an extra degree of freedom in this calculation. Because our data is band-limited, there is an upper limit to the radiated energy we can determine [*Ide and Beroza*, 2001]. However, in practice the underestimation of energy for this dataset is very small since our corner frequencies are generally 1/5 to 1/10 of the Nyquist frequency.

Our values of M_0 correlate well with those of the catalog, though the catalog value tends to be greater (Figure 5-2a). The correlation coefficient is 0.94. Based on

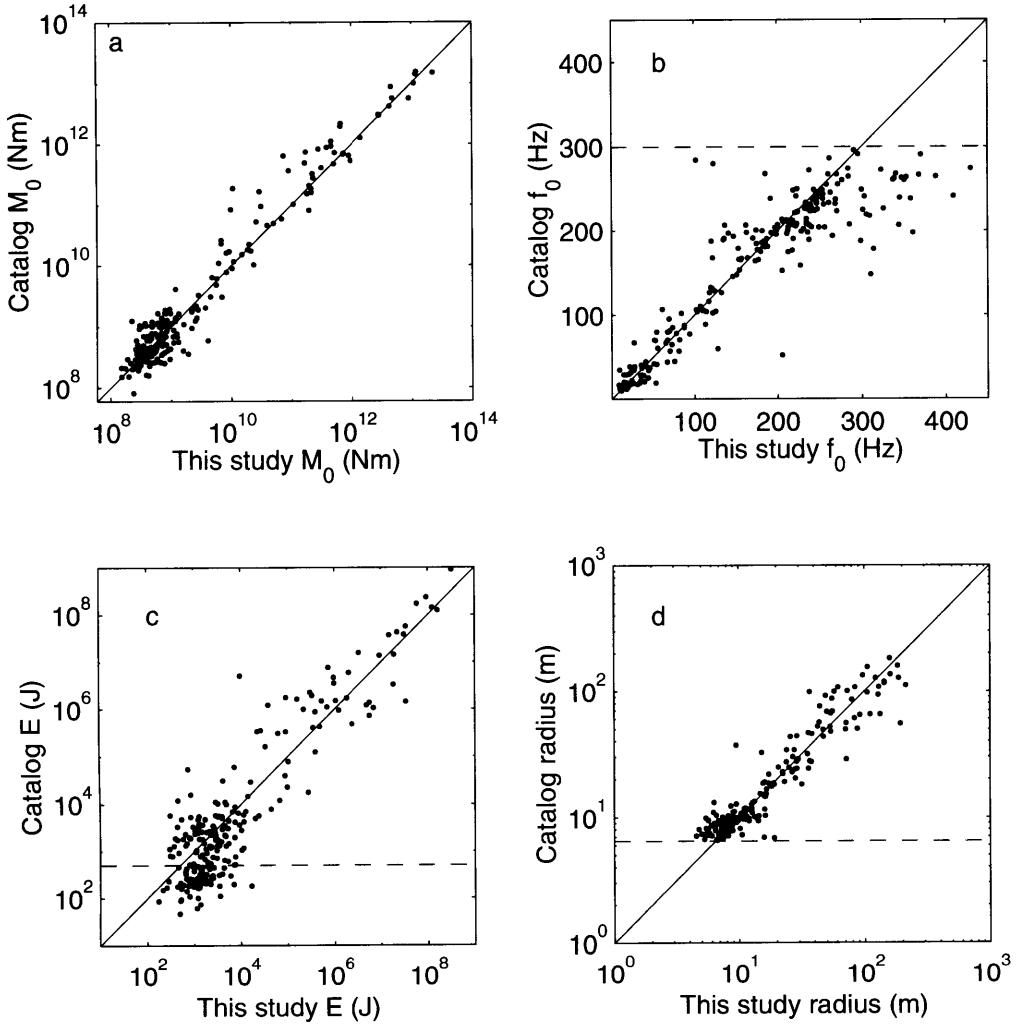

Figure 5-2: Comparison between our values determined by reprocessing and the values in the mine catalogs of M_0 (a), f_0 (b), E_R (c), and R (d) for 228 events in Mponeng, Elandsrand, and TauTona. Solid lines show 1:1 correspondence. Dashed lines in (b) and (d) show the the 300-Hz f_0 ceiling for the catalog data. Values below the dashed line in (c) are underestimated in the catalog due to the 300-Hz ceiling.

an error analysis in which we assume that the catalog error is some multiple of our error estimate, we find that the amount of scatter due to uncertainty is greater than the mean difference between our value and the catalog value. Both our measure and the catalog measure of M_0 have an estimated error of about 2%. Our measure of f_0 matches the catalog well for $1 \leq f_0 \leq 200$ Hz (Figure 5-2b). The mean difference between the two measures is approximately 6 Hz, which is less than the expected uncertainty. For $f_0 > 200$ Hz, the discrepancies are much larger (mean difference is ≈ 20 Hz). Except for two outliers, the catalog consistently underestimates f_0 for small events due to the 300-Hz ceiling (dashed line in Figure 5-2b). The effect of the 300-Hz ceiling is not as sharply evident in Figure 5-2c because in the catalog, E_R is a nonlinear function of both f_0 and Ω_0 [see Equation (5.3)]. Events with $E < 500$ J in the catalog are underestimated by the catalog because these correspond to the events whose corner frequencies are also underestimated. However, for $E > 500$ J, our values match the catalog values well within the expected uncertainty, which is $\approx 10\%$ for our estimate and $\approx 12\%$ for the catalog. The values of R we determined correlate well with catalog values (correlation coefficient = 0.85) above $R \approx 10$m. The scatter due to uncertainty is again greater than the mean difference between the two measures. Below $R \approx 10$ m the catalog consistently overestimates R because of the 300-Hz ceiling in corner frequency. Overall, the catalog does a good job of determining source parameters for the Type-B events. The accuracy of calculations for the Type-A events suffers somewhat from the imposed restrictions on corner frequency that speed up the processing. The errors in source parameter estimation for the Type-A events is not an issue that compromises hazard analysis at the mines because damaging events are generally large slip-type events. In order to understand the properties of Type-A events thoroughly for scientific purposes, more sensitive instrumentation together with more accurate processing techniques are necessary.

5.4 Scaling of Type-A and Type-B Events

Type-A and Type-B events have distinctly different energy-moment relationships (Figure 5-3a). Energy increases with moment for the Type-B events we reprocessed (open circles in Figure 5-3). We do not have the bandwidth to assess the scaling of E_R with M_0 for the Type-A events, though we observe that Type-A events (black filled circles in Figure 5-3) tend to have higher energies and therefore higher apparent stresses for the same moment as the Type-B events. The apparent stress of Type-B events increases with moment, though there is much scatter (Figure 5-3b). In Figure (5-3b), plotted circles are the reprocessed events, and the grey diamonds represent the median values of σ_a and $\widetilde{\Delta\sigma}$ for the whole catalog ($\approx 450,000$ events not sorted by type) binned in units of 0.1 order of magnitude in moment. We plot the median values here to avoid overplotting and to show that there is indeed a trend of increasing apparent stress with moment that underlies the scatter. At $M_0 < 3 \times 10^9$ Nm, the catalog data underestimates σ_a and $\widetilde{\Delta\sigma}$ compared to our measurements of reprocessed Type-A events, but for the Type-B events, the catalog values correlate well with those we determined. A similar relationship of increasing $\widetilde{\Delta\sigma}$ with M_0 is also visible (Figure 5-3c). In addition, $\Delta\sigma$ and σ_a are well-correlated (Figure 5-3d), even though they are measured independently. The straight line in Figure 5-3d shows the exact relationship between $\widetilde{\Delta\sigma}$ and σ_a for a Brune model shape [*Andrews*, 1986]. The Type-B events scatter about this line, but the Type-A events are better described by a line with a shallower slope, i.e. Type-A events have a higher stress drop than a Brune model spectrum predicts. Given the correlation between $\widetilde{\Delta\sigma}$ and σ_a, the Type-B events appear to be have increasing $\widetilde{\Delta\sigma}$ with M_0. In the following section we develop a model to explain these observations of increasing σ_a and $\widetilde{\Delta\sigma}$ with seismic moment.

5.5 Implication of Source Scaling for Earthquake Rupture

Having seismic data covering such a wide range of sizes allows us to test whether

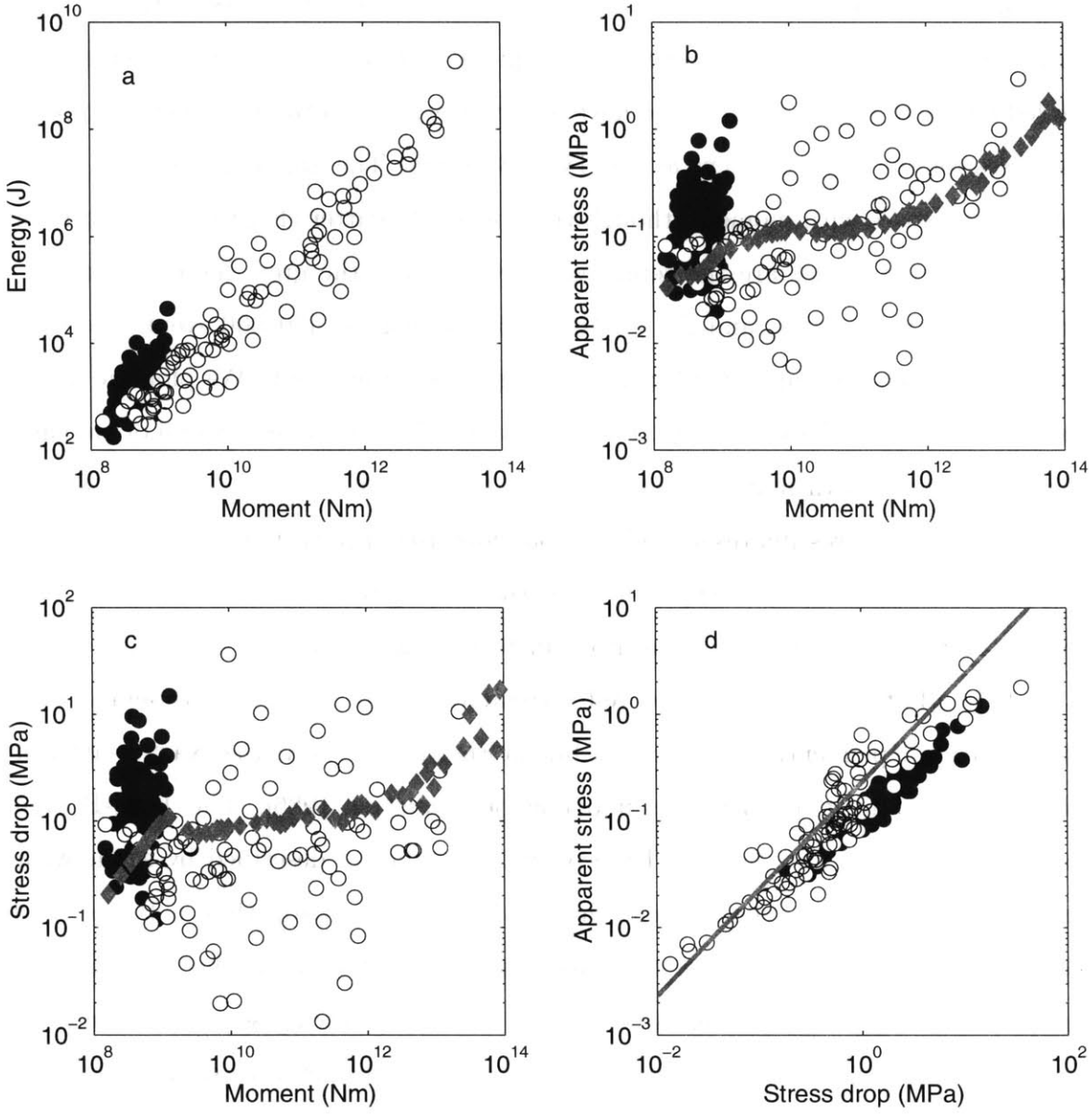

Figure 5-3: E_R vs. M_0 (a), σ_a vs. M_0 (b), $\widetilde{\Delta\sigma}$ vs. M_0 (c), and σ_a vs. $\widetilde{\Delta\sigma}$ (d) for the events we reprocessed. Type-A events are solid and Type-B events are open. In (b) and (c), grey diamonds represent the median values from the whole catalog ($\approx 450,000$ events) binned in 0.1 order-of-magnitude units in moment. In (d), the straight line shows the exact relationship between σ_a and $\widetilde{\Delta\sigma}$ for a spectrum with a Brune model shape.

scaling laws motivated by laboratory data and theoretical work in fracture dynamics can be appropriately applied to the entire continuum of earthquake source data. One key question is whether small and large earthquakes are fundamentally different. Another important area of investigation is the attempt to discern a mode of rupture initiation and propagation that can be corroborated by seismic observations.

5.5.1 Observations of Apparent Stress and Stress Drop

Many previous workers have observed apparent stress to increase with seismic moment within individual datasets (e.g. *Kanamori et al.* [1993], *Abercrombie* [1995], *Mayeda and Walter* [1996], *Prejean and Ellsworth* [2001], and *Izutani and Kanamori* [2001]). *McGarr* [1999] compared several of these datasets and concluded that there is a consistent upper limit to apparent stress across 17 orders of magnitude in seismic moment. He found that while each dataset's apparent stress scales with moment, it is unclear whether there is significant overall scaling behavior [*McGarr*, 1999]. In addition, both the study of *McGarr* [1999] and recent work by *Ide and Beroza* [2001] suggest that the perceived scaling within each dataset is due to finite recording bandwidth that causes the underestimation of the energy of the smallest events and/or the omission of small events with high energies. *Ide and Beroza* [2001] applied a correction to account for the underestimated energy and compared the corrected datasets again. They concluded that while apparent stress values scatter over three orders of magnitude, there is no prominent scaling of apparent stress from 10^4 Nm to 10^{20} Nm.

We argue that there is indeed scaling of apparent stress with moment, yet the comparison of such a large range of event sizes has disguised the scaling for two reasons. First, as our characterization of the two different kinds of mining-induced seismicity shows, fracture- and friction-dominated events have different scaling properties (see Figure 5-3). These events should be considered separately. Second, data spanning the range of magnitudes in which the break between the two types of events occurs has been lacking from previous studies. The data in this study cover this gap and overlap

with previous studies as well. Once all datasets are combined, scaling of apparent stress with moment is discernible for each of the two kinds of events.

We compare the apparent stresses of the Type-A events in this study with data from Canada's Underground Research Laboratory [*Gibowicz et al.*, 1991], Strathcona Mine in Ontario, Canada [*Urbancic et al.*, 1993], and hydrofracturing events from the KTB borehole [*Jost et al.*, 1998]. For the *Gibowicz et al.* [1991] data and the *Jost et al.* [1998] data, we used the corrected values of energy from *Ide and Beroza* [2001] in order to calculate apparent stress. This correction assumes a Brune model shape spectrum and that stress drop is constant. The ratio R_E between the estimated energy and the true energy is

$$R_E = (2/\pi)\frac{-f_M/f_0}{(1+(f_M/f_0))^2} + \arctan(f_M/f_0) \tag{5.7}$$

in which f_M is highest usable frequency (determined by the Nyquist or by attenuation) [*Ide and Beroza*, 2001] and f_0 is again the corner frequency. Assumed values of f_M for *Gibowicz et al.* [1991] and *Jost et al.* [1998] were 500 Hz and 100 Hz. We applied this correction to the *Urbancic et al.* [1993] data assuming $f_M = 500$ Hz. For the Type-A events in our datset, the Nyquist frequency is 5000 Hz. We applied the energy correction to our data assuming conservatively that $f_M = 1000$ Hz, and the correction was minimal (typically 5%), which we expected since the corner frequencies of Type-A events are at least ten times less than the Nyquist frequency.

We binned each dataset in bins of one order of magnitude in moment and calculated the median value of σ_a and M_0 for each bin with its 95% confidence limit (black open symbols in Figure 5-4). We also found the mean and standard error of the mean (grey open symbols in Figure 5-4) by averaging the log of the data in each bin. These results were not significantly different from the medians. The apparent stress of these combined datasets decreases with seismic moment (Figure 5-4).

In laboratory tests, material strength of rock decreases with increasing sample size as (size$^{-1/2}$) for samples on the order of 1 m. This is thought to occur because larger structural flaws are possible in larger samples. This scaling relationship is known as

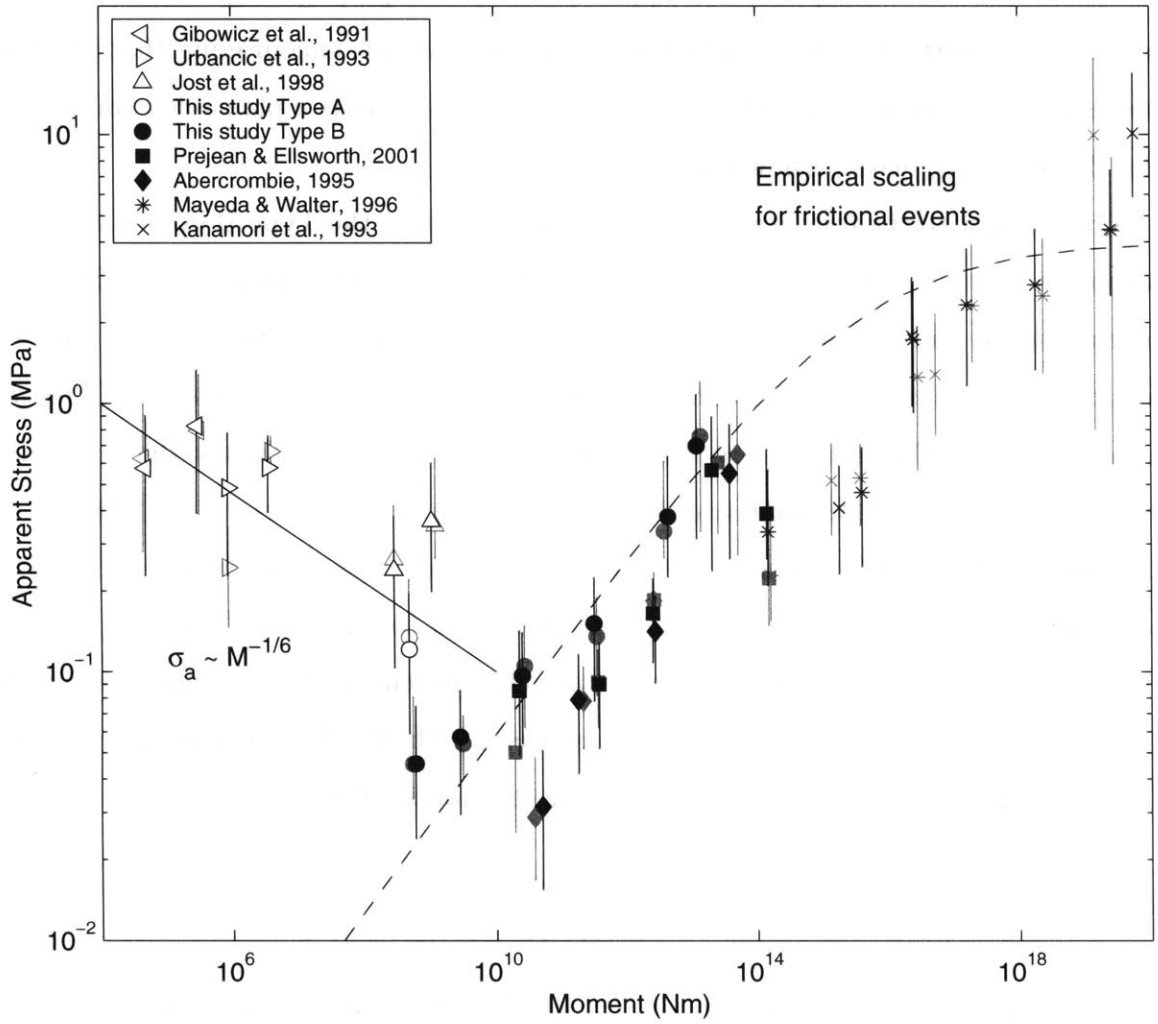

Figure 5-4: Medians (black symbols) with 95% confidence error bars and means (grey symbols) with standard error bars of σ_a vs. M_0 for the events in our study and several other studies. Each dataset is binned in order-of-magnitude units in moment. Open symbols represent fracture-dominated events and the other symbols indicate friction-controlled data. Solid line shows the empirical scaling $\sigma_a \sim M_0^{-1/6}$ for fracturing events. The dashed line shows empirical scaling $\sigma_a = \frac{2\sigma_a^*}{1+(M_0^*/M_0)^{\alpha/3}}$ for frictional events.

Petch's Law [*Scholz*, 1990]. If we assume that apparent stress is a proxy for material strength, then σ_a should scale as $M_0^{-1/6}$. This slope does predict the behavior of Type-A events well (solid line in Figure 5-4). We have incomplete physical understanding of the actual relationship between apparent stress of a propagating fracture and the material strength of an intact laboratory sample, but it is encouraging that the two seem to be related in a straightforward way and that there is a plausible explanation for decreasing σ_a with seismic moment.

In contrast to the fracture-dominated Type-A events, the Type-B events are analogous to tectonic earthquakes in that their nucleation occurs under near-lithostatic normal stress and is therefore friction-controlled. We compared the apparent stresses of our Type-B data to studies of borehole recordings at Long Valley Caldera [*Prejean and Ellsworth*, 2001], and Cajon Pass [*Abercrombie*, 1995] as well as to the regionally recorded datasets of *Mayeda and Walter* [1996], and *Kanamori et al.* [1993]. For *Kanamori et al.* [1993], we used the the corrected values of apparent stress from *Ide and Beroza* [2001]. We also applied their correction to our Type-B dataset and, as with the Type-A events, found no significant change relative to our original estimate ($\approx 10\%$). For this ensemble of data, σ_a increases with M_0 (Figure 5-4). The dashed line in Figure 5-4 shows an empirical scaling relation for frictional events given by

$$\sigma_a = \frac{2\sigma_a^*}{1 + (M_0^*/M_0)^{\alpha/3}} \tag{5.8}$$

in which the characteristic moment $M_0^* = 10^{15}$ Nm, the characteristic apparent stress $\sigma_a^* = \sigma_a(M_0^*) = 2$ MPa, and $\alpha = 1$. Based on our choices of parameters in (5.8) we find that for events of $M_0 < 10^{15}$ Nm, $\sigma_a \sim M_0^{1/3}$, above which there is a scale break. Models of enhanced velocity weakening due to melting have proposed that above $M_0 \approx 10^{15}$ Nm, apparent stress saturates at $\approx 2 - 4$ MPa as stress drop becomes total [*Kanamori and Heaton*, 1998]. Given the scatter in the regional datasets we examine here, the conclusion that apparent stress is constant above $M_0 \approx 10^{15}$ Nm cannot be ruled out. We note that the smallest values of apparent stress occur at the boundary between fracturing and frictional events where the slip of frictional events

is barely larger than the critical slip distance necessary for earthquake nucleation, so that the overall plot of apparent stress vs. seismic moment has a "V" shape.

We find that the overall scaling behavior of $\Delta\sigma$ for Type-A events cannot be determined without additional observations, though each dataset individually shows an increase of stress drop with moment (open symbols in Figure 5-5). These data were binned in moment as in Figure 5-4, and again we show the medians (black) and means (grey) of stress drop. The *Gibowicz et al.* [1991] dataset has high stress drops compared to the *Urbancic et al.* [1993] dataset. The Type-A data from our study matches the *Jost et al.* [1998] data. We surmise that stress drop increases with moment for Type-A events in general, though the scatter is large and the limited bandwidth in each study makes it difficult to assess the quality of the data.

Previous studies of tectonic events have claimed no significant correlation between $\Delta\sigma$ and M_0, but we note that *Prejean and Ellsworth* [2001] found that $\widetilde{\Delta\sigma}$ and σ_a were correlated, as do we (Figure 5-3d). In addition, we do detect a trend of increasing $\widetilde{\Delta\sigma}$ with M_0 for friction-dominated events (filled symbols in Figure 5-5). Further investigation into the implications of stress drop scaling for small events is necessary to understand the relationships between small and large earthquakes and to determine whether any particular model of rupture growth for small earthquakes can account for the observed deviation from constant stress drop. In fact, this observed scaling of stress drop with moment is an artifact of the assumption that rupture velocity is a constant, as detailed in the following section.

5.5.2 Scaling Relations for an Expanding Circular Crack

Proposed explanations of increasing apparent stress with seismic moment for friction-dominated events include the hypothesis of enhanced velocity weaking of faults via melting during large events. In addition, scaling of rupture velocity with earthquake size, near-fault damage, or normal force fluctuations during rupture could cause large events to have higher radiated seismic energy and therefore higher apparent stress. We now develop a model in which rupture velocity scales with source

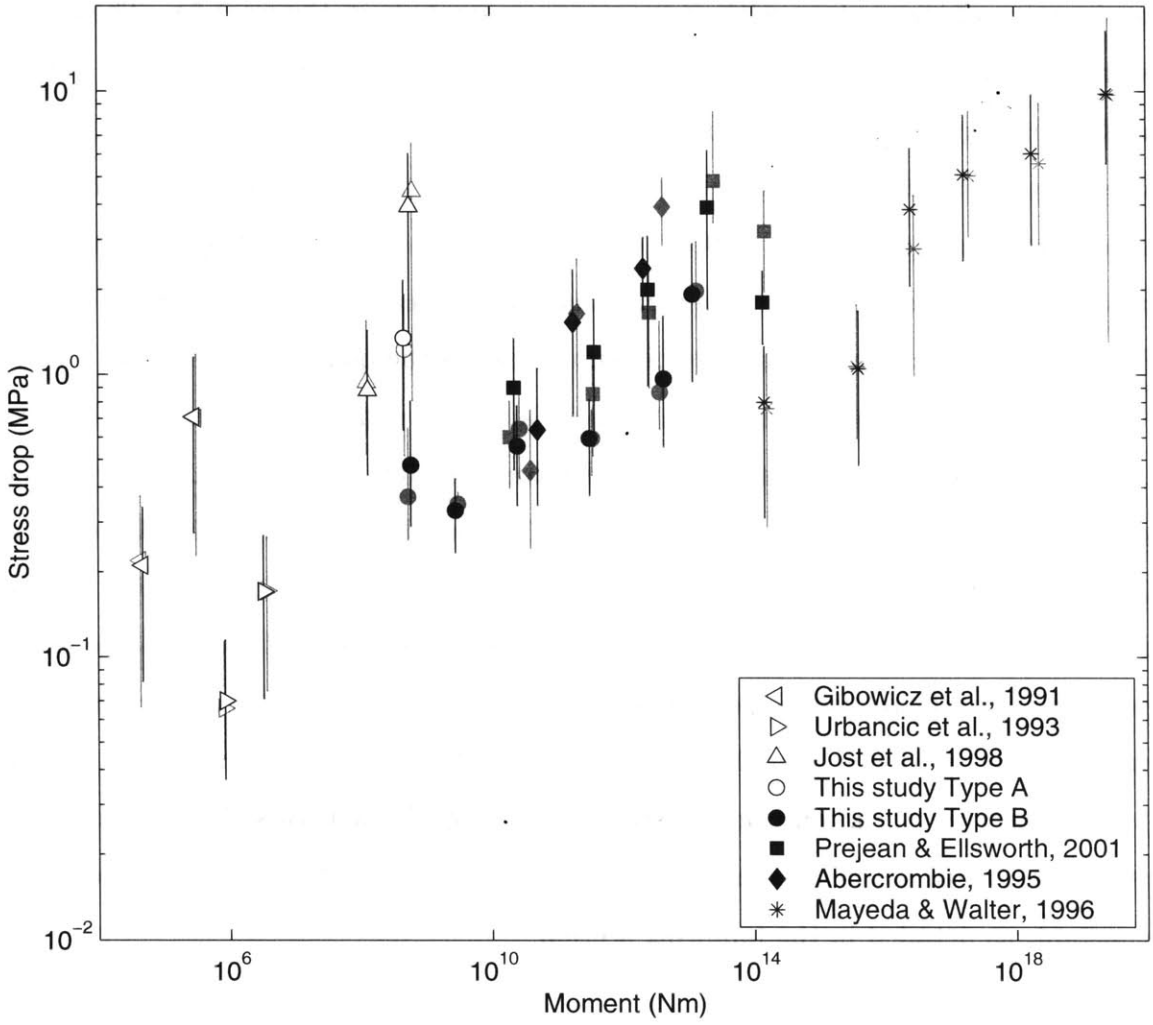

Figure 5-5: Medians (black symbols) with 95% confidence error bars and means (grey symbols) with standard error bars of $\widetilde{\Delta\sigma}$ vs. M_0 for the events in our study and several other studies. Each dataset is binned in order-of-magnitude units in moment. Open symbols represent fracture-dominated events and the other symbols indicate friction-controlled data.

dimension, and hence, seismic moment.

In this model, we first consider a circular crack that expands from a nucleation patch of dimension R_c at $t = 0$ to a patch of radius $R(t)$ and area $A = \pi R^2(t)$. The rupture velocity is $v_R(t)$, and the displacement across the crack is $u(r,t), r < R$. The local dynamic stress drop is $\delta\sigma(r,t) = \sigma_D(r,t) - \sigma_F(r,t)$ in which $\sigma_D(r,t)$ is the total driving stress and $\sigma_F(r,t)$ is the resisting stress. The energy balance for such a rupture is

$$E_T = E_H + E_F + E_R \tag{5.9}$$

in which E_T is the total energy, E_F and E_H are the energies dissipated by fracture and friction, respectively, and E_R is the radiated energy. In terms of stress,

$$\sigma_T = GE_T/M(t) \tag{5.10}$$

$$\sigma_H = GE_H/M(t) \tag{5.11}$$

$$\sigma_G = GE_F/M(t) \tag{5.12}$$

$$\sigma_a = GE_R/M(t) \tag{5.13}$$

where seismic moment is defined as $M_0 = GuA$. If we assume that frictional stress is a constant and that there is no overshoot, then the static stress drop $\Delta\sigma$ is given by $\sigma_T - \sigma_H = \Delta\sigma$. Therefore, $\Delta\sigma - \sigma_G = \sigma_a$. Using the empirical scaling relation of Equation 5.8 for $\sigma_a(M)$, we find a similar scaling relation for the effective process zone fracture stress:

$$\sigma_G = \frac{\Delta\sigma}{1 + (M^*/M)^{\alpha/3}}. \tag{5.14}$$

The fracture energy $E_F = \pi E_G R^2(t)$ in which E_G is the specific fracture energy, the fracture energy per unit area of faulting. Combining this with Equations 5.12 and 5.14 yields

$$\frac{\Delta\sigma}{1 + R/R^*} = \frac{14\pi G}{16\Delta\sigma R^3} \int_0^R E_G(r) r dr \tag{5.15}$$

in which $R^* = R(M^*)$. Differentiating and solving for $E_G(R)$ gives

$$E_G(R) = \left(\frac{24\Delta\sigma^2}{7\pi G}\right)\left(\frac{R}{1+R/R^*}\right) - \left(\frac{16\Delta\sigma^2}{14\pi G}\right)\left(\frac{R^2/R^*}{(1+R/R^*)^2}\right) \tag{5.16}$$

in which we have used $\frac{R^3}{1+R/R^*} = \frac{M}{1+(M^*/M)^{\alpha/3}}$ assuming $\alpha = 1$. We approximate the above expression as

$$E_G(R) = \left(\frac{24\Delta\sigma^2}{7\pi G}\right)\left(\frac{R}{1+R/R^*}\right) \tag{5.17}$$

as shown in Figure 5-6. Specific fracture energies are generally assumed to be a constant value for earthquake rupture, though wide ranges of values have been determined through various methods [*Kostrov and Das*, 1988]. For example, *McGarr et al.* [1979] estimated E_G at 10^3 J/m^2 using seismic data from small vents in South African gold mines. *Aki* [1979] arrived at values of $10^6 - 10^8$ J/m^2 based on strong motion data from large events. The scatter in these values has been interpreted to be due to fault conditions such as fluid pressure or gouge layer thickness *Kostrov and Das* [1988], but our model indicates that the continuum of E_G is a function of the rupture size.

If every friction-dominated event has a finite acceleration and deceleration time and/or slip associated with its nucleation and stopping phases, then very small events that are barely larger than the critical event will have slower average rupture velocity than large events. This is because small events spend the minimum time at their peak seismic velocity. Therefore, rupture velocity may be an increasing function of seismic moment. Through the concept of radiation efficiency, as introduced by *Husseini and Randall* [1976] and *Husseini* [1977], rupture velocity can be related to both seismic moment and to apparent stress. In order to extend the model of specific fracture energy scaling to one of rupture velocity scaling, we consider the energy balance of a mode-III propagating crack. Conservation of energy in the vicinity of the crack tip requires [*Freund*, 1979]

$$\dot{E}_F(t) = 2\pi R(t) v_R(t) \frac{K_{III}(t)}{2G\sqrt{1 - v_R^2(t)/\beta^2}} \tag{5.18}$$

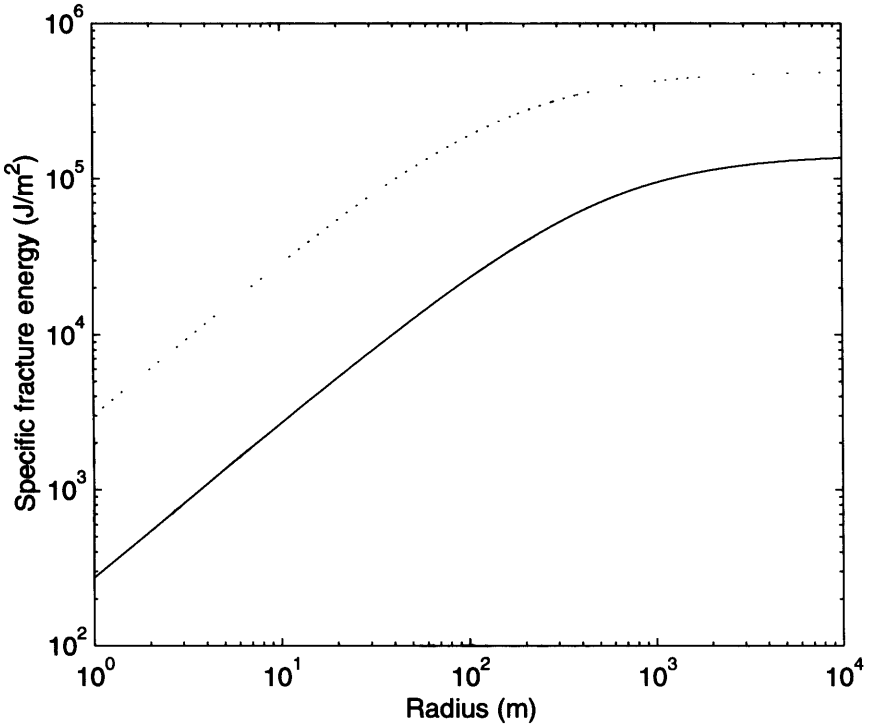

Figure 5-6: Specific fracture energy E_G vs. source radius. The solid line is for the constants $\Delta\sigma = 3$ MPa, $R^* = 526$ m, $M^* = 10^{15}$ Nm. The dotted line is for the constants $\Delta\sigma = 10$ MPa, $R^* = 163$ m, $M^* = 10^{14}$ Nm. The solid line uses the choice of constants that fits the apparent stress data, but the dotted line corresponds more closely to calculations of specific fracture energy for tectonic events.

where β is the shear wave speed of the material and K_{III} is the time-dependent stress intensity factor for a mode-III rupture:

$$K_{III} = K^0_{III} k(t) \tag{5.19}$$

in which the quasistatic stress intensity factor $K^0_{III} = 2\Delta\sigma\sqrt{2R/\pi}$ and $k(t) = k(v_R(t)) = \sqrt{1 - v_r(t)/\beta}$ [*Freund*, 1972; *Fossum and Freund*, 1975; *Freund*, 1990]. We can now use this result to obtain another expression for E_G:

$$E_G(R) = \frac{4\Delta\sigma^2 R}{\pi G}\sqrt{\frac{\beta - v_R}{\beta + v_R}}. \tag{5.20}$$

If E_G is a constant, then this expression reduces to the radiation efficiency η [*Husseini and Randall*, 1976],

$$\eta = 1 - \sqrt{\frac{\beta - v_R}{\beta + v_R}}. \tag{5.21}$$

However, our model indicates that E_G scales with source dimension as in Equation 5.17. We approximate $\sqrt{\frac{\beta - v_R}{\beta + v_R}}$ as $1 - v_R/\beta$ following *Freund* [1979] and obtain

$$1 - v_R/\beta \cong \frac{R^*/R}{1 + R^*/R} \tag{5.22}$$

so that the scaling relation of rupture velocity with source dimension is

$$v_R(R) = \frac{\beta}{1 + R^*/R} \tag{5.23}$$

as shown in Figure 5-7.

5.5.3 Observations of Ground Motion

We can test our scaling relation of increasing rupture velocity with source dimension using observations of ground motion recorded close to seismic events. In the near

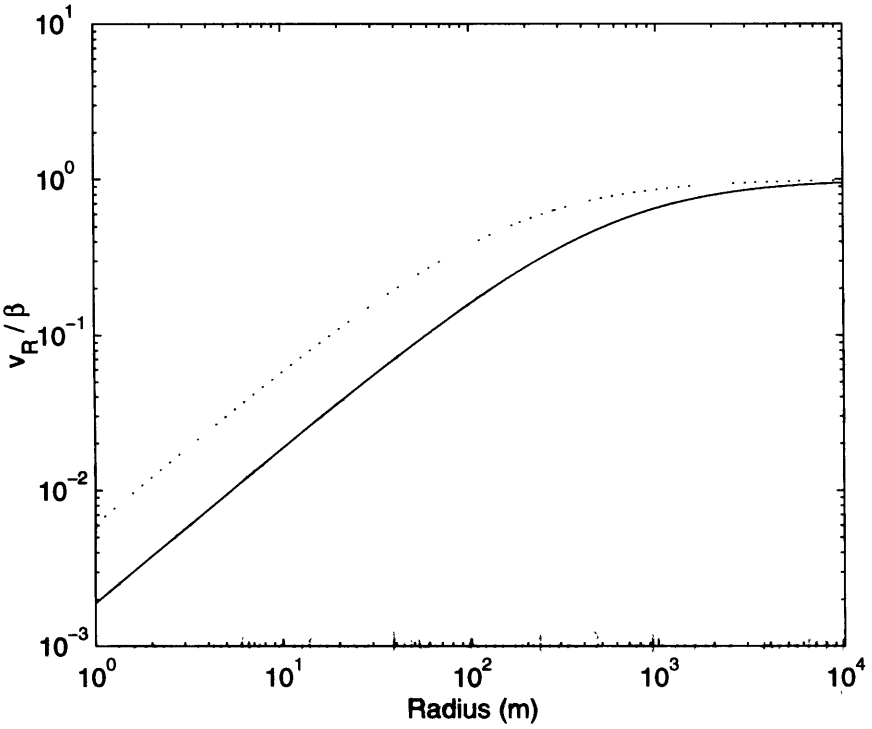

Figure 5-7: Rupture velocity v_R normalized by shear wave speed β vs. source radius. As in Figure 5-6, the solid line uses the choice of constants $\Delta\sigma = 3$ MPa, $R^* = 526$ m, $M^* = 10^{15}$ Nm. The dotted line is for the constants $\Delta\sigma = 10$ MPa, $R^* = 163$ m, $M^* = 10^{14}$ Nm.

field, fault displacement is given by [*Brune*, 1970]

$$u(t) = \frac{\Delta\sigma v_R}{G} t e^{-t/\tau} \tag{5.24}$$

where $\tau \sim R/\beta$. Differentiating and multiplying by a factor $\Re R/X$ in which X is hypocentral distance to account for spherical spreading gives

$$\dot{u}(t) = \frac{\Re R v_R \Delta\sigma}{XG} e^{-t/\tau}(1 - t/\tau) \tag{5.25}$$

and solving for the particle velocity at $t = 0$ yields [*McGarr*, 1984a]

$$X\dot{u} = \frac{\Re \Delta\sigma R v_R}{G} \tag{5.26}$$

in which the rupture velocity is taken to be a constant.

We measured peak velocity on seismograms at the closest station to the event for 37 events in Savuka and compared them to data from *McGarr* [1984a]. The *McGarr* [1984a] data is combination of measurements from East Rand Proprietary Mine, South Africa; Blyvooruitzicht Mine (adjacent to north of the Western Deep Levels lease area in the Far West Rand region); Monticello, South Carolina; Mammoth Lakes geothermal area, California; Oroville, California; and various other large tectonic events in California. We plot Equation 5.26 in Figure 5-8 as in *McGarr* [1984a] in which $\Delta\sigma$ is assumed constant and equal to 3 MPa, the source radius R scales with seismic moment as $(\frac{7M_0}{16\Delta\sigma})^{1/3}$, the shear modulus $G = 36$ GPa, and $\beta = 3650$ m/s which is the value in the Far West Rand region.

This scaling predicts the relationship between ground motion and seismic moment of the larger tectonic events adequately, but overestimates the ground motion for events smaller than about 10^{15} Nm. If we use our scaling relationship from Equation 5.23 instead of assuming $v_R = \beta$, we find

$$X\dot{u} = \frac{\Re \Delta\sigma R \beta}{G(1 + R^*/R)}. \tag{5.27}$$

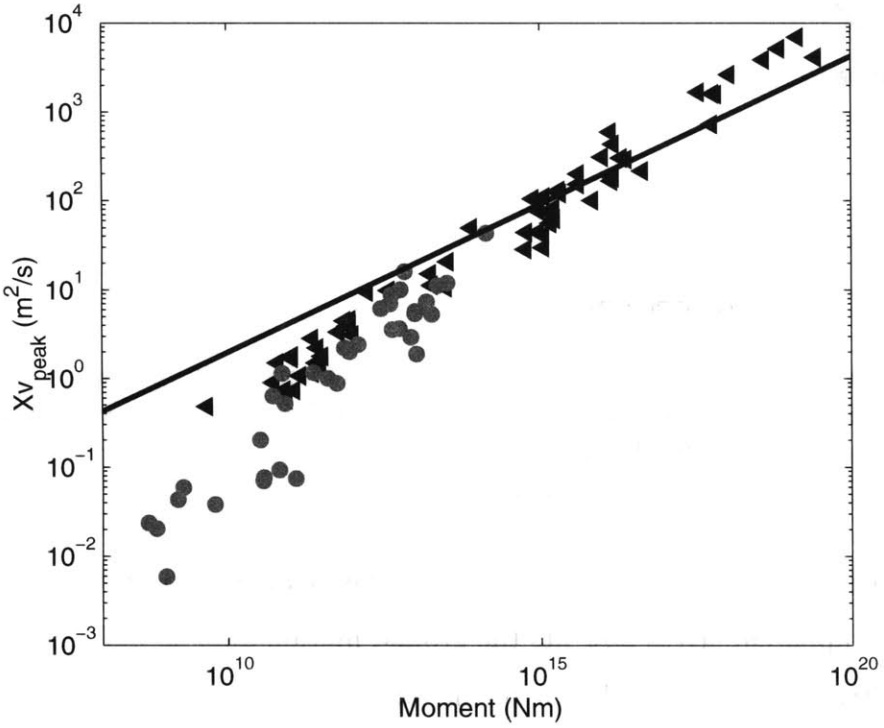

Figure 5-8: Ground motion parameter vs. moment for data from Savuka (circles) and from *McGarr* [1984a] (triangles) which includes a mixture of mining-induced, reservoir, volcanic, and tectonic seismicity. The line shows the scaling law of Equation 5.26.

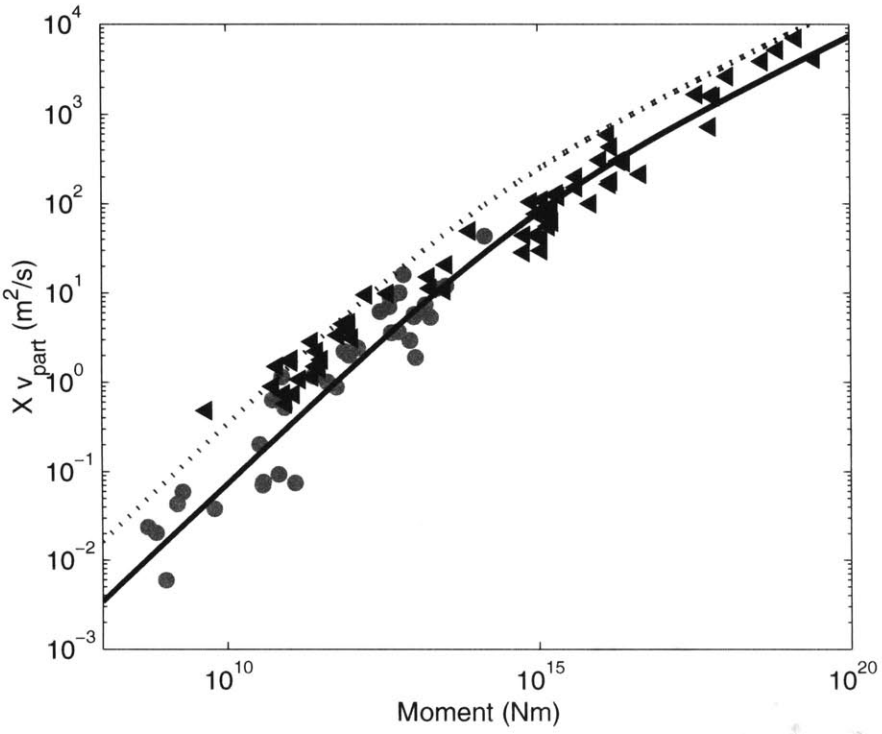

Figure 5-9: Same data as in Figure 5-8 with rupture velocity scaling lines. The constants for the solid and dotted lines are as in Figures 5-6 and 5-7. Note that there are no free parameters in this fit; the empirical scaling for the apparent stress observations fits ground motion observations as well.

Using the same choices of constants as in Figure 5-4, this scaling relation that was found empirically for apparent stress now fits the ground motion data as well (Figure 5-9). There are no free parameters in this fit to the data.

In addition, this model of increasing rupture velocity with source dimension can explain the observation of increasing stress drop with seismic moment for the friction-dominated events. The "observed" stress drop $\widetilde{\Delta\sigma}$ calculated assuming that rupture velocity is constant is related to the true stress drop by $\widetilde{\Delta\sigma} = \eta \cong v_R/\beta$ [*Husseini*, 1977] so that

$$\widetilde{\Delta\sigma} = \frac{\Delta\sigma}{1 + R^*/R}. \tag{5.28}$$

We corrected the stress drops for the reprocessed Type-B events in our catalog using this relation and obtained constant stress drop of approximately 10 MPa (Figure 5-10). In Figure 5-10, we plot the median values of the data binned in one order-of-

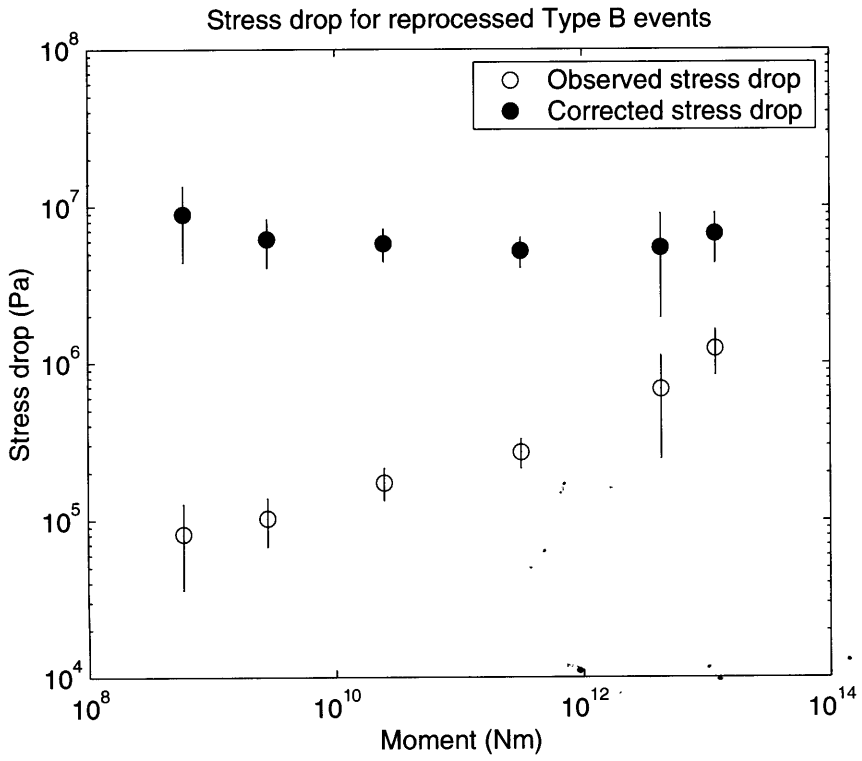

Figure 5-10: Stress drop vs. seismic moment for the observed median values of the Type-B events in our catalog calculated assuming a model of constant rupture velocity (solid symbols) and for these same events correcting the stress drop for increasing rupture velocity with radius (open symbols).

magnitude in seismic moment bins. The value of stress drop is higher than expected; we typically assume $\Delta\sigma = 3$ MPa for the Far West Rand. However, $\Delta\sigma = 10$ MPa fits the ground motion data adequately as an upper bound and also provides a better fit to the scaling of E_G. If we recalculate the nucleation dimensions of the critical earthquake from Chapter 4 using $\Delta\sigma = 10$ MPa, we find that $R_c = 6$ m and $D_c = 1.2$ mm.

Combining our data with the tectonic datasets of *Prejean and Ellsworth* [2001], *Abercrombie* [1995], and *Mayeda and Walter* [1996] and applying the same stress drop correction also yields constant stress drop (Figure 5-11). Here again we show the medians of each dataset in bins of one order of magnitude in moment. The largest median datapoint in study by *Prejean and Ellsworth* [2001] and the smallest two in the study by *Mayeda and Walter* [1996] are not fit well by our scaling model (Figure 5-11).

5.6 Conclusions

The 228 mining-induced seismic events we reprocessed have scaling relations that enable us to distinguish between the two types of evens found in the mines. This is in addition to distinguishing them based on their spatio-temporal characteristics and seismic spectra as in Chapter 3. The Type-A events compare favorably with datasets of fresh fracturing events. We observe that for fracture-dominated events, stress drop increases with seismic moment, but apparent stress decreases with seismic moment. Wider bandwidth studies are necessary to confirm these observations and to understand their physical significance. The Type-B events are the smallest friction-controlled events recorded in a tectonic setting. They have scaling relations that agree with extrapolations from larger tectonic events in that, if standard assumptions are used, stress drop and apparent stress both scale with seismic moment.

The increase in apparent stress with seismic moment for frictional events can be fit well with an empirical scaling relation in which there is a scale break at $M \approx 10^{14} - 10^{15}$ Nm. This same empirical expression can be stated in terms of increasing

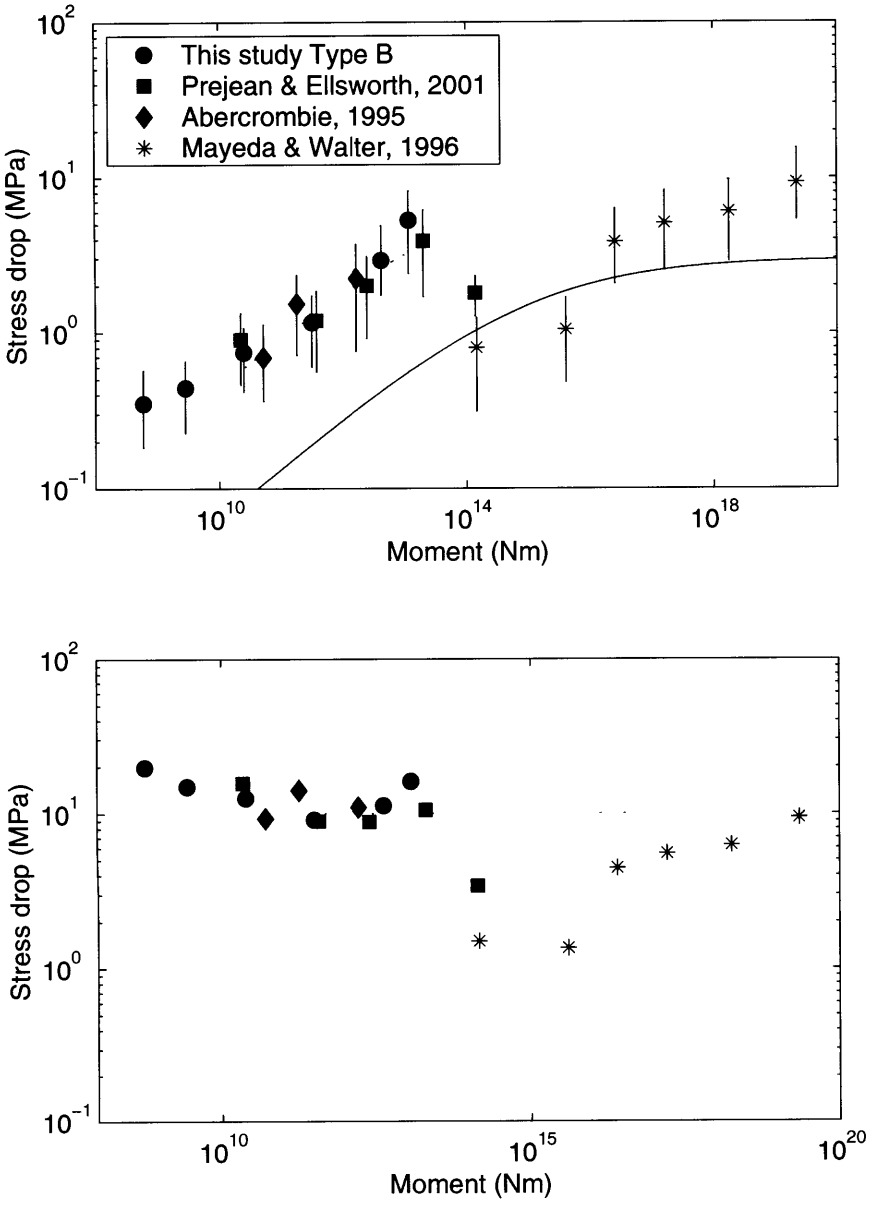

Figure 5-11: Stress drop vs. seismic moment for the observed median values of the Type-B events in our catalog compared with the other friction-dominated events from Figure 5-5. The values in the top panel were calculated assuming a model of constant rupture velocity and are shown with two scaling lines from Equation 5.28 using the two sets of constants as in Figures 5-6 and 5-7. The same data is shown in the bottom panel corrected using the scaling relation given by the dashed line in the top panel.

fracture energy and rupture velocity with seismic moment. The scaling of fracture energy we infer is corroborated by evidence of a continuum of estimated values over a range of event sizes. The scaling of rupture velocity is confirmed by observations of ground motion.

Chapter 6

Low-Frequency Properties of Intermediate-Focus Earthquakes

Published in *Bulletin of the Seismological Society of America* by E. Richardson and T. H. Jordan, in press 2002. Copyright by the Seismological Society of America.

Abstract. Intermediate-focus earthquakes are known to show features such as non-double-couple focal mechanisms that indicate source complexities. To characterize these features, we have studied systematically the low-frequency radiation from 108 intermediate-focus earthquakes recorded by high-performance seismic networks from 1989-1997 whose total moment was greater than 3×10^{18} N-m. We determined frequency-dependent focal mechanisms and source phase and amplitude spectra for each earthquake, estimating the uncertainties for all parameters. Frequency-dependent focal mechanisms were obtained from vertical-component free-oscillation data in 1-mHz bands over the range of 1-11 mHz. Source amplitude and phase-delay spectra were determined to 20 mHz from a combination of free-oscillation and surface-wave data. The population of intermediate-focus earthquakes in our catalog is not equally divided between compressional and tensional stress-release mechanisms; instead 59% are downdip tensional, 25% are downdip compressional, and 16% are neither. We have assessed the statistical significance of any non-double-couple component of the source for every earthquake in the catalog. We represent a deviatoric

focal mechanism by its principle axes and a scalar ξ that ranges from -1 for a compensated linear vector dipole (CLVD) with a compressional axis of symmetry through 0 for a double couple to +1 for a CLVD with a tensional axis of symmetry. ξ varies from -0.91 to +0.64 in this dataset. 56 of the 108 events have a significant CLVD component ($\xi \neq 0$) at the 95% confidence level. 15 events have an unusually large CLVD component of the focal mechanism ($|\xi| \geq 0.4$). We do not observe a correlation between the CLVD component and seismic moment or depth. T-type CLVD mechanisms correlate weakly with slab stress state, but no correlation was similarly found for P-type CLVD events. Seven earthquakes in the catalog are slow or compound, and three show strong frequency dependence of the moment tensor.

6.1 Introduction

Intermediate-focus earthquakes present several unsolved problems. Their focal mechanisms indicate that they are brittle shear failures like shallow earthquakes, but the lithostatic stress is too great at intermediate depths for ordinary stick-slip instabilities [*Griggs and Handin*, 1960; *Brune*, 1968]. They may require dehydration embrittlement [*Frohlich*, 1989; *Meade and Jeanloz*, 1991; *Peacock*, 2001] or other weakening mechanisms related to phase transitions [*Knopoff and Randall*, 1970; *Green and Burnley*, 1989; *Houston and Williams*, 1991; *Green and Houston*, 1995; *Frohlich*, 1994] but there is little evidence to confirm this. Nevertheless, they have proven useful in mapping the stress field in descending lithospheric slabs. The classic work by *Isacks and Molnar* [1971] developed the model of slabs as stress-guides, in which a principal axis of the focal mechanism parallels the inferred dip angle of the subducting slab. This model predicts that downdip compressional events are caused by compressive stresses in deep slabs resulting from increased resistance to further penetration into the mantle, whereas the negative buoyancy of shallow slabs creates tensional stress that is released through downdip tensional earthquakes.

However, intermediate-focus earthquakes display some anomalous behaviors, such

as double seismic zones [*Sleep*, 1979; *Fujita and Kanamori*, 1981] and non-double couple focal mechanisms [*Giardini*, 1983, 1984; *Dziewonski and Woodhouse*, 1983; *Kuge and Kawakatsu*, 1993] that may not be fit easily into a simple model. Proposed explanations for non-double couple events below shallow depths include mineral phase transitions [*Knopoff and Randall*, 1970; *Frohlich*, 1994], slip along curved surfaces [*Kubas and Sipkin*, 1987; *Frohlich*, 1990], or "complex faulting", in which multiple subevents with differently oriented double-couple mechanisms having one principal axis in common sum to produce a compensated linear vector dipole (CLVD) [*Giardini*, 1983; *Frohlich et al.*, 1989; *Riedesel and Jordan*, 1989; *Kuge and Kawakatsu*, 1990, 1992, 1993; *Frohlich*, 1994; *Kuge and Lay*, 1994b; *Frohlich*, 1995]. The latter explanation is by far the most popular because it is consistent with the model of the slab as a stress guide. It predicts that the dominant principal axis (the axis of symmetry of the CLVD) coincides with the downdip axis of the slab.

In this study we have cataloged 108 large intermediate-focus earthquakes that were recorded by high-performance digital seismometers from 1989-1997 in order to study systematically their source characteristics at low frequencies (0-20 mHz). We have determined moment tensors to assess the statistical significance of non-double-couple source mechanisms at this depth range, and we have measured the orientation of the principal axes of the focal mechanisms with respect to their slabs to test the model of the slab as a stress guide. We have also examined source spectra to investigate other anomalous source properties, such as slow earthquakes and frequency-dependent moment tensors.

6.2 Observations

Our catalog comprises 108 earthquakes that occurred from 1989-1997 having centroid depths between 50 and 300 km and total scalar seismic moment, M_T^0, greater than 10^{18} N-m. This is ten fewer than in the Harvard CMT catalog because we rejected events for which fewer than ten seismograms were available, or that nearly

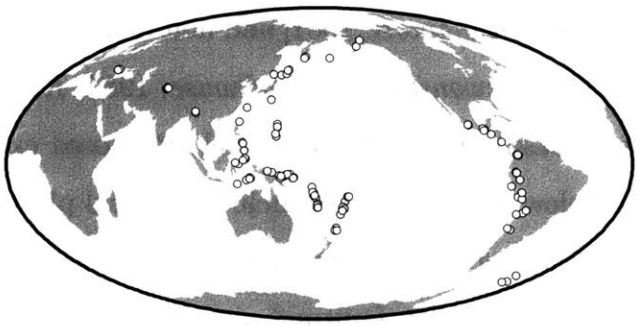

Figure 6-1: Epicenters of the intermediate-focus earthquakes in this catalog.

coincided in time with another large event, or that had inadequate variance reduction, indicating a low signal-to-noise ratio. Figure 6-1 shows a map of the earthquakes in our catalog.

For each earthquake, we compiled vertical very long period digital seismograms from GEOSCOPE and the Global Seismic Network (GSN) via the IRIS Data Management Center. These data were edited to seven-hour time series beginning one hour prior to the centroid time of the earthquake. They were then compared to synthetic seismograms calculated by complete normal mode summation using the asymptotic intramode coupling formulae of *Woodhouse and Dziewonski* [1984], the source parameters of the Harvard CMT catalog, the 3-D earth model SH12-WM13 of *Su et al.* [1994], and the 1-D reference model, PREM [*Dziewonski and Anderson*, 1981], to account for radial anisotropy.

Following *Riedesel and Jordan* [1985, 1989], we obtained ten spectral estimates of each event's frequency-dependent moment-rate tensor $\mathbf{M}(\omega) = \sqrt{2}M_T(\omega)\hat{\mathbf{M}}(\omega)$ in which M_T is the total scalar moment and $\hat{\mathbf{M}}(\omega)$ is the source mechanism. These estimates were made for ten separate 1-mHz bands from 1-11 mHz by inverting complex-valued spectral integrals over ~ 0.1 mHz bands. Stations with low variance reduction were removed to eliminate noisy seismograms, nodal stations, and records with strong Coriolis coupling effects; and the inversion procedure was then repeated. When there was no significant frequency dependence of the moment tensor, we averaged the source mechanism over the ten bands using a least-squares procedure that accounted for the full covariance in each frequency band. The rigorous error analysis allowed us to

assess the statistical significance of any non-DC component of the source mechanism.

Moment tensors were constrained to be deviatoric ($tr\mathbf{M}(\omega) = 0$). Each source mechanism can thus be described by three principal axes P, T, and N and a mechanism vector $\hat{\boldsymbol{\lambda}} = \sum_{i=1}^{3} \lambda_i \hat{\mathbf{e}}_i$, in which the $\hat{\mathbf{e}}_i$'s are eigenvectors of $\mathbf{M}$ that correspond to P, T, and N, and the eigenvalues (λ_i) of $\mathbf{M}$ are ordered such that $\lambda_1 \geq \lambda_2 \geq \lambda_3$. Errors in $\hat{\boldsymbol{\lambda}}$, to first order, are uncorrelated with those of the principal axes [*Riedesel and Jordan*, 1989]. The angular separation of $\hat{\boldsymbol{\lambda}}$ from the $\hat{\mathbf{d}}$, the vector corresponding to a pure double-couple (DC) source is expressed by a scalar

$$\xi = \frac{\cos^{-1}(\hat{\boldsymbol{\lambda}} \cdot \hat{\mathbf{d}})}{\pi/6}, \tag{6.1}$$

which ranges from -1 for a pure CLVD with a compressional axis of symmetry, through 0 for a pure DC, to +1 for a pure CLVD with a tensional axis of symmetry. Earlier workers have expressed the non-double-coupleness of a source with slightly different measures, such as $\epsilon = -\frac{\lambda_2}{\max(|\lambda_1|,|\lambda_3|)}$, [*Giardini*, 1984] and $\Gamma_{\text{norm}} = \frac{3^{3/2}\det(\hat{\mathbf{M}})}{2\|M_T\|^3}$ [*Frohlich*, 1990, 1995]. Our measure is the most conservative of the three in that for any fixed mechanism $|\xi| \leq |2\epsilon| \leq |\Gamma_{\text{norm}}|$ (Figure 6-2). We also obtained the amplitude spectra $M_T(\omega)$ in twenty separate 1-mHz bands from 1 - 21 mHz by the power-spectra inversion technique of *Silver and Jordan* [1982], as well as the phase-delay spectra $\Delta t(\omega)$ in the same twenty bands by modal cross-correlation [*Riedesel and Jordan*, 1989]. These methods for estimating source spectra have been applied to the recovery of source time functions by *Ihmlé et al.* [1993] and *McGuire et al.* [1996].

6.2.1 Example Events

To illustrate some of the source characteristics in the catalog, we discuss the results of our data processing for three example events. One is an "average" event and the other two show anomalous low-frequency properties.

Vanuatu, 11 October 1992. The Vanuatu/New Hebrides subduction zone is the source of the greatest number and largest moment release of intermediate-focus

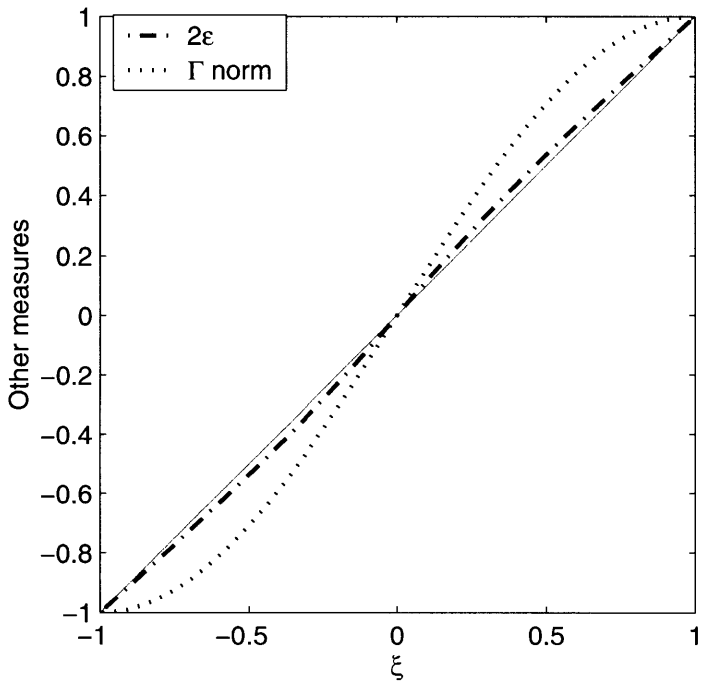

Figure 6-2: Comparison among the parameters ξ, 2ϵ, and Γ_{norm}. The dash-dot line shows 2ϵ as a function of ξ and the dotted line shows Γ_{norm} as a function of ξ. The solid grey line has a slope of one. The measures are all equal in the case of pure DC and CLVD mechanisms, but the magnitude of ξ is less than the others for linear combinations of DC and CLVD sources.

earthquakes [*Astiz et al.*, 1988]. This earthquake from the Vanuatu slab is a typical intermediate-focus earthquake, although it is larger than most ($M_T^0 = 1.65 \pm 0.05 \times 10^{20}$ N-m). Like nearly all events in the catalog, the source mechanism (Figure 6-3a) does not show significant frequency dependence, and it agrees well with that of the Harvard CMT solution in the 6-8 mHz range, which is the approximate frequency band sampled by the Harvard solution. The ten-band averaged focal mechanism is purely DC at the 95% confidence level, which is also true for 52 of 108 earthquakes in this study, and the T axis is within 45° of $\hat{s}$, the slab dip axis, like the majority of earthquakes in this study and ten of the sixteen earthquakes from this slab.

Amplitude and phase-delay spectra (Figure 6-3b,c) are stable, showing that the energy radiation is constant over this frequency range. The source time function derived from these spectra is consistent with moment release beginning at the high frequency origin time of the earthquake.

Colombia, 02 September 1997. This earthquake from the Nazca plate is of average size ($M_T^0 = 2.35 \pm 0.10 \times 10^{19}$ N-m). The lack of frequency dependence of the moment tensor, phase delay, and amplitude spectra indicates that this source does not have unusual spectral characteristics at low frequencies (Figure 6-4). However, this event has an anomalously large CLVD component ($\xi = -0.774 \pm 0.004$). The negative value of ξ and the symmetric zonal pattern in the beachball diagram about the P axis indicate a "P-type" CLVD (Figure 6-4a). We note, however, that this event occurs in a slab which releases moment predominantly in downdip tension. This is a significant observation because if the slab acts as a stress guide, the axis of symmetry of a CLVD event should correspond to the mode of strain release in the slab, which is not the case for this event.

Northern Peru, 28 October 1997. This earthquake also occurred in the Nazca subduction zone. The 95% confidence ellipse for the $\hat{\boldsymbol{\lambda}}$ vector includes the pure double-couple vector ($\hat{\mathbf{d}}$), and the source shows no frequency dependence (Figure 6-5a). Like the majority of earthquakes in the Nazca subduction zone, the T axis is close to the slab dip axis ($\hat{s} \angle T = 17°$). It does have an anomalous amplitude spectrum (Figure 6-5b), which rolls off by about 50% from 1-6 mHz, then continues at a nearly constant

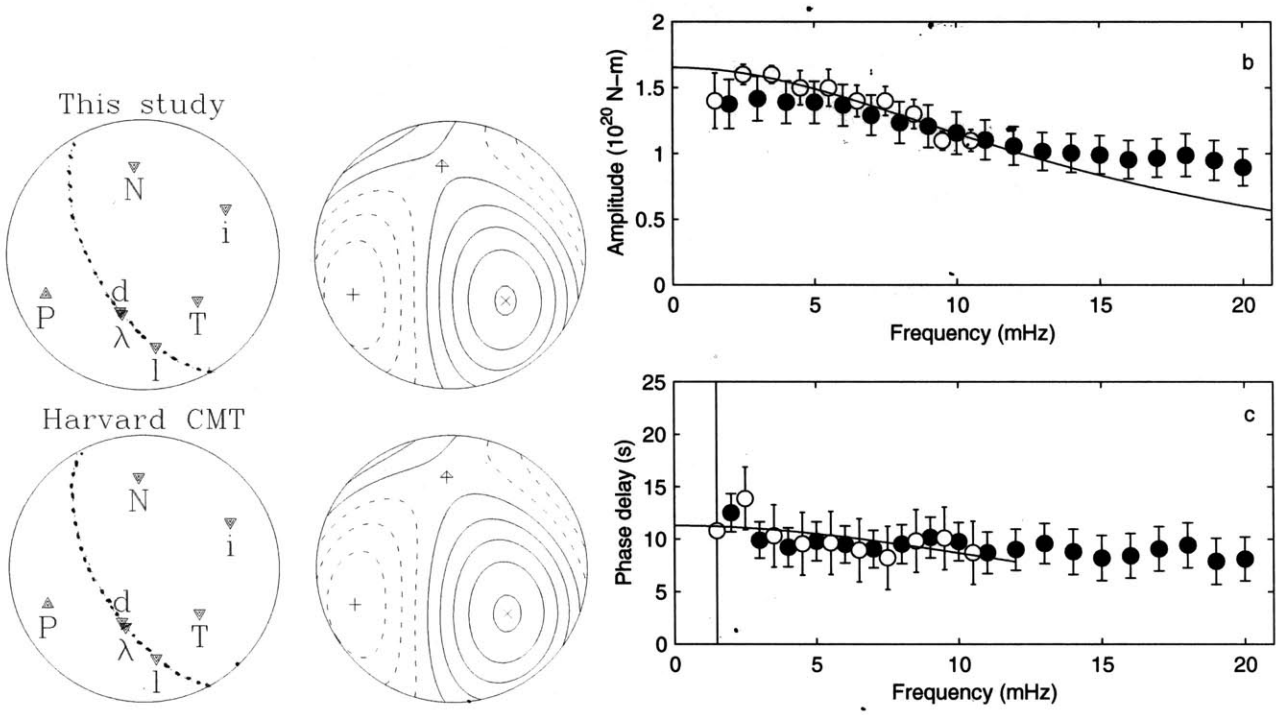

Figure 6-3: 11 October 1992 Vanuatu event (19.17°S, 168.83°E, 141km). The average focal mechanism is shown in (a) along with the Harvard CMT solution. Amplitude (b) and phase-delay spectra (c) were calculated from normal modes (open symbols) and first-orbit surface waves (filled symbols). We fit the total-moment spectrum in (b) with the function $M_T(\omega) = M_T^0 \left(1 + \frac{\omega^2 \tau_c^2}{8}\right)^{-1}$ to recover M_T^0, the total static seismic moment, and τ_c, the characteristic duration of the source. We fit the phase-delay spectrum in (c) with $\Delta t(\omega) = (1-\alpha)\Delta t_1 + \frac{\alpha}{\omega} tan^{-1} \omega \Delta t_1$ to obtain Δt_1, the centroid time shift relative to the high-frequency origin time [*Ihmlé and Jordan*, 1994; *Jordan*, 1991].

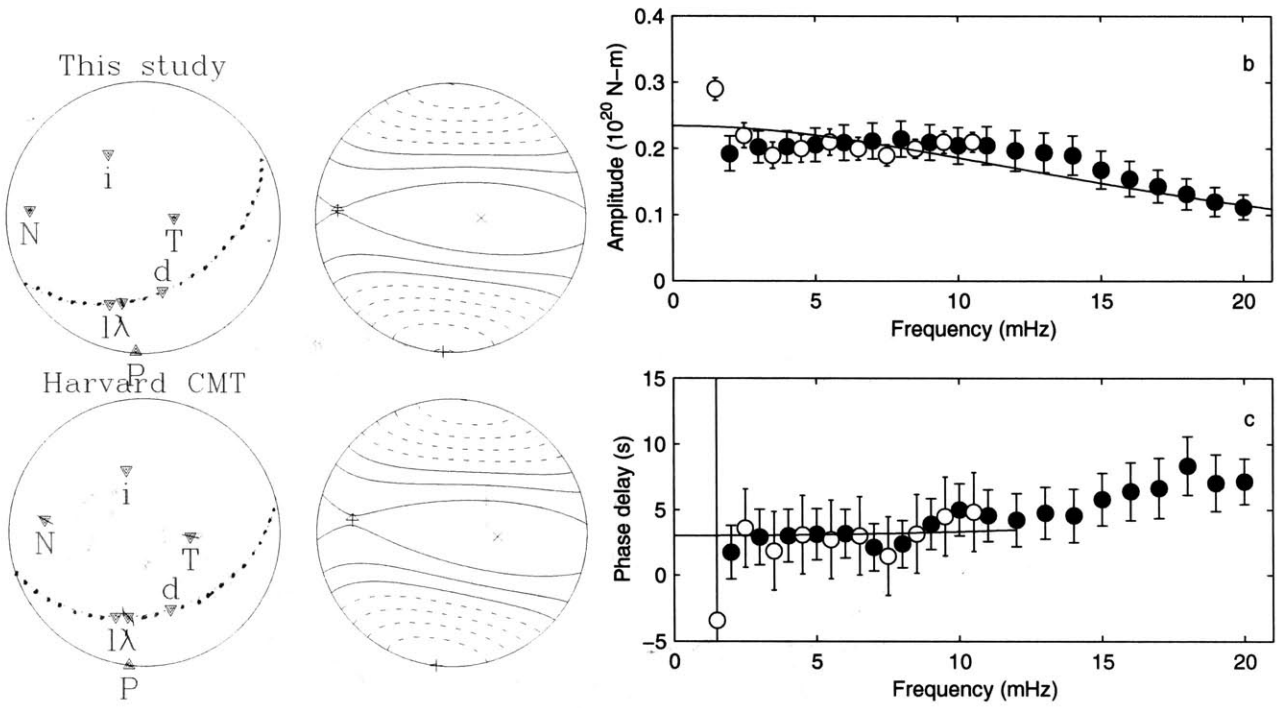

Figure 6-4: 02 September 1997 Colombia event (4.00°N, 75.56°W, 213km). Source-mechanism (a), amplitude (b), and phase-delay spectra (c). Symbols are as in Figure 6-3.

value out to 20 mHz. The characteristic duration derived from the slow component (< 6 mHz) $\tau_c = 43.8 \pm 1.7$ s. This type of kinked spectrum has been observed for another intermediate-focus earthquake in this region [*Jordan*, 1991; *Harabaglia*, 1993]. Such spectra are also observed for some large earthquakes on oceanic transform faults, and have been interpreted to be compound events [*Ihmlé and Jordan*, 1994; *McGuire et al.*, 1996].

The phase-delay spectrum is nearly flat and $\Delta t_1 = 8.7 \pm 1.2$ s. $M_T^0 = 9.1 \pm 0.34 \times 10^{19}$ N-m. We applied the same inequalities described in *Jordan* [1991] and found that this event, too, requires a slow precursor, i.e. significant moment release must have preceded the high-frequency origin time. Detection of precursory slip remains a controversial issue. Recently, *Abercrombie and Ekström* [2001] have argued that observed precursors for large oceanic transform fault events are artifacts resulting from uncertainties in source depth. We recalculated the spectra for this event at several different depths within 25 km of the depth determined by the Harvard CMT

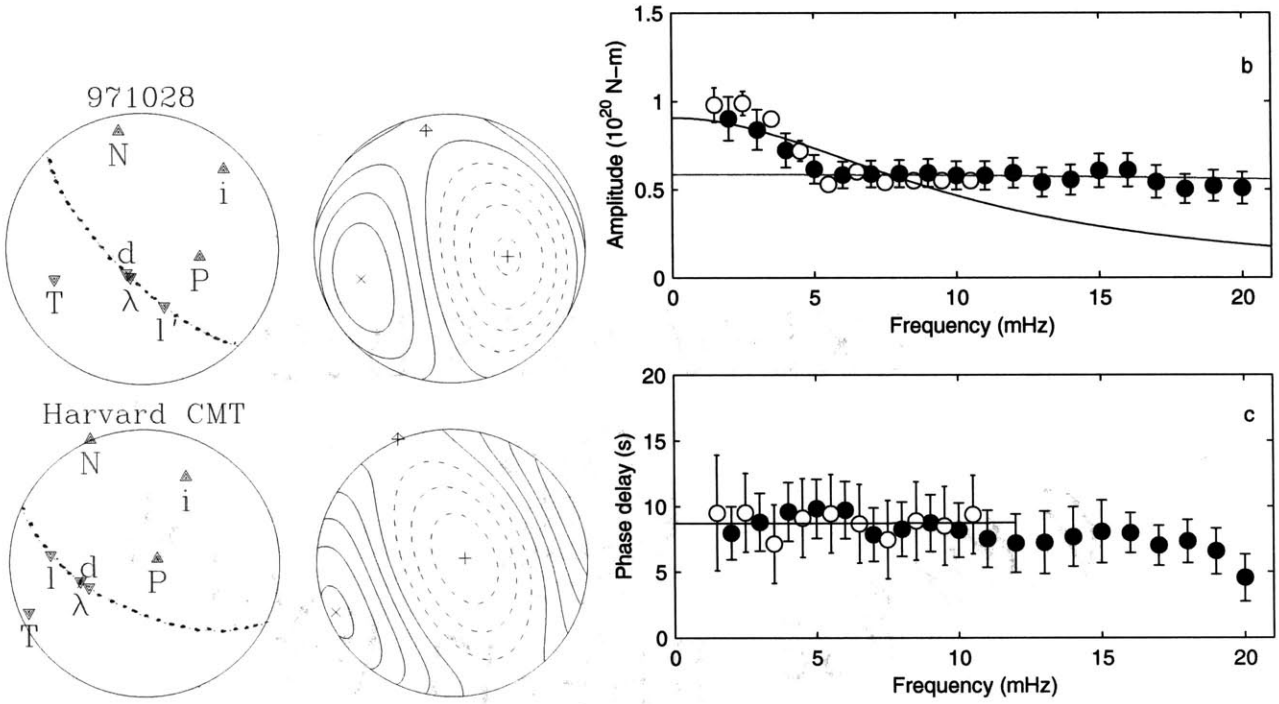

Figure 6-5: 28 October 1997 Peru event (4.23°S, 76.63°W, 125km). Average focal mechanism is shown in (a), anomalous amplitude (b), and phase-delay spectra (c) indicate that this event has a slow precursor. In (b), the black line is fit from 1-11 mHz and the grey line is fit from 11-21 mHz. Symbols are as in Figure 6-3.

catalog (125 km) and found no appreciable change in our results. Furthermore, other nearby events in this catalog do not require a precursor (compare the spectra for the nearby event of 03 December 1989 in Figure 6-6), therefore we do not believe this observation results from modelling errors, such as incorrect depth or Coriolis coupling, nor from anomalous wave propagation effects.

6.2.2 Comparison with the Harvard CMT catalog.

For the 108 events in this catalog, our determination of M_T^0 correlates well (correlation coefficient = 0.99) with the moment reported by the Harvard CMT catalog (Figure 6-7a). Our measurement is generally slightly higher ($\sim$ 6%) because it is a lower-frequency measure. We performed an error analysis in which we assumed that the Harvard CMT catalog error is some multiple of our error, then determined the

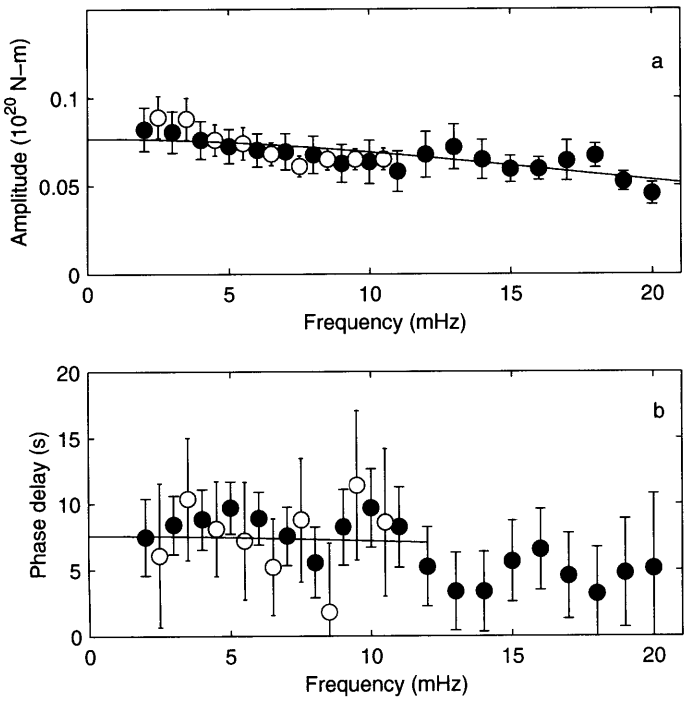

Figure 6-6: 03 December 1989 Peru event (7.37°S, 74.27°W, 151km). Neither the amplitude spectrum (a), nor the phase-delay spectrum (b) indicate anomalous low-frequency behavior such as that seen for the event in Figure 6-5. Symbols are as in Figure 6-3.

ratio of the residual between our measure and the Harvard CMT measure and our known error estimate. Based on these calculations, we infer that the standard CMT errors are approximately 3.8 times as large as ours. There is a greater scatter between our measure of Δt_1 and the half-duration of the source determined by the Harvard CMT catalog (Figure 6-7b). Based on the same error analysis as previously described, the Harvard CMT uncertainty is 3.6 times the size of ours, yielding in an expected variance of Δt_1 of 13.5 s. The average residual between the measures in each catalog is 1.3 s. Therefore, the two measures agree within each one's uncertainty estimates. We also compared the value of ξ determined from the ten-band average of frequency dependent moment tensors from 1-11 mHz with that determined from the Harvard CMT catalog moment tensor solution (Figure 6-7c). The few large discrepancies are generally small events and/or events with poor azimuthal station coverage. The same error analysis yields an expected catalog variance in ξ for Harvard of 0.02. We assume that this is the amount of scatter due to noise and use this information to calibrate the Harvard catalog in other depth ranges, assuming that the amount of noise present at all depth levels is the same.

To do this, we calculated ξ for all events in the Harvard CMT catalog from 1989-1997 having $M_0 > 3 \times 10^{18}$ Nm. For shallow events, ξ ranges from -0.88 to 0.71 with a mean of 0.00 ± 0.20 and a variance of 0.04; for intermediate-focus events, it ranges from -0.80 to 0.59 with a mean of 0.00 ± 0.24 and a variance of 0.06; and for deep events, it ranges from -0.55 to 0.26 with a mean of $-0.06 \pm .17$ and a variance of 0.03. Using our previous result for variance in the Harvard CMT catalog due to noise at intermediate depth ranges, 0.02, we estimate that the true variances are 0.02, 0.04, and 0.01 for shallow, intermediate, and deep-focus events, respectively. Therefore, for events with $M > 10^{18}$ Nm, intermediate-focus earthquakes do show greater deviation from the double-couple model of the source than do deep and shallow events.

6.2.3 Spectral properties

We obtained phase-delay and amplitude spectra for each event and we deter-

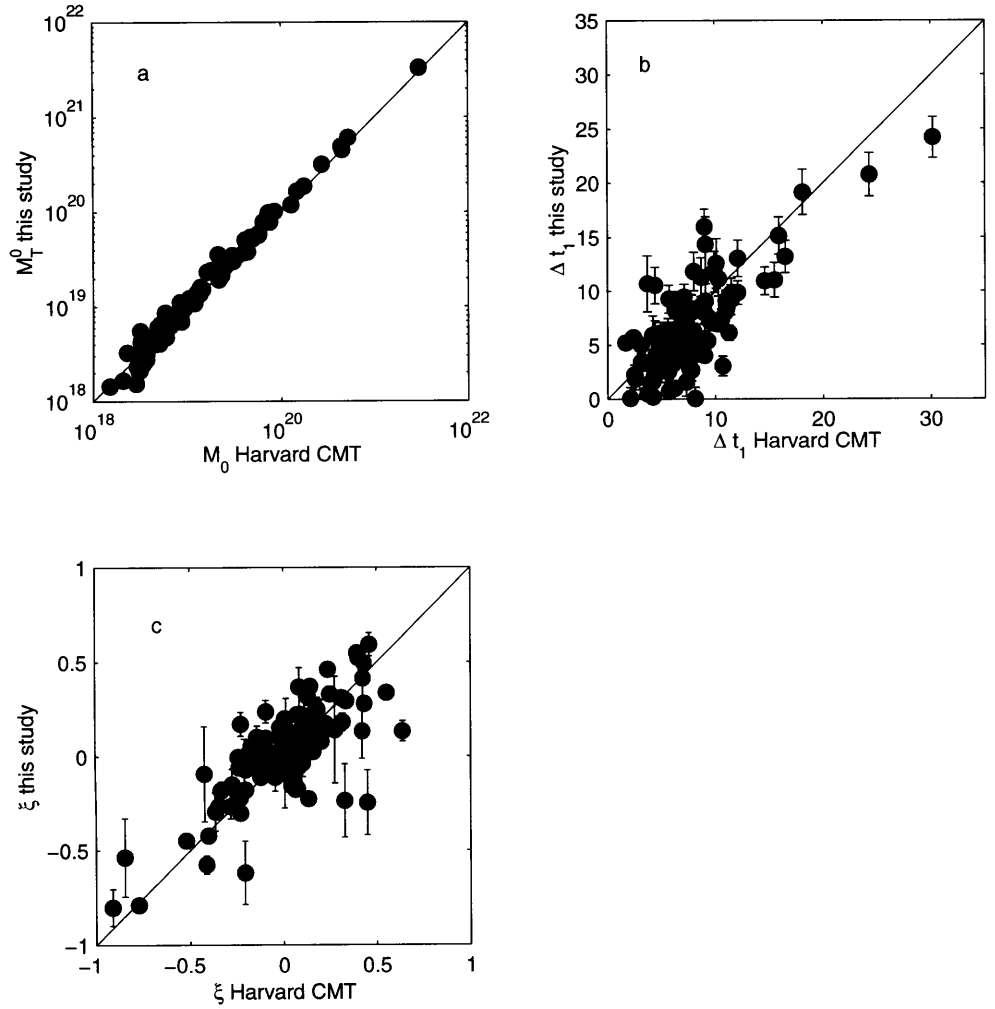

Figure 6-7: Comparisons between our M_T^0 with the seismic moment from the Harvard CMT catalog (a), between our Δt_1 and that of the Harvard CMT catalog (b), and between our ξ and that calculated from the Harvard CMT moment tensor (c). In (a), the correlation between the two measures is 0.99. In (b), the straight line has a slope of one, and the correlation coefficient is 0.83. In (c), the straight line has a slope of one, and the correlation coefficient is 0.77.

mined the moment tensors in ten separate frequency bands in order to observe any anomalous low-frequency behavior of these events. We found that 98 of the 108 intermediate-focus earthquakes in our catalog lack significant spectral anomalies over the frequency range of our study. The exceptions are seven events that are slow or compound with a slow subevent: 19930115, 19940314, 19941016, 19950502, 19951219, 19960222, and 19971028; and three that show frequency-dependent mechanisms: 19900109, 19900205, and 19900713. Details of these sources are listed in Appendix B. We note that we used the same methods as previous studies that did find prevalent anomalous low-frequency behavior for oceanic transform faults [see *Ihmlé and Jordan*, 1994; *McGuire et al.*, 1996]. Although we know that CLVD mechanisms are common at intermediate depths, we cannot link these CLVD mechanisms with anomalous spectral properties since the earthquakes in our catalog rarely exhibit the latter.

6.2.4 Mechanism properties

In order to test whether the rupture complexity indicated by non-double-couple mechanisms are linked to unusual stress fields in the slab, we cataloged the orientations of the principal axes of the focal mechanisms of all the earthquakes in our catalog and estimated local orientation of the slab at each source's centroid location.

Principal axes orientation. For each earthquake in the catalog except three, we determined $\hat{s}$, the local dip angle and azimuth of the slab based on published studies of regional seismicity. In cases where the authors contoured the seismogenic zone of the slab in depth, we used their results, otherwise we assumed the slab followed the locations of events. References used are listed in Table 2 of Appendix B. The three omitted earthquakes (09 December 1989 Minahassa Peninsula, 18 May 1993 Philippines, and 29 September 1993 Minahassa Peninsula) occurred in extremely complicated slab environments, so the orientations of those slabs could not be determined at the location of the earthquakes.

The majority of the earthquakes in the catalog (59%) have $\hat{s}$ within 45° of the T

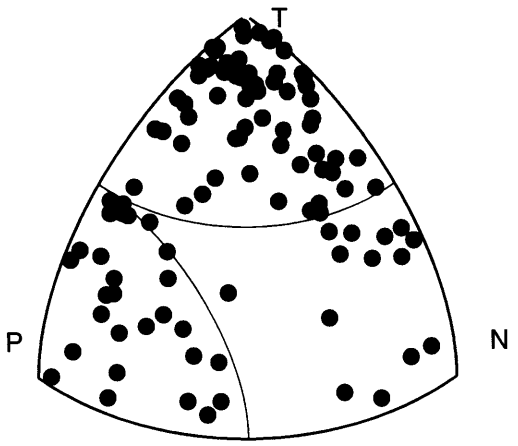

Figure 6-8: Distribution of slab orientations ($\hat{\mathbf{s}}$) with respect to the principal axes of the moment tensor (T, P, and N). The endpoints of $\hat{\mathbf{s}}$ are projected onto 1/8 of a sphere bounded by the T (top), P (bottom left), and N (bottom right) axes. The curved lines across the top and in the left corner are 45° small circles around the T and P axes, respectively.

axis; that is, the slab dip axis is closer to the T axis than to either of the other two principal axes. Only 25% of earthquakes have $\hat{s}$ within 45° of the P axis, while 16% have $\hat{s}$ separated from both the P and T axes by more than 45°. Of the downdip tensional events, 45 of 63 have $\hat{s}$ within 30° of T. Only 9 of the 27 downdip compressional events have $\hat{s}$ within 30° of P (Figure 6-8). We projected $\hat{s}$ onto an eighth of a sphere spanned by the T, P, and N axes of the focal mechanism. Events for which the T axis lies close to $\hat{s}$ plot near the top; those for which the P axis lies close to $\hat{s}$ plot in the bottom left corner, and those for which the N axis lies close to $\hat{s}$ plot near the bottom right corner (Figure 6-8).

Non-double-couple mechanisms. 56 of 108 earthquakes in our catalog have significant ξ at the 95% confidence level and 15 have $|\xi| > 0.4$. The possibility that deviation from DC is merely an artifact resulting from unmodeled velocity structures [*Foulger and Julian*, 1993; *Tada and Shimazaki*, 1994] or waveform inversion instabilities [*Kuge and Lay*, 1994a] is plausible only for shallow-focus earthquakes for which some moment tensor components cannot be well-resolved, or for high-frequency waveform analyses in which the seismic wavelengths are comparable to the slab thickness.

We found the variance reduction to be much higher for intermediate-focus events than for shallow-focus events processed using the same techniques, so we infer that the moment tensors are well-resolved. Slab thickness does not interfere with this analysis because of the very low frequency range of this study. In addition, the lack of frequency-dependence of the focal mechanism is evidence for robustness of our results.

We constrained the moment tensors of earthquakes in this study to be deviatoric, so if a source contained a significant isotropic component, it could conceivably be resolved as a CLVD component instead. To test this, we compared the solution from one of our events with large $|\xi|$ to a solution that was not constrained to be deviatoric and found that the resolved isotropic part was insignificant compared to the uncertainty in ξ. In addition, previous analyses of earthquakes using our methods that did not constrain the moment tensor to be deviatioric also did not find evidence for significant isotropic source components [*Riedesel and Jordan*, 1989].

For the earthquakes in our catalog, ξ does not correlate strongly with the other source properties we measured, including seismic moment, depth of rupture, source duration, and rupture velocity. The distribution of ξ for the earthquakes in this study is shown with respect to their total moment (Figure 6-9a) and depth (Figure 6-9b). The magnitude of ξ appears to deviate less from the DC model as total moment increases, but this is not significant compared to the level of noise in the data for earthquakes with $M_T^0 < 1 \times 10^{19}$ N-m. No trend in the distribution of ξ with depth is apparent. There is a slight (correlation coefficient = 0.27) tendency for T-type CLVDs to be downdip tensional events (Figure 6-10). Correlation between the value of ξ and the angular separation from the P or N axes is insignificant given the scatter of the data. Earthquakes with large ($|\xi| > 0.4$) CLVD components do not necessarily prefer that the axis of the CLVD mechanism is also close to the downdip direction of the slab (Figure 6-11). Half of the T-type CLVD events have the T axis within 30° of the slab dip axis, but none of the P-type CLVDS have the P axis that close to $\hat{s}$.

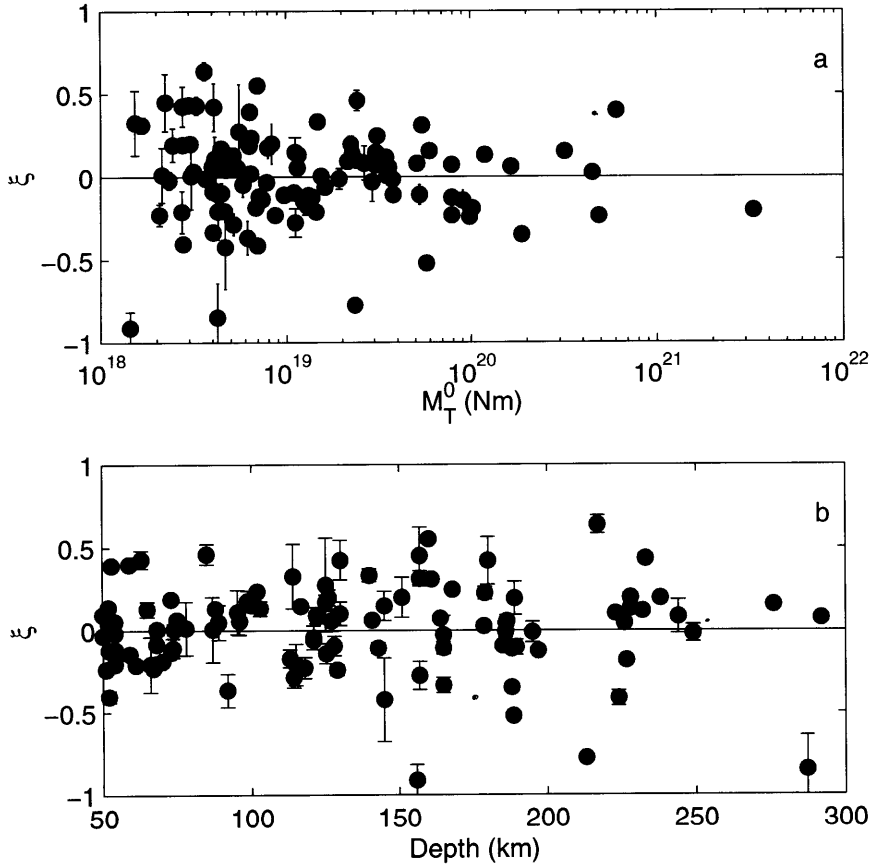

Figure 6-9: Distribution of ξ with respect to total moment (a) and depth (b). The horizontal line in each is $\xi = 0$.

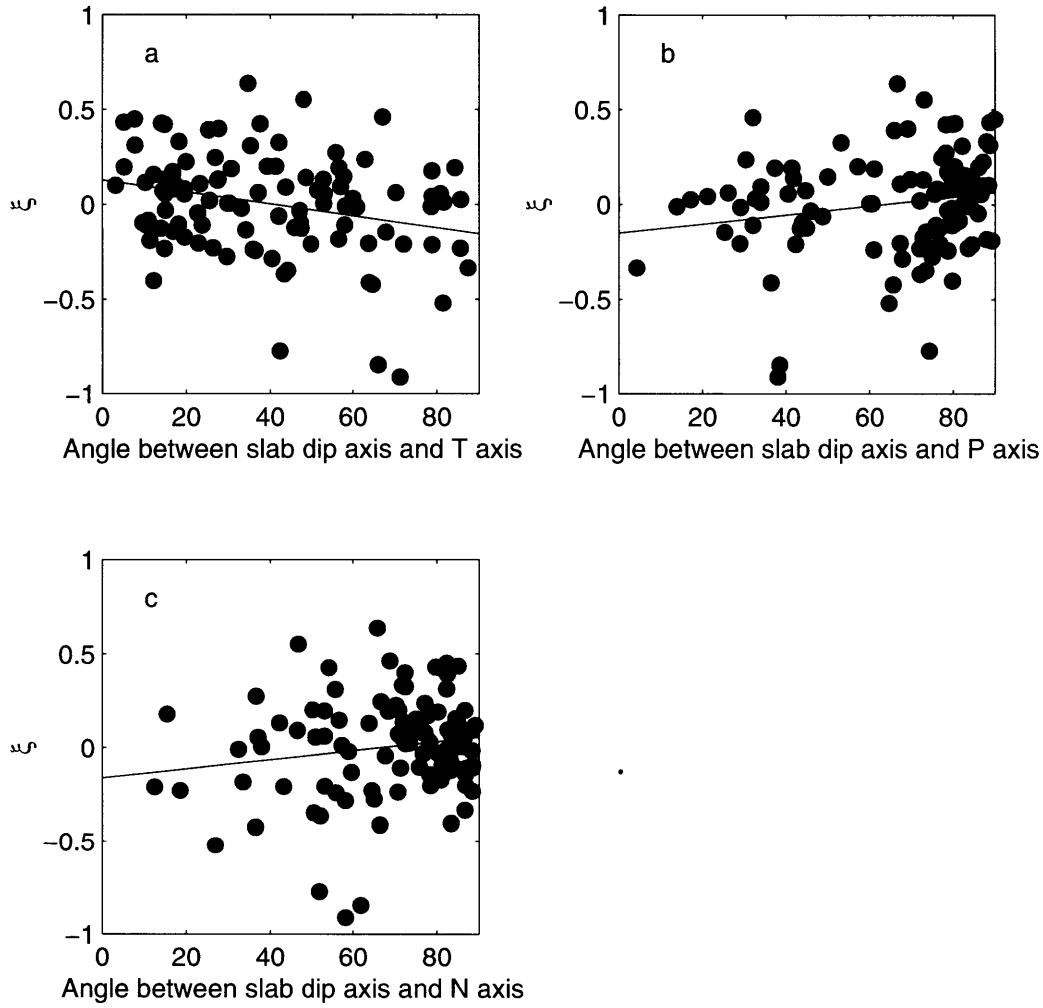

Figure 6-10: CLVD fraction (ξ) as a function of the angular separation between the slab dip axis and the T axis (a), between the slab dip axis and the P axis (b), and between the slab dip axis and the N axis (c). Correlation coefficients for each of the three distributions are 0.27 in (a), 0.19 in (b), and 0.16 in (c). Lines drawn are least-squares best fit lines to the data. Error bars have been omitted for clarity.

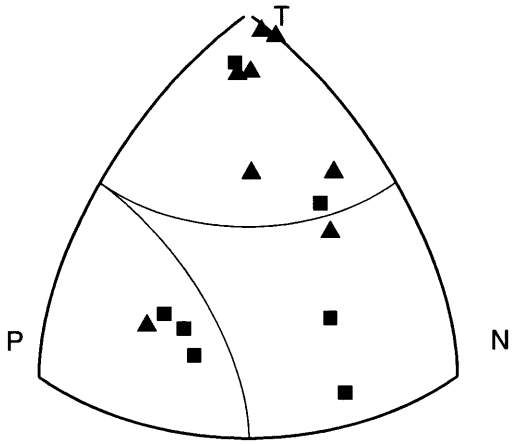

Figure 6-11: Distribution of slab orientations with respect to the principal axes of the moment tensor for events with $|\xi| > 0.4$. Triangles indicate T-type CLVDs, and squares represent P-type CLVDs. Axes and annotations are as in Figure 6-8.

6.3 Discussion

The clearest result of this study is the lack of significant anomalies in *most* of the source properties we cataloged. That having been said, we do find a large number of earthquakes whose focal mechanisms significantly deviate from the DC model. We investigated the relationship between non-double-coupleness and the slab-axis orientation to test the hypothesis that the two are related and are indicative of the complexity of intermediate-focus sources.

Previous studies have correlated slab stress regime with large CLVD components of earthquakes, e.g. *Giardini* [1983, 1984]; *Frohlich et al.* [1989]; *Frohlich* [1995]; *Kuge and Kawakatsu* [1993]; *Kuge and Lay* [1994b]. These investigators have proposed that the axis of symmetry of the CLVD mechanism is also the axis that corresponds to the downdip direction of the slab, and that the two should align in space. Therefore, $\xi < 0$ in compressional slabs and $\xi > 0$ in tensional slabs. This idea is supported by regional analyses of focal mechanisms in which source regions are dominated by a singular orientation of one of the three principal axes. For example, *Fischer and Jordan* [1991] showed cases where two axes of a focal mechanism rotate randomly about the plane

that is perpendicular to the slab-aligned dominant axis. A summation of moment tensors from events in such a region produces a CLVD solution. Following this logic, one earthquake with a large CLVD component would likely be due to summation of mechanisms of some number of subevents with one consistent principal axis but different positions of the other two. Evidence consistent with this hypothesis includes the study by *Kuge and Kawakatsu* [1992] in which three events (two deep events in the Japan subduction zone and one intermediate-focus event from the Philippines) with large CLVD component were decomposed into separate DC subevents with varying geometries about one mean stress axis. If all CLVD sources are produced this way, then source regions with greater subfault distributions may be expected to produce most of the earthquakes with large CLVD components, and the dominant CLVD axis in these events should align with the downdip axis of the slab.

Visual inspection of Figure 6-11 shows that this hypothesis does not prove to be valid on a global scale. Here we show only events with $|\xi| > 0.4$. Triangles are T-type events and squares are P-type events. The subevent summation hypothesis predicts that the triangles should be located at the top of the diagram, and the squares should be located at the bottom left of the diagram. Six of eight of the T-type CLVD events have their T axis within 45° of the slab dip axis, and four of these are within 30°. Only three of seven P-type CLVD events have their P axis within 45° of the slab dip axis, and none of these are within 30° (Figure 6-11). Therefore, the majority of T-type CLVD events can be explained by subevent structure in a uniaxial stress field, but P-type CLVD events are likely caused by another manner of 3-D event complexity.

We tested this hypothesis further by searching the Harvard CMT catalog for smaller events within 50 km of the fifteen events in this study with $|\xi| > 0.4$ and made composite focal mechanisms by summing their normalized moment tensors. Only nine had enough nearby events (ten or more) to make this approach reasonable. In general, the position of the principal axes were consistent between the CLVD event and its composite mechanism for the T-type events, but not for the P-type events (see Figure 6-12). In most cases, the composite mechanisms were double-couples, thus the stress-fields at intermediate-focus depths do not appear to be uniformly uniaxial. An

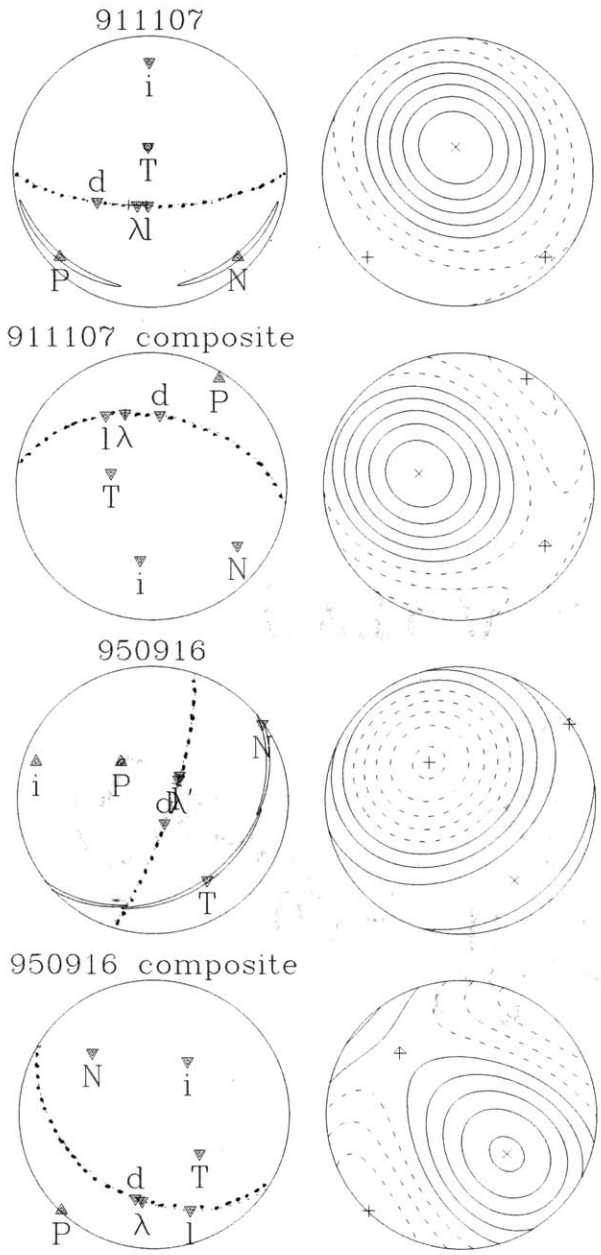

Figure 6-12: T-type CLVD event and its composite mechanism summed from 83 other sources (top two) and P-type CLVD event and its composite mechanism summed from 34 other sources (bottom two). The T-type event and its composite match well, but the P-type and its composite do not, which is typical in this catalog.

exception to this is the 11 July 1991 Banda Sea event shown in Figure 6-12 in which both the actual event and its composite mechanism are T-type CLVDs. This event is best example of successful subevent summation in this catalog. Most P-type CLVD events, including the 16 September 1995 Solomon Islands event in Figure 6-12, occur not in regions of dominant downdip compression, but in regions where there is a mix of tensional and compressional events. Therefore, local peculiarities in the stress field provide better explanation for the cause of P-type CLVD events.

6.4 Conclusions

We have cataloged the properties of large intermediate focus earthquakes at low frequencies to characterize the nature of these sources and enable comparison with other populations of well-studied earthquakes. We find that in general, the vast majority of the intermediate focus earthquakes we studied are well described by ordinary rupture processes and simple source time functions, except for seven events with slow rupture components. We found no frequency-dependence of the moment tensor for all but three events. However, more than half (52%) of the events we studied significantly deviate from the DC model of shear failure on a planar fault. Therefore, there is undoubtedly some manner of complexity in the source of these earthquakes that is not resolved by low-frequency spectral properties. The subevent summation hypothesis can explain six of eight T-type CLVD events with $\xi > 0.4$, but only three of seven P-type CLVD events with $\xi < -0.4$. We therefore infer that there is not one simple explanation that encompasses every CLVD mechanism at intermediate-focus depths. Perhaps each anomalous event is produced by the three-dimensional complexity of rupture induced by local peculiarities of the slab's stress field. In this case, detailed regional studies of smaller events in the areas where most of the anomalous earthquakes in this catalog occur may help characterize the regional stress-field anomalies that produce non-double-couple behavior. This undertaking requires a different methodology than that in this study since the low-frequency techniques

presented here are not useful at $M_0^T < 10^{18}$ N-m.

Acknowledgments. The authors thank Götz Bokelmann and two anonymous reviewers for their thoughtful comments which improved this paper. Discussions with Jeff McGuire and Pierre Ihmlé helped refine our interpretations. This work was sponsored by NSF grant EAR-0049042.

Chapter 7

Summary and Future Research

The goal of studying the nucleation and rupture process of earthquakes is the development of quantitative descriptions that correctly predict the initial onset of instability, the processes that occur during an event and finally, the event's arrest. This problem encompasses a vast range of size and time scales and so is most logically approached in pieces. Laboratory experiments, such as those detailed in Chapter 2, provide much of the data and corroboration of models that predict scaling behavior and nucleation characteristics of earthquakes.

Testing the predictions of models and lab data with seismic observations is a not a simple task. One part of the problem is the assumption that extrapolations over ten or more orders of magnitude in seismic moment are valid. Complexities of rupture and breaks in scaling behavior will not be discerned if only end-member sizes of events are studied. For example, in Chapter 6 we found that large intermediate-focus earthquakes often have anomalous source mechanisms, but that this complexity could not be linked to any observations of anomalous seismic spectra. The key to understanding these events likely lies in studying smaller events and the specific mechanical properties of their nucleation environment. Another problem in seismic source studies is the ability to measure enough independent parameters from seismic data to test specific parts of models. The processing technique we used to reprocess the mining-induced seismicity discussed in Chapter 5 measures three mathematically

independent parameters, so the scaling behaviors of stress drop and apparent stress can be studied separately. The difference in the scaling of apparent stress between the Type-A and Type-B events is an important diagnostic that distinguishes these events.

By focusing on mining-induced seismicity we have been able to study the rupture process of small earthquakes very close to their sources. We have used the relationship between this seismicity and other datasets spanning a large range of sizes to test models of earthquake nucleation via a slip-weakening model and models of rupture growth for mode-III rupture of small and large events. The evidence for the critical smallest shear-rupturing event discussed in Chapter 4 is an important step towards marrying theoretical predictions with seismic observations. Further work is necessary to determine if a single critical slip distance exists throughout the lifetime of a rupture, or whether the average slip in the process zone of an earthquake at any one time grows throughout the rupture process.

Distinguishing between fracture-dominated and friction-controlled events as discussed in Chapter 3 is crucial for understanding different scaling behaviors. In particular, there is limited understanding of the process zones of fracturing events. In addition, we do not know the physical meaning of the observed decrease in apparent stress with seismic moment for fracturing events. How faults interact in the interseismic period is largely unknown. Further experimental work, such as that in Chapter 2, along with precise relocations of mining seismicity and controlled blasting experiments may help elucidate this issue in the mining environment, with the hope of extending the knowledge to the tectonic environment.

The scaling relations for frictional events described in Chapter 5 contain many interesting facets worthy of further study. For example, the scale break we observe at $M \approx 10^{14} - 10^{15}$ Nm is a feature of two independent datasets: apparent stress and ground motion. What is the physical significance of this source size? We developed a model in which an increase in rupture velocity with increasing source dimension simultaneously explains the apparent stress, ground motion, and fracture energy observations as well as providing an explanation for the systematic underestimation of

stress drop for small earthquakes. However, other explanations are possible and must be investigated, including enhanced velocity weakening, shear melting, and normal force fluctuations during rupture.

Appendix A

Source Parameters of Reprocessed Mine Events

In this table, events are listed as yyyymmddhhmmss, seismic moment M_0 is in Nm, corner frequency f_0 is in Hz, energy E is in J, and stress drop $\Delta\sigma$ is in MPa. Event locations X, Y, and Z are in meters. The basis for the coordinate system used at the mines is a modified version of the "LO system", which is commonly used in South Africa [*Webb et al.*, 2001]. In this system, the origin of the X axis (which runs north-south) is 2,900,000 meters south of the equator and is positive to the south; the origin of the Y axis (which runs east-west) is at 29° longitude and is positive to the west [*Webb et al.*, 2001]. The origin, or "datum" of the Z axis is a reference point in Johannesburg, and is about 250 m above ground level and 1800 m above sea level in the Carletonville District. The Z axis is positive down. Also listed in the table is the type of event (A or B) and the mine in which each event is located: E=Elandsrand, M=Mponeng, T=TauTona.

Table A.1: Mine Events

Event	X	Y	Z	M_0	f_0	E	$\Delta\sigma$	Type	Mine
19990103155836	27008	-41932	1748	1.10e+13	12.1	1.24e+08	0.87	B	M
19990118102526	27897	-44467	3422	8.98e+11	27.3	9.41e+06	0.80	B	T
19990118112405	27808	-44437	3443	1.98e+11	36.1	1.07e+06	0.68	B	T

19990118124758	29738	-35292	4741	2.15e+11	44.8	2.41e+06	1.32	B	T
19990118141501	28821	-42790	2614	2.13e+11	10.1	2.72e+04	0.01	B	T
19990118143555	28737	-42079	2386	6.55e+11	20.1	2.02e+06	0.45	B	T
19990118154117	29518	-41278	2568	4.59e+11	9.1	9.28e+04	0.03	B	T
19990118155019	24652	-47071	3111	1.97e+11	67.6	6.89e+06	6.99	B	T
19990118160226	29504	-42164	2733	4.56e+11	53.4	1.83e+07	12.31	B	T
19990118165830	29478	-43180	2956	3.14e+10	54.5	9.18e+04	0.59	B	T
19990118173604	28380	-44246	3614	9.89e+09	205.3	4.88e+05	36.09	B	T
19990118173650	28332	-44227	3696	2.59e+10	54.5	6.26e+04	0.53	B	T
19990118184338	26123	-46026	3538	1.81e+11	27.4	3.88e+05	0.23	B	T
19990118184403	29402	-42274	2682	1.07e+11	38.9	3.90e+05	0.48	B	T
19990118200717	27291	-42114	2039	2.86e+12	15.9	1.89e+07	0.51	B	T
19990118201014	26733	-45280	3159	1.51e+10	128.3	2.77e+05	4.72	B	T
19990118201040	27136	-44409	3106	6.38e+08	310.3	7.02e+03	5.14	A	T
19990118201312	28872	-42844	2587	1.97e+10	67.2	6.77e+04	1.23	B	T
19990118202651	28861	-41427	3456	6.85e+09	94.3	2.27e+04	0.77	B	T
19990118205250	27296	-44466	3177	3.87e+08	345.5	3.56e+03	4.68	A	T
19990118213352	26663	-42755	2879	9.07e+12	15.0	1.62e+08	1.00	B	T
19990118213444	26657	-42805	2903	6.88e+10	87.7	1.84e+06	4.01	B	T
19990118213537	28511	-43640	2720	3.95e+08	285.4	2.09e+03	2.96	A	T
19990118213539	28561	-43690	2766	4.20e+08	262.6	1.85e+03	1.73	A	T
19990118213546	28559	-43688	2793	3.86e+08	360.6	4.04e+03	9.53	A	T
19990118213558	28579	-43692	2749	3.81e+08	305.7	2.39e+03	2.50	A	T
19990118213626	28678	-43822	2597	3.37e+08	298.7	1.75e+03	2.07	A	T
19990118213629	28571	-43730	2710	2.68e+08	265.1	7.75e+02	0.88	A	T
19990118213639	28614	-43729	2724	3.54e+08	309.5	2.15e+03	2.45	A	T
19990118213642	28590	-43704	2755	3.62e+08	325.9	2.62e+03	2.70	A	T
19990118220023	27070	-44388	3092	3.37e+08	313.9	2.02e+03	2.67	A	T
19990118220950	27011	-44363	3035	2.22e+09	61.5	6.62e+02	0.05	B	T
19990118225211	27062	-44392	3115	2.27e+08	344.1	1.21e+03	2.77	A	T
19990201130324	25662	-38840	2439	4.68e+08	237.9	1.70e+03	1.57	A	E
19990201130804	26225	-38748	2631	4.35e+08	247.2	1.65e+03	2.00	A	E

19990201130838	26208	-38721	2580	7.28e+08	260.8	5.43e+03	3.62	A	E
19990201131918	27906	-35634	3056	5.19e+08	241.9	2.20e+03	1.05	A	E
19990201131919	27908	-35652	3050	6.34e+08	222.3	2.54e+03	1.40	A	E
19990201131928	27904	-35651	3048	7.13e+08	261.5	5.24e+03	2.08	A	E
19990201131944	27914	-35659	3044	6.13e+08	260.3	3.83e+03	1.53	A	E
19990201131948	27910	-35660	3025	7.07e+08	249.1	4.46e+03	1.47	A	E
19990201131953	27905	-35658	3036	6.86e+08	224.1	3.06e+03	1.10	A	E
19990201132009	27917	-35646	3054	1.10e+09	237.5	9.40e+03	2.06	A	E
19990201132014	27904	-35647	3045	9.73e+08	240.3	7.59e+03	2.42	A	E
19990201132019	27921	-35655	3048	4.02e+08	290.7	2.29e+03	1.75	A	E
19990201132028	27912	-35654	3046	6.67e+08	242.8	3.68e+03	1.66	A	E
19990201132049	27922	-35650	3035	3.75e+08	283.9	1.86e+03	1.38	A	E
19990201132105	27908	-35650	3042	6.81e+08	246.6	4.02e+03	1.81	A	E
19990201132144	26761	-37946	2306	8.34e+09	70.6	1.41e+04	0.54	B	E
19990201132724	28671	-34106	3017	1.51e+08	295.7	3.42e+02	0.93	B	E
19990201132948	26412	-35875	2018	4.37e+08	218.5	1.15e+03	0.67	B	E
19990201192239	30112	-43219	3211	1.73e+11	31.5	5.38e+05	0.49	B	M
19990201194832	28193	-40623	3137	4.83e+12	13.6	3.37e+07	0.53	B	M
19990202121231	31197	-42405	3341	2.79e+08	253.2	3.92e+02	0.39	A	M
19990202121236	31192	-42389	3358	2.58e+08	220.7	3.71e+02	0.47	A	M
19990202121251	31277	-42415	3275	3.48e+08	218.7	3.05e+02	0.30	A	M
19990202121257	31211	-42375	3357	5.19e+08	252.4	4.72e+02	0.19	A	M
19990202121303	31192	-42303	3425	8.55e+08	256.1	1.26e+03	0.44	A	M
19990202121308	31285	-42437	3203	3.16e+08	234.5	4.43e+02	0.31	A	M
19990202121319	31202	-42384	3350	2.24e+08	303.2	7.65e+02	1.59	A	M
19990202121333	31216	-42411	3308	4.72e+08	223.3	8.08e+02	0.62	A	M
19990202121339	31285	-42435	3217	2.99e+08	243.5	8.69e+02	0.83	A	M
19990202121343	31305	-42457	3157	2.65e+08	337.4	1.04e+03	1.41	A	M
19990202121352	31256	-42436	3201	3.69e+08	162.4	8.46e+02	0.54	A	M
19990202121404	31220	-42411	3260	4.81e+08	205.2	5.81e+02	0.42	A	M
19990202121408	31267	-42430	3213	4.51e+08	237.8	1.30e+03	1.62	A	M
19990202121425	31209	-42395	3335	4.54e+08	284.1	1.04e+03	1.02	A	M

19990202121437	31279	-42444	3210	4.65e+08	253.6	4.60e+02	0.29	A	M
19990202121438	31294	-42459	3160	4.85e+08	235.7	8.42e+02	0.59	A	M
19990202121442	31201	-42373	3294	2.96e+08	300.1	1.26e+03	1.50	A	M
19990202122323	29638	-41345	2628	2.51e+09	72.7	1.22e+03	0.09	B	M
19990202122337	29607	-43456	2685	1.97e+08	249.5	4.94e+02	0.95	A	M
19990202122356	29382	-43455	3017	4.21e+08	234.2	1.35e+03	1.16	A	M
19990202122405	29399	-43446	3004	5.59e+08	270.1	4.33e+03	2.73	A	M
19990202122415	29431	-43505	2959	4.06e+08	276.8	3.05e+03	2.89	A	M
19990202122416	29381	-43449	3002	4.08e+08	213.9	1.43e+03	0.84	A	M
19990202122431	29385	-43317	3144	4.74e+08	246.4	3.15e+03	3.04	A	M
19990202122449	29405	-43474	2977	3.12e+08	235.6	1.46e+03	1.65	A	M
19990202122451	29372	-43424	3008	6.66e+08	269.0	1.73e+03	0.90	A	M
19990202122602	30757	-42469	3034	6.93e+08	186.9	1.28e+03	0.36	A	M
19990202122629	30685	-42486	3076	3.24e+08	234.5	9.59e+02	0.82	A	M
19990202122737	30581	-42364	3196	3.99e+08	217.7	9.49e+02	0.66	A	M
19990202122749	30605	-42442	3184	8.50e+08	231.0	3.29e+03	0.93	A	M
19990202122751	30618	-42483	3067	3.74e+08	234.7	5.38e+02	0.42	A	M
19990202122818	30691	-42610	3012	5.22e+08	239.0	1.72e+03	0.95	A	M
19990202122821	30696	-42432	3152	4.75e+08	235.4	1.21e+03	0.72	A	M
19990202122822	30761	-42419	3103	7.92e+08	211.0	2.86e+03	1.04	A	M
19990202122831	30692	-42445	3111	7.02e+08	212.1	3.95e+03	2.24	A	M
19990202122838	30600	-42407	3257	4.74e+08	210.8	2.67e+03	1.77	A	M
19990202122840	30665	-42465	3115	6.22e+08	227.9	4.59e+03	2.48	A	M
19990202122846	30696	-42468	3055	5.96e+08	232.2	2.89e+03	1.31	A	M
19990202122850	30719	-42382	3246	6.01e+08	205.2	3.27e+03	2.0436	A	M
19990202122855	30639	-42456	3125	6.77e+08	212.6	4.76e+03	2.4061	A	M
19990202122900	30640	-42486	3100	4.16e+08	183.0	1.35e+03	0.86	A	M
19990202122905	30743	-42454	3039	6.33e+08	176.8	3.43e+03	1.89	A	M
19990202122908	30659	-42464	3110	4.34e+08	254.8	2.13e+03	1.51	A	M
19990202122909	30451	-42394	3443	1.20e+09	179.8	1.15e+04	4.08	A	M
19990202122915	30745	-42459	3034	9.46e+08	221.7	4.61e+03	1.26	A	M
19990202122920	30604	-42417	3231	6.73e+08	218.9	3.95e+03	1.44	A	M

19990202122923	30686	-42394	3236	9.72e+08	212.5	7.47e+03	2.46	A	M
19990202122929	30675	-42433	3150	6.94e+08	211.7	2.87e+03	1.25	A	M
19990202122941	30656	-42435	3152	6.90e+08	196.6	3.23e+03	1.31	A	M
19990202122944	30577	-42431	3227	7.85e+08	174.5	4.19e+03	1.37	A	M
19990202122945	30668	-42470	3107	8.16e+08	198.4	4.89e+03	2.00	A	M
19990202122953	30581	-42400	3257	7.46e+08	184.3	3.21e+03	1.50	A	M
19990202122956	30624	-42503	3098	9.67e+08	185.4	8.82e+03	3.45	A	M
19990202122957	30691	-42409	3167	8.27e+08	157.1	2.27e+03	0.80	A	M
19990202123002	30677	-42439	3130	5.45e+08	173.2	1.22e+03	0.51	A	M
19990202123012	30596	-42499	3074	4.46e+08	156.0	6.45e+02	0.34	A	M
19990202123021	29502	-41414	2582	1.17e+13	13.6	3.20e+08	2.97	B	M
19990202123040	29311	-41570	2589	3.84e+11	24.6	9.77e+05	0.29	B	M
19990202123139	30712	-42474	3014	1.17e+09	301.3	6.64e+03	1.98	A	M
19990202123322	29330	-41539	2582	2.60e+09	110.1	7.40e+03	0.58	B	M
19990202123416	29460	-41437	2368	9.05e+08	122.1	1.94e+03	0.48	B	M
19990202123439	29383	-41435	2516	7.10e+08	132.6	5.15e+02	0.16	B	M
19990202123441	29345	-41505	2464	2.19e+09	121.6	7.15e+03	0.69	B	M
19990202123449	29316	-41542	2566	1.11e+09	119.6	2.50e+03	0.53	B	M
19990202123513	29402	-41417	2365	6.96e+09	55.5	1.35e+03	0.02	B	M
19990202123608	29371	-41506	2553	1.93e+09	146.8	6.03e+03	0.64	B	M
19990202123610	29301	-41549	2541	1.59e+09	154.5	5.30e+03	1.01	B	M
19990202123647	29362	-41503	2556	8.39e+08	102.5	6.62e+02	0.23	B	M
19990202123802	29361	-41483	2564	1.08e+09	103.2	1.30e+03	0.32	B	M
19990202123856	29299	-41558	2493	4.54e+09	51.8	1.46e+03	0.05	B	M
19990202123929	29349	-41451	2409	4.09e+09	113.2	1.68e+04	1.06	B	M
19990202123932	29347	-41524	2537	6.87e+09	46.1	1.27e+04	0.34	B	M
19990202123949	28937	-41591	3180	2.36e+10	21.3	1.14e+04	0.08	B	M
19990202123959	28971	-42652	3554	4.93e+08	198.7	2.55e+03	1.71	A	M
19990202124005	29393	-41419	2564	1.17e+09	87.6	1.21e+03	0.26	B	M
19990202124011	28991	-42607	3534	4.69e+08	233.4	1.33e+03	0.77	A	M
19990202124012	29069	-42698	3540	3.35e+08	246.2	2.25e+03	2.07	A	M
19990202124013	29085	-41552	2498	1.23e+09	67.4	7.94e+02	0.18	B	M

19990202124020	29025	-42646	3538	8.32e+08	197.1	4.62e+02	0.12	A	M
19990202124021	28893	-42520	3546	3.25e+08	223.9	1.05e+03	0.82	A	M
19990202124027	28935	-42607	3556	4.73e+08	162.9	1.15e+03	0.65	A	M
19990202124028	28960	-42522	3544	3.94e+08	233.1	3.46e+03	2.89	A	M
19990202124033	29049	-42682	3495	5.50e+08	153.0	6.55e+02	0.33	A	M
19990202124037	29026	-42657	3547	4.70e+08	239.1	1.54e+03	0.88	A	M
19990202124053	29008	-42576	3525	3.95e+08	153.9	5.13e+02	0.43	A	M
19990202124233	29364	-41468	2545	1.32e+09	124.8	3.42e+03	0.77	B	M
19990202124413	29526	-41371	2537	1.10e+10	36.6	1.86e+03	0.02	B	M
19990202124516	29407	-41392	2590	4.80e+09	41.6	7.65e+03	0.33	B	M
19990202124632	29416	-41410	2578	4.40e+08	125.7	4.41e+02	0.49	B	M
19990202124649	29371	-41494	2424	8.16e+08	107.2	5.97e+02	0.20	B	M
19990202124704	29309	-41560	2514	2.35e+09	78.0	1.98e+03	0.14	B	M
19990202124712	29378	-41473	2454	2.80e+09	111.2	1.03e+04	0.84	B	M
19990202124718	29332	-41477	2430	1.62e+09	151.3	4.31e+03	0.58	B	M
19990202124929	30030	-41770	2806	4.71e+08	206.6	1.11e+03	0.54	B	M
19990202124934	29072	-41638	2479	1.87e+10	51.2	2.41e+04	0.18	B	M
19990202124950	29725	-42852	2394	3.66e+08	245.8	6.86e+02	0.51	A	M
19990202125001	29708	-42859	2368	4.86e+08	268.6	1.80e+03	1.52	A	M
19990202125056	29745	-42875	2356	1.90e+08	176.0	2.16e+02	0.34	A	M
19990202125102	29772	-42895	2362	1.72e+08	270.6	2.86e+02	0.42	A	M
19990202125111	29707	-42839	2469	4.11e+08	240.2	7.06e+02	0.60	A	M
19990202125117	29706	-42842	2463	4.24e+08	233.7	1.79e+03	2.04	A	M
19990202125118	29745	-42952	2377	3.34e+08	191.4	1.12e+03	1.59	A	M
19990202125135	29779	-42908	2315	2.83e+08	200.0	1.07e+03	1.05	A	M
19990202125146	29718	-42839	2456	2.56e+08	243.2	1.18e+03	1.57	A	M
19990202125155	29754	-42883	2365	3.40e+08	181.5	6.87e+02	0.76	A	M
19990202125357	29325	-41568	2545	5.61e+09	75.9	2.26e+03	0.06	B	M
19990202125852	29346	-41536	2552	1.26e+09	118.3	1.21e+03	0.23	B	M
19990203221201	27858	-36264	2638	1.43e+12	23.4	1.50e+07	1.98	B	E
19990204214044	25101	-38397	3210	2.23e+11	35.1	1.24e+06	0.60	B	E
19990205025535	27589	-41668	2991	4.27e+12	17.6	5.78e+07	1.37	B	M

19990205144857	24324	-37161	2887	2.30e+11	22.3	3.35e+05	0.11	B	E
19990205161819	29570	-33084	2515	2.82e+11	15.2	1.61e+05	0.37	B	E
19990205175933	27867	-36260	2686	3.14e+11	44.3	4.96e+06	3.07	B	E
19990205205457	27924	-36087	2558	2.89e+12	18.5	3.05e+07	0.96	B	E
19990207144834	29374	-33041	2607	1.06e+10	53.1	9.74e+03	0.47	B	E
19990208174155	29272	-33213	2544	2.93e+10	114.4	7.40e+05	10.30	B	E
19990209154922	29538	-33006	2738	6.62e+11	10.7	3.05e+05	0.19	B	E
19990211134724	28372	-33764	2226	7.36e+10	23.2	3.88e+04	0.11	B	E
19990213192055	28454	-34289	2713	7.31e+11	14.7	9.72e+05	0.08	B	E
19990215172644	28397	-34479	2503	7.21e+11	26.7	5.69e+06	0.92	B	E
19990216053511	28854	-43046	3761	1.19e+13	10.4	9.22e+07	0.56	B	M
19990224143824	28275	-36179	2700	5.04e+11	33.9	5.69e+06	3.26	B	E
19990224194309	25155	-38573	2206	9.63e+11	39.8	3.37e+07	11.60	B	E
19990225171021	24684	-38107	3100	5.27e+11	27.7	3.39e+06	0.96	B	E
19990226140059	26316	-37730	2596	1.03e+10	117.6	9.92e+04	2.85	B	E
19990226140848	28290	-36129	2752	5.05e+10	41.3	1.04e+05	0.42	B	E
19990226140853	28275	-36118	2835	2.66e+09	122.2	7.42e+03	0.55	A	E
19990226140959	27222	-37471	2757	7.78e+08	141.2	9.83e+02	0.34	B	E
19990226141106	27208	-37482	2699	9.51e+08	137.1	1.34e+03	0.36	A	E
19990226141246	27212	-37450	2785	5.87e+08	181.6	1.19e+03	0.48	A	E
19990226141303	27210	-37397	2804	5.69e+08	192.3	1.33e+03	0.49	A	E
19990226141323	27218	-37487	2630	7.22e+08	174.8	1.61e+03	0.56	A	E
19990226141339	27229	-37537	2705	8.75e+08	147.6	1.42e+03	0.45	A	E
19990226141416	27218	-37489	2607	5.87e+08	170.5	9.85e+02	0.48	B	E
19990226141507	27222	-37492	2633	7.30e+08	135.1	7.60e+02	0.36	A	E
19990226141516	27221	-37514	2636	6.04e+08	164.0	9.29e+02	0.44	A	E
19990226141553	27208	-37515	2606	7.80e+08	136.1	8.84e+02	0.36	B	E
19990226141701	28276	-36152	2766	1.18e+09	82.0	4.44e+02	0.13	B	E
19990226142733	29215	-33163	3253	5.76e+09	120.8	3.37e+04	2.05	B	E
19990226143150	25355	-38607	1981	4.53e+12	12.3	2.20e+07	0.53	B	E
19990226143247	25163	-38547	1784	1.67e+11	35.2	7.01e+05	0.88	B	E
19990226143421	25111	-38368	2070	9.19e+09	69.5	1.63e+04	0.29	B	E

19990226143641	29419	-35110	1918	6.18e+09	69.4	7.36e+03	0.36	B	E
19990226145447	25145	-38509	2105	3.71e+09	84.6	4.81e+03	0.27	B	E
19990226145456	28235	-36150	2712	2.11e+10	70.1	8.87e+04	0.69	B	E
19990226145926	28429	-36040	2750	8.35e+09	65.7	1.14e+04	0.28	B	E
19990226151012	28800	-35627	3040	5.34e+08	123.4	3.09e+03	0.14	B	E
19990226151016	28653	-35598	2420	6.98e+08	102.3	3.01e+02	0.11	B	E
19990226152215	25108	-38535	2129	2.85e+09	81.2	2.51e+03	0.28	B	E
19990226154327	24927	-39597	2144	3.93e+10	73.5	3.53e+05	2.02	B	E
19990226155650	25158	-41180	2545	8.97e+10	36.2	2.19e+05	0.45	B	E
19990703110423	28186	-44423	3405	3.71e+08	409.1	5.43e+03	5.96	A	T
19990703110429	28199	-44436	3417	2.91e+08	388.6	2.86e+03	4.40	A	T
19990703110446	28249	-44502	3419	2.57e+08	340.9	1.51e+03	2.56	A	T
19990703110457	28206	-44433	3416	2.38e+08	353.3	1.44e+03	2.63	A	T
19990703110512	28225	-44455	3419	2.28e+08	370.2	1.52e+03	2.48	A	T
19990703110513	28195	-44410	3465	3.10e+08	338.8	2.15e+03	2.57	A	T
19990703110516	28211	-44484	3521	1.03e+09	323.1	2.05e+04	6.17	A	T
19990703110538	28240	-44491	3419	2.87e+08	368.2	2.38e+03	3.26	A	T
19990703110544	28192	-44427	3442	3.47e+08	347.4	2.91e+03	3.55	A	T
19990703110547	28240	-44491	3419	1.33e+09	350.8	4.43e+04	14.80	A	T
19990703110554	28202	-44393	3412	4.72e+08	429.8	1.02e+04	8.77	A	T
19990703110556	28221	-44449	3411	4.12e+08	358.4	4.50.2763	4.51	A	T
19990703111216	23677	-49579	3099	2.24e+13	18.5	1.83e+09	10.62	B	T
19990703112456	28657	-44003	2652	3.47e+08	227.0	8.13e+02	0.83	B	T
19990703112625	28566	-43906	2714	3.01e+08	237.2	6.96e+02	0.95	A	T
19990703112627	28554	-43904	2767	2.12e+08	188.1	1.73e+02	0.24	A	T
19990703112639	28579	-43922	2725	1.50e+08	271.8	2.60e+02	0.56	A	T
19990703112643	28575	-43918	2712	4.33e+08	217.5	1.11e+03	1.24	A	T
19990703112701	28619	-43956	2713	3.78e+08	185.3	5.24e+02	0.44	A	T
19990703112733	28651	-43960	2703	2.89e+08	222.9	5.33e+02	0.75	B	T
19990703113105	28472	-43600	2687	3.36e+08	244.0	9.43e+02	0.84	A	T
19990703113117	28497	-43641	2647	8.66e+08	185.4	2.77e+03	0.97	A	T
19990703113120	28472	-43634	2706	3.97e+08	253.9	1.49e+03	1.06	A	T

19990703113124	28387	-43590	2734	2.83e+08	258.1	7.96e+02	0.79	A	T

Appendix B

Source Parameters of Intermediate-Focus Earthquakes

In the following table, event date is listed as yyyymmdd, and the values of latitude, longitude, and depth have been obtained from the Harvard CMT catalog. M_T^0 is the total scalar seismic moment, Δt_1 is the centroid time shift of the source, and τ_c is the characteristic duration of the source. M_T^0, Δt_1, and τ_c have all been determined by the spectral processing technique outlined in Chapter 6.

Table B.1: Spectral Quantities

Date	Lat(°N)	Lon(°E)	Depth(km)	M_T^0(Nm)	Δt_1(s)	τ_c(s)
19890311	-17.78	-174.77	244	2.66±0.08e+19	15.1±1.7	18.9±3.0
19890406	-19.48	168.94	165	2.94±0.01e+19	8.9±0.7	27.8±2.7
19890427	30.48	140.41	78	2.13±0.20e+18	5.7±0.6	28.1±6.2
19890722	2.39	127.94	145	4.67±0.45e+18	3.4±0.8	18.8±8.9
19890925	-20.52	169.00	54	7.15±0.36e+18	8.0±1.0	13.2±7.7
19891129	-15.68	-73.31	66	4.28±0.28e+18	9.1±1.6	15.3±10.0
19891203	-7.37	-74.27	151	8.36±0.68e+18	12.6±2.3	29.7±5.0
19891209	0.00	123.69	145	1.12±0.06e+19	10.5±1.7	30.3±3.1

19891223	17.26	145.73	186	3.67±0.74e+18	5.2±0.5	20.2±17.2
19900109	24.42	94.95	130	2.76±0.19e+18	1.6±1.3	4.3±26.8
19900205	36.56	70.84	114	1.53±0.19e+18	0.0±0.8	5.8±12.3
19900315	-15.17	167.22	121	5.84±0.30e+18	9.3±1.3	10.3±11.9
19900321	-30.71	-179.38	157	1.12±0.08e+19	11.2±1.6	22.1±5.6
19900501	58.83	-157.05	224	6.97±0.51e+18	6.2±0.7	0.6±8.5
19900502	-5.74	150.12	96	4.07±0.47e+18	4.8±0.6	9.2±21.2
19900530	45.92	26.81	74	3.53±0.18e+19	8.1±1.9	21.9±5.4
19900531	45.67	26.00	87	3.07±0.16e+18	0.0±1.6	27.2±3.9
19900623	-21.29	-176.22	195	1.94±0.05e+19	5.8±0.4	6.2±8.8
19900713	36.68	70.61	217	3.63±0.23e+18	6.7±1.9	5.2±7.8
19900727	-15.50	167.26	129	9.85±0.36e+19	7.6±0.9	22.6±4.4
19900812	-19.58	169.05	165	3.82±0.14e+19	13.0±1.7	25.8±2.9
19900928	-13.47	166.84	185	1.10±0.06e+19	7.4±0.7	17.9±21.8
19901230	-5.23	150.73	188	1.88±0.07e+20	13.2±1.5	27.4±3.3
19910123	52.13	179.02	102	6.47±0.57e+18	3.1±0.8	18.5±8.5
19910131	36.01	70.23	126	2.25±0.07e+19	8.2±1.9	19.9±3.2
19910501	62.47	-151.42	118	2.07±0.19e+18	5.8±1.5	5.3±5.6
19910517	-3.95	142.87	75	3.99±0.41e+18	6.1±0.7	18.0±12.2
19910524	-16.69	-70.68	127	3.60±0.15e+19	2.8±0.8	35.4±2.5
19910609	-20.15	-175.9	292	3.06±0.09e+19	3.1±0.6	5.4±7.3
19910706	-13.41	-71.88	85	2.44±0.79e+19	11.8±1.9	37.4±4.4
19910714	36.12	70.74	228	1.16±0.05e+19	0.1±1.0	20.6±4.1
19910815	-15.89	167.95	189	2.44±0.11e+18	4.7±0.6	14.6±3.9
19911015	-6.22	129.78	157	1.66±0.10e+18	8.4±0.9	4.8±5.0
19911107	-7.07	128.62	157	2.23±0.13e+18	11.8±1.8	25.8±3.8
19920302	52.85	160.36	50	2.16±0.12e+19	9.5±1.2	17.2±5.6
19920305	52.88	160.17	52	3.16±0.28e+18	8.0±1.6	12.8±5.6
19920307	10.23	-84.09	73	6.32±0.37e+18	4.0±0.5	20.8±6.0
19920713	-3.88	-76.72	115	2.73±0.24e+18	4.4±0.5	4.6±30.3

19920816	-5.39	146.87	249	2.33±0.31e+18	4.0±0.6	7.1±28.5
19921011	-19.17	168.83	141	1.65±0.05e+20	11.3±1.8	29.7±2.5
19921015	-14.44	166.72	52	2.29±0.09e+19	9.1±0.8	19.9±3.6
19921220	-6.60	130.52	70	1.02±0.03e+20	19.1±2.1	23.9±3.6
19930110	-59.42	-25.78	61	1.45±0.06e+19	5.8±1.4	36.9±2.4
19930115	43.06	144.29	100	3.20±0.09e+20	7.4±0.9	39.4±1.5
19930320	-56.11	-27.70	128	4.47±0.34e+18	4.9±1.1	21.4±6.4
19930518	19.97	122.65	188	1.32±0.05e+19	5.9±1.8	29.9±2.7
19930524	-23.45	-66.88	232	3.47±0.12e+19	3.2±0.8	6.4±10.6
19930608	-31.62	-69.13	125	5.56±0.15e+18	0.7±1.3	41.2±1.9
19930807	26.68	125.84	165	4.03±0.32e+18	3.5±0.8	37.8±3.4
19930808	13.06	145.31	59	6.10±0.22e+20	20.7±2.0	35.5±2.1
19930904	-9.42	122.39	63	3.28±0.12e+18	5.4±0.4	30.2±4.7
19930906	-4.78	153.13	59	1.24±0.05e+19	4.0±0.6	28.0±3.2
19930929	0.62	121.70	89	4.17±0.17e+18	5.0±1.2	31.9±2.6
19931113	52.00	159.27	54	3.78±0.15e+19	9.9±1.1	21.6±3.4
19940211	-18.89	169.08	223	2.39±0.11e+19	4.6±0.6	29.1±3.1
19940314	15.98	-92.64	168	3.12±0.11e+19	6.1±2.1	47.1±1.7
19940418	-6.61	154.92	52	1.38±0.04e+19	5.1±0.7	13.0±4.3
19940630	36.34	71.00	233	2.99±0.13e+18	2.0±0.5	3.4±10.8
19940713	-7.63	127.90	179	6.14±0.54e+18	3.1±1.0	30.7±4.5
19941004	43.6	147.63	68	3.32±0.11e+21	24.2±1.9	40.2±2.2
19941016	45.78	149.32	121	1.62±0.06e+19	0.0±1.1	46.7±2.0
19941210	18.18	-101.39	54	4.63±0.28e+18	5.6±1.1	19.7±5.3
19941227	-31.84	179.82	226	4.73±0.35e+18	3.6±0.8	23.3±5.6
19941230	18.66	145.59	228	3.03±0.25e+18	5.3±1.5	27.0±6.0
19950208	4.09	-76.36	68	4.03±0.30e+18	6.3±0.8	32.1±4.3
19950407	-15.37	-173.15	88	1.19±0.04e+20	11.0±1.6	9.9±7.3
19950420	6.33	126.89	103	4.77±0.15e+18	4.9±1.5	14.0±5.9
19950502	-3.77	-77.07	113	1.30±0.05e+19	6.2±1.4	39.0±1.7

19950506	24.83	95.02	122	5.01±0.35e+18	8.2±1.7	42.9±2.3
19950629	-19.42	168.95	143	9.73±0.44e+18	5.1±0.7	29.0±2.8
19950726	2.78	127.47	52	2.77±0.28e+18	6.2±2.0	23.2±7.3
19950728	-21.18	-174.90	125	4.46±0.25e+18	2.2±0.9	28.4±2.2
19950814	-4.90	151.80	140	1.48±0.04e+19	3.8±0.7	31.6±2.0
19950916	-6.18	155.50	156	1.44±0.06e+18	4.1±1.0	27.0±2.8
19950923	-10.62	-78.47	73	7.40±0.39e+18	1.5±1.0	36.0±3.2
19951021	16.67	-93.42	164	7.91±0.21e+19	9.2±1.4	34.0±1.7
19951219	-3.42	140.26	67	8.71±0.24e+18	5.2±1.7	41.9±1.6
19951225	-6.93	129.65	161	5.45±0.16e+19	9.8±1.4	36.0±2.2
19960222	45.29	148.56	130	4.38±0.23e+18	1.8±1.0	61.5±1.0
19960228	1.73	126.10	92	6.17±0.29e+18	0.2±1.0	47.7±2.3
19960416	-24.06	-177.04	116	7.89±0.26e+19	7.2±0.7	37.9±2.5
19960419	-23.95	-70.58	50	7.83±0.43e+18	5.6±1.4	32.2±2.4
19960429	-6.65	155.07	54	7.89±0.20e+19	7.0±0.5	15.4±3.4
19960609	17.50	145.74	160	7.01±0.38e+18	4.8±1.2	36.3±3.6
19960610	-13.54	166.99	197	1.32±0.03e+19	6.2±0.8	25.0±2.8
19960805	-15.27	-172.76	54	1.15±0.05e+19	7.2±0.9	14.2±6.0
19960914	-10.84	165.94	65	5.16±0.19e+18	6.4±1.1	12.4±1.4
19960928	10.19	125.33	238	2.76±0.42e+18	1.6±0.5	52.8±2.6
19961222	43.19	138.94	227	6.84±0.33e+18	6.1±1.0	30.3±3.1
19961231	15.67	-93.03	95	4.12±0.22e+18	10.7±2.6	46.9±2.4
19970123	-22.10	-65.74	276	5.99±0.13e+19	16.0±1.6	21.0±2.0
19970405	-6.57	147.67	53	6.37±0.25e+18	4.5±0.5	30.9±2.1
19970421	-13.21	166.20	51	4.90±0.17e+20	36.3±3.2	23.6±2.6
19970423	14.23	144.58	99	7.97±0.46e+18	2.6±1.1	42.7±2.9
19970503	-31.79	-178.95	117	3.08±0.08e+19	2.6±1.0	44.7±2.5
19970513	36.53	71.00	186	5.43±0.31e+18	5.0±0.5	23.5±4.5
19970521	-20.44	169.11	68	1.55±0.06e+19	4.3±0.9	27.5±3.5
19970522	18.41	-101.52	53	6.40±0.11e+18	1.0±0.0	26.9±2.6

19970902	4.00	-75.56	213	2.35±0.10e+19	3.0±0.9	23.0±4.2
19971005	-59.89	-29.18	287	4.24±0.18e+18	0.0±1.0	23.8±3.5
19971006	9.75	126.04	114	5.18±0.35e+18	2.5±1.0	25.8± 5.3
19971014	-21.99	-176.08	179	4.53±0.10e+20	10.9±1.3	21.7±2.5
19971015	-30.94	-71.43	74	5.29±0.20e+19	14.4±2.5	36.1±2.3
19971028	-4.32	-76.63	125	9.08±0.34e+19	8.7±1.2	43.8±1.7
19971109	13.91	-89.20	180	4.08±0.19e+18	3.3±0.7	28.3±2.9
19971115	-14.92	167.26	122	5.12±0.12e+19	8.4±1.3	29.4±2.0
19971211	4.15	-75.84	190	4.32±0.28e+18	0.5±0.5	22.0±6.1
19971222	-5.68	148.07	189	5.76±0.34e+19	4.4±0.5	43.4±2.1

In this table, event date is give as yyyymmdd, and ξ is our measure of deviation from a pure double-couple mechanism. $\hat{s}\angle T$, $\hat{s}\angle N$, and $\hat{s}\angle P$ are the angles between the slab axis and the tension, neutral, and compression axes of the focal mechanism, respectively. T, P, and N are determined from the 10-band average of the moment tensor determined in this study, and $\hat{s}$ is determined from the reference listed in the table.

Table B.2: Mechanism Quantities

Date	ξ	$\hat{s}\angle T$	$\hat{s}\angle N$	$\hat{s}\angle P$	Reference
19890311	0.08±0.10	20	76	76	*Fischer and Jordan* [1991]
19890406	-0.03±0.12	15	80	79	*Pascal et al.* [1978]
19890427	0.01±0.16	82	57	34	*Zhou* [1990]
19890722	-0.42±0.25	65	36	66	*Hatherton and Dickinson* [1969]
19890925	-0.12±0.02	47	86	44	*Pascal et al.* [1978]
19891129	-0.21±0.17	72	53	42	*Cahill and Isacks* [1992]
19891203	0.20±0.12	39	71	57	*James and Snoke* [1994]
19891209	0.15±0.09	-	-	-	no data
19891223	-0.01±0.04	58	32	84	*Zhou* [1990]
19900109	0.43±0.12	38	54	80	*Kumar and Rao* [1995]
19900205	0.33±0.20	42	72	53	*Chatelain et al.* [1980]
19900315	-0.05±0.07	23	68	86	*Prévot et al.* [1994]
19900321	-0.28±0.09	30	65	75	*Zhou* [1990]
19900501	-0.41±0.05	64	66	37	*Ratchkovsky et al.* [1997]
19900502	0.06±0.09	81	51	40	*McGuire and Wiens* [1995]
19900530	0.01±0.03	30	85	61	*Kiratzi* [1993]
19900531	0.01±0.20	30	86	60	*Kiratzi* [1993]
19900623	-0.01±0.06	79	82	14	*Fischer and Jordan* [1991]
19900713	0.64±0.05	35	66	67	*Chatelain et al.* [1980]
19900727	-0.24±0.03	36	56	79	*Prévot et al.* [1994]
19900812	-0.11±0.04	10	88	80	*Pascal et al.* [1978]

19900928	-0.10±0.02	10	89	80	*Pascal et al.* [1978]
19901230	-0.35±0.02	44	51	73	*McGuire and Wiens* [1995]
19910123	0.24±0.01	63	77	30	*Davies and House* [1979]
19910131	0.20±0.05	5	87	86	*Chatelain et al.* [1980]
19910501	-0.23±0.07	26	64	84	*Ratchkovsky et al.* [1997]
19910517	0.06±0.02	70	74	26	*Pegler et al.* [1995]
19910524	0.06±0.06	15	87	75	*Cahill and Isacks* [1992]
19910609	0.07±0.02	52	71	45	*Fischer and Jordan* [1991]
19910706	0.46±0.06	67	69	32	*Cahill and Isacks* [1992]
19910714	0.13±0.03	15	76	84	*Chatelain et al.* [1980]
19910815	0.19±0.10	57	68	41	*Prévot et al.* [1994]
19911015	0.31±0.05	8	82	89	*Cardwell and Isacks* [1978]
19911107	0.45±0.17	8	82	90	*Cardwell and Isacks* [1978]
19920302	0.09±0.01	57	83	34	*Kao and Chen* [1994]
19920305	0.03±0.03	60	78	33	*Kao and Chen* [1994]
19920307	0.19±0.03	31	80	61	*Protti et al.* [1995]
19920713	-0.21±0.13	50	43	77	*Barazangi and Isacks* [1976]
19920816	-0.02±0.05	33	59	80	*Pegler et al.* [1995]
19921011	0.06±0.02	37	53	86	*Pascal et al.* [1978]
19921015	0.14±0.01	49	85	42	*Pascal et al.* [1978]
19921220	-0.19±0.01	11	79	89	*Cardwell and Isacks* [1978]
19930110	-0.21±0.03	79	12	84	*Forsyth* [1975]
19930115	0.15±0.03	17	75	83	*Kosuga et al.* [1996]
19930320	-0.10±0.06	47	81	44	*Forsyth* [1975]
19930518	-0.11±0.03	-	-	-	no data
19930524	0.12±0.02	10	89	80	*Araujo and Suárez* [1994]
19930608	0.27±0.28	56	37	78	*Araujo and Suárez* [1994]
19930807	-0.33±0.05	87	87	4	*Kao and Chen* [1991]
19930808	0.40±0.02	28	72	69	*Chiu et al.* [1991]
19930904	0.43±0.05	14	80	80	*Cardwell and Isacks* [1978]

19930906	-0.15±0.02	68	78	25	*Pascal* [1979]
19930929	0.05±0.11	-	-	-	no data
19931113	-0.02±0.01	61	88	29	*Kao and Chen* [1994]
19940211	0.10±0.02	17	73	88	*Pascal et al.* [1978]
19940314	0.25±0.01	27	67	77	*Ponce et al.* [1992]
19940418	-0.12±0.01	46	83	45	*Pascal* [1979]
19940630	0.43±0.03	5	85	89	*Chatelain et al.* [1980]
19940713	0.23±0.04	20	70	87	*Cardwell and Isacks* [1978]
19941004	-0.20±0.01	23	87	67	*Kosuga et al.* [1996]
19941016	-0.06±0.01	42	83	49	*Kao and Chen* [1994]
19941210	-0.20±0.02	64	78	29	*Singh and Mortera* [1991]
19941227	0.04±0.01	79	72	21	*Zhou* [1990]
19941230	0.20±0.03	41	50	80	*Zhou* [1990]
19950208	-0.09±0.02	11	83	81	*Molnar and Sykes* [1969]
19950407	0.13±0.01	53	42	73	*Fischer and Jordan* [1991]
19950420	0.13±0.04	28	72	70	*Hatherton and Dickinson* [1969]
19950502	-0.17±0.06	20	81	73	*Barazangi and Isacks* [1976]
19950506	0.09±0.05	44	46	86	*Kumar and Rao* [1995]
19950629	-0.11±0.03	24	71	76	*Pascal et al.* [1978]
19950726	-0.40±0.03	12	83	80	*Hatherton and Dickinson* [1969]
19950728	0.17±0.04	17	78	79	*Fischer and Jordan* [1991]
19950814	0.33±0.04	18	72	88	*McGuire and Wiens* [1995]
19950916	-0.91±0.10	71	58	38	*Pascal* [1979]
19950923	-0.13±0.02	34	60	76	*James and Snoke* [1994]
19951021	0.07±0.02	14	83	77	*Ponce et al.* [1992]
19951219	-0.23±0.02	86	19	72	*Pegler et al.* [1995]
19951225	0.31±0.02	35	56	82	*Cardwell and Isacks* [1978]
19960222	0.10±0.07	3	88	87	*Kao and Chen* [1994]
19960228	-0.37±0.10	43	52	72	*Hatherton and Dickinson* [1969]
19960416	-0.23±0.02	15	88	75	*Fischer and Jordan* [1991]

19960419	-0.03±0.02	47	77	46	*Delouis et al.* [1996]
19960429	-0.13±0.01	48	82	43	*Pascal* [1979]
19960609	0.55±0.03	48	47	73	*Zhou* [1990]
19960610	-0.13±0.01	14	86	77	*Pascal et al.* [1978]
19960805	0.05±0.01	53	37	87	*Zhou* [1990]
19960914	0.13±0.05	27	64	82	*Pascal et al.* [1978]
19960928	0.19±0.01	84	53	37	*Acharya and Aggarwal* [1980]
19961222	-0.18±0.02	57	33	88	*Kosuga et al.* [1996]
19961231	0.11±0.14	23	85	67	*Ponce et al.* [1992]
19970123	0.16±0.01	12	84	79	*Araujo and Suárez* [1994]
19970405	0.39±0.01	25	82	66	*Pegler et al.* [1995]
19970421	-0.24±0.01	36	71	61	*Pascal et al.* [1978]
19970423	0.18±0.06	79	15	80	*Zhou* [1990]
19970503	0.15±0.01	58	57	50	*Zhou* [1990]
19970513	0.06±0.04	20	72	83	*Chatelain et al.* [1980]
19970521	0.00±0.03	53	38	83	*Pascal et al.* [1978]
19970522	0.02±0.01	26	72	72	*Singh and Mortera* [1991]
19970902	-0.77±0.00	42	52	74	*Molnar and Sykes* [1969]
19971005	-0.85±0.21	66	62	39	*Forsyth* [1975]
19971006	-0.28±0.07	40	58	68	*Acharya and Aggarwal* [1980]
19971014	0.03±0.02	86	73	17	*Fischer and Jordan* [1991]
19971015	-0.11±0.06	58	87	32	*Araujo and Suárez* [1994]
19971028	-0.14±0.06	17	87	73	*Barazangi and Isacks* [1976]
19971109	0.42±0.14	15	81	78	*Bevis and Isacks* [1984]
19971115	0.08±0.02	17	77	80	*Pascal et al.* [1978]
19971211	-0.10±0.05	18	76	79	*Molnar and Sykes* [1969]
19971222	-0.52±0.01	82	26.91	65	*Pegler et al.* [1995]

Appendix C

Sensitivity Tests for Rupture Velocity Scaling Model

C.1 Introduction

In Chapter 5 of this thesis, a model was presented in which rupture velocity scales with increasing event size. This model corroborates observations of increase of apparent stress with event size as well as increase in particle velocity with event size. In addition it can explain why estimations of specific fracture energy show an increase with earthquake moment and it corrects the underestimation of stress drop for small events. Because the increase in apparent stress with event size is observed to saturate at about $M = 5$ *Kanamori and Heaton* [1998], the parameter M_0^* is introduced in the empirical model describing the behavior of apparent stress. This parameter defines the point at which the rate of increase of the dependent variable (apparent stress, rupture velocity, particle velocity, specific fracture energy, etc.) begins to saturate.

In Chapter 5, one set of optimal parameters was presented, which were chosen after repeated forward modelling to be a best fit to all observations simultaneously. In order to test the sensitivity of this model to the choices of the parameters M_0^*, $\Delta\sigma$, G, and β, we varied each one independently of the others and recalculated the scaling relations accordingly. In addition we tested the effectiveness of an empirical

scaling without M_0^*.

C.2 Optimal Choice of Parameters as Presented in Chapter 5

Here we summarize the results of the model presented in Chapter 5 with the original choice of parameters for comparison with the following sections in which each parameter is varied. Medians of apparent stress for our data and several other datasets binned in 1-order-of-magnitude bins in moment are shown in Figure C-1. The datasets we use for comparison with our mining data (circles) are: *Prejean and Ellsworth* [2001] (squares), *Abercrombie* [1995] (diamonds), *Mayeda and Walter* [1996] (asterisks), and *Kanamori et al.* [1993] (x's). We only show the friction-dominated events in Figure C-1 because we do not intend that the fracture-dominated events pertain to this model. The scaling line is that of Equation 5.8:

$$\sigma_a = \frac{2\sigma_a^*}{1 + (M_0^*/M_0)^{1/3}} \tag{C.1}$$

in which $M_0^* = 3 \times 10^{15}$ Nm, and $\sigma_a^* = \sigma_a(M_0^*) = 2$ MPa.

The relation for specific fracture energy is that of Equation 5.17:

$$E_G(R) = \left(\frac{24\Delta\sigma^2}{7\pi G}\right)\left(\frac{R}{1 + R/R^*}\right) \tag{C.2}$$

where $\Delta\sigma = 3$ MPa, $G = 36$ GPa, and $R^* = R(M_0^*) = 729$ m as calculated through the constant-stressdrop relationship $R = (7M_0/16\Delta\sigma)^{1/3}$. For consistency all figures have M_0 as the independent variable.

The scaling of rupture velocity with source size is given by Equation 5.23

$$v_R(R) = \frac{\beta}{1 + R^*/R} \tag{C.3}$$

in which β is the shear wave speed of the material. In Figure C-3, $\beta = 3650$ m/s and

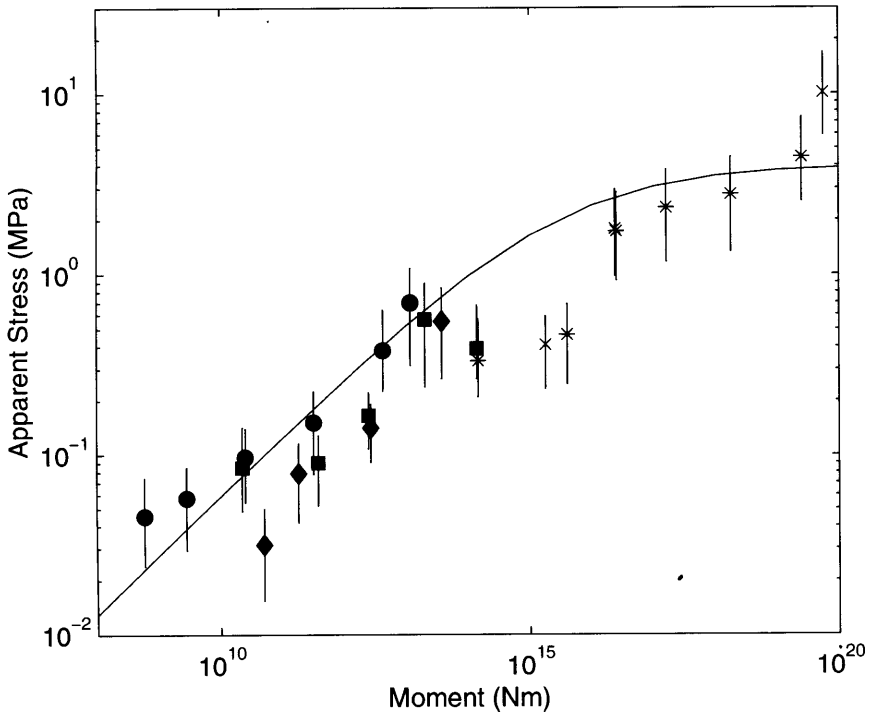

Figure C-1: Medians with 95% confidence error bars of σ_a vs. M_0 for the events in our study and several other studies. Each dataset is binned in order-of-magnitude units in moment. Symbols are as in Figure 5-4. Solid line shows the empirical scaling $\sigma_a = \frac{2\sigma_a^*}{1+(M_0^*/M_0)^{1/3}}$ for frictional events in which $\sigma_a^* = 2$ MPa, and $M_0^* = 3 \times 1015$ Nm.

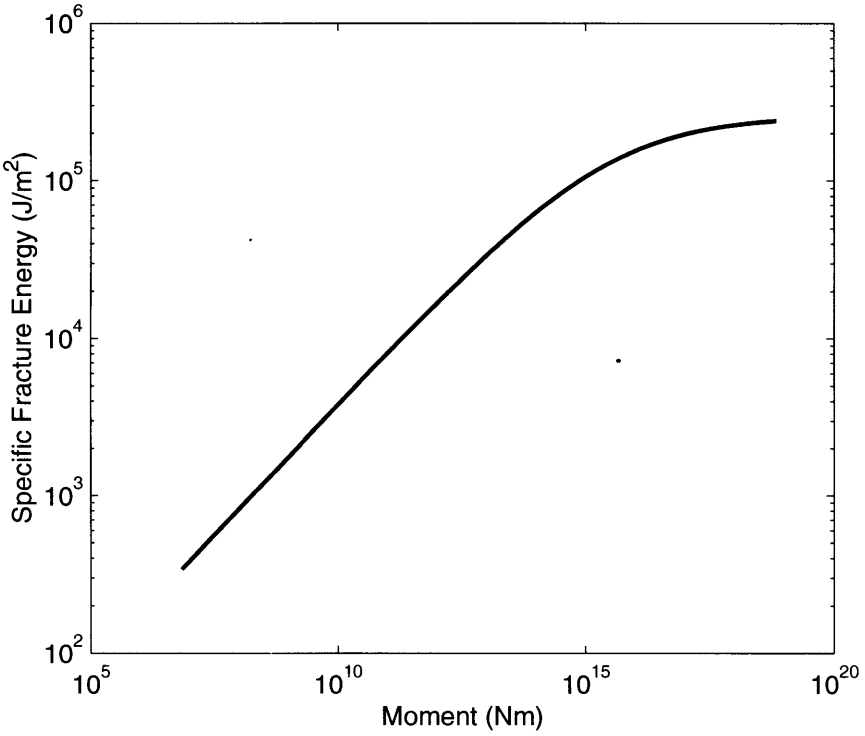

Figure C-2: Specific fracture energy E_G vs. moment for the constants $\Delta\sigma = 3$ MPa, $M_0^* = 3 \times 10^{15}$ Nm, and $G = 36$ GPa.

$R^* = 729$ m.

The scaling relation for particle velocity is given by Equation 5.27:

$$X\dot{u} = \frac{\Re \Delta\sigma R\beta}{G(1 + R^*/R)}. \tag{C.4}$$

where X is hypocentral distance, $\dot{u}$ is peak particle velocity, and $\Re$ is a constant that accounts for radiation pattern. In Figure C-4, the same choices of constants are used as in Figures C-1, C-2, and C-3.

C.3 Omitting M_0^*

We tested the viability of a model in which rupture velocity increases with increasing source size in a way that does not have an associated M_0^* to account for the saturation of the rupture velocity. In Figure C-5 the same data is shown as in Figure

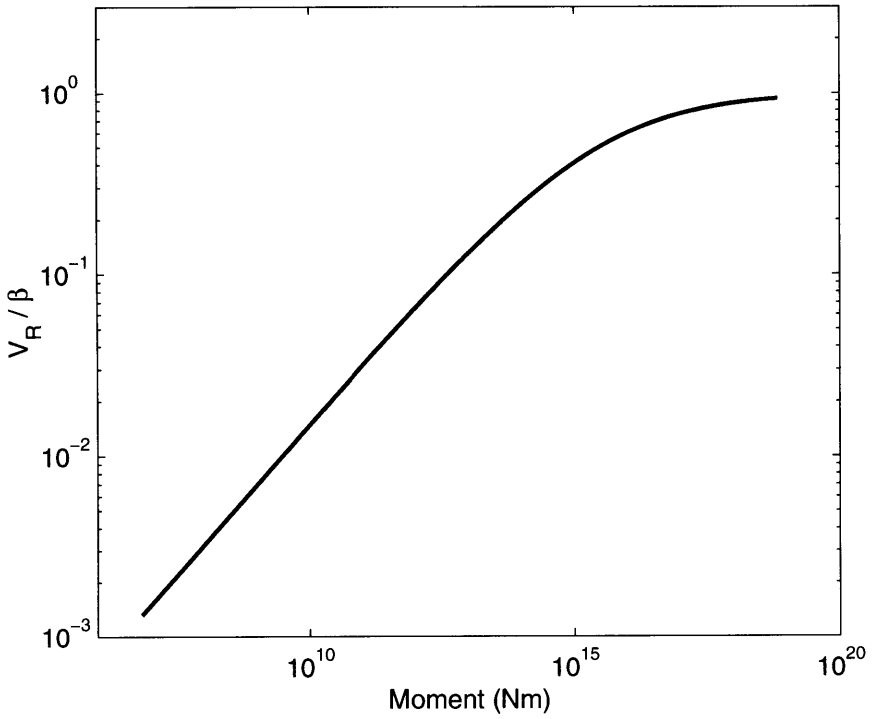

Figure C-3: Rupture velocity v_R normalized by shear wave speed β vs. moment. Parameters are $\Delta\sigma = 3$ MPa, $M^* = 3 \times 10^{15}$ Nm, and $\beta = 3650$ m/s.

C-1, but the three scaling lines drawn represent $\sigma_a \sim M_0^{1/3}$ (dashed), $\sigma_a \sim M_0^{1/4}$ (solid), and $\sigma_a \sim M_0^{1/5}$ (dotted). The relation $\sigma_a \sim M_0^{1/4}$ fits the apparent stress data well, but the problem with a model without an M_0^* becomes clear in Figures C-6 and C-7. Experimental data shows that there is an upper limit to specific fracture energy; furthermore, rupture velocity cannot grow larger than the shear wave speed of a material. Without any M_0^* this model has no way of satisfying those two criteria. The successful model should account for all observations simultaneously.

In addition, the scaling relation $v_R \sim M^{1/4}$, does not fit observations well at $M_0 \geq 10^{18}$ Nm (see solid line in Figure C-8).

C.4 Sensitivity to choice of M_0^*

We tested the sensitivity of this model to the choice of M_0^* because there is a range of values over which forward models fit the apparent stress data (Figure C-9).

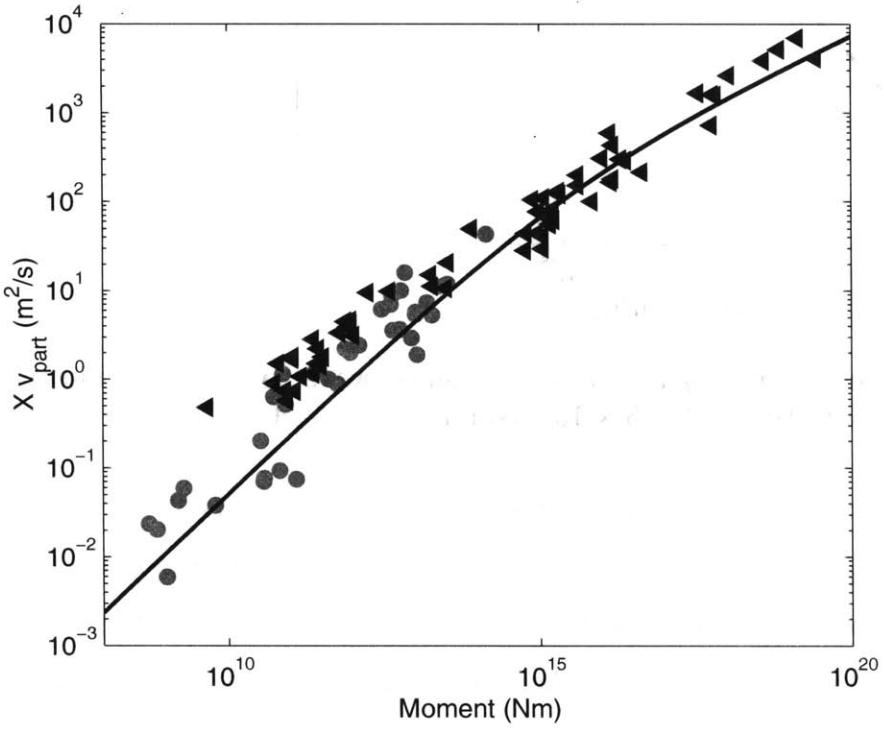

Figure C-4: Ground motion parameter vs. moment for data from Savuka (circles) and from *McGarr* [1984a] (triangles) which includes a mixture of mining-induced, reservoir, volcanic, and tectonic seismicity. The line shows the scaling law of Equation 5.27 using the constants $M_0^* = 3 \times 10^{15}$ Nm, $\Delta\sigma = 3$ MPa, $G = 36$ GPa, and $\beta = 3650$ m/s.

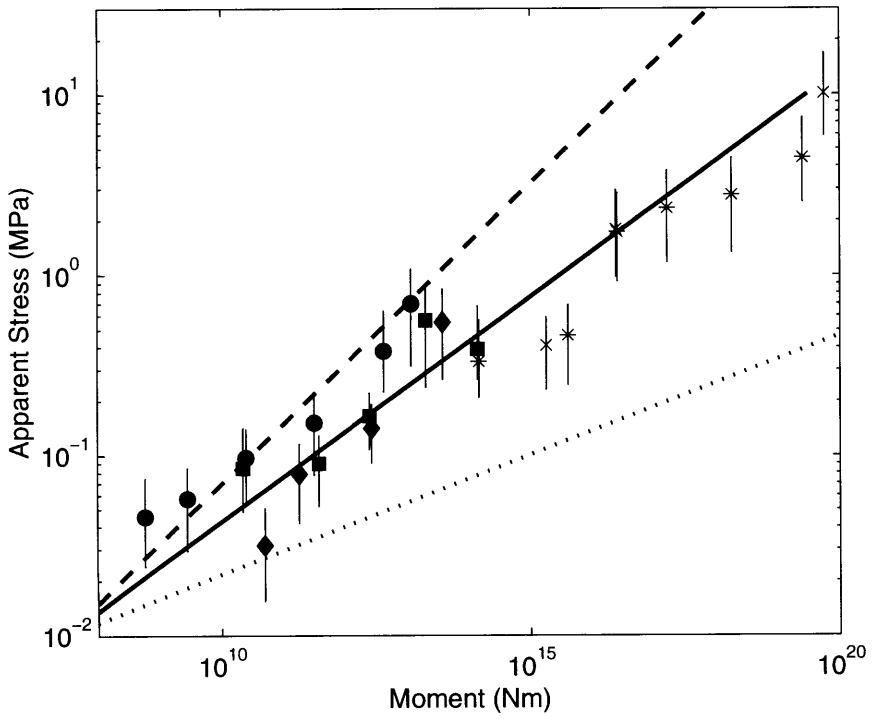

Figure C-5: Medians with 95% confidence error bars of σ_a vs. M_0 for the events in our study and several other studies. Each dataset is binned in order-of-magnitude units in moment. Symbols are as in Figure 5-4. Dashed line shows the scaling $\sigma_a \sim M_0^{1/3}$, solid line shows $\sigma_a \sim M_0^{1/4}$, and dotted line shows $\sigma_a \sim M_0^{1/5}$.

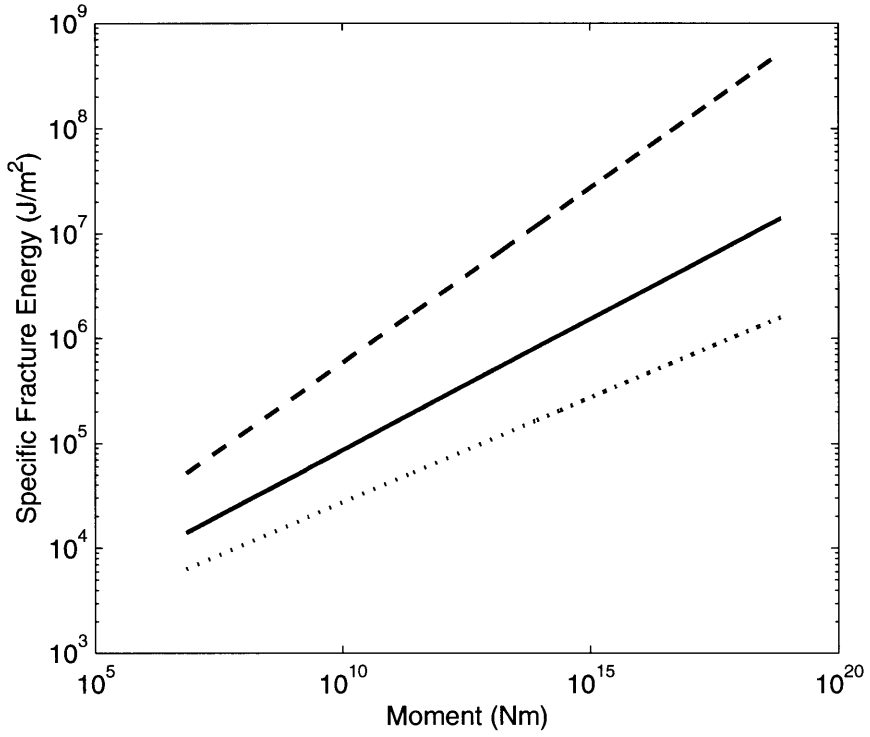

Figure C-6: Specific fracture energy E_G vs. moment for the same scaling relations as in Figure C-5.

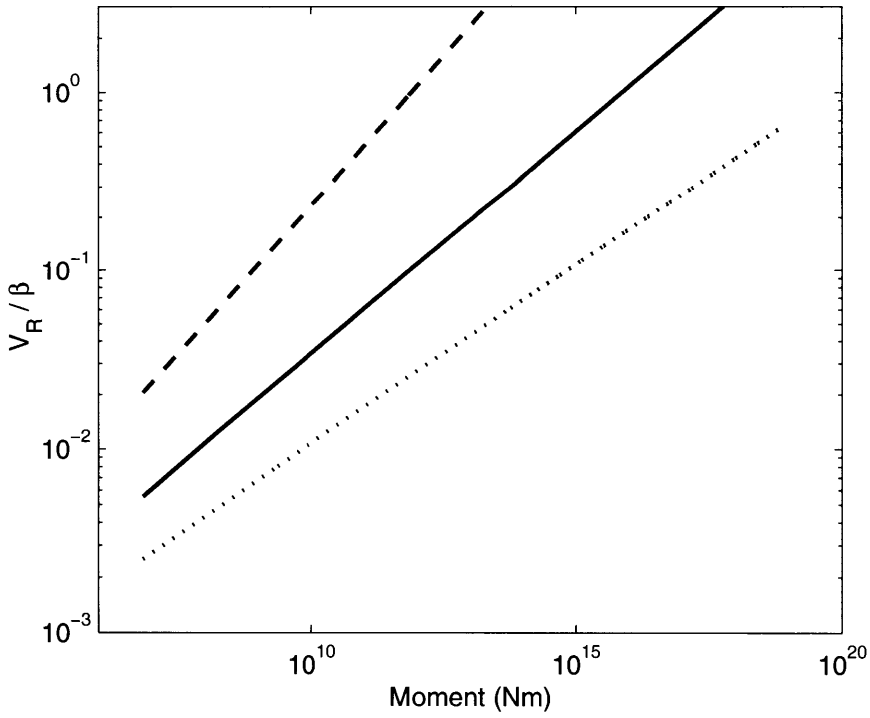

Figure C-7: Rupture velocity v_R normalized by shear wave speed β vs. moment for the same scaling relations as in Figure C-5.

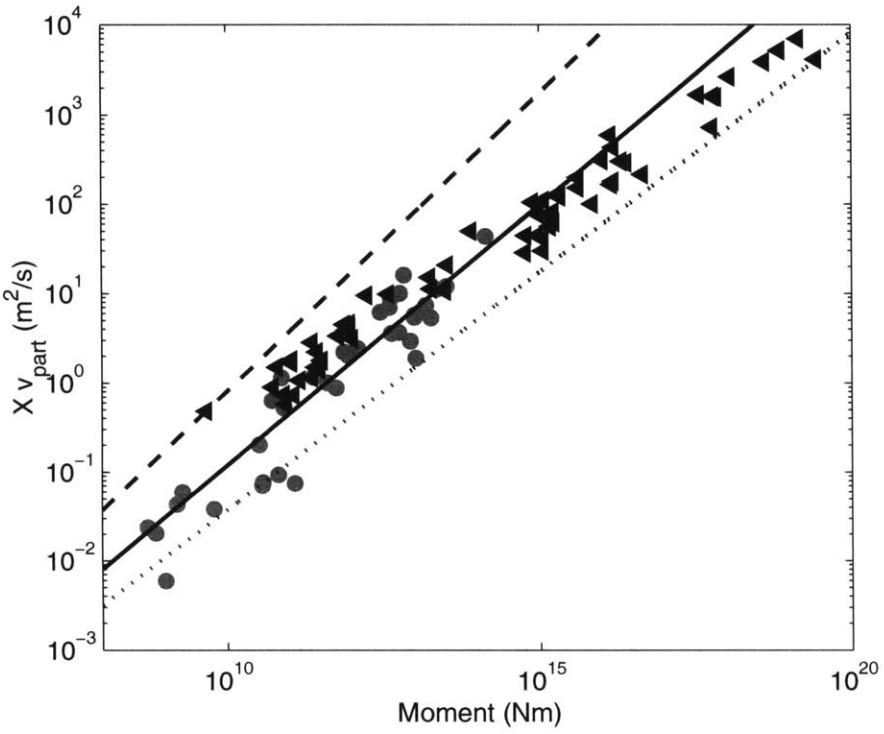

Figure C-8: Ground motion parameter vs. moment. Data symbols are as in Figure C-4. Scaling relations are as in Figure C-5.

In Figure C-9 we show our original choice, $M_0^* = 3 \times 10^{15}$ Nm (solid line), along with two other models in which all other parameters are fixed but M_0^* is an order of magnitude smaller (dashed line) and greater (dotted line) than the original choice. The model with $M_0^* = 3 \times 10^{14}$ Nm overestimates the apparent stress of all but the largest events. The other two models provide acceptable fits (Figure C-9). There is no effect on specific fracture energy of changing the value of M_0^* below about 10^{12} Nm (Figure C-10). Above this value the three models saturate at different values of specific fracture energy, though these values are not greatly different. All could accommodate the scatter of estimated calculations. In terms of rupture velocity, as M_0^* increases, the seismic moment at which the rupture velocity approaches the shear wave speed increases, so that smaller earthquakes are slower for larger values of M_0^* (Figure C-11).

Particle velocity is underestimated for small events by the model in which $M_0^* = 3 \times 10^{16}$ Nm (dotted line in Figure C-12). The other two models give an acceptable

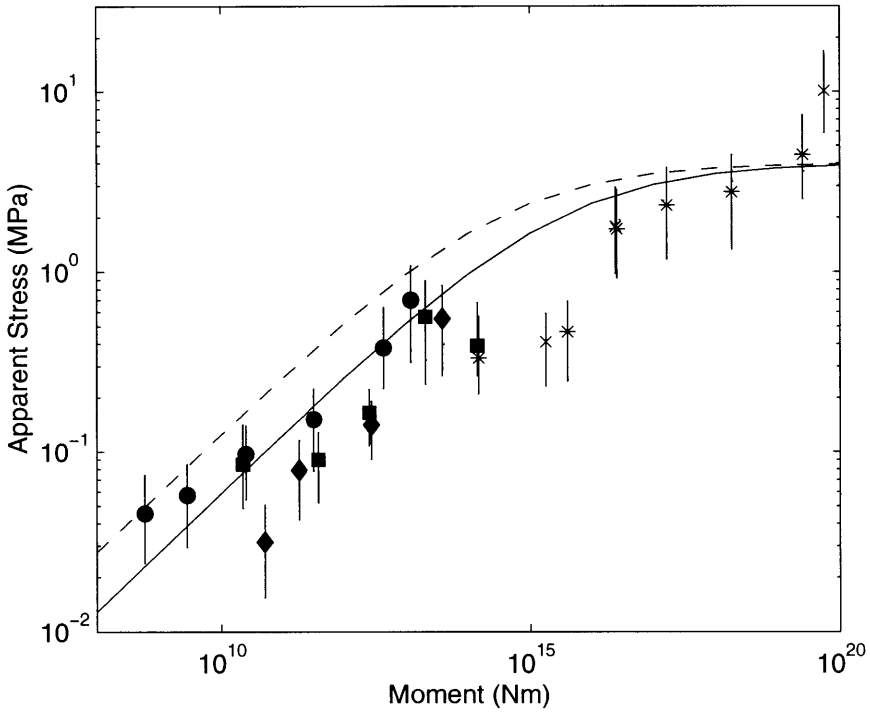

Figure C-9: Medians with 95% confidence error bars of σ_a vs. M_0. Data symbols are as in Figure C-1. All scaling lines are for the empirical relation $\sigma_a = \frac{2\sigma_a^*}{1+(M_0^*/M_0)^{1/3}}$. Dashed, solid, and dotted lines represent $M_0^* = 3 \times 10^{14}$ Nm, $M_0^* = 3 \times 10^{15}$ Nm, and $M_0^* = 3 \times 10^{16}$ Nm, respectively.

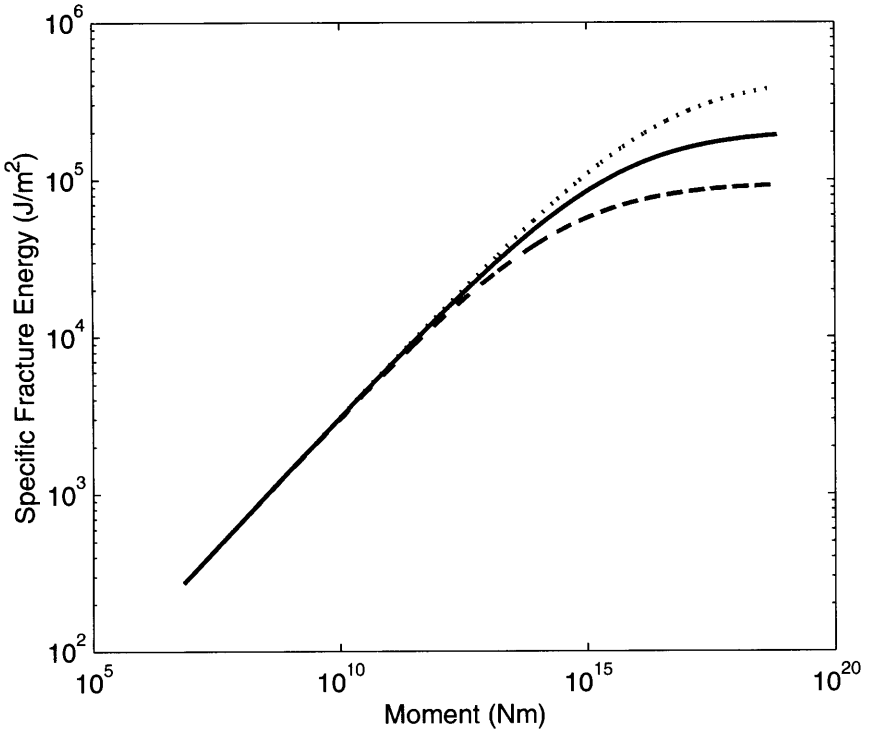

Figure C-10: Specific fracture energy E_G vs. moment for the same choices of M_0^* as in Figure C-9.

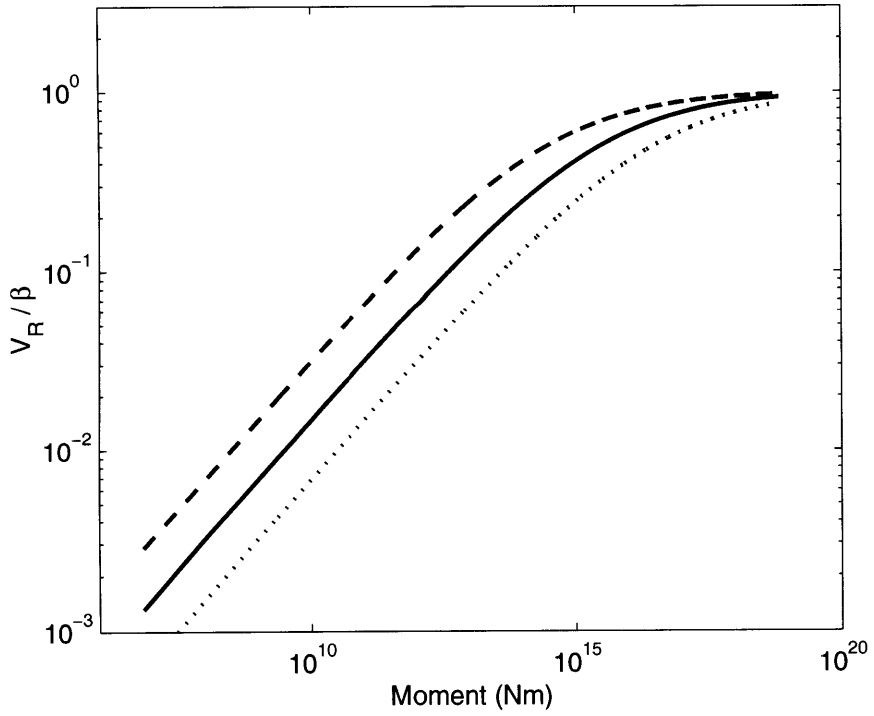

Figure C-11: Rupture velocity v_R normalized by shear wave speed β vs. moment for the same choices of M_0^* as in Figure C-9.

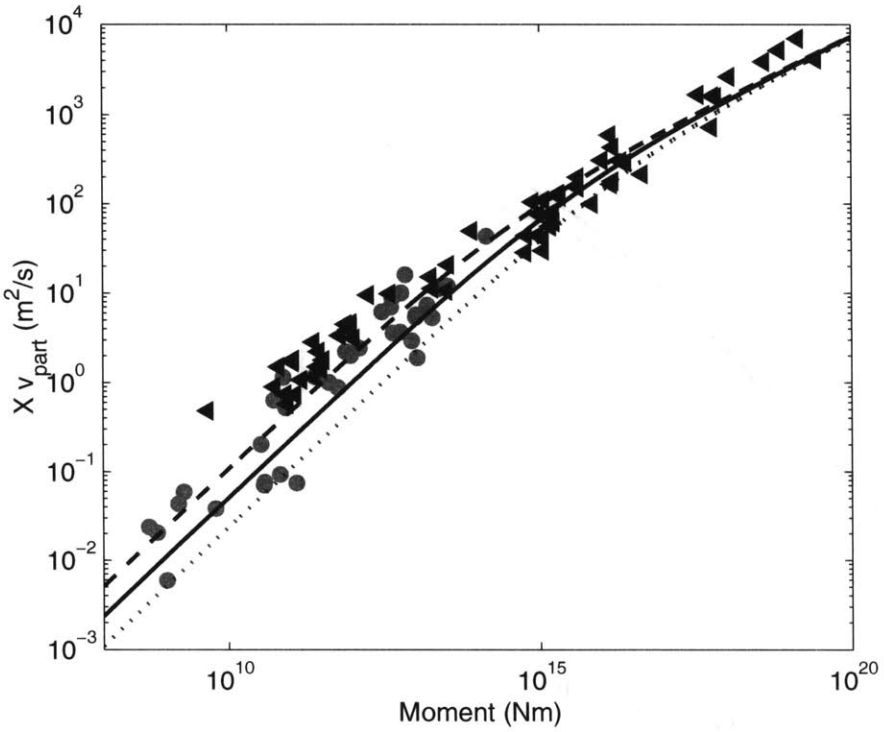

Figure C-12: Ground motion parameter vs. moment. Data symbols are as in Figure C-4. Choices of M_0^* are as in Figure C-9.

fit to this data. However, the model in which $M_0^* = 3 \times 10^{14}$ Nm (dashed line in Figure C-12) did not fit the apparent stress data well. Therefore, the original choice of $M_0^* = 3 \times 10^{15}$ Nm best fits both sets of observations simultaneously.

C.5 Sensitivity to choice of $\Delta\sigma$

Because the form of the model that characterizes increasing apparent stress with seismic moment does not depend on $\Delta\sigma$, we do not show a figure of the apparent stress data in this section. Specific fracture energy does depend on $\Delta\sigma$, both directly, and through calculation of R^* (see Equation C.2). We tested the sensitivity to our model to the following stress drops, as shown in Figure C-13: 0.3 MPa (black dashed line), 1 MPa (black solid line), 3 MPa (black dotted line), 10 MPa (grey dashed line), and 30 MPa (grey solid line). Choices of 0.3 MPa and 1 MPa underestimate the

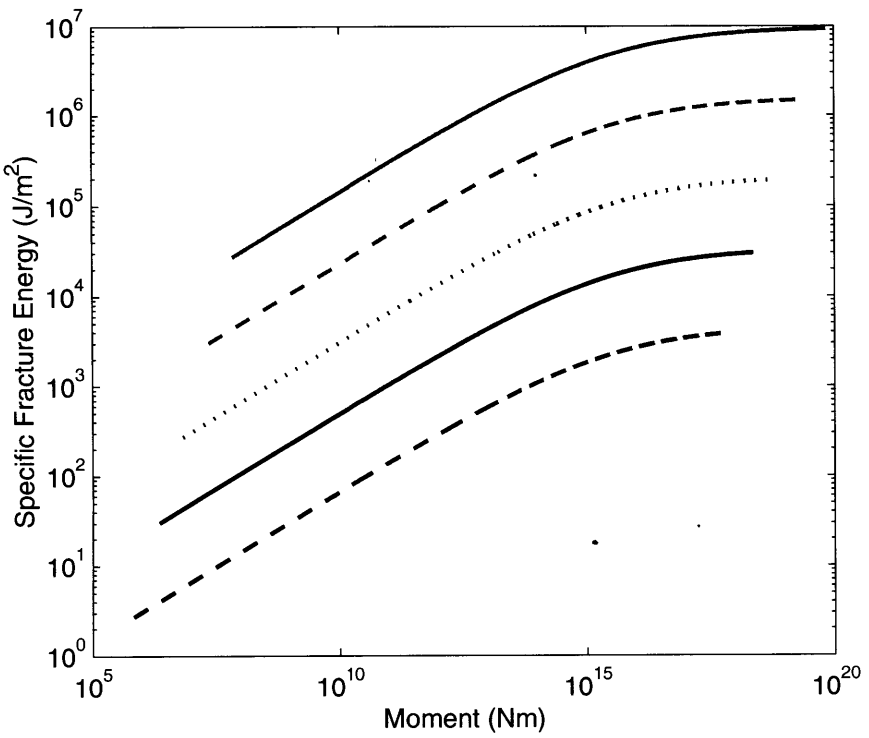

Figure C-13: Specific fracture energy E_G vs. moment. The black dashed line, solid line and dotted line represent $\Delta\sigma = 0.3$ MPa, $\Delta\sigma = 1$ MPa, and $\Delta\sigma = 3$ MPa. The grey dashed line and solid line represent $\Delta\sigma = 10$ MPa and $\Delta\sigma = 30$ MPa.

value of E_G for large events, and the choice of 30 MPa overestimates E_G for small events. Because we show rupture velocity in non-dimensional units, there is no effect of changing stress drop on this part of the model. Therefore, we do not show a figure of rupture velocity vs. moment in this section.

Changing the stress drop does not change the form of the model for particle velocity, it merely translates the model on the y-axis (Figure C-14). Choices of 0.3 and 1 MPa underestimate all observations of particle velocity, whereas the choice of 30 MPa overestimates most observations, except in the range of $10^{10} - 10^{12}$ Nm. The choices of 3 and 10 MPa both fit the data adequately and also correlate well with the range of measured stress drops in earthquake source studies in general. In light of previous observations of the critical earthquake presented in Chapter 4, 3 MPa is a better choice. If we instead assume $\Delta\sigma = 10$ MPa, the critical patch size $R_c = 6$ m and the critical slip distance $D_c = 1.2$ mm. The upper frequency cutoff $f_{\max}$ would become 325 Hz, approximately 100 Hz higher than what we observe.

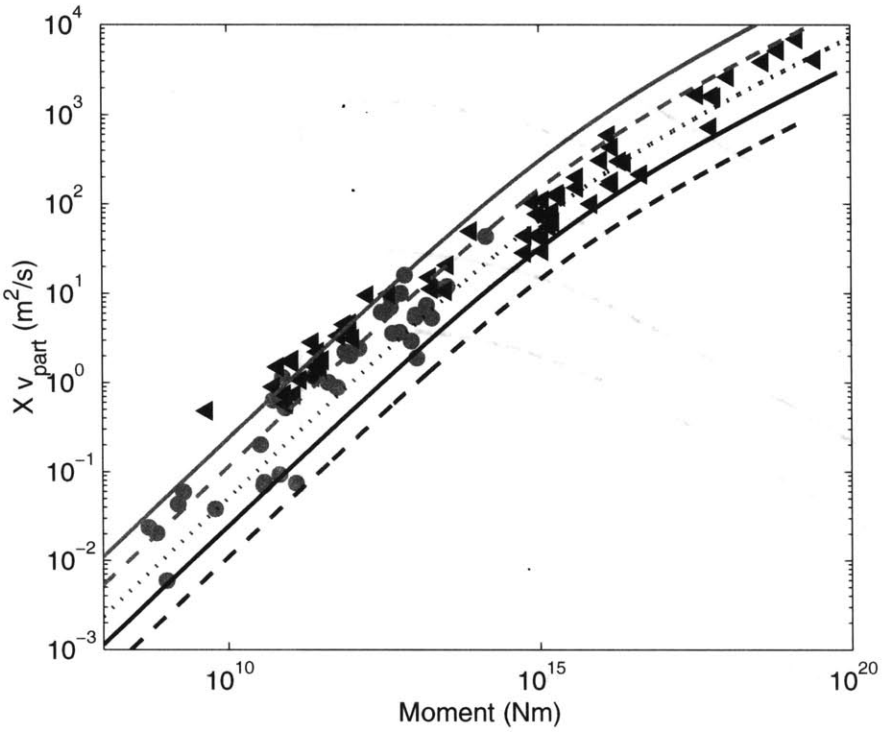

Figure C-14: Ground motion parameter vs. moment. Data symbols are as in Figure C-4. Choices of $\Delta\sigma$ are as in Figure C-13.

C.6 Sensitivity to choice of G

Our model does not involve G when describing apparent stress or rupture velocity, so these figures are not included in this section. We estimate that the value of the shear modulus is only uncertain by 10%, but we tested the sensitivity of our model to this parameter by varying it by $\pm 20\%$ and $\pm 10\%$. This variation has little effect (Figure C-15). In addition, the model for ground motion is insensitive to this variation in G (Figure C-16).

C.7 Sensitivity to choice of β

Since apparent stress and specific fracture energy do not depend on shear wave speed, we do not show figures of those in this section. Also, the non-dimensionalization

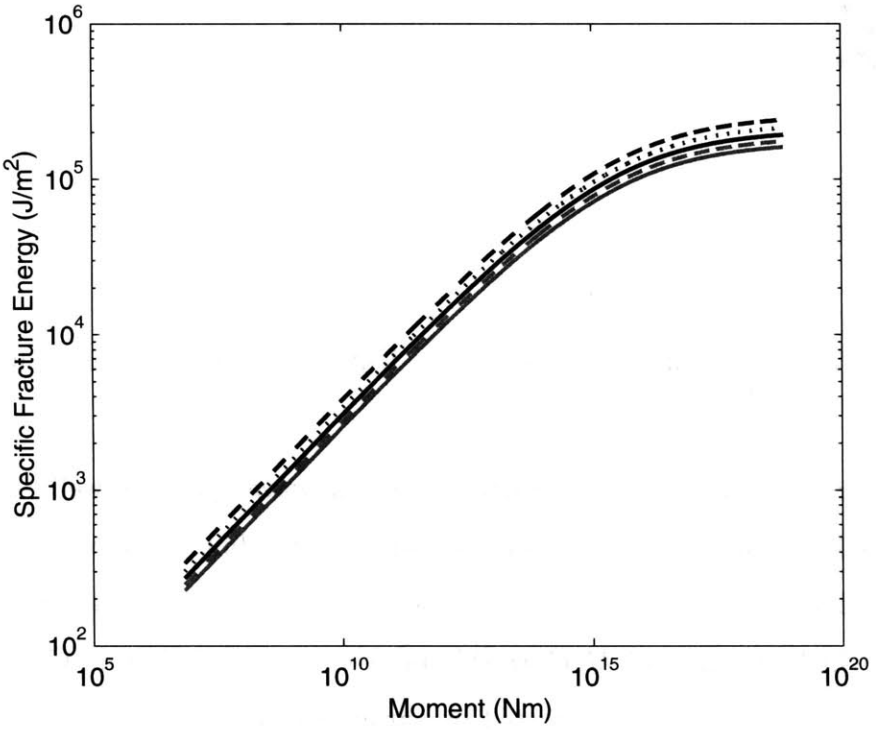

Figure C-15: Specific fracture energy E_G vs. moment. The black dashed line, solid line and dotted line represent $G = 28.8$ GPa, $G = 32.4$ GPa, and $G = 36.0$ GPa. The grey dashed line and solid line represent $G = 39.6$ GPa and $G = 43.2$ GPa.

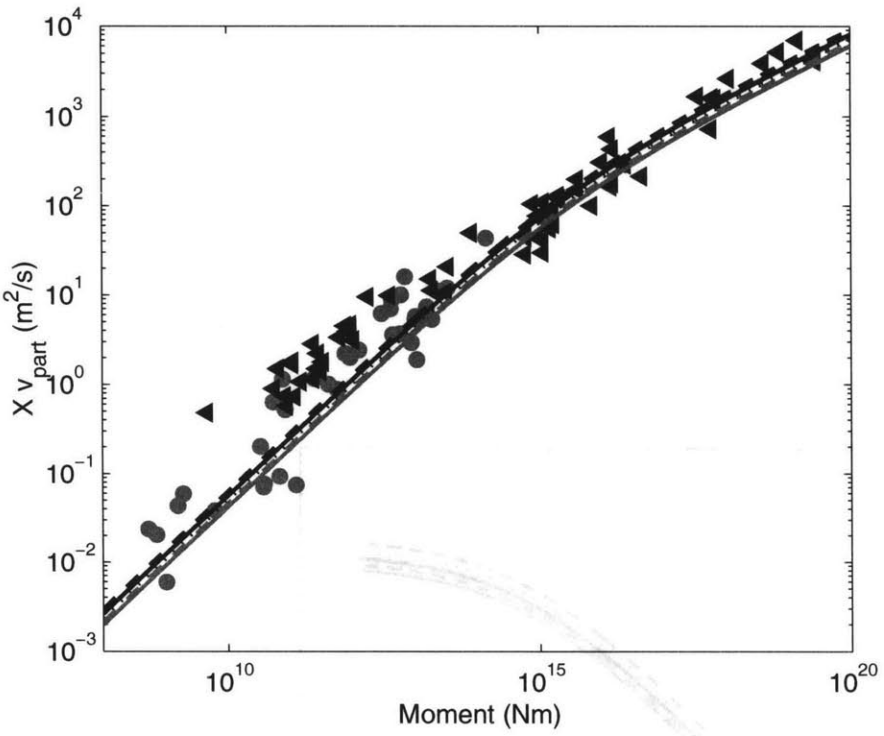

Figure C-16: Ground motion parameter vs. moment. Data symbols are as in Figure C-4. Choices of G are as in Figure C-15.

of rupture velocity renders that model insensitive to shear wave speed as well. As with G, we expect a 10% uncertainty in β for the mining data, but we have tested our model with $\beta = 3650 \pm 20\%$ and $\beta = 3650 \pm 10\%$ to account for the variety of tectonic settings in which the data of *McGarr* [1984a] were recorded (Figure C-17). It is clear that this model is not greatly affected by variations in β.

C.8 Conclusions

We have verified that the form of our model is correct by testing a version in which there is no M_0^* included that can account for the eventual saturation of apparent stress and rupture velocity with increasing seismic moment. In a model such as this, specific fracture energy and rupture velocity both grow larger than their maximum possible values as determined by material properties. Therefore, we conclude that our model

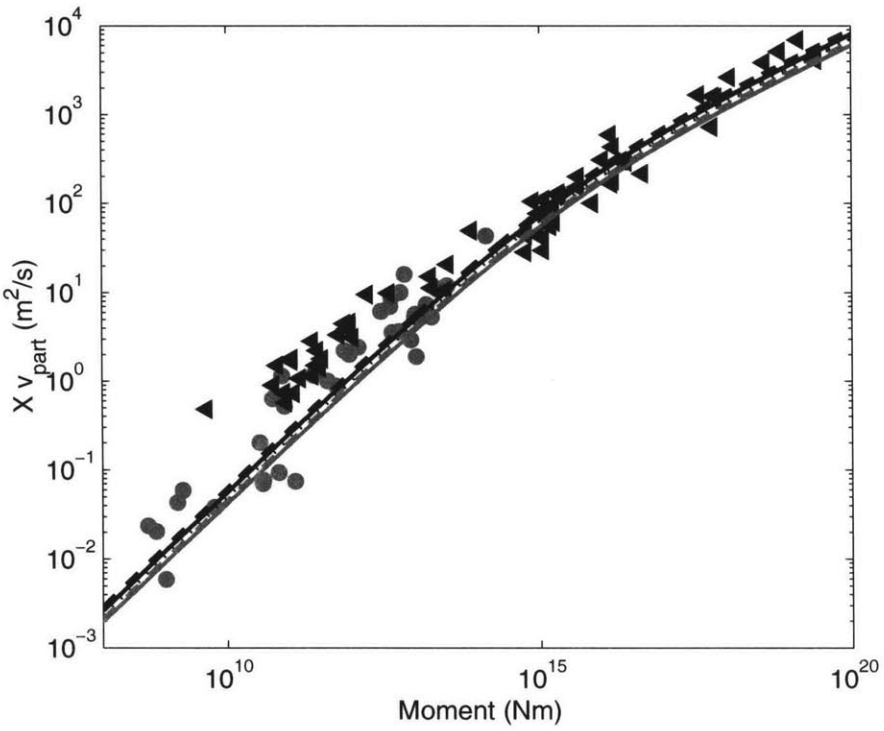

Figure C-17: Ground motion parameter vs. moment. Data symbols are as in Figure C-4. The black dashed, solid, and dotted lines represent $\beta = 2920$ m/s, $\beta = 3285$ m/s, and $\beta = 3650$ m/s. The grey dashed and solid lines are for $\beta = 4015$ m/s and $\beta = 4380$ m/s.

must involve an M_0^*.

We further tested our model's sensitivity to choices of the constants M_0^*, $\Delta\sigma$, G, and β. In each case the form of the model was not affected by these variations and the original choices of the values of each of these parameters was determined to be the best fit to all observations simultaneously.

Bibliography

Abercrombie, R. E., Earthquake locations using single-station deep borehole recordings: Implications for microseismicity on the San Andreas fault in southern California, *J. Geophys. Res.*, *100*, 24,003–24,014, 1995.

Abercrombie, R. E., and G. Ekström, Earthquake slip on oceanic transform faults, *Nature*, *410*, 74–77, 2001.

Acharya, H. K., and Y. P. Aggarwal, Seismicity and tectonics of the Philippine Islands, *J. Geophys. Res.*, *85*, 3239–3250, 1980.

Aki, K., Scaling law of seismic spectrum, *J. Geophys. Res.*, *72*, 1217–1231, 1967.

Aki, K., Characterization of barriers on an earthquake fault, *J. Geophys. Res.*, *84*, 6140–6148, 1979.

Aki, K., Asperities, barriers, characteristic earthquakes and strong motion prediction, *J. Geophys. Res.*, *89*, 5867–5872, 1984.

Aki, K., Magnitude-frequency relation for small earthquakes: A clue to the origin of $f_{\max}$ of large earthquakes, *J. Geophys. Res.*, *92*, 1349–1355, 1987.

Andersen, L. M., A relative moment tensor inversion technique applied to seismicity induced by mining, Master's thesis, University of the Witwatersrand, Johannesburg, Republic of South Africa, 1999.

Anderson, J. G., Implication of attenuation for studies of the earthquake source, in *Earthquake Source Mechanics*, edited by S. Das, J. Boatwright, and C. H. Scholz, vol. 6 of *Geophysical Monograph 37*, pp. 311–318, Am. Geophys. Union, 1986.

Anderson, J. G., and S. E. Hough, A model for the shape of the Fourier amplitude spectrum of acceleration at high frequencies, *Bull. Seismol. Soc. Am.*, *74*, 1969–1993, 1984.

Andrews, D. J., Rupture propagation with finite stress in antiplane strain, *J. Geophys. Res.*, *81*, 3575–3582, 1976a.

Andrews, D. J., Rupture velocity of plane strain shear cracks, *J. Geophys. Res.*, *81*, 5679–5687, 1976b.

Andrews, D. J., Objective determination of source parameters and similarity of earthquakes of different size, in *Earthquake Source Mechanics*, edited by S. Das, J. Boatwright, and C. H. Scholz, vol. 6 of *Geophysical Monograph 37*, pp. 259–267, Am. Geophys. Union, 1986.

Araujo, M., and G. Suárez, Geometry and state of stress of the subducted Nazca plate beneath central Chile and Argentina: Evidence from teleseismic data, *Geophys. J. Int.*, *116*, 283–303, 1994.

Astiz, L., T. Lay, and H. Kanamori, Large intermediate-depth earthquakes and the subduction process, *Phys. Earth and Plan. Int.*, *53*, 80–166, 1988.

Baker, C., and R. P. Young, Evidence for extensile crack initiation in point source time-dependent moment tensor solutions, *Bull. Seism. Soc. Am.*, *87*, 1442–1453, 1997.

Barazangi, M., and B. L. Isacks, Spatial distribution of earthquakes and subduction of the Nazca plate beneath South America, *Geology*, *4*, 686–692, 1976.

Barenblatt, G. S., Concerning equilibrium cracks forming during brittle fracture: The stability of isolated cracks, relationships with energetic theories, *Appl. Math. Mech.*, *23*, 1273–1282, 1959.

Beeler, N. M., T. E. Tullis, and J. D. Weeks, The roles of time and displacement in the evolution effect in rock friction, *Geophys. Res. Lett.*, *21*, 1987–1990, 1994.

Beeler, N. M., T. E. Tullis, M. L. Blanpied, and J. D. Weeks, Frictional behavior of large displacement experimental faults, *J. Geophys. Res.*, *101*, 8697–8715, 1996.

Bevis, M., and B. L. Isacks, Hypocentral trend surface analysis: Probing the geometry of Benioff zones, *J. Geophys. Res.*, *89*, 6153–6170, 1984.

Biegel, R. L., C. G. Sammis, and J. H. Dieterich, The frictional properties of a simulated gouge having a fractal particle distribution, *J. Struct. Geol.*, *11*, 827–846, 1989.

Boore, D. M., The effect of finite bandwidth of seismic scaling relationships, in *Earthquake Source Mechanics*, edited by S. Das, J. Boatwright, and C. H. Scholz, vol. 6 of *Geophysical Monograph 37*, pp. 275–283, Am. Geophys. Union, 1986.

Broniec, Z., and W. Lenkiewicz, Static friction processes under dynamic loads and vibration, *Wear*, *80*, 261–271, 1982.

Brune, J. N., Seismic moment, seismicity, and rate of slip along major fault zones, *J. Geophys. Res.*, *73*, 777–784, 1968.

Brune, J. N., Tectonic stress and the spectra of seismic shear waves from earthquakes, *J. Geophys. Res.*, *75*, 4997–5009, 1970, correction, *J. Geophys. Res.*, *76* 5002, 1971.

Cahill, T., and B. L. Isacks, Seismicity and shape of the subducted Nazca plate, *J. Geophys. Res.*, *97*, 17,503–17,529, 1992.

Cardwell, R. K., and B. L. Isacks, Geometry of the subducted lithosphere beneath the Banda Sea in eastern Indonesia from seismicity and fault plane solutions, *J. Geophys. Res.*, *83*, 2825–2838, 1978.

Chatelain, J. L., S. W. Roecker, D. Hatzfeld, and P. Molnar, Microearthquake seismicity and fault plane solutions in the Hindu Kush region and their tectonic implications, *J. Geophys. Res.*, *85*, 1365–1387, 1980.

Chiu, J.-M., B. L. Isacks, and R. K. Cardwell, 3-D configuration of subducted lithosphere in the western Pacific, *Geophys. J. Int.*, *106*, 99–111, 1991.

Cichowicz, A., R. W. E. Green, A. van Zyl Brink, P. Grobler, and P. I. Mountfort, The space and time variation of micro-event parameters occurring in front of an active stope, in *Rockbursts and Seismicity in Mines*, edited by C. Fairhurst, vol. 2, pp. 171–175, 1990.

Cook, N. G. W., The seismic location of rockbursts, in *Proc. 5th Symp. Rock Mech.*, pp. 493–516, Pergamon Press, Oxford, 1963.

Davies, J. N., and L. House, Aleutian subduction zone seismicity, volcano-trench separation, and their relation to great thrust-type earthquakes, *J. Geophys. Res.*, *84*, 4583–4591, 1979.

Delouis, B., A. Cisternas, L. Dorbath, L. Rivera, and E. Kausel, The Andean subduction zone between 22 and 25°S (northern Chile): Precise geometry and state of stress, *Tectonophysics*, *259*, 81–100, 1996.

Delour, J., A. Kudrolli, and J. P. Gollub, Velocity statistics in excited granular media, *Chaos*, *9*, 682–690, 1999.

Dieterich, J. H., and M. F. Linker, Fault stability under conditions of variable normal stress, *Geophys. Res. Lett.*, *19*, 1691–1694, 1992.

Dieterich, J. H., Time-dependent friction in rocks, *J. Geophys. Res.*, *77*, 3690–3697, 1972.

Dieterich, J. H., Time-dependent friction and the mechanics of stick-slip, *Pure Appl. Geophys.*, *116*, 790–805, 1978.

Dieterich, J. H., Modeling of rock friction, 1, Experimental results and constitutive equations, *J. Geophys. Res.*, *84*, 2161–2168, 1979.

Dieterich, J. H., Constitutive properties of faults with simulated gouge, in *Mechanical Behavior of Crustal Rocks, Geophys. Monogr. Ser.*, edited by N. L. Carter et al., vol. 24, pp. 103–120, AGU, Washington, D.C., 1981.

Dieterich, J. H., A model for the nucleation of earthquake slip, in *Earthquake Source Mechanics*, edited by S. Das, J. Boatwright, and C. H. Scholz, vol. 6 of *Geophysical Monograph 37*, pp. 37–47, Am. Geophys. Union, 1986.

Dieterich, J. H., Probability of earthquake recurrence with nonuniform stress rates and time-dependent failure, *Pure and Appl. Geophys.*, *126*, 589–617, 1988.

Dziewonski, A. M., and D. L. Anderson, Preliminary reference Earth model, *Phys. Earth Plan. Int.*, *25*, 297–356, 1981.

Dziewonski, A. M., and J. H. Woodhouse, An experiment in systematic study of global seismicity: Centroid-moment tensor solutions for 201 moderate and large earthquakes of 1981, *J. Geophys. Res.*, *88*, 3247–3271, 1983.

Eccles, C. D., and J. A. Ryder, Seismic location algorithms: A comparative evaluation, in *Proceedings of the 1st International Congress on Rockbursts and Seismicity in Mines*, edited by N. C. Gay and E. H. Wainwright, pp. 89–92, S. Afr. Inst. Min. Met., 1984.

Feignier, B., and R. P. Young, Moment tensor inversion of induced microseismic events: Evidence of non-shear failures in the $-4 < m < -2$ moment magnitude range, *Geophys. Res. Lett.*, *19*, 1503–1506, 1992.

Finnie, G. J., Using neural networks to discriminate between genuine and spurious seismic events in mines, *Pure Appl. Geophys.*, *154*, 41–56, 1999a.

Finnie, G. J., Some statistical aspects of mining induced seismic events, in *2nd Southern African Rock Engineering Symposium,*, edited by T. O. Hagan, Johannesburg, South Africa, 1999b.

Fischer, K. M., and T. H. Jordan, Seismic strain rate and deep slab deformation in Tonga, *J. Geophys. Res.*, *96*, 14,429–14,444, 1991.

Forsyth, D. W., Fault plane solutions and tectonics of the South Atlantic and Scotia Sea, *J. Geophys. Res.*, *80*, 1429–1443, 1975.

Fossum, A. F., and L. B. Freund, Nonuniformly moving shear crack model of a shallow focus earthquake mechanism, *J. Geophys. Res.*, *80*, 3343–3347, 1975.

Foulger, G. R., and B. R. Julian, Non-double-couple earthquakes at the Hengill-Grensdalur volcanic complex, Iceland: Are they artifacts of crustal heterogeneity?, *Bull. Seismol. Soc. Am.*, *83*, 38–52, 1993.

Freund, L. B., Energy flux into the tip of an extending crack in an elastic solid, *J. Elasticity*, *2*, 341–349, 1972.

Freund, L. B., The mechanics of dynamic shear crack propagation, *J. Geophys. Res.*, *84*, 2199–2209, 1979.

Freund, L. B., *Dynamic Fracture Mechanics*, Cambridge University Press, 1990.

Frohlich, C., The nature of deep focus earthquakes, *Annu. Rev. Earth Planet. Sci.*, *17*, 227–254, 1989.

Frohlich, C., Note concerning non-double-couple source components from slip along surfaces of revolution, *J. Geophys. Res.*, *95*, 6861–6866, 1990.

Frohlich, C., Earthquakes with non-double-couple mechanisms, *Science*, *264*, 804–809, 1994.

Frohlich, C., Characteristics of well-determined non-double-couple earthquakes in the Harvard CMT catalog, *Phys. Earth and Plan. Int.*, *91*, 213–228, 1995.

Frohlich, C., M. A. Riedesel, and K. D. Apperson, Note concerning possible mechanisms for non-double-couple earthquake sources, *Geophys. Res. Lett.*, *16*, 523–526, 1989.

Frye, K. M., and C. Marone, The effect of humidity on granular friction at room temperature, in review.

Fujita, K., and H. Kanamori, Double seismic zones and stresses of intermediate depth earthquakes, *Geophys. J. R. Astr. Soc.*, *66*, 131–156, 1981.

Giardini, D., Regional deviation of earthquake source mechanisms from the double-couple model, in *Earthquakes: Observations, Theory and Interpretation*, edited by H. Kanamori and E. Boschi, vol. 85 of *Proc. Enrico Fermi Int. Sch. Phys.*, pp. 345–353, North Holland, 1983.

Giardini, D., Systematic analysis of deep seismicity: 200 centroid-moment tensor solutions for earthquakes between 1977 and 1980, *Geophys. J. R. astr. Soc.*, *77*, 883–914, 1984.

Gibowicz, S. J., The mechanism of seismic events induced by mining – a review, in *Rockbursts and Seismicity in Mines*, edited by C. Fairhurst, pp. 3–28, Balkema, Rotterdam, 1990.

Gibowicz, S. J., An anatomy of a seismic sequence in a deep gold mine, *Pure Appl. Geophys.*, *150*, 393–414, 1997.

Gibowicz, S. J., and A. Kijko, *An Introduction to Mining Seismology*, Academic Press, 1994.

Gibowicz, S. J., R. P. Young, S. Talebi, and D. J. Rawlence, Source parameters of seismic events at the Underground Research Laboratory in Manitoba, Canada: Scaling relations for events with moment magnitude smaller than -2, *Bull. Seism. Soc. Am.*, *81*, 1157–1182, 1991.

Gomberg, J., M. L. Blanpied, and N. M. Beeler, Transient triggering of near and distant earthquakes, *Bull. Seismol. Soc. Am.*, *87*, 294–309, 1997.

Gomberg, J., N. M. Beeler, M. L. Blanpied, and P. Bodin, Earthquake triggering by transient and static deformation, *J. Geophys. Res.*, *103*, 24,411–24,426, 1998.

Green, H. W., and P. C. Burnley, A new self-organizing mechanism for deep-focus earthquakes, *Nature*, *341*, 733–735, 1989.

Green, H. W., and H. Houston, The mechanics of deep earthquakes, *Ann. Rev. Earth Plan. Sci.*, *23*, 169–213, 1995.

Green, R. W. E., Keynote lecture: Instrumentation networks for observation of mine-induced seismicity, in *Rockbursts and Seismicity in Mines*, edited by C. Fairhurst, pp. 165–169, Balkema, Rotterdam, 1990.

Griggs, D., and J. Handin, *Rock Deformation*, GSA Memoir 79, 1960.

Hanks, T. C., $f_{\max}$, *Bull. Seism. Soc. Am.*, *72*, 1867–1879, 1982.

Hanks, T. C., a_{rms} and seismic source studies, in *Proceedings of the 1st International Congress on Rockbursts and Seismicity in Mines*, edited by N. C. Gay and E. H. Wainwright, pp. 39–44, S. Afr. Inst. Min. Met., 1984.

Hanks, T. C., and H. Kanamori, A moment magnitude scale, *J. Geophys. Res.*, *84*, 2348–2350, 1979.

Harabaglia, P., Low-frequency source parameters of twelve large earthquakes, Master's thesis, Massachusetts Institute of Technology, 1993.

Hatherton, T., and W. R. Dickinson, The relationship between andesitic volcanism and seismicity in Indonesia, the Lesser Antilles, and other island arcs, *J. Geophys. Res.*, *74*, 5301–5310, 1969.

Hess, D., and A. Soom, Normal vibrations and friction under harmonic loads, Part I, Hertzian contacts, *J. Tribol.*, *113*, 80–86, 1991.

Hill, D., et al., Seismicity remotely triggered by the magnitude 7.3 Landers, California, earthquake, *Science*, *260*, 1617–1623, 1993.

Houston, H., and Q. Williams, Fast rise times and the physical mechanism of deep earthquakes, *Nature*, *352*, 520–522, 1991.

Husseini, M. I., Energy balance for motion along a fault, *Geophys. J. R. astr. Soc.*, *49*, 699–714, 1977.

Husseini, M. I., and M. J. Randall, Rupture velocity and radiation efficiency, *Bull. Seis. Soc. Am.*, *66*, 1173–1187, 1976.

Ida, Y., Cohesive force across the tip of a longitudinal shear crack and Griffith's specific surface energy, *J. Geophys. Res.*, *77*, 3796–3805, 1972.

Ida, Y., The maximum acceleration of seismic ground motion, *Bull. Seis. Soc. Am.*, *63*, 959–968, 1973.

Ide, S., and G. C. Beroza, Does apparent stress vary with earthquake size?, *Geophys. Res. Lett.*, *28*, 3349–3352, 2001.

Ihmlé, P. F., and T. H. Jordan, Teleseismic search for slow precursors to large earthquakes, *Science*, *266*, 1547–1551, 1994.

Ihmlé, P. F., P. Harabaglia, and T. H. Jordan, Teleseismic detection of a slow precursor the the great 1989 Macquarie Ridge earthquake, *Science*, *261*, 177–183, 1993.

Isacks, B., and P. Molnar, Distribution of stresses in the descending lithosphere from a global survey of focal-mechanism solutions of mantle earthquakes, *Rev. Geophys. and Space Phys.*, *9*, 103–174, 1971.

Izutani, Y., and H. Kanamori, Scale-dependence of seismic energy-to-moment ratio for strike-slip earthquakes in Japan, *Geophys. Res. Lett.*, *28*, 4007–4010, 2001.

James, D. E., and J. A. Snoke, Structure and tectonics in the region of flat subduction beneath central Peru: Crust and uppermost mantle, *J. Geophys. Res.*, *99*, 6899–6912, 1994.

Johnson, T., Time-dependent friction of granite: Implications for precursory slip on faults, *J. Geophys. Res.*, *86*, 6017–6028, 1981.

Johnston, J. C., A survey of mining associated rockbursts, Master's thesis, Massachusetts Institute of Technology, 1988.

Johnston, J. C., and M. H. Einstein, A survey of mining associated seismicity, in *Rockbursts and Seismicity in Mines*, edited by C. Fairhurst, pp. 121–125, Balkema, Rotterdam, 1990.

Jordan, T. H., Far-field detection of slow precursors to fast seismic ruptures, *Geophys. Res. Lett.*, *18*, 2019–2022, 1991.

Jost, M. L., T. Büßelberg, Ö. Jost, and H. P. Harjes, Source parameters of injection-induced microearthquakes at 9 km depth at the KTB deep drilling site, Germany, *Bull. Seism. Soc. Am.*, *88*, 815–832, 1998.

Joughin, N. C., The measurement and analysis of earth motion resulting from underground rock failure, Ph.D. thesis, University of the Witwatersrand, 1966.

Joughin, N. C., and A. J. Jager, Fracture of rock at stope faces in South African gold mines, in *Rockbursts: Prediction and Control*, edited by L. Richards, pp. 53–66, Inst. Min. and Metall., London, U. K., 1983.

Kanamori, H., and D. Anderson, Theoretical basis of some empirical relations in seismology, *Bull. Seism. Soc. Am.*, *65*, 1073–1095, 1975.

Kanamori, H., and T. H. Heaton, Constraints on earthquake inferred from radiated energy, *EOS Trans. AGU*, *79*, F. 610, 1998.

Kanamori, H., J. Mori, E. Hauksson, T. H. Heaton, L. K. Hutton, and L. M. Jones, Determination of earthquake energy release and m_l using TERRAscope, *Bull. Seismol. Soc. Am.*, *83*, 330–346, 1993.

Kao, H., and W.-P. Chen, Earthquakes along the Ryukyu-Kyushu arc: Strain segmentation, lateral compression, and the thermomechanical state of the plate interface, *J. Geophys. Res.*, *96*, 21,443–21,485, 1991.

Kao, H., and W.-P. Chen, The double seismic zone in Kuril-Kamchatka: The tale of two overlapping single zones, *J. Geophys. Res.*, *99*, 6913–6930, 1994.

Karner, S. L., and C. Marone, The effect of shear load on frictional healing in simulated fault gouge, *Geophys. Res. Lett.*, *25*, 4561–4564, 1998.

Karner, S. L., and C. Marone, Frictional restrengthening in simulated fault gouge: Effect of shear load perturbations, *J. Geophys. Res.*, *106*, 19,319–19,337, 2001.

Kijko, A., B. Drzezla, and T. Stankiewicz, Bimodal character of the distribution of extreme seismic events in Polish mines, *Acta Geophys. Pol.*, *35*, 159–168, 1987.

King, C. Y., R. D. Nason, and R. O. Burford, Coseismic steps recorded on creepmeters along the San Andreas fault, *J. Geophys. Res.*, *82*, 1655–1661, 1977.

Kiratzi, A. A., Active deformation in the Vrancea Region, Rumania, *Pure Appl. Geophys.*, *140*, 391–402, 1993.

Knopoff, L., and M. Randall, The compensated linear-vector dipole: A possible mechanism for deep earthquakes, *J. Geophys. Res.*, *75*, 4957–4963, 1970.

Kostrov, B. V., and S. Das, *Principles of Earthquake Source Mechanics*, Cambridge Univ. Press, 1988.

Kosuga, M., T. Sato, A. Hasegawa, T. Matsuzawa, S. Suzuki, and Y. Motoya, Spatial distribution of intermediate-depth earthquakes with horizontal or vertical nodal planes beneath northeastern Japan, *Phys. Earth Plan. Int.*, *93*, 63–89, 1996.

Kubas, A., and S. A. Sipkin, Non-double-couple earthquake mechanisms in the Nazca plate subduction zone, *Geophys. Res. Lett.*, *14*, 339–342, 1987.

Kudrolli, A., M. Wolpert, and J. P. Gollub, Cluster formation due to collisions in granular material, *Phys. Rev. Lett.*, *78*, 1383–1386, 1997.

Kuge, K., and H. Kawakatsu, Analysis of a deep "non double couple" earthquake using very broadband data, *Geophys. Res. Lett.*, *17*, 227–230, 1990.

Kuge, K., and H. Kawakatsu, Deep and intermediate-depth non-double couple earthquakes: Interpretation of moment tensor inversions using various passbands of very broadband seismic data, *Geophys. J. Int.*, *111*, 589–606, 1992.

Kuge, K., and H. Kawakatsu, Significance of non-double couple components of deep and intermediate-depth earthquakes: Implications from moment tensor inversions of long-period seismic waves, *Phys. Earth and Plan. Int.*, *75*, 243–266, 1993.

Kuge, K., and T. Lay, Data-dependent non-double-couple components of shallow earthquake source mechanisms: Effect of waveform inversion instability, *Geophys. Res. Lett.*, *21*, 9–12, 1994a.

Kuge, K., and T. Lay, Systematic non-double-couple components of earthquake mechanisms: The role of fault zone irregularity, *J. Geophys. Res.*, *99*, 15,457–15,467, 1994b.

Kumar, M. R., and N. P. Rao, Significant trends related the the slab seismicity and tectonics in the Burmese arc region from Harvard CMT solutions, *Phys. Earth Plan. Int.*, *90*, 75–80, 1995.

Linker, M., and J. H. Dieterich, Effects of variable normal stress on rock friction: Observations and constitutive equations, *J. Geophys. Res.*, *97*, 4923–4940, 1992.

Lockner, D., R. Summers, and J. Byerlee, Effects of temperature and sliding rate on frictional strength of granite, *Pure Appl. Geophys.*, *124*, 445–469, 1986.

Madariaga, R., Dynamics of an expanding circular fault, *Bull. Seis. Soc. Am.*, *66*, 639–666, 1976.

Mair, K., and C. Marone, Friction of simulated fault gouge for a wide range of velocities, *J. Geophys. Res.*, *104*, 28,899–28,914, 1999.

Marone, C., Laboratory-derived friction laws and their application to seismic faulting, *Annu. Rev. Earth Planet. Sci.*, *26*, 643–696, 1998a.

Marone, C., The effect of loading rate on static friction and the rate of fault healing during the earthquake cycle, *Nature*, *391*, 69–72, 1998b.

Marone, C., and B. Kilgore, Scaling of the critical slip distance for seismic faulting with shear strain in fault zones, *Nature*, *362*, 618–621, 1993.

Marone, C., C. B. Raleigh, and C. H. Scholz, Frictional behavior and constitutive modeling of simulated fault gouge, *J. Geophys. Res.*, *95*, 7007–7025, 1990.

Marone, C., J. E. Vidale, and W. L. Ellsworth, Fault healing inferred from time dependent variations in source properties of repeating earthquakes, *Geophys. Res. Lett.*, *22*, 3095–3098, 1995.

Mavko, G. M., Fault interaction near Hollister, California, *J. Geophys. Res.*, *87*, 7807–7816, 1982.

Mavko, G. M., S. Schulz, and B. D. Brown, Effects of the 1983 Coalinga, California, earthquake on creep along the San Andreas fault, *Bull. Seismol. Soc. Am.*, *75*, 475–489, 1985.

Mayeda, K., and W. R. Walter, Moment, energy, stress drop, and source spectra of western United States earthquakes from regional coda envelopes, *J. Geophys. Res.*, *101*, 11,195–11,208, 1996.

McGarr, A., Violent deformation of rock near deep-level tabular excavations–seismic events, *Bull. Seism. Soc. Am.*, *61*, 1453–1466, 1971.

McGarr, A., Scaling of ground motion parameters, state of stress, and focal depth, *J. Geophys. Res.*, *89*, 6969–6979, 1984a.

McGarr, A., Some applications of seismic source mechanism studies to assessing underground hazard, in *Proceedings of the 1st International Congress on Rockbursts and Seismicity in Mines, Johannesburg*, edited by N. C. Gay and E. H. Wainwright, pp. 199–208, South Afr. Inst. Mining & Metallurgy, 1984b.

McGarr, A., Moment tensors of ten Witwatersrand mine tremors, *Pure Appl. Geophys.*, *139*, 781–800, 1992.

McGarr, A., On relating apparent stress to the stress causing earthquake fault slip, *J. Geophys. Res.*, *104*, 3003–3011, 1999.

McGarr, A., S. M. Spottiswoode, N. C. Gay, and W. D. Ortlepp, Observations relevant to seismic driving stress, stress drop, and efficiency, *J. Geophys. Res.*, *84*, 2251–2261, 1979.

McGuire, J. J., and D. A. Wiens, A double seismic zone in New Britain and the morphology of the Solomon plate at intermediate depths, *Geophys. Res. Lett.*, *22*, 1965–1968, 1995.

McGuire, J. J., P. F. Ihmlé, and T. H. Jordan, Time-domain observations of a slow precursor to the 1994 Romanche transform earthquake, *Science*, *274*, 82–85, 1996.

Meade, C., and R. Jeanloz, Deep-focus earthquakes and recycling of water into the earth's mantle, *Science*, *252*, 68–72, 1991.

Mendecki, A. J., ed., *Seismic Monitoring in Mines*, Chapman & Hall, 1997.

Mendecki, A. J., G. V. Aswegen, J. N. R. Brown, and P. Hewlett, The Welkom seismological network, in *Rockbursts and Seismicity in Mines*, edited by C. Fairhurst, pp. 237–244, Balkema, Rotterdam, 1990.

Molnar, P., and L. R. Sykes, Tectonics of the Caribbean and Middle America regions from focal mechanisms and seismicity, *Geol. Soc. Am. Bull.*, *80*, 1639–1684, 1969.

Nadeau, R. M., and L. R. Johnson, Seismological studies at Parkfield VI: Moment release rates and estimates of source parameters for small repeating earthquakes, *Bull. Seismol. Soc. Am.*, *88*, 790–814, 1998.

Nadeau, R. M., and T. V. McEvilly, Fault slip rates at depth from recurrence intervals of repeating microearthquakes, *Science*, *285*, 718–721, 1999.

Nakatani, M., A new mechanism of slip weakening and strength recovery of friction associated with the mechanical consolidation of gouge, *J. Geophys. Res.*, *103*, 27,239–27,256, 1998.

Ortlepp, W. D., *Rock Fracture and Rockbursts: An Illustrative Study*, South African Inst. Min. and Metall., 1997.

Palmer, A. C., and J. R. Rice, The growth of slip surfaces in the progressive failure of over-consolidated clay, *Proc. Roy. Soc. London, Ser. A*, *332*, 527–548, 1973.

Papageorgiou, A., and K. Aki, A specific barrier model for the quantitative description of inhomogeneous faulting and the prediction of strong ground motion, I, Description of the model, *Bull. Seismol. Soc. Am.*, *73*, 693–722, 1983a.

Papageorgiou, A., and K. Aki, A specific barrier model for the quantitative description of inhomogeneous faulting and the prediction of strong ground motion, II, Applications of the model, *Bull. Seismol. Soc. Am.*, *73*, 953–978, 1983b.

Papageorgiou, A. S., On two characteristic frequencies of acceleration spectra: Patch corner frequency and $f_{\max}$, *Bull. Seismol. Soc. Am.*, *78*, 509–529, 1988.

Pascal, G., Seismotectonics of the Papua New Guinea-Solomon Islands region, *Tectonophysics*, *57*, 7–34, 1979.

Pascal, G., B. L. Isacks, M. Barazangi, and J. Dubois, Precise relocation of earthquakes and seismotectonics of the New Hebrides island arc, *J. Geophys. Res.*, *83*, 4957–4973, 1978.

Peacock, S. M., Are the lower planes of double seismic zones caused by serpentine dehydration in subducting oceanic mantle?, *Geology*, *29*, 299–302, 2001.

Pegler, G., S. Das, and J. H. Woodhouse, A seismological study of the eastern New Guinea and the western Solomon Sea regions and its tectonic implications, *Geophys. J. Int.*, *122*, 961–981, 1995.

Polycarpou, A. A., and A. Soom, Boundary and mixed friction in the presence of dynamic normal loads, Part I, System model, *J. Tribol.*, *117*, 255–260, 1995a.

Polycarpou, A. A., and A. Soom, Boundary and mixed friction in the presence of dynamic normal loads, Part II, Friction transients, *J. Tribol.*, *117*, 261–266, 1995b.

Ponce, L., R. Gaulon, G. Suárez, and E. Lomas, Geometry and state of stress of the downgoing Cocos plate in the Isthmus of Tehuantepec, Mexico, *Geophys. Res. Lett.*, *19*, 773–776, 1992.

Prejean, S. G., and W. L. Ellsworth, Observations of earthquake source parameters at 2 km depth in the Long Valley caldera, eastern California, *Bull. Seismol. Soc. Am.*, *91*, 165–177, 2001.

Prévot, R., J. L. Chatelain, S. W. Roecker, and J. R. Grasso, A shallow double seismic zone beneath the central New Hebrides (Vanuatu): Evidence for fragmentation and accretion of the descending plate?, *Geophys. Res. Lett.*, *21*, 2159–2162, 1994.

Protti, M., F. Güendel, and K. McNally, Correlation between the age of the subducting Cocos plate and the geometry of the Wadati-Benioff zone under Nicaragua and Costa Rica, in *Geologic and Tectonic Development of the Caribbean Plate Boundary in Southern Central America*, edited by P. Mann, vol. 295 of *GSA Special Papers*, pp. 309–326, GSA, 1995.

Prugger, A. F., and D. J. Gendzwill, Results of microseismic monitoring at the Cory mine, 1981-1984, in *Rockbursts and Seismicity in Mines*, edited by C. Fairhurst, pp. 215–219, Balkema, Rotterdam, 1990.

Ratchkovsky, N. A., J. Pujol, and N. N. Biswas, Relocation of earthquakes in the Cook Inlet area, south central Alaska, using the Joint Hypocenter Determination method, *Bull. Seism. Soc. Am.*, *87*, 620–636, 1997.

Rice, J. R., and J.-C. Gu, Earthquake aftereffects and triggered seismic phenomena, *Pure Appl. Geophys.*, *121*, 187–219, 1983.

Riedesel, M. A., and T. H. Jordan, Multiple-band estimates of moment tensors at low frequencies and their uncertainties, *EOS*, *66*, 301, 1985.

Riedesel, M. A., and T. H. Jordan, Display and assessment of seismic moment tensors, *Bull. Seismol. Soc. Am.*, *79*, 85–100, 1989.

Rubin, A. M., D. Gillard, and J.-L. Got, Streaks of microearthquakes along creeping faults, *Nature*, *400*, 635–641, 1999.

Ruina, A., Slip instability and state variable friction laws, *J. Geophys. Res.*, *88*, 10,359–10,370, 1983.

Rundle, J. B., Derivation of the complete Gutenberg-Richter magnitude-frequency relation using the principle of scale invariance, *J. Geophys. Res.*, *94*, 12,337–12,342, 1989.

Rydelek, P. A., and I. S. Sacks, Testing the completeness of earthquake catalogues and the hypothesis of self-similarity, *Nature*, *337*, 251–253, 1989.

Sammis, C. G., and S. J. Steacy, The micromechanics of friction in a granular layer, *Pure Appl. Geophys.*, *142*, 777–794, 1994.

Scholz, C. H., The critical slip distance for seismic faulting, *Nature*, *336*, 761–763, 1988.

Scholz, C. H., *The Mechanics of Earthquakes and Faulting*, Cambridge University Press, New York, 1990, 439 pp.

Scott, D. R., C. J. Marone, and C. G. Sammis, The apparent friction of granular fault gouge in sheared layers, *J. Geophys. Res.*, *99*, 7231–7246, 1994.

Silver, P. G., and T. H. Jordan, Optimal estimation of scalar seismic moment, *Geophys. J. R. Astr. Soc.*, *70*, 755–787, 1982.

Singh, S. K., and F. Mortera, Source time functions of large Mexican subduction earthquakes, morphology of the Benioff zone, age of the plate, and their tectonic implications, *J. Geophys. Res.*, *96*, 21,487–21,502, 1991.

Skåre, T., and J.-E. Ståhl, Static and dynamic friction processes under the influence of external vibrations, *Wear*, *154*, 177–192, 1992.

Sleep, N. H., The double seismic zone in downgoing slabs and the viscosity of the mesosphere, *J. Geophys. Res.*, *84*, 4565–4571, 1979.

Sleep, N. H., E. Richardson, and C. Marone, Physics of friction and strain rate localization in synthetic fault gouge, *J. Geophys. Res.*, *105*, 25,875–25,890, 2000.

Spottiswoode, S. M., Management application of mine seismicity studies, in *Rockbursts and Seismicity in Mines*, edited by N. C. Gay and E. H. Wainwright, p. 347, S. Afr. Inst. Min. Met., 1984.

Spottiswoode, S. M., and A. McGarr, Source parameters of tremors in a deep-level gold mine, *Bull. Seism. Soc. Am.*, *65*, 93–112, 1975.

Spudich, P., L. K. Steck, M. Hellweg, J. B. Fletcher, and L. M. Baker, Transient stresses at Parkfield, California, produced by the M 7.4 Landers earthquake of June 28, 1992: Observations from the UPSAR dense seismograph array, *J. Geophys. Res.*, *100*, 675–690, 1995.

Su, W.-J., R. L. Woodward, and A. M. Dziewonski, Degree-12 model of shear velocity heterogeneity in the mantle, *J. Geophys. Res.*, *99*, 6945–6980, 1994.

Tada, T., and K. Shimazaki, How much does a high-velocity slab contribute to the apparent non-double-couple components in deep-focus earthquakes?, *Bull. Seismol. Soc. Am.*, *84*, 1272–1278, 1994.

Talebi, S., and R. P. Young, Characterizing microseismicity associated with stope development, in *Rockbursts and Seismicity in Mines*, edited by C. Fairhurst, pp. 189–194, Balkema, Rotterdam, 1990.

Tanton, J. H., T. F. McCarthy, and T. O. Hagan, The introduction of stabilizing pillars to reduce rockbursts at western deep levels, limited, in *Proceedings of the 1st International Congress on Rockbursts and Seismicity in Mines*, edited by N. C. Gay and E. H. Wainwright, pp. 245–252, S. Afr. Inst. Min. Met., 1984.

Taylor, D. W. A., J. A. Snoke, I. S. Sacks, and T. Takanami, Nonlinear frequency-magnitude relationships for the Hokkaido Corner, Japan, *Bull. Seism. Soc. Am.*, *80*, 340–353, 1990.

Trifu, C.-I., and M. Radulian, Frequency-magnitude distribution of earthquakes in Vrancea: Relevance for a discrete model, *J. Geophys. Res.*, *96*, 4301–4311, 1991.

Trifu, C.-I., T. I. Urbancic, and R. P. Young, Non-similar frequency-magnitude distribution for $m < 1$ seismicity, *Geophys. Res. Lett.*, *20*, 427–430, 1993.

Tullis, T. E., and J. D. Weeks, Constitutive behavior and stability of frictional sliding of granite, *Pure Appl. Geophys.*, *124*, 383–414, 1986.

Tworzydlo, W. W., and E. Becker, Influence of forced vibrations on the static coefficient of friction–Numerical modeling, *Wear*, *143*, 175–196, 1991.

Urbancic, T. I., C.-I. Trifu, and R. P. Young, Microseismicity derived fault-planes and their relationship to focal mechanism, stress inversion, and geologic data, *Geophys. Res. Lett.*, *20*, 2475–2478, 1993.

Vidale, J. E., W. L. Ellsworth, A. Cole, and C. Marone, Variations in rupture process with recurrence interval in a repeated small earthquake, *Nature*, *368*, 624–626, 1994.

Wang, C., and Y. Cai, Sensitivity of earthquake cycles on the San Andreas fault to small changes in regional compression, *Nature*, *388*, 158–161, 1997.

Wang, W., and C. H. Scholz, Micromechanics of the velocity and normal stress dependence of rock friction, *Pure and Appl. Geophys.*, *143*, 303–315, 1994.

Wong, I. G., and A. McGarr, Implosional failure in mining-induced seismicity: A critical review, in *Rockbursts and Seismicity in Mines*, edited by C. Fairhurst, pp. 45–51, Balkema, Rotterdam, 1990.

Woodhouse, J. H., and A. M. Dziewonski, Mapping the upper mantle: Three-dimensional modeling of earth structure by inversion of seismic waveforms, *J. Geophys. Res.*, *89*, 5953–5986, 1984.

Young, R. P., S. Talebi, D. A. Hutchins, and T. I. Urbancic, Analysis of mining-induced microseismic events at Strathcona Mine, Sudbury, Canada, *Pure Appl. Geophys.*, *129*, 455–474, 1989.

Zhou, H., Observations on earthquake stress axes and seismic morphology of deep slabs, *Geophys. J. Int.*, *103*, 377–401, 1990.